



POLITECNICO DI MILANO  
DEPARTMENT OF CIVIL AND ENVIRONMENTAL ENGINEERING  
DOCTORAL PROGRAMME STRUCTURAL, SEISMIC AND GEOTECHNICAL ENGINEERING

---

**STEEL FIBRE REINFORCED CONCRETE PLATES:  
STRUCTURAL RESPONSE AND RELIABILITY OF  
DESIGN METHODS**

Doctoral Dissertation of:  
**Ali Pourzarabi**

Supervisor:

**Prof. Marco di Prisco**

Tutor:

**Prof. Gabriella Bolzon**

The Chair of the Doctoral Program:

**Prof. Umberto Perego**

XXXII cycle

Ali Pourzarabi

**Steel fibre reinforced concrete plates: Structural response and reliability of design methods**

©September 2021. All rights reserved.

e-mail:

`ali.pourzarabi@polimi.it`

STEEL FIBRE REINFORCED CONCRETE PLATES: STRUCTURAL  
RESPONSE AND RELIABILITY OF DESIGN METHODS

A thesis presented to  
the academic faculty

by:

**Ali Pourzarabi**

In Partial Fulfillment of  
the Requirements for the Degree  
*Doctoral of Philosophy*  
*in*

Structural, Seismic and Geotechnical Engineering

XXXII cycle



Doctoral Programme Structural, Seismic and Geotechnical Engineering  
Department of Civil and Environmental Engineering  
POLITECNICO DI MILANO  
XXXII cycle

**The chair of the Doctoral Programme:**

Prof. Umberto Perego

**Board Committee:**

Prof. Raffele Ardito  
Prof. Patrick Bamonte  
Prof. Fabio Biondini  
Prof. Gabriella Bolzon  
Prof. Matteo Bruggi  
Prof. Claudia Comi  
Prof. Alberto Corigliano  
Prof. Dario Coronelli  
Prof. Gabriele Della Vecchia  
Prof. Claudio Di Prisco  
Prof. Marco Di Prisco  
Prof. Roberto Fedele  
Prof. Roberto Felicetti  
Prof. Liberato Ferrara  
Prof. Attilio Frangi  
Prof. Aldo Ghisi  
Prof. Cristina Jommi  
Prof. Maurizio Lualdi  
Prof. Stefano Mariani  
Prof. Luca Martinelli  
Prof. Roberto Paolucci  
Prof. Lorenza Petrini  
Prof. Gianpaolo Rosati



*To Fariba and Shahrokh,  
To the love of my life, Ava,  
and in memory of my dear Arash and Pouneh and all 176+1 gone souls in the  
downing of Flight PS752 by the IRGC on January 8th, 2020.*

Mohammad Abaspourqadi (33), Mojtaba Abbasnezhad (26), Seyedmehran Abtahiforoushani (37), Maryam Agha Miri (46), Iman Aghabali (28), Motahereh Ahmadi (8), Mohsen Ahmadi (5), Ramtin Ahmadi (9), Sakineh Ahmadi (30), Mitra Ahmady (46), Mahsa Amiriravi (30), Fareed Arasteh (32), Arshia Arbabbahrami (19), Evin Arsalani (29), Mohammadhossein Asadilari (23), Zeynab Asadilari (21), Amir Ashrafi Habibabadi (28), Mahmood Attar (69), Roja Azadian (42), Ghanimat Azhdari (36), Mehraban Badieli Ardestani (18), Samira Bashiri (29), Mohammad Amin Beirut (29), Negar Borghei (30), Shekoufeh Choupannejad (56), Delaram Dadashnejad (26), Mojgan Daneshmand (43), Asgar Dhirani (74), Hamidreza Djavadi Asll (52), Kian Djavadi Asll (17), Ardalan Ebnoddin Hamidi (48), Kamyar Ebnoddin Hamidi (15), Niloufar Ebrahim (34), Behnaz Ebrahimi Khoei (45), Shahrokh Eghbali Bazoft (59), Shahzad Eghbali Bazoft (8), Parisa Eghbalian (42), Mohammad Mahdi Elyasi (28), Sayedmahdi Emami (60), Sophie Emami (5), Mehdi Eshaghian Dorcheh (24), Reera Esmaeilion (9), Mansour Esnaashary Esfahani (29), Sharieh Faghihi (58), Faezeh Falsafi (46), Faraz Falsafi (31), Aida Farzaneh (33), Shakiba Feghahati (39), Marzieh Foroutan (37), Volodymyr Ivanovych Gaponenko (50), Iman Ghaderpanah (34), Parinaz Ghaderpanah (33), Siavash Ghafouri Azar (35), Daniel Ghandchi (8), Dorsa Ghandchi (16), Kiana Ghasemi (19), Milad Ghasemi Ariani (32), Fatemeh Ghasemi Dastjerdi (25), Amirhossein Ghassemi (32), Mahdieh Ghavi (20), Masoumeh Ghavi (30), Farideh Gholami (38), Amirhossein Ghorbani Bahabadi (21), Suzan Golbabapour (49), Pouneh Gorji (25), Saharnaz Haghighoo (37), Bahareh Hajefandiari (41), Sadaf Hajiaghavand (27), Mahdieh Hajighassemi (38), Sara Hamzei (33), Zahra Hasani/sadi (25), Shahrzad Hashemi (45), Parsa Hassannezhad (16), Sahand Hatefi Mostaghim (32), Hadis Hayatdavoudi (27), Elsa Jadidi (8), Pedram Jadidi (28), Shadi Jamshidi (31), Mohammadamin Jebelli (29), Mohammadreza Kadkhoda Zadeh (40), Saeed Kadkhodazadeh Kashani (29), Bahareh Karamimoghadam (33), Rahimeh Katebi (20), Azadeh Kaveh (40), Fatemeh Kazerani (32), Forough Khadem (38), Serhii Anatoliiovych Khomenko (48), Olga Kobiuk (61), Emil Lindberg (7), Erik Lindberg (9), Raheleh Lindberg (37), Mikael Lindberg (40), Denys Mykhailovych Lykhno (24), Firouzeh Madani (54), Siavash Maghsoudlouestarabadi (43), Paria Maghsoudlouestarabadi (15), Fatemeh Mahmoodi (30), Olena Malakhova (38), Maryam Malek (40), Fereshteh Maleki Dizaje (47), Sara Mamani (36), Ihor Valeriiovych Matkov (34), Mohammadjavand Mianji (27), Mohammad Moieni (35), Rossstin Moghaddam (9), Mehdi Mohammadi (20), Hiva Molani (38), Kurdia Molani (1), Amir Moradi (21), Arvin Morattab (35), Soheila Moshref Razavi Moghaddam (55), Daria Mousavi (14), Dorina Mousavi (9), Pedram Mousavibafrooei (47), Mariia Mykhailivna Mykytiuk (24), Elnaz Nabiyi (30), Farzaneh Naderi (38), Mehrdad Naghib Lahouti (32), Zahra Naghibi (32), Milad Nahavandi (34), Oleksii Yevhenovych Naumkin (42), Arnica Niazi (8), Arsam Niazi (11), Farhad Niknam (44), Alireza Norouzi (19), Ghazal Nourian (26), Alma Oladi (27), Roja Omidbakhsh (23), Amir Hossein Ovaysi (41), Asal Ovaysi (6), Valeriia Yevheniivna Ovcharuk (28), Fatemeh Pasavand (17), Alireza Pey (47), Ayeshe Pourghaderi (36), Mansour Pourjam (53), Naser Pourshabanoshibi (53), Arash Pourzarabi (26), Shahab Raana (36), Jiwan Rahimi (3), Razgar Rahimi (38), Nasim Rahmanifar (25), Niloufar Razzaghi Khamisi (45), Hossain Rezae (20), Mahdi Rezaei (19), Saba Saadat (21), Sara Saadat (23), Zeinolabedin Saadat (29), Kasra Saati (47), Alvand Sadeghi (29), Anisa Sadeghi (10), Mirmohammadmehdi Sadeghi (43), Sahand Sadeghi (39), Neda Sadighi (50), Niloufar Sadr (61), Seyed Noojan Sadr (11), Amirhossein Saedinia (25), Pegah Safarpour (20), Mohammadhossein Saket (33), Mohsen Salahi (31), Mohammad Saleheh (32), Sajedah Saraeian (26), Hamid Reza Setareh Kokab (31), Sheyda Shadkhoo (41), Masoud Shaterpour Khiaban (31), Yuliia Mykolaiivna Solohub (25), Paniz Soltani (29), Kateryna Olehivna Statnik (27), Saeed Tahmasebi Khademasi (35), Mahdi Tajik (20), Shahram Tajik (21), Affa Tarbhai (55), Alina Tarbhai (31), Darya Toghian (22), Arad Zarei (17), Maya Zibaie (15), Sam Zokaie (42)





# Abstract

One of the most intriguing applications of Steel Fibre Reinforced Concrete (SFRC), is in design and construction of slabs. High stress redistribution capacity of these structural elements leads to the creation of large crack areas which allows for exploitation of the benefits that come from the presence of fibres. With the advent of design codes and guidelines, designers are now equipped with tensile laws that enable them to introduce tensile resistance for a cracked concrete. Therefore, it is of utmost importance to investigate the benefits and the shortcomings of application of steel fibres as partial or complete replacement of reinforcing bars in slabs, and to study the reliability of the available tools and methods for design of these elements. A normal design procedure is based on the characteristic properties of the material, i.e. the 5% fractile of its distribution. The tensile properties of SFRC which are derived from tests on small specimens show a large scatter, which results in small characteristic values. On the contrary, the structural resistance of SFRC redundant slabs exhibits a narrow dispersion, very different from the material properties by which they are designed. Corrective factors are suggested in order to fill the gap between the highly dispersed tensile properties and narrowly dispersed structural strength of SFRC slabs.

In this thesis, the behaviour of SFRC plate elements are studied and their combination with rebars is investigated and compared to RC plates. A yield line approach is adopted to predict the load bearing capacity and design resistance of the plates. Proper direct tensile law are derived and implemented in a Non Linear Finite Element Model (NLFEM) to predict the structural response of the plates. Furthermore, a relatively large sample of identical SFRC plates are tested and the scatter of their bearing capacity is compared to the results of the standard characterization tests, in order to find corrective coefficients. Shallow beams are tested in order to highlight the advantages and shortcomings of application of fibres in statically determinate structural schemes. Finally the cracking behaviour of plates and beams are investigated and compared to the available formulations on crack spacing.

The obtained results highlight the significant advantages of applications of fibres. Fibres substantially reduce deflection and crack openings and considerably increase the load bearing capacity of the plates. However, without the presence of rebars, ductility of these elements might be compromised. If so, application of limit analysis which entails considerable rotation capacity at the

---

plastic hinges could be jeopardized. Based on experimental evidence for the ultimate crack opening of the SFRC plates, modified tensile laws are proposed. With Implementation of the modified tensile laws, and with the average residual tensile strength parameters of the SFRC material, the load bearing capacity of the SFRC plates are predicted with satisfactory results. Afterwards, the behaviour of the plates are modeled in a NLFEM, and the importance of the choice of the internal parameter for regularization is highlighted. Some challenges in modelling of the SFRC material which shows hardening after an initial softening in its tensile behaviour is shown. It is discussed that application of fibres in determinate beams can be unreliable and controlled by the heterogeneity of the SFRC, and addition of fibres to RC beams leads to a reduction of ductility. The narrow distribution of structural resistance for the SFRC redundant plates are depicted and proper magnification factors, which compensate the small characteristic values of tensile properties of the SFRC, are derived. Finally the limitations and strength of formulas adopted to predict crack spacing in beams and slabs that incorporated fibres are shown and some suggestions are given.

**Keywords:** Fibre reinforced concrete, slab, plate, tensile constitutive law, characteristic value, design, non linear finite element, yield line analysis, crack spacing.

## Acknowledgements

My sincere appreciation to my supervisor, Prof. Marco di Prisco, for trusting me and making this research possible. I like to thank Prof. Matteo Colombo, for his kind support and his technical advice in conducting the experiments and discussing the results. My appreciations go to Dr. Giulio Zani for his help by generously sharing his expertise, specifically on modelling, and to my friends and colleagues Dr. Isabella Georgia Colombo, Dr. Marco Carlo Rampini, Dr. Paolo Martinelli, and Eng. Katherina Flores Ferreira for their priceless supports and encouragements. I am thankful to Andrea Giovanni Stefanoni without whose help, I would have not been able to test all the specimens I tested. I also owe a dept of gratitude to my former supervisors and friends, Prof. Nicolas Ali Libre, and Dr. Rahil Khoshnazar from whom I learnt the alphabets of research.

I can not thank my parents, Shahrokh and Fariba, enough, for their unconditional love and support. And I honor the memory of my lovely Arash and Pouneh. There is not a second that passes by that I don't have them on my heart and mind.

Last but not least, I owe a lot to my one and only, my dear Ava, that if it was not for her, things would have been very different.

Ali Pourzarabi



# Contents

<b>1</b>	<b>Introduction</b>	<b>1</b>
1.1	Overview . . . . .	3
<b>2</b>	<b>State of the art</b>	<b>7</b>
2.1	Fresh Concrete . . . . .	7
2.2	Compressive behavior . . . . .	8
2.3	Tensile behavior . . . . .	9
2.4	Flexural behavior . . . . .	13
2.5	Fibre pull-out . . . . .	16
2.6	Testing methods and scatter of results . . . . .	19
2.6.1	Testing methods . . . . .	19
2.6.1.1	EN 14651 . . . . .	19
2.6.1.2	ASTM C1399 . . . . .	20
2.6.1.3	ASTM C1609 . . . . .	20
2.6.1.4	RILEM TC 162-TDF . . . . .	20
2.6.1.5	ASTM C1550 . . . . .	21
2.6.1.6	EN 14488-5:2006 . . . . .	21
2.6.1.7	Wedge Splitting Test (WST) . . . . .	22
2.6.1.8	Double Edge Wedge Splitting Test (DEWST) . . . . .	22
2.6.1.9	Double Punch Test (Barcelona) . . . . .	22
2.6.2	Scatter of results . . . . .	22
2.7	Fibre orientation . . . . .	25
2.7.1	Orientation factor . . . . .	31
2.7.1.1	Model Code . . . . .	31
2.7.1.2	Norwegian guideline . . . . .	32
2.7.1.3	German code and Danish guideline . . . . .	33
2.7.1.4	French recommendation . . . . .	33
2.8	Slab testing . . . . .	33
2.8.1	Flat slabs . . . . .	33
2.8.1.1	Aidarov et al . . . . .	34
2.8.1.2	Destrée & Mandl . . . . .	35
2.8.1.3	Fall et al. . . . .	35
2.8.1.4	Facconi et al. . . . .	36
2.8.1.5	di Prisco et al., Parmentier & Van Itterbeek (Limelette slab) . . . . .	37
2.8.1.6	Hedebratt & Silfwerbrand . . . . .	37
2.8.1.7	Døssland . . . . .	37

2.8.1.8	Pujadas et al. . . . .	38
2.8.1.9	Blanco et al. . . . .	38
2.8.2	Slab on grade . . . . .	38
2.9	Durability . . . . .	39
<b>3</b>	<b>Experimental program</b>	<b>43</b>
3.1	Introduction . . . . .	43
3.2	Experiments . . . . .	44
3.2.1	<i>Part A</i> ; RC, SFRC, and R/FRC plates . . . . .	44
3.2.2	<i>Part B</i> ; Scatter of strength of SFRC plates . . . . .	46
3.2.3	Shallow beams . . . . .	46
3.3	Material and casting . . . . .	47
3.4	Testing methods . . . . .	49
3.4.1	Three-point bending test . . . . .	49
3.4.2	Plate tests . . . . .	50
3.4.2.1	Loading . . . . .	50
3.4.2.2	Support condition . . . . .	51
3.4.2.3	Measurements . . . . .	53
3.4.3	Shallow beams . . . . .	55
<b>4</b>	<b><i>Part A</i>: Comparison between SFRC, R/C, and R/FRC plates</b>	<b>57</b>
4.1	Introduction . . . . .	57
4.2	Experimental results . . . . .	58
4.2.1	Tensile characterization of the SFRC . . . . .	58
4.2.2	Plate results . . . . .	59
4.2.2.1	Crack patterns . . . . .	60
4.2.2.2	Load-deflection . . . . .	61
4.2.2.3	Positive cracks . . . . .	65
4.2.2.4	Negative cracks . . . . .	69
4.3	Design resistance and prediction of load bearing capacity of plates . . . . .	72
4.3.1	Yield lines . . . . .	72
4.3.2	SFRC tensile law . . . . .	74
4.3.3	Average and design resisting bending moment . . . . .	77
4.3.4	Failure mechanism . . . . .	82
4.3.5	Design resistance and expected load bearing capacity . . . . .	82
4.3.5.1	Conservative $P_d$ for SFRC and R/FRC plates . . . . .	87
4.3.5.2	Conservative $P_m$ prediction for the SFRC plates . . . . .	88
<b>5</b>	<b>Modelling</b>	<b>95</b>
5.1	Introduction . . . . .	95
5.2	Background . . . . .	96
5.2.1	Concrete tensile constitutive law . . . . .	96
5.2.2	Fracture energy and characteristic length . . . . .	98
5.2.3	Post-peak tensile behaviour . . . . .	102
5.2.4	Fracture energy regularization . . . . .	103
5.3	Derivation of FRC tensile constitutive law . . . . .	106
5.4	Model details: constitutive law, elements, descritization . . . . .	111

5.5	NLFEM of notched beams . . . . .	113
5.5.1	Element type, integration rule, and localization . . . . .	113
5.5.1.1	Quadrilateral element . . . . .	113
5.5.1.2	Triangular element . . . . .	114
5.6	NLFEM of plates . . . . .	117
5.6.1	RC plates . . . . .	117
5.6.2	SFRC plates . . . . .	118
5.6.3	R/FRC plates . . . . .	122
5.6.4	R/FRC-Alt plates . . . . .	122
5.6.5	Comparison of failure patterns . . . . .	123
<b>6</b>	<b>Shallow beams</b>	<b>125</b>
6.1	Introduction . . . . .	125
6.2	Experimental results . . . . .	125
6.3	Estimation of load bearing capacity . . . . .	129
<b>7</b>	<b>Part B: Structural plates Vs. Notched beam specimens; the <math>\kappa</math> factor</b>	<b>133</b>
7.1	Introduction and background . . . . .	133
7.1.1	Reliability analysis of structures . . . . .	137
7.2	Tensile characterization of the SFRC . . . . .	140
7.3	Plate results . . . . .	142
7.4	Magnification of 5% fractile values; the $\kappa$ factor . . . . .	149
7.4.1	Magnification factor in EC2 and CNR-DT 204 . . . . .	153
7.4.1.1	EC 2-Annex L . . . . .	153
7.4.1.2	CNR DT 204-2006 (Italy) . . . . .	155
7.5	Normal or Log-normal? . . . . .	156
7.6	Anomaly in experimental results of plates . . . . .	157
7.7	Derivation of $\kappa$ factor through a global safety format . . . . .	162
<b>8</b>	<b>Cracking</b>	<b>169</b>
8.1	Introduction . . . . .	169
8.2	Crack spacing; state of the art and standards . . . . .	169
8.3	Maximum crack spacing, $S_{r,max}$ . . . . .	174
8.4	Experimental results . . . . .	176
8.4.1	Shallow beams . . . . .	176
8.4.2	Plates; <i>Part A</i> . . . . .	179
8.4.3	Plates; <i>Part B</i> . . . . .	184
8.5	Suggestions to MC2020 and EC2 1992:2020 formulations . . . . .	185
<b>9</b>	<b>Conclusions</b>	<b>191</b>
9.1	Future developments . . . . .	193
	<b>Bibliography</b>	<b>193</b>
	<b>Appendices</b>	<b>211</b>
	A - Shallow beams . . . . .	213

Contents

---

*B* - Crack spacing . . . . . 217  
*C* - Blind prediction of the behavior of S2 plates . . . . . 221



# List of Figures

2.1	Effect of (a) fibre volume for the same aspect ratio (b) aspect ratio for the same volume on the compressive stress-strain curve [92]. . . . .	9
2.2	(a) the parameters of the stress-crack opening law (b) effect of the post-peak slope $a_1$ and (c) the position of the knee-point, $b_2$ , of the tension softening law on the ultimate load reached in the splitting tensile model w.r.t the ultimate load reached with the assumption of linear elasticity [147]. . . . .	11
2.3	(a) modified splitting test with measurement of lateral deformation (b) load-deformation result of such test for FRC showing the presence of two peaks. . . . .	12
2.4	(a) Load versus average strain for the bare bar, RC, and R/FRC specimens, Cracking pattern of the (b) RC specimen, and (c) R/FRC specimen [145]. . .	13
2.5	load-deflection curve for (a) bonded and (b) unbonded specimens [137]. . . .	14
2.6	load-deflection curve for (a) singly reinforced beam with $\rho_s=0.4\rho_b$ (b) with $\rho_s=0.65\rho_b$ and (c) doubly reinforced beam with $\rho_s=0.9\rho_b$ and $\rho'_s=0.0083$ [146]. . . . .	15
2.7	Different stages of the pull-out of a hooked-end fibre [6]. . . . .	17
2.8	influence of fibre and concrete strength on pull-out [35]. . . . .	18
2.9	Test setups according to (a) EN14651 [86](b) four-point bending test [38] (c) wedge splitting test (figure adopted from [131]) (d) panel test according to ASTM C1550 [8](figure adopted from [24]) (e) panel test [87] (f) DEWST [72] and (g) Barcelona test [140]. . . . .	23
2.10	variation of the results of the bending test according to four different methods and two concrete types (NC-HSC) [150]. . . . .	25
2.11	Effect of increasing beam width on (a) fracture energy and (b) coefficient of variation [124]. . . . .	25
2.12	(a) Alignment of fibres in a plane perpendicular to the direction of vibration and the two two directions for the compression test (b) The stress versus lateral strain of the tested specimens in two directions [81]. . . . .	26
2.13	Direct tension test on specimens with aligned fibres (ASFRC) and normal SFRC in a mixture with a w/c of (a) 0.42 (b) 0.36 ,and (c) 0.32 [160]. . . . .	27
2.14	fibre orientation in a (a) smaller rectangular slab (b) larger square slab [31]. . .	27
2.15	Effect of fibre orientation on flexural behaviour of FRC, (a) slab cast from the center (b) Specimens cut from 30 cm distance from the center and (c) from 50 cm [209]. . . . .	29
2.16	Fibre orientation in polymeric material with yield stress of (a) $\tau_0=25$ Pa (b) $\tau_0=70$ Pa [34]. . . . .	30
2.17	(a) slab and specimen geometries and casting direction (b) results of 4 point bending test on specimens cut from the slabs [94]. . . . .	31

2.18	3D fibre orientation [185]. . . . .	32
2.19	(a) The overall configuration of the flat slab and loading condition and (b) formation of yield lines on top and bottom of the slab panels [3]. . . . .	34
2.20	(a) The column-slab system [68] (b) SFRC slab and the APC rebars [134] and (c) the finished structure [134]. . . . .	35
2.21	load deflection results of the slabs reinforced with rebars (CR), reinforced with rebars and fibres (CFR), and reinforced with only fibres (FR) [91]. . . . .	36
2.22	(a) load-deflection response and (b) the experimental configuration [52]. . . . .	40
3.1	Experimental program of <i>Part A</i> . Twenty plates are tested in three testing configurations of S1, S2 and S3. RC, SFRC, R/FRC and R/FRC-Alt reinforcing solutions are implemented. Two specimens are tested for each reinforcing type. . . . .	45
3.2	Experimental programme of <i>Part B</i> . Twelve SFRC plates were tested along with eleven notched beams. The number in parenthesis is the age, expressed in days, at which the test was carried out. . . . .	46
3.3	(a) The dimensions of the shallow beams and the loading condition (b) three SFRC (B-SFRC) and three R/FRC (B-R/FRC) beams were tested. . . . .	47
3.4	Direct tensile test on four rebar specimens. . . . .	49
3.5	(a) The job-site (b) placement of the anchorage device (c) casting of the plates (d) prismatic beams and cubes for compressive strength measurement (e) casting of the shallow beams. . . . .	50
3.6	The load-deformation of the neoprene sheet which was placed between the loading head and the plate surface. . . . .	51
3.7	(a)left- Detailing of the support and, right- positioning of the support and dimensions related to the placement of rebars (b)The anchorage device adopted to create a bilateral support for the plate elements and its specifications. . . . .	52
3.8	The measurements regarding the corner displacement of the slabs and the deformation of the anchorage. . . . .	53
3.9	The position and label of instruments adopted to measure the opening of positive and negative crack on plates in series (a) S1, (b) S2, and (c) S3. . . . .	54
3.10	The position and gauge length of the instruments. . . . .	55
4.1	Nominal stress-CMOD results obtained at (a) 34 days and (b) 167, 220, and the average of 167 and 220 days. . . . .	59
4.2	Crack pattern of SFRC, R/C, and R/FRC plates tested in S1, S2 and S3 configurations. Bottom cracks are shown with gray lines and the top cracks are shown with black lines. . . . .	62
4.3	Load-deflection curve for (a) S1 and (b) S2 series. . . . .	63
4.4	Load-deflection curves of S3 plates. . . . .	66
4.5	Load-COD measurements carried out on (a) COD <sub>b</sub> instruments on the S1 series (b) COD <sub>b</sub> instruments on S2 series (c) COD-L <sub>b</sub> measurements on S1 series and (d) COD-L <sub>b</sub> measurements on S2 series. . . . .	67
4.6	Load-COD measurements for the S3 plates at different positions. . . . .	70
4.7	def-COD measurements on the top surface of the plates for (a) S1, (b) S2, and (c) S3 series. . . . .	71

4.8	(a) Assumptions made by kwiecinski in formulating a yield line criteria with partial kinking of rebars at inclined crack (b) Graphical representation of ultimate resisting moment at different inclination angles of yield line for different assumptions [125]. . . . .	74
4.9	The bilinear $\sigma - CMOD$ tensile constitutive law given in (a) MC2010 and CNR-DT 204 and (b) in EC2-annex L. . . . .	75
4.10	The ratio of the safety factor corresponding to the design resistance $\gamma_d = P_{Exp}/P_d$ , to the safety factor corresponding to the realistic prediction of the load bearing capacity of the plates $\gamma_m = P_{Exp}/P_m$ , for the (a) R/FRC plates with CNR-DT 204 tensile law, (b) R/FRC plates with EC2-Annex L draft tensile law (c) SFRC plates with CNR-DT 204 tensile law, and (d) SFRC plates with EC2-Annex L tensile law. The computation of design resistance is carried out with design value of tensile parameters from tests carried out at 34 days, or at an age close to the plate test with the original or magnified values. magnified values are shown with $P_{d*}$ . . . . .	89
4.11	The ratio of the experimental maximum load to the predicted average load bearing capacity of the plates, $\gamma_m = P_{Exp}/P_m$ , based on a yield line method, and adopting the tensile constitutive law according to (a) CNR-DT 204 and (b) EC2- Annex L draft. . . . .	90
4.12	Load-CMOD <sub>Ave</sub> for the SFRC plates of the S1 and S2 series. CMOD <sub>Ave</sub> is the COD measured by each of the COD-L <sub>b</sub> long instruments divided by the number of cracks that are captured by these instruments. . . . .	90
4.13	Assumptions for a direct tensile law driven for different values of $w_u$ . . . . .	92
4.14	The ratio $\gamma_m = P_{Exp}/P_m$ , with variation of $w_u$ . . . . .	93
5.1	Process of cracking in plain concrete [170]. . . . .	96
5.2	(a) Position of strain gauges and (b) the experimental results for gauge 2 and 3 in the fracture zone and for gauge 1, 4 and 9 outside of this zone [109] (c) simple model for tensile fracture where stresses depend on the width of a slit [155]. . . . .	97
5.3	A general case for the variation of stress with crack opening [112]. . . . .	98
5.4	(a) the FPZ comprised of a inner softening zone and an outer micro-fracture zone with strips of material having different local fracture energy $g_f(x)$ (b) the contour of the maximum tensile stresses and the fact that the extent of the FPZ contracts approaching the back of the specimen (c) the decrease of $g_f$ along the ligament and the size dependency of $G_f$ [114]. . . . .	100
5.5	Bilinear cohesive law and the designation of fracture energy $G_F$ and the initial fracture energy $G_f$ [17]. . . . .	101
5.6	(a) Calculated load-displacement diagrams for a three-point bending test for (b) 36 different strain-softening diagrams with the same fracture energy, $G_f$ [168]. . . . .	103
5.7	Effect of (a) different tension softening models on the (b) load-displacement curve of three-point bending test [195]. . . . .	103
5.8	(a) Tensile stress-w diagram versus (b) tensile stress-strain diagram [171]. . . . .	105
5.9	Introduction of a numerical characteristic length to adjust the softening branch of the tensile constitutive law to regularize the fracture energy. . . . .	105
5.10	Estimate of the crack band width, $h$ , in (a) symmetric mode I problem and (b) non-symmetric problem [171]. . . . .	106

5.11	The $f_{ct,fl}$ values for the notched beams tested in <i>Part A</i> of the campaign at two different ages. . . . .	108
5.12	(a) comparison of the post-cracking tensile constitutive law given in MC 1990 and MC 2010 (b) Tensile constitutive law devised and adopted for FRC. . . .	109
5.13	(a) The obtained direct tensile law for the SFRC material tested at 167 and 220 days through inverse analysis, and The comparison of the experimental nominal stress-CMOD curves with the curves obtained from a multi-layer plane section approach based on these tensile constitutive laws for (b) 167 days and (c) 220 days results of <i>Part A</i> . . . . .	110
5.14	Boundary conditions and descritization of the models for plates when C3D8R elements are adopted. When C3D20 elements are utilized, element size is increased. . . . .	112
5.15	Results of FEM with different elements with an element size of (a) 5 mm and (b) 2.5 mm. . . . .	114
5.16	Comparison of spread of plastic strains on three points on the nominal stress-CMOD curves of the notched beams for two element sizes of (a) 2.5 mm in which a flaw is also introduced in the model, and (b) 5 mm. . . . .	115
5.17	(a) comparison of experimental nominal stress-CMOD result with the result of the model with constant strain triangular elements (CPE3) (b) mesh of the notched beam (c) distribution of maximum principal plastic strain (P.E.) on the elements on top of the notch for points 1 and 2 on curve related to the model result with transformation of the P.E values to crack opening and (d) the crack opening corresponding to the elements on top of the notch at points 1 and 2 on the model curve. . . . .	116
5.18	(a) Stress-Crack opening relation according to the model of Cornelissen et al. [54] and (b) Compressive stress-strain relationship adopted for modeling of the plates according to Eq.5.8. . . . .	118
5.19	Results of the NLFEM for the (a) load-deflection response and (b) load-COD behaviour of the RC plates of the S2 series. . . . .	118
5.20	Comparison of NLFEM results with the experimental load-deflection curves of SFRC plates, and the effect of the regularizaiton for (a) S1 and (b) S2 plates. . . . .	119
5.21	Extent of numerical crack width shown by mapping maximum principal plastic strain on the crack patterns of the plates for a point shown shown on the load deflection behaviour of the S1 SFRC plates in (a) and (b), for S2 SFRC plate in (c) and (d). . . . .	120
5.22	Comparison of NLFEM results with the experimental load-COD response of the SFRC plates in (a) S1 and (b) S2 series. . . . .	121
5.23	Comparison of the experimental load-deflection response for the SFRC plates of the S3 series with different element types and in one case, with introduction of a realistic temperature profile. . . . .	121
5.24	Comparison of NLFEM results with the experimental curves of (a) load-deflection and (b) load-COD, for the R/FRC plates. . . . .	123
5.25	Comparison of NLFEM results with the experimental curves of (a) load-deflection and (b) load-COD, for the R/FRC-Alt plates. . . . .	123
5.26	Distribution of maximum principal plastic strain for the (a) RC, (b) SFRC, (c) R/FRC, and (d) R-FRC-Alt plates of the S2 configuration. . . . .	124

6.1	Crack pattern of the tested beams. The localized crack is shown with a thick line, and the dashed lines show the length of the gauge by which the COD is measured. . . . .	126
6.2	Load-deflection curves of the (a) B-FRC and (b) B-R/FRC beams. . . . .	127
6.3	Load-COD curves of the (a) B-FRC and (b) B-R/FRC beams. . . . .	127
6.4	Comparison of the nominal stress-CMOD of the B-FRC1 shallow beam with the average and 5% fractile curve of the nominal stress-CMOD of the tested notched beams. The elastic part of the tensile deformation for the shallow beam is removed from the readings, therefore, the curve corresponding to this specimen starts from negative values. . . . .	128
6.5	Comparison of the load-COD curves of the B-R/FRC beams taking into account that the localized crack was out of the gauge length for the B-R/FRC3 beam. . . . .	129
6.6	The load-CMOD <sub>Ave</sub> curve for the (a) B-FRC and (b) B-R/FRC specimens. CMOD <sub>Ave</sub> is obtained by dividing the overall reading of the gauge by the number of cracks as shown in Fig. 6.1. . . . .	130
6.7	The tensile constitutive laws adopted for prediction of the load bearing capacity of the beams. Once the tensile law given in EC2 is selected and once the tensile law is found through back analysis of the stress-CMOD results with an assumption of $w_u=0.7$ mm for B-FRC beam and $w_u=0.9$ mm for B-R/FRC beams. . . . .	131
7.1	Variation of the coefficient of variation of the measured fracture energy, $G_f$ with the ratio of ligament size, $A_{lig}$ , to the maximum aggregate size, $D_{max}$ . . . . .	135
7.2	Theoretical flexural strength of notched and unnotched concrete beams [110]. . . . .	135
7.3	Nominal stress-CMOD curve for the eleven notched prismatic beams. The thick black and gray lines show the average and the characteristic curves. . . . .	141
7.4	(a) complete load-deflection response of the twelve plates, (b) load-deflection response up to the maximum load, (c) and (d) average load-COD <sub>b</sub> and load-COD-L <sub>b</sub> measured those of instruments shown on the figure which record the final crack. . . . .	143
7.5	Dispersion, average, 5% fractile corresponding to the characteristic response of the plates, 0.1% fractile corresponding to the design response of the plates, and the curve corresponding to the design resistant of the plates according to the requirements of the EC2. . . . .	144
7.6	Normalized load-deflection response of the twelve SFRC plates. The measured results are normalized by the expected tensile strength at the testing age of each plate considering the curing temperature. . . . .	145
7.7	(a) Variation of the load-bearing capacity of the plates in time and (b) categorizing the twelve plates in two groups of six plates based on the age of testing. . . . .	146
7.8	The results of the nominal stress-CMOD for the notched beams of (a) G1 and (b) G2 groups, and the load-deflection response of the plates for the (c) G1 and (d) G2 groups of specimens. . . . .	147
7.9	Comparison of the average and characteristic curves of the stress-CMOD response of the notched beam specimens for G1 and G2 groups. . . . .	148

7.10 The  $K_{Rd}$  factor according to MC2010 depending on the number of tested specimens in a three-point bending test and for two coefficients of variation of (a) 5% and (b) 8%, for the structural resistance. . . . . 151

7.11 The magnification factor,  $\kappa$  defined as the ratio between the characteristic value of residual strength with the assumption of a reduced coefficient of variation,  $V_{red}$  of (a) 5% and (b) 8%, to the experimental characteristic values based on the number of tested specimens. . . . . 152

7.12 Comparison of ratio between the characteristic value and average value of compressive and tensile strength (bottom and left axes) and for the residual tensile strength value for FRC depending on the number of tested specimens (top and right axes). . . . . 152

7.13 Effect of considering the unsymmetry in the log-normal distribution. . . . . 158

7.14 Comparison of SFRC plates and notched beams of *PartA* and *PartB* of the experimental campaign. . . . . 158

7.15 Shifting the results of the plates tested in *Part B* to 186 days of age to be compared with the plates of *Part A*. . . . . 159

7.16 Average daily temperature for the whole curing period for the plate elements tested in *Part A* and *Part B*. . . . . 160

7.17 Variation of nominal residual strength values of eleven tested notched beam specimens in *Part B* with time for (a)  $f_{R1}$  (b)  $f_{R2}$  (c)  $f_{R3}$ , and (d)  $f_{R4}$ . . . . . 160

7.18 Number of fibres at the failure plane for notched beams of *PartA* and *PartB* and its effect on residual-tensile strength values. . . . . 161

7.19 (a) Tensile constitutive law of the SFRC material obtained through the back analysis of the average and 5% fractile of stress-CMOD response of the notched beam specimens for G1 and G2 groups and (b) comparison of the experimental nominal stress-CMOD curves with the simulated results with a non-linear hinge model. . . . . 163

7.20 Comparison of experimental curves an modeling for nominal stress-CMOD results for the average curves of (a) G1 , and (b) G2 specimens and the characteristic curves of (c) G1, and (d) G2 series. . . . . 164

7.21 NLFE results of the plates based on average and 5% fractile material properties for the (a) G1 and, (b) G2 series, and derivation of the coefficient of variation of structural resistance for these elements. Results are compared with the structural resistance obtained from the experiments. . . . . 165

7.22 The magnification factor,  $\kappa$ , in light of the E-COV method defined as the ratio of design resistance considering a reduced coefficient of variation,  $exp(-3.04 \times V_{red})$ , to the design resistance based on the structural resistance scatter obtained from E-COV method,  $exp(-3.04 \times V_{E-COV})$ . . . . . 168

8.1 (a) Formation of internal cracks around reinforcing steel [101] (b) wider cracks at a distance from rebar [4]. . . . . 170

8.2 (a) Response of ties and and (b) crack patterns [1]. . . . . 172

8.3 The image of cracks at the bottom of the beams. . . . . 178

8.4	Illustration of minimum, average, and maximum crack spacing for each side of the B-FRC3 and B-R/FRC shallow beams and comparison of experimental crack spacing with average and maximum crack spacing formulations from MC2010, MC2020, and EC2. The tensile strength and residual strength parameters for the FRC are taken from the tests closer in age to the tested beams. The experimental ratio of $S_{r,max}/S_{r,m}$ for each side of the B-R/FRC beams is written on the figure. . . . .	179
8.5	Minimum, average, and maximum crack spacing for each side of the S1 series plates and the comparison with predictions of different standards for the maximum crack spacing. The average crack spacing values are given in the lower bottom right part of the figure. . . . .	181
8.6	Minimum, average, and maximum crack spacing for each side of the S2 series plates and the comparison with predictions of different standards for the maximum crack spacing. The average crack spacing values are given in the lower bottom right part of the figure. . . . .	183
8.7	Minimum, average, and maximum crack spacing for each side of the S3 series plates and the comparison with predictions of different standards for the maximum crack spacing. The average crack spacing values are given in the lower bottom right part of the figure. . . . .	184
8.8	(a) Minimum, average and maximum crack spacing for each side of the twelve nominally identical SFRC plates and (b) the relationship between minimum and maximum crack spacing with the average spacing of the cracks. . . . .	186
8.9	Schematic representation of how the narrow cover can restrict the presence of fibres in this zone (adapted from [210]). . . . .	188
8.10	Minimum, average, and maximum crack spacing for the R/FRC shallow beams and comparison with the predictions given by suggested formulas. . .	189
8.11	Comparison of the modified formula given in MC2010 with MC2020 and EC2 1992:2020 prediction for $S_{r,max}$ . . . . .	189
A.1	position and gauge length of LVDTs adopted to measure deformations on the shallow beams . . . . .	213
A.2	(left column) Load-COD and (right column) Load-contraction curves, for the B-FRC beams and for the three instruments shown separately . . . . .	214
A.3	(left column) Load-COD and (right column) Load-contraction curves, for the B-R/FRC beams and for the three instruments shown separately . . . . .	215
B.1	S1 series . . . . .	218
B.2	S2 series . . . . .	219
B.3	S3 series . . . . .	220
C.1	Dispersion curves for the (a) RC, (b) SFRC, and (c) R/FRC plates . . . . .	223





# List of Tables

3.1	Mix design of the SFRC material used in the study. . . . .	48
3.2	Determination of the compressive strength of the SFRC material for both <i>Parts A</i> and <i>Part B</i> . . . . .	48
4.1	The tensile strength parameters of the three-point bending tests carried out on the notched specimens divided in four categories based on their testing age. . . . .	60
4.2	Classification of the SFRC material following the MC 2010 approach and the check of the allowable limits for a structural FRC. . . . .	60
4.3	Maximum load reached in each of the plates from S1, S2 and S3 series in kN. . . . .	66
4.4	All strength parameters related to the fourteen tested notched beams. Average and characteristic values of $f_{fts}$ and $f_{ftu}$ are given following the provisions of CNR-DT 204 [50] and EC2-Annex L draft [43]. . . . .	78
4.5	Resisting bending moment for design and prediction of the load bearing capacity of plates of different series. . . . .	81
4.6	kinematic mechanisms considered for the yield line analysis of the plates and the maximum load for each case. . . . .	83
4.7	Design resistant load and estimated actual bearing capacity of the plates computed through a yield line analysis with the bending moments reported in Table 4.5. . . . .	86
4.8	Estimated actual load bearing capacity of the RC and R/FRC plates with the tensile strength of the rebars, $f_t=640$ MPa. . . . .	87
4.9	The results of the yield line method using the average material properties for different assumptions on $w_u$ for the SFRC plates in S1 ad S2 series. . . . .	92
5.1	Parameters of the CDP adopted for modeling of plain and fibre reinforced concrete . . . . .	111
5.2	The element types and their Gauss points adopted for modeling the notched beams and plates. . . . .	112
6.1	Computation of the load bearing capacity of the beams and the safety factor $\gamma_m=P_{Exp}/P_m$ . . . . .	132
7.1	Flexural tensile strength and residual strength values and their statistical parameters. . . . .	141
7.2	Coefficients $k_n$ for a 5% characteristic value. . . . .	142
7.3	Results of the three-point bending test for G1 series . . . . .	148
7.4	Results of the three-point bending test for G2 series. . . . .	149
7.5	Parameters of the load-deflection curves for the plate elements. . . . .	149
7.6	Coefficients $k_n$ for a 0.1% design value . . . . .	156

7.7	Coefficient $-t_p$ from equation for $p = 0,05$ and a log-normal distribution with the skewness $\alpha_X$ . . . . .	157
7.8	The ratio of the average resistance to design resistance, $\gamma_R = P_m/P_d$ based on PSF, PSF* (partial safety factor with the introduction of magnification factors), E-COV method, and the required safety factor based on experimental measurements for maximum load on six specimens in each group. . . . .	166
8.1	comparison of experimental crack spacing values with predictions of different codes based on the characterization tests at 34 days of age for the concrete. . . . .	180
8.2	The experimental values of minimum, average, and maximum crack spacing for <i>Part A</i> plates with the predictions made for the R/FRC plates with the 34 days tensile properties of the SFRC material. . . . .	185
C.1	Main features of the models received from the participanat groups . . . . .	222
C.2	features of SFRC modeling . . . . .	222
C.3	Maximum load reported by each group and its comparison with the experimental value. . . . .	226

# CHAPTER 1

---

## INTRODUCTION

---

With the emergence of design codes and guidelines [50, 53, 56, 122, 178] for Fibre Reinforced Concrete (FRC), there are more and more opportunities for the introduction of FRC in construction of civil engineering structures. FRC has been utilized in many different applications, e.g. tunnel linings [9, 63], retaining wall [74], pipe elements [62], ground supported slabs [90, 169], suspended flat slabs [3, 70, 73], etc. For structural purposes, very commonly, long fibres with 30-60 mm of length, with varying dosages between 25-100 kg/m<sup>3</sup> are adopted which needs to be tailored to the case of application. Reducing the crack width [197], improved bond between rebars and concrete [201], elimination of splitting cracks [145], increased toughness [179], enhanced tension stiffening behaviour [99], more effective stress redistribution [91] etc, are only some of the advantages that fibres can impart to a concrete mixture.

In the available standards, very commonly, the residual tensile strength properties of FRC are derived in an indirect manner. These tests include and are not limited to three-point bending [86], four-point bending [39, 117], circular panel on three pivots [8], panel on continuous simple support [87, 186], and tests in which a tensile field is created through a compression test [72, 130, 140]. The commonality between these tests, other than [72] in which a pure mode

I tensile field is created, is that the attainment of the direct tensile law of the FRC requires the inverse analysis of the results. A major difference between the testing methods is the failure volume involved in the characterization test.

The most common test method for characterization of FRC, is the three-point bending test on a notched beam [86], which is also the basis of classification of this material in the Model Code (MC) [53] and EC2 1992:2020 [43]. In this test, the residual tensile strength at a Crack Mouth Opening Displacement of 0.5 mm and 2.5 mm are taken as benchmark values based on which the direct tensile constitutive law of the FRC is obtained. The 0.5 mm corresponds to SLS condition and the 2.5 mm reflects the situation at ULS. An inverse analysis with some assumptions on the shape of the tensile law, give the direct tensile constitutive law. Both above mentioned standards, give two tensile constitutive law: one, which is characterized by a bilinear law, and the other which assumes a rigid plastic behaviour for the tensile response of the cracked FRC. The tensile laws are built up upon  $f_{fts}$  and  $f_{ftu}$  values (notation of MC) for CMODs of 0.5 mm and 2.5 mm. In this manner, one can compute the resisting bending moment of a FRC cross section which can be integrated in a design problem.

Incorporation of fibres in concrete mix can lead to design solutions which are economical. When fibres are adopted as partial replacement of rebars, construction time is reduced and saving of material can be achieved [89]. The most exemplary case would be the construction of slab elements in which the only reinforcement is fibres and rebars are adopted only from column to column (Anti-Progressive Collapse rebars). In fact, redundant two-way slab elements, are of specific interest for the application of FRC. Such structural scheme allows for a stable multiple cracking phase, and consequently, a more efficient use of the fibres is realized. With this view, adoption of limit analysis for design of FRC slabs enables the exploitation of the full capacity of strength reserve. There are many examples of successful application of yield line method to design FRC slabs [3,67].

In this regard, there are two topics that deserve attention. *First*, the adoption of a yield line method entails assuring enough rotation capacity to allow for the formation of a complete failure mechanism. Reduced ductility of FRC elements, specifically in beams and tensile members [59, 149, 208], has been shown in multiple works. When a crack propagates and widens, at a certain opening,  $w_u$ , the effect of fibres subside. It is not easy to predict when this occurs because often times, the maximum crack opening could be controlled by the heterogeneous nature of a FRC material. If the limit of ductility

is reached before the full failure mechanism is achieved, a limit analysis can give unsafe predictions for the load bearing capacity of such element. *Second*, it is well-known that the coefficient of variation of the residual tensile strength parameters of FRC obtained from a standard test on a relatively small specimen, are much higher than the scatter of resistance of a structure in which considerable cracking occurs before failure. Moreover, it has been shown that [3] the average tensile properties of FRC is capable of explaining the average structural response of slab element. The small characteristic values of tensile properties of FRC, lead to very safe design solutions which compromises the economy of a design project. This is why in both MC and EC2 1992:2020 magnification factors are introduced to compensate for the small characteristic values of residual tensile parameters of FRC.

Apart from the topics explained which are mostly focused on practical design issues related to FRC slab elements, NLFEM is a strong tool which can bring about considerable insight when the overall behaviour of a FRC element is of interest. Given that the behaviour of FRC elements is dominated by the nonlinear post-cracking response of the material, with NLFEM overall structural safety can be checked and strength reserves coming from redistribution of stresses can be controlled. This however requires proper derivation of tensile constitutive law for the FRC which can cover the whole range of crack openings. Moreover, the extended post-cracking response of FRC which can exhibit hardening and/or softening at different crack openings requires some attention on the choice of the internal parameter for regularization of the model. This can be somewhat different from what is commonly adopted for plain concrete.

## 1.1 Overview

The present PhD thesis is organized in the following chapters:

- **Chapter 2** present and overall review of the available literature with focus on the topics that are of importance to the content of the present work.
- **Chapter 3** presents the experimental program carried out within the scope of the thesis. Specifically, thirty two concrete plates of  $2000 \times 2000 \times 150$  mm, and six shallow beams of  $1500 \times 350 \times 150$  mm are tested. In *Part A* of the experimental campaign, twenty plates are tested which are reinforced with reinforcing bars (RC),  $35 \text{ kg/m}^3$  of steel fibres (SFRC), or the combination of the two (R/FRC). Three different configurations for the concentrated load and the four supports are adopted. In *Part B*,

twelve identical SFRC plates are tested under a concentrated load while supported on the four edges. The tested shallow beams are reinforced with  $35 \text{ kg/m}^3$  of fibres or with a combination of rebars and fibres. In each case, the SFRC material is properly characterized through a three-point bending test.

- **Chapter 4** presents the results of the *Part A* of the experimental campaign, i.e. the twenty plate elements. The structural response of the plates under different configurations are compared in terms of load-deflection and load-crack opening (COD). With the tensile properties derived from CNR-DT 204 [50](similar to MC2010) the bearing capacity and design resistance of the plates are obtained through a yield line method. Based on experimental observations on the ultimate crack opening for the SFRC plates, the tensile constitutive law is modified and the bearing capacity of the plates is re-calculated. The repercussions of the large scatter of the results of the bending tests on prediction and design of the plates are discussed and the applicability and effectiveness of the magnification factors given in CNR-DT 204 and EC2 1992:2020 are investigated.
- **Chapter 5** regards modelling of the plates. Specific attention is given to derivation of a proper tensile constitutive law for the SFRC material and modelling of the three-point bending test results and the behaviour of the SFRC plates in three configuration of loading and support condition. The importance of adoption of an internal parameter that is capable of regularizing the model is underlined.
- **Chapter 6** demonstrates the results of the six tested shallow beams.
- **Chapter 7** reports the results of the twelve identical SFRC plates that are tested under a central point load while supported at the four corners. Comparison is made between the scatter of the results of the companion beams tested under a three-point bending test. The consequence of the difference between the scatter of the tensile parameters of the SFRC material and the structural resistance of the SFRC plates on the safety margins for obtained design resistance of the plates is discussed. A curve is given that represents the possible magnification factor that can be adopted to compensate for the small characteristic values of the SFRC tensile parameters.
- **Chapter 8** is attributed to a study on the crack spacing in the tested plates and beams. Although the experiments were not designed to give a conclusive results on this issue, the available results are checked against the available formulations in the literature, and some suggestions are given.

- **Chapter 9** recapitulates the conclusions derived and gives some suggestions for the future possible developments.





---

## STATE OF THE ART

---

### 2.1 Fresh Concrete

The adverse effect of fibres on fresh properties of concrete mixtures has been studied from the early 70s of the past century. Edington et al. [82] investigated the effect of the aspect ratio and volume content on the VEBE-time of fibre reinforced mortars. Workability generally appeared to depend upon the diameter, length and volume fraction of the fibres. Hughes and Fattuhi [115] demonstrated that workability depends on volume of fibre and aspect ratio. The higher the aspect ratio, the more fibre interferes with consolidation of the concrete matrix. They showed that the “fibre factor”,  $V_f \times (l_f/d_f)$  is a proper indicator for comparison of fresh FRC properties. Grünewald and Walraven [103] demonstrated that surpassing a critical fibre content makes it impossible for concrete to flow under its own weight. They also highlighted that large amounts of fibres can still be incorporated into a self-consolidating concrete, depending on the mix design. Ferrara and Meda [93] have tested the effect of adding Viscosity Modifying Admixture (VEA) on the distribution of fibres in prolonged vibration for self consolidating concrete. Even after 16 min of vibration the mixture incorporating VEA showed homogeneous distribution of fibres. In [94], high viscosity of mixture shown through high flow time in the V-funnel test is counted as an indicator

of “fibre driving ability”. Ferrara et al. [95] have shown the effect of suitably adjusted fresh properties of concrete on fibre distribution through Alternative Current Impedance Spectroscopy (AC-IS) measurements which shows lower dispersion of the results obtained for normalized conductivity of the matrices for self-compacting SFRC (SCSFRC) compared to a segregation consolidating and a vibrated SFRC. In the same work, the beam specimens made from a mixture that suffered from segregation and tested in a four-point bending test in an upside-down position with respect to the casting side, showed higher rate of crack opening for a certain deflection when compared to the stable SCC mixtures. In [73], cores were taken from a concrete slab made of FRC and then were cut in four slices to be tested in a Double Edge Wedge Splitting Tensile Test (DEWST). The number of fibres in the slice taken from the top part of the slab were almost twice the number of fibres in the bottom slice. At all crack opening displacements higher stresses were found for the specimens taken from the bottom slice. The FRC characterized based on the top slice leads to a “5c” class material, while the bottom slice gives an FRC of between “3e” and “1.5e”. Testing shallow SFRC beams of  $1.5 \times 0.5 \times 0.25$  m in a four point bending setup, specimens which were tested upright with respect to the casting direction showed a weaker mechanical response compared to those that were tested in an inverted position [136]. In the same work, cores were taken from the beams and were tested in both a DEWST and a Double Punch Test (DPT). Slices that were extracted from the top part of the beams displayed an inferior mechanical behavior compared to those taken from the formwork side. These results highlight the importance of rheological properties of the mixture on securing a quasi-homogenous FRC.

## 2.2 Compressive behavior

Observations on the effect of fibres on compressive strength of concrete comprises results showing reduction [34], ineffectiveness [28, 145], and increase [146] of strength. This mainly depends on the volume, dimensions, fibre type, and degree of compaction achieved if high volumes are utilized. However, the prominent effect of moderate dosages of fibres on compressive behaviour, is an increase of the strain at peak and a significant increase of the ductility by a substantial change in the post-peak slope [88, 92, 142, 207], the effect of which depends on the volume and fibre properties. Both [88, 142] developed analytical relationship for compressive stress-strain relationship of FRC as a function of reinforcing index, which is equivalent to the fibre factor with amount of fibre expressed in terms of its weight. Ezeldin et al. [88] showed that steeper slope of the descending branch of the compressive stress-strain curve as a result of addition of silica fume, can be counteracted

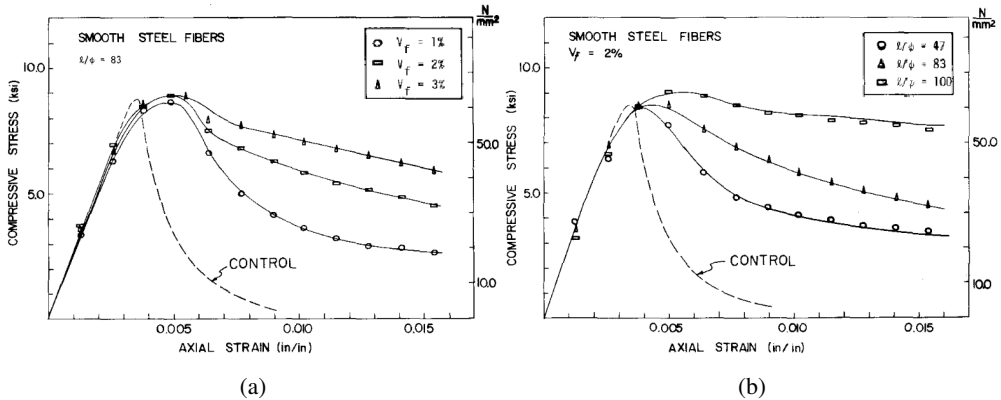


Figure 2.1: Effect of (a) fibre volume for the same aspect ratio (b) aspect ratio for the same volume on the compressive stress-strain curve [92].

by increasing the fibre index. Fanella and Naaman [92] tested different fibre types and volumes on three mix designs to study the compressive stress-strain curves for FRC. Fig. 2.1 shows a part of these results which highlights the effect of fibre volume and aspect ratio on compressive toughness. In 1971, Shah and Ranagan [179] tested small concrete specimens in compression. These specimens of  $5 \times 5 \times 25$  cm dimension were reinforced with 0.5% of steel, either in form of randomly distributed fibres, or stirrups with different spacing. All these specimens showed much higher energy absorption after the peak compared to the plain concrete, and the fibre reinforced ones, outperformed two of the samples reinforced with stirrups. They also pointed out that fibres and stirrups reduced volume dilation under compression. Enhancement in concrete toughness in compression is reported in [137] while testing concrete beams in flexure. The ultimate experimental strain reached in the compressive zone of the beams obtained from curvature measurements and considering a plane section assumption were  $6.6 \times 10^{-3}$ , which is twice the conventional limit accepted for concrete ultimate strain in compression. The authors attributed this observation to fibre capacity in increasing compression toughness of concrete. Nevertheless, disregarding the nonlinearity of concrete response in compression should have accentuated these results.

## 2.3 Tensile behavior

Due to difficulties in carrying out a direct tensile test, it is more common to measure tensile strength in an indirect manner. Oh [146] added 1% and 2% of volume of 40 mm long fibres with 0.7 mm of diameter and measured compressive strength, flexural strength, and the splitting tensile strength of the mixture. He observed that fibre addition increased all the three measured

parameters, with the most significant effect on the splitting tensile strength. Splitting tensile strength went from 3.07 MPa for the plain concrete, to 5.41 MPa, and 8.10 MPa for the mixture with 1% and 2% of fibres. He concluded that fibres considerably enhance the tensile strength of concrete. However, determination of FRC tensile strength from a Brazilian test, needs some modifications and considerations that were probably overlooked by Oh. In such test, the splitting crack begins at the center line of the specimen and propagates towards the loading point. For a brittle concrete, the ultimate load would then depend on the tensile strength as well as the tension softening response of the material. Olesen et al. [147] carried out a FE model to investigate the effect of some parameters of the tension softening curve on the ultimate load reached in a tensile splitting test. As demonstrated in Fig. 2.2 the post-cracking slope and the position of the knee-point connecting the first branch and second branch of the tension softening law can notably deviate the ultimate load,  $P$ , from the ultimate load that would be obtained from a linear-elastic solution,  $P_E$  [147]. Rocco et al. [167] tested different sizes of specimens with different bearing strip sizes in a Brazilian test and reported two fracture mechanisms, one including the central cracks, and the other consisting of secondary cracks on both sides of the loading strips. These secondary cracks that stem from stress redistribution after the initial central cracks, lead to the appearance of a second peak in the load-deformation of the test, if carried out by controlling displacement. In their work, the ratio of the second peak to the first one depended on the size of specimen and the width of the loading strip. Smaller specimens and wider loading strip led to an increase in the second peak. Malárics and Müller [133] carried out an extensive work to find out conversion factors between splitting tensile strength and direct tensile strength. They tested cast cylinders and cores of different sizes and showed that in majority of cases, splitting tensile strength gives an underestimation for the tensile strength. Only for small cores with a diameter of 75 mm and length of 150 mm the splitting test led to values that were in line with the conversion factor of 0.9 given in MC 1990 [53]. Denneman et al. [65] looked into the measurement of splitting tensile strength for FRC. The tested FRC had 80 kg/m<sup>3</sup> or 120 kg/m<sup>3</sup> of 30 mm length and 0.5 mm diameter of steel fibres, and 2 kg/m<sup>3</sup> of 12 mm long polypropylene fibres. To do so, they measured the lateral deformation of the cylinders to catch both peaks. Doing so, they were able to determine the tensile strength corresponding to the initial nonlinearity in the load-deformation response. Fig. 2.3 shows the measurement configuration and the results. In the study by Denneman et al., relatively high volumes of fibres were adopted. Nevertheless, some trial tests were carried out on the SFRC material utilized in the present thesis where a similar behaviour was observed. This is despite of the fact that the fibres adopted in this study have

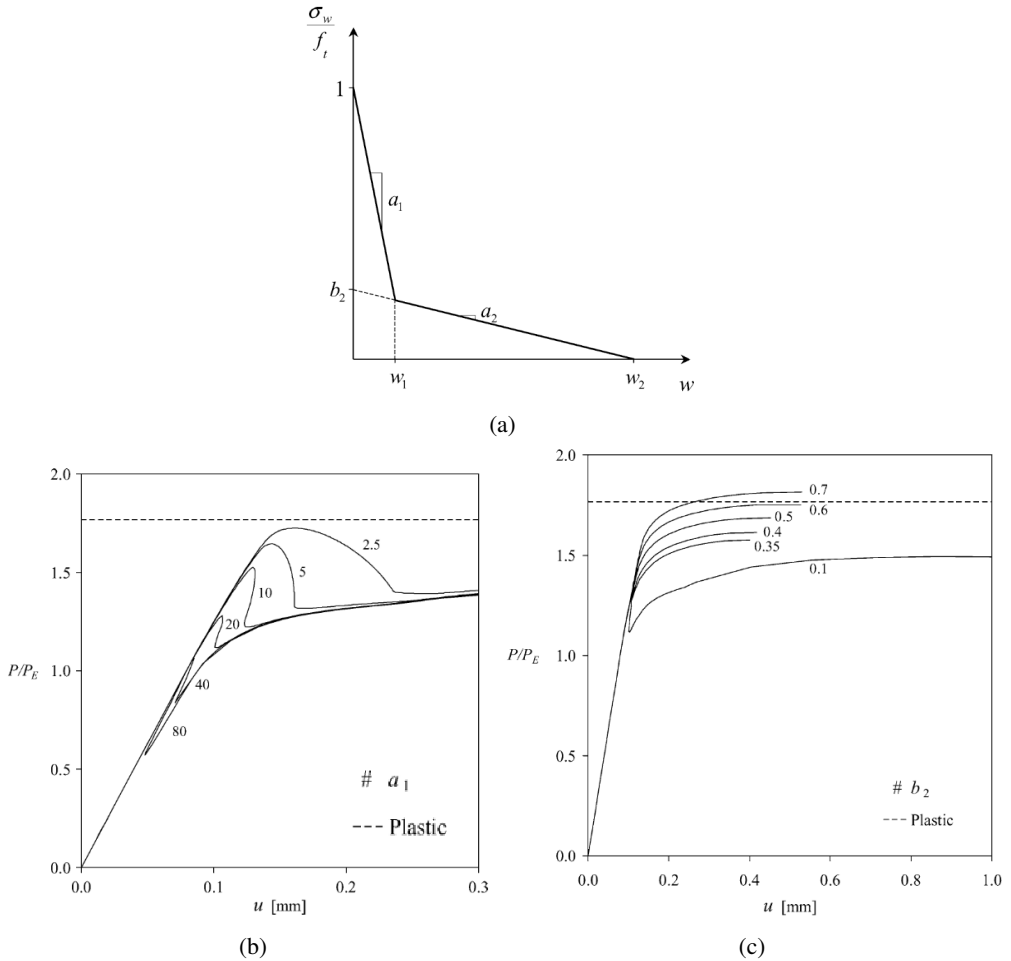


Figure 2.2: (a) the parameters of the stress-crack opening law (b) effect of the post-peak slope  $a_1$  and (c) the position of the knee-point,  $b_2$ , of the tension softening law on the ultimate load reached in the splitting tensile model w.r.t the ultimate load reached with the assumption of linear elasticity [147].

a length of 60 mm and a dosage of  $35 \text{ kg/m}^3$ . These findings highlights the considerable stabilization effect of fibres that needs to be taken into account when doing a splitting tensile test, specifically under load control conditions. It will be shown in Chapter 5 that a similar behaviour may prevail also when conducting a three-point bending test for determination of the flexural tensile strength of such SFRC material.

Qing et al. [160] carried out direct tensile tests on normal SFRC specimens and specimens in which the orientation of fibres were favorably aligned containing 2% of steel fibres. Utilizing smooth straight fibres in three mixtures

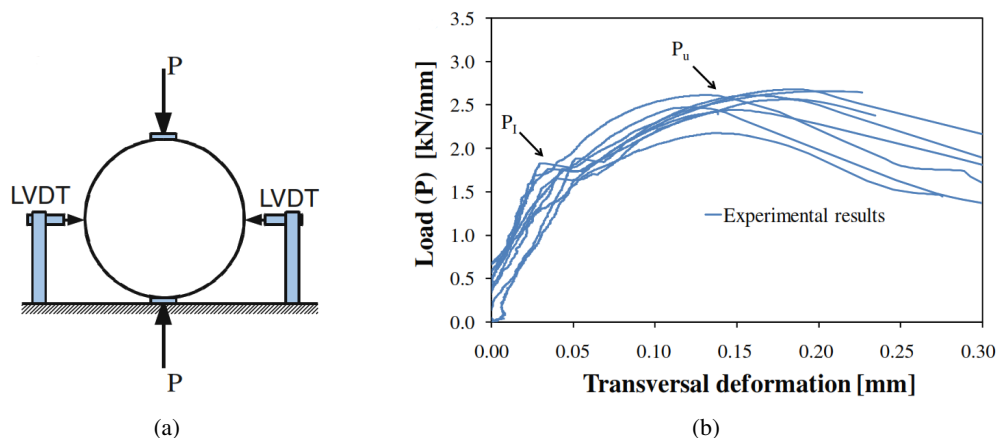


Figure 2.3: (a) modified splitting test with measurement of lateral deformation (b) load-deformation result of such test for FRC showing the presence of two peaks.

with varying  $w/c$  ratio, they showed the importance of matrix strength on the post-cracking response of the FRC specimens. Stronger matrices allowed for a much pronounced hardening response after cracking. These results are shown in Fig. 2.13, in the section where the effect of orientation of fibres is discussed.

Presence of fibres also considerably modifies the behaviour of RC tie elements. Bischoff [30] tested axially loaded tension specimens reinforced with a single bar incorporating steel fibres in which the first cracking load was equal to the specimens made without steel fibres. However, after cracking significant differences were evident between the specimen with and without fibres. Nguyen et al. [145] carried out tensile test on RC and R/FRC prismatic specimens with a reinforcement ratio of  $\rho = 0.6\%$  and a combination of three types of fibres with an overall volume fraction of 1.5%. The R/FRC specimens showed a 33% increase in the peak load which was followed abruptly by a softening behavior, unlike the RC beams that after cracking followed a smooth slightly hardening behavior approaching the yield plateau of the reinforcing steel. These results are shown in Fig. 2.4. The effect of fibres was also appreciated in controlling the splitting cracks formed on the surface of the specimens. The importance of this observation is in the fact the the failure of the RC tie occurred at the position where the splitting cracks were formed, in which strain measurements on the steel rebar exhibited a considerable increase of deformation in the rebar. The images corresponding to the cracking of RC and R/FRC specimens are shown as well in Fig. 2.4.

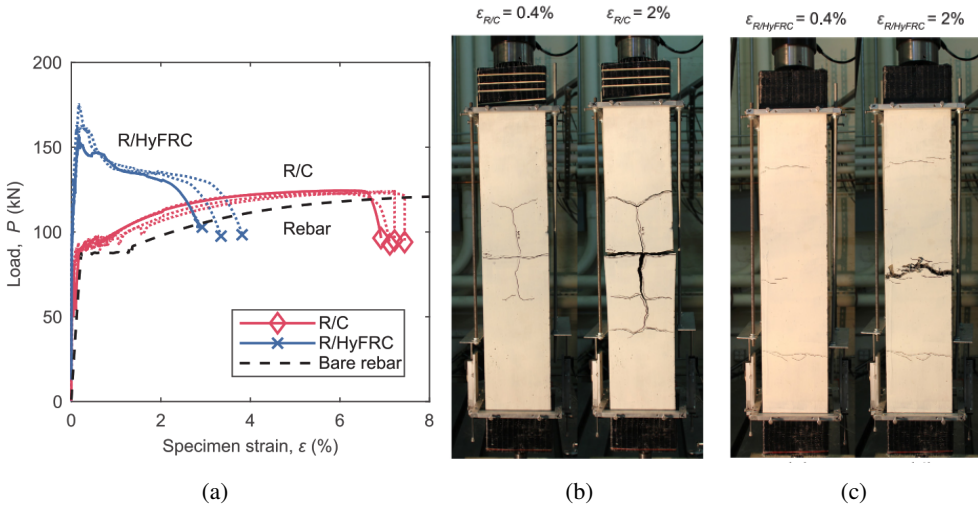


Figure 2.4: (a) Load versus average strain for the bare bar, RC, and R/FRC specimens, Cracking pattern of the (b) RC specimen, and (c) R/FRC specimen [145].

## 2.4 Flexural behavior

From the very early works on FRC, the considerable effect of fibres on increasing the flexural toughness of concrete has been observed. Back in 1971, Shah and Rangan [179], tested small FRC beam specimens in a three-point bending test with volumes up to 1.25%, where a substantial increase in toughness of specimens was obtained with increasing fibre volume. However, the flexural strength of concrete had only a two fold increase at the highest fibre dosage. While steel fibres mainly affect the post-peak behavior of concrete [28], Oh [146] has reported the effectiveness of fibres in increasing the flexural strength of concrete. Nevertheless, for moderate dosage of macro fibres commonly adopted for structural purposes, Limit of Proportionality (LOP) depends on concrete strength and is not affected by the fibre volume and type [119, 128]. It is emphasized that in structural beam elements, fibres are almost always accompanied by rebars. Heterogeneity of FRC and shortcoming of FRC elements in providing enough ductility, deters the application of fibres as the sole reinforcement in beam elements. Therefore, in the following paragraphs, effect of fibres on structural behaviour of R/FRC beams is explained, which is more aligned with the goals of the present thesis work.

In an experiment carried out by Meda et al. [137] on reinforced concrete beams with a 3.6 m span and a depth of 300 mm with and without incorporation of steel fibres in a four-point bending scheme, the presence of fibres did not

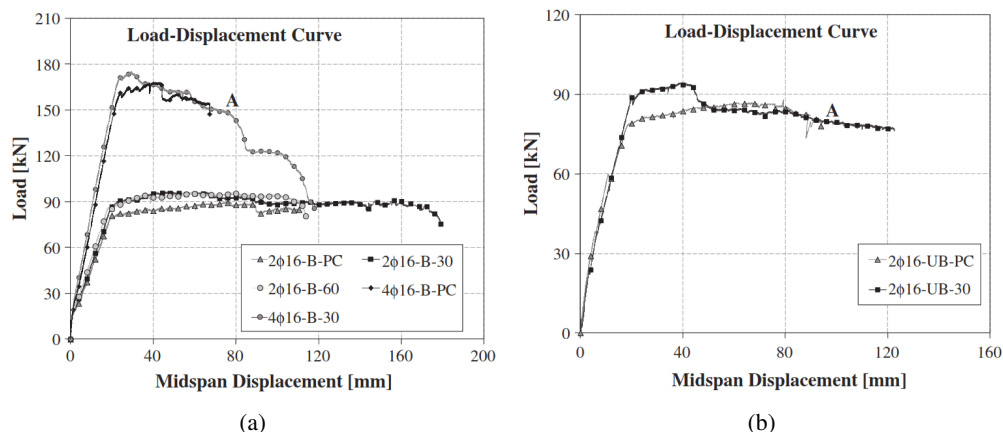


Figure 2.5: load-deflection curve for (a) bonded and (b) unbonded specimens [137].

affect the maximum load attained in the beams with bonded rebars. Dosage of fibres were  $30 \text{ kg/m}^3$  and  $60 \text{ kg/m}^3$  and the reinforcement ratio was  $\rho_s=0.75\%$  and  $1.5\%$ . In the beam with  $\rho_s=0.75\%$ ,  $30 \text{ kg/m}^3$  of fibres led to a starking increase in ductility of  $73\%$ , while for  $60 \text{ kg/m}^3$  of fibres the change in ductility was marginal. A considerable observation was that for the beam cast with normal concrete the failure was due to concrete crushing in compression, while the higher compressive toughness provided by the fibres along with better rebar-concrete bond led to a failure controlled by bottom reinforcement and gradual crushing for beams reinforced with fibres. Also, the lower ductility of the beam with  $60 \text{ kg/m}^3$  of fibres was related to improved bond between concrete and rebar that leads to strain localization at a short stretch of the sections. The load-displacement curves are shown in Fig. 2.5(a). In the same work, reinforced beams with unbonded bars were tested with and without fibres. The sudden opening of the cracks, led to the disappearance of the effect of fibres shortly after the peak load. Fig. 2.5(b) depicts this observation.

Oh et al. [146] tested singly reinforced concrete beams with two steel ratios and two dosages of  $1\%$  and  $2\%$  of steel fibres and also a doubly reinforced concrete beam with the same dosages of fibre. The beams had a span of  $1.8 \text{ m}$  and a cross section of  $12 \times 18 \text{ cm}$  and the fibres were straight with a length of  $40 \text{ mm}$  and diameter of  $0.7 \text{ mm}$ . Tests were carried out in a four-point bending scheme, the results of which are shown in Fig. 2.6.  $2\%$  of fibres reduced deflection values for singly reinforced beams. The effect of  $2\%$  of fibres on ductility of the beams is different. The singly reinforced beams with higher reinforcement ratio undergo larger deflection in comparison to the reference specimen, while for the doubly reinforced beam, considerable reduction of ductility is observed. Measuring concrete strain at the top fibres,



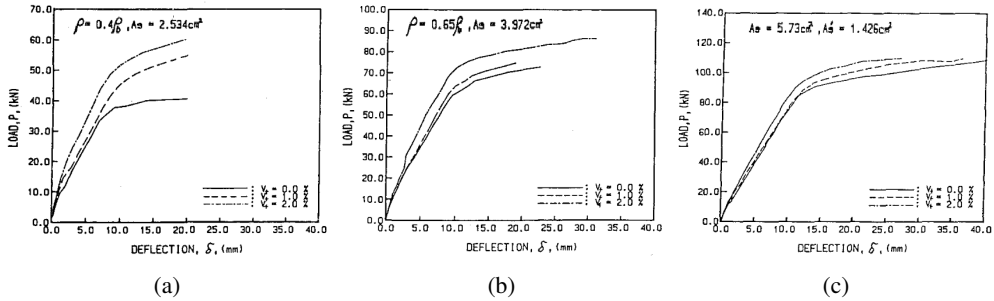


Figure 2.6: load-deflection curve for (a) singly reinforced beam with  $\rho_s=0.4\rho_b$  (b) with  $\rho_s=0.65\rho_b$  and (c) doubly reinforced beam with  $\rho_s=0.9\rho_b$  and  $\rho'_s=0.0083$  [146].

he demonstrated that for a certain load level, addition of fibres reduce concrete strain.

Schumacher in her PhD thesis [149], tested reinforced concrete beams of 3 m long with a cross section of  $150 \times 300$  mm under a three-point bending scheme. She studied the effect of addition of  $60 \text{ kg/m}^3$  of steel fibres and the presence of an axial compressive force on the rotation capacity self compacting SFRC beams. She observed that the beams that were cast with the SFRC showed less deflection at the ultimate load. She points out that the chance of yielding of the reinforcing bars may be only at the position of the localized crack. Considering the maximum load and deflections attained, the beams reinforced with steel fibres in addition to reinforcing bars showed some 10% increase in the load bearing capacity, however, almost 30% less deflection was reached at failure. This was due to the fact that in the SFRC beams the localization appeared only in one single crack while in the beam without fibres, failure was triggered after localization of deformation in more number of cracks. She indicates that this observation is due to the dominance of the softening behavior of the SFRC material with respect to the hardening of the reinforcing bars which leads to a global softening behavior without the possibility of propagation of more cracks in the proximity of the localized crack.

Alsayed [5] tested R/FRC beams of 2.5 m length in a four-point bending setup. The fibres were 60 mm long with a diameter of 1 mm or 0.8 mm at dosages of 0.5% to 1.5%. 0.5% volume of fibres slightly increased the ultimate load, but for higher dosages, the reduction of ultimate deflection was easily appreciated. Yet, as expected, the cracking point was not altered by the addition of fibres. Dancygier and Savir [61] tested eleven beams with 3.5 m of span under a four-point bending setup. Two fibre types with an aspect ratio of 65

and a length of 60 mm and 35 mm were added to a high strength concrete. Fibre mixtures had  $60 \text{ kg/m}^3$  of fibres and two reinforcement ratios were adopted. In all cases, presence of fibres led to a decrease in ductility. The reduction was less pronounced when reinforcement ratio was higher. Ductility of fibre beams with lower reinforcement ratio was around one-fifth of that of the corresponding RC companions. Absence of fibres allowed for the formation of well distributed flexural cracks, while localization of strains in a single crack in beams with fibres led to the rupture of the rebar at much smaller deflection values. Through measurement of curvature values, they showed that the RC beams had higher and more uniform curvature in the loading span as compared to the beams with fibres. This observation was attributed to improved bond of rebars due to the confining effect of fibres which gave rise to localization. A probabilistic model was also given in [58] to explain this observation. In the continuation of the research on ductility of fibrous beams at Israel Institute of Technology [57], beams with varying reinforcement ratios in the range of  $\rho=0.15\%$  to  $3.3\%$  were tested with and without fibres in order to better investigate the effect of reinforcement ratio on ductility of fibrous beams. It was observed that for larger reinforcement ratios, fibres helped increase ductility, while for lower ratios, significant reduction in ductility was reported. Deluce and Vecchio [64] observed a similar phenomena in testing R/FRC tensile specimens. They point out that the presence of fibres triggers post-yield localization. When a crack width surpasses some threshold, effect of fibres subsides and this weak cross section becomes even weaker. This is followed by local yielding of the rebar. Hardening behaviour of the rebar may give rise to a second localization at another crack. Dancygier et al. [59, 60] showed that for a given reinforcement ratio, higher fibre dosage leads to a stronger localization. They measured the extent of localization by the ratio between the significantly wide cracks to the total number of cracks,  $m/n$ . Also Yang et al. [208] reported higher chance of single localization for tensile specimens with higher dosage of fibres. They attributed this effect to higher inhomogeneity due to scatter in fibre content along the specimen. If this holds, one can expect that for high fibre contents,  $100 \text{ kg/m}^3$  and beyond, in which a more homogenous behavior is expected, this observation would be reduced.

## 2.5 Fibre pull-out

The post-cracking behavior of a FRC material depends on the number, orientation, and the pull-out behavior of the fibres. The most important factors affecting the pull-out response of a fibre are its shape, inclination, tensile strength, and the strength class of the hosting concrete. Generally speaking, the pull-out behavior of straight fibres is controlled by an elastic-adhesive,

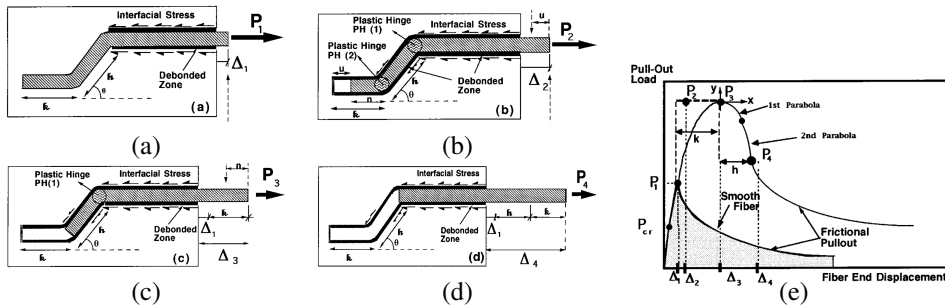


Figure 2.7: Different stages of the pull-out of a hooked-end fibre [6].

and a frictional response, while hooked-end fibres benefit from mechanical clamping as well. Alwan et al. [6] formulated the pull-out behavior of hooked-end fibres as a frictional pulley with two plastic hinges. Fig. 2.7 (a) to (d) show different stages they considered for the pull-out of a hooked-end fibre. For a straight fibre only the first and last stages hold. Markovich et al. [135], through vacuum impregnation of a low-viscosity epoxy, showed the considerable extent of cracking around the hook.

Very often, a higher angle of inclination w.r.t to the loading direction reduces the peak load and shifts the slip at the peak load to larger values. However, slight inclination for hooked-end fibres, around  $15^\circ$ - $30^\circ$ , may increase pull-out toughness [11, 35, 166]. Furthermore, for inclined straight fibres, the post-debonding response may show superior pull-out force compared to aligned fibres [182] which may be due to the plasticity of the fibre and a more effective frictional resistance at the surface of the crack [45]. In [55], three inclination angles of  $0^\circ$ ,  $30^\circ$ , and  $60^\circ$  were chosen for straight and hooked-end fibres among which the pull-out load corresponding to  $30^\circ$  inclination was the highest for both fibres.

After debonding, the pull-out mechanism for the straight and hooked-end fibres are very different. The post-debonding pull-out response of straight fibres is characterized by a considerable load reduction [182], while the mechanical anchorage of hooked-end fibres allows increasing the load [35]. According to these authors, the initial part of the response is followed by plasticity in the fibre and it is only after the plasticity of both curved segments of the fibre that sliding in the channel takes place. The sliding of fibre in its curved initial bedding leads to compressive damage in concrete. Cunha et al. [55] indicate that for hooked-end fibres the mobilization and straightening of the hook is the major player and the embedment length has less influence

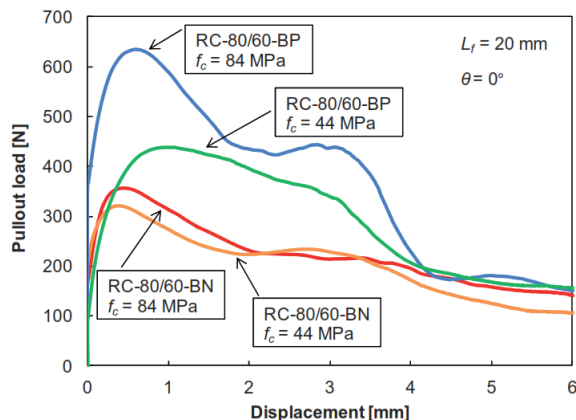


Figure 2.8: influence of fibre and concrete strength on pull-out [35].

on its pull-out behavior. Breitenbücher et al. [35] tested the pull-out response of a normal strength and a high strength hooked-end fibre in a normal strength and a high strength concrete. Fig. 2.8 demonstrates the results. The fibres were 60 mm long. The fibre designated with BP has a diameter of 0.71 mm and a tensile strength of 2600 MPa, and the one identified with BN has 0.75 mm of diameter and a tensile strength of 1250 MPa. The BN fibre, in terms of tensile strength value is very similar to the fibres that were utilized in our study in this thesis. The results indicated that the pull-out response of the BN fibres were only slightly different at small displacement values in both normal and high strength concrete. They highlighted the importance of fibre strength that substantially increased the maximum pull-out force. For the high strength fibres, they attributed the much higher pull-out load experienced in the high strength concrete as opposed to the normal concrete, to the energy consumption in straightening of the hook. They did not take into account the possibility that the crushing and plasticization of concrete close to the hook may have had an effect. The straightening of the fibres has surely occurred also for the BP fibre in the weaker concrete with much smaller maximum pull-out force. Hence, it is more probable that the pull-out load is affected by a combination of the concrete crushing and fibre strengthening. Noticeably, after 4 mm of displacement, in a region that the pull-out behavior is mostly controlled by the frictional pull-out, there is no effect of either the fibre nor the concrete strength and the four curves are almost identical. To the belief of the author of this thesis, the damage caused to the fibre-concrete interface after pulling out of the straightened hook diminishes the effect of fibre and matrix quality.

## 2.6 Testing methods and scatter of results

Unlike plain concrete in which fracture energy alone, may sufficiently explain its post cracking behaviour in tension, for FRC, the post-peak response should be explained by a complete  $\sigma - w$  curve. These parameters may be obtained from a direct tensile test by separating the discrete crack opening from the presumably uniform strains that unload after the localization [180]. However, direct tensile test is not an easy test to perform and there are many subtleties with respect to the stiffness of the testing machine, the choice of rotating versus fixed-end modalities, etc. This is why very commonly, tensile fracture properties of concrete are determined in an indirect manner, e.g. bending and wedge splitting tests [130]. Nevertheless, the derivation of the tensile constitutive relationship of concrete on the basis of these indirect testing methods entails the inverse analysis of the results. Variety of testing methods are investigated for derivation of tensile properties of FRC. The main difference between these tests are the measured parameters, size and type of the specimens, and presence and absence of a notch. Some of these tests can be categorized as *structural* tests, in that internal and external redundancies affect the results, and the measured parameter can hardly be regarded as a *material property*. On the other side are the tests in which the effect of the boundary conditions are minimized and failure is controlled by propagation of cracks at cross sections that are commonly predefined by the presence of a notch. Some of these tests are described in the following.

### 2.6.1 Testing methods

#### 2.6.1.1 EN 14651: Measuring the flexural tensile strength (limit of proportionality (LOP), residual)

This is probably the most common test for determination of residual tensile strength properties of FRC and is used for the classification of such material according to the MC2010 and EC2-annex L standards. The specimen is  $600(550) \times 150 \times 150$  mm and is tested under a three-point bending test on a span of 500 mm. After casting of the specimen, it is rotated for  $90^\circ$  and a notch is sawn to a depth of 25 mm, leaving a ligament depth of 125 mm. Test is carried out under a displacement control scheme and the opening of the mouth of the notch is measured with a clip gauge. The residual tensile strength values,  $f_{R,i}$ , at Crack Mouth Opening Displacements (CMOD) of 0.5, 1.5, 2.5, and 3.5 mm are found as  $3F_i l / 2bh_{sp}^2$ .

**2.6.1.2 ASTM C1399: Obtaining Average Residual-Strength of fibre-Reinforced Concrete [38]**

In this standard the average residual strength values of FRC are determined in a four-point bending test. The test can be carried out on cast samples or on cut specimens. Initially the specimen is cracked by imposing a deflection of 0.2 mm, and then the specimen is reloaded again. The load at deflection values of 0.5, 0.75, 1.00, and 1.25 mm is averaged to get the average residual strength (ARS) as  $P_{ave}L/bd^2$ , where  $L$ ,  $b$ , and  $d$  are the span, width and depth of the beam. At least five specimens are suggested to be tested.

**2.6.1.3 ASTM C1609: Flexural Performance of fibre-Reinforced Concrete (Using Beam With Third-Point Loading) [39]**

This is another four-point bending test suggested by the ASTM in which specimens with different sizes can be tested. However, the preferred sizes for the beam are mentioned to be  $100 \times 100 \times 350$  mm or  $150 \times 150 \times 500$ , tested on a span of 300 mm and 450 mm respectively. Load and deflection is measured during the test. It is preferred to measure deflection on the two sides of the beam with transducers positioned on a jig that is attached to the mid-depth of the beam. The residual strength values are computed at two deflections of  $L/600$  and  $L/150$ , with  $L$  being the span, as  $f_{600}^D$  and  $f_{150}^D$ . Moreover, on the basis of the toughness value computed up to a deflection of  $L/150$ , an equivalent flexural strength is obtained as,  $f_{e,150}^D = 150T_{150}^D/bd^2$ . An equivalent flexural strength ratio is derived as,  $R_{T,150}^D = f_{e,150}^D/f_1$ , in which the  $f_1$  is the first-peak strength. The repeatability coefficient of variation of different parameters of the test are reported based on a database of 26 tests consisting of three or four replicate specimens. A coefficient of variation of 17.8% and 16.4% are given for  $f_{150}^D$  and  $f_{600}^D$  respectively.

**2.6.1.4 RILEM TC 162-TDF: Uni-axial tension test for steel fibre reinforced concrete [199]**

The tested specimen is a notched cylinder of  $150 \times 150$  mm of dimension and displacement at the notch is measured with at least three transducers of maximum 40 mm long. In the computation of the crack opening, the elastic unloading phase is neglected for simplicity and the characteristic  $\sigma - w$  relationship is obtained based on the fractiles of the dissipated energy as:  $\sigma_{w,k}(w) = \bar{\sigma}(w)W_{F,k}/\bar{W}_F$ . The  $\bar{\sigma}$  and  $\bar{W}$  refer to the average values and the “ ${}_k$ ” expresses the characteristic values.

**2.6.1.5 ASTM C1550: Flexural Toughness of fibre Reinforced Concrete (Using Centrally Loaded Round Panel) [8]**

The test, proposed by Bernard [22], is carried out on a circular specimen with a diameter of 800 mm and a thickness of 75 mm. The specimen is supported on three symmetrical pivots that are on a pitch circle diameter of 750 mm. The failure of the specimen creates cracks with large surface areas. This leads to a low within-batch scatter in the results. A successful test demonstrates, at least, three radial cracks. The test is suitable both for cast and shotcrete specimens. The dissipated energy at deflections of 5, 10, 20, 30, and 40 mm are of interest.

Cianico et al. [48] point out that Round Determinate Panel (RDP) on three supports has the advantage of a clear failure consisting of always three cracks while the EFNARC panel test [186] exhibits different failure modes in different tests. The large cracks in the RDP test having 400mm of length and 75 mm depth gives consistency and stability to the results with the dispersion of the residual values in the order of actual structural elements unlike the beam tests that show fictitiously large scatter due to small size of the fracture zone. In the same work they suggest the application of RDP test with three notches of 15mm deep and triangular section. Vandewalle et al. [200] adopted this test to derive the  $\sigma - w$  relation based on a two-level approach [78] with which they predicted the  $\sigma - \text{CMOD}$  response of a three-point bending test with adequate precision.

**2.6.1.6 EN 14488-5:2006 Testing sprayed concrete. Determination of energy absorption capacity of fibre reinforced slab specimens [87]**

The test is designed for sprayed concrete and is carried out on square specimens of 600×600×100 mm supported on all sides on a rigid plate with internal dimensions of 500 mm. The test is done controlling the deflection up to 30 mm. Load-deflection and energy-deflection curves are reported. This is similar to the testing method proposed by EFNARC [186]. Minelli et al. [139] points out that this test due to the irregularities of the specimen leads to three point supports with random configuration, hence not suitable for material characterization due to unreliability. Similar to this test, Destrée and Mandl [69] tested a circular concrete slab with diameter of 150 cm and a thickness of 15 cm simply supported all around the perimeter to derive the material properties for design of flat slabs. They remarked that such a test is needed before designing a flat slab as the indeterminacy allows for multiple cracking and plasticity which in turn leads to ultimate loading intensities that are 3 to 6 times higher than what is derived from standard test. Still, with the properties derived from the circular plate test, they reached to global safety factor of around 5.

### **2.6.1.7 Wedge Splitting Test (WST) [130]**

In this test method which was originally proposed by Linsbauer and Tschegg [130] and further developed by Brühwiler and Wittmann [36], a wedging device pushes between the rollers on the sides of a groove, which allows the propagation of a crack starting at the tip of the notch. of course, the magnitude of the splitting force depends on the angle between the wedging device and the rollers. Löfgren et al. [131] and Berrocal et al. [27] have adopted this test for characterization of FRC with success. The residual tensile values obtained from WST was slightly lower than that of the three-point bending test which was attributed to the unfavorable crack branching occurred in the three-point bending test that was not observed in WST [131].

### **2.6.1.8 Double Edge Wedge Splitting Test (DEWST) [72]**

This test which is a modification to the WST, is an indirect test which through the application of a compressive force creates a purely mode I tensile field at the ligament of the specimen and does not need an inverse analysis to get the tensile constitutive law of the FRC. The specimen has the groove and notch on both sides and in this manner the compression field will be deviated from the ligament. The test can be done on cast samples as well as cut or cored specimens. Depending on the direction of the groove and notch, the anisotropy induced by favorable or unfavorable orientation of fibres can be investigated.

### **2.6.1.9 Double Punch Test (Barcelona) [140]**

The Double punch Test (DPT) that was originally proposed by Chen [47] for determination of tensile strength of concrete was adopted during the construction of line 9 of Barcelona's subway to test the adopted SFRC material. The goal was to propose a test method which was easy to be carried out and which does not suffer from the high scatter of the bending tests. In the first stage of the test, radial tensile stresses are resisted by concrete. In stage two, tensile strength is reached and conical wedges are formed at the top and bottom of the specimen accompanied by the formation of two to four radial cracks. The last stage consists of opening of the stabilized cracks with the cones being pushed and the increase of the Total Crack Opening Displacement (TCOD) measured by a chain extensometer positioned at the perimeter of the mid-height of the specimen. An analytical method is given to translate the axial load-TCOD to  $\sigma - w$  relationship [32].

## **2.6.2 Scatter of results**

Small standard specimens for characterization of FRC show a high scatter in the post-peak tensile strength values. There are generally different sources



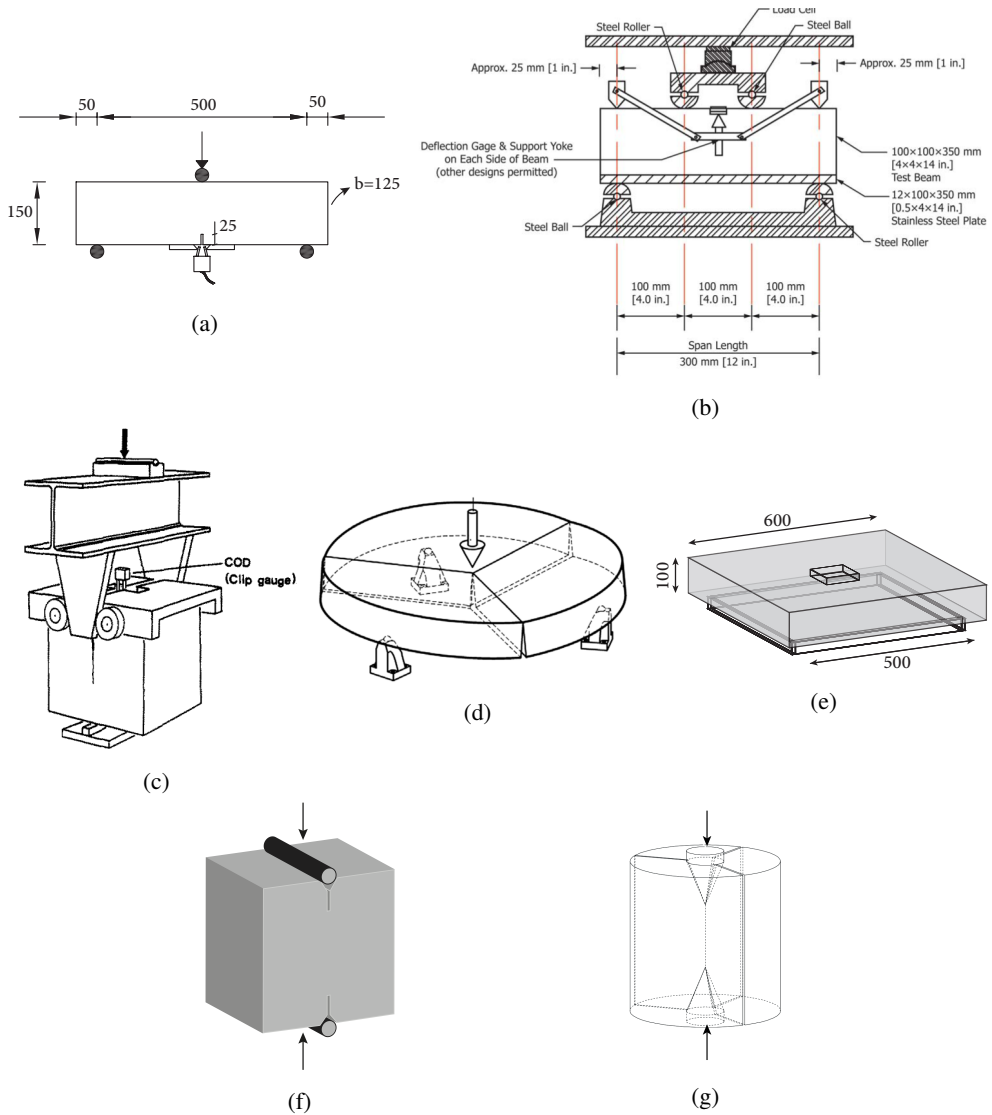


Figure 2.9: Test setups according to (a) EN14651 [86](b) four-point bending test [38] (c) wedge splitting test (figure adopted from [131]) (d) panel test according to ASTM C1550 [8](figure adopted from [24]) (e) panel test [87] (f) DEWST [72] and (g) Barcelona test [140].

for the scatter of the results, being the testing conditions, production process and the intrinsic variability in the material due to the random distribution of fibres in the matrix [41]. Coefficient of variations are often higher than 15% , and 20%-25% of variations very common to observe [91, 137]. Under a given casting modality, the main reason behind this high intrinsic scatter is the number and orientation of fibres as the main sources of material variability [51]. The small fracture plain and consequently low number of

fibres crossing the crack means that the results from one specimen to the other can be very different. Higher dosage of fibres leads to statistically more uniform mixes with a reduced distribution variation [124, 150]. Bigger fracture planes as well, lead to smaller scatter in the results [25, 40, 74]. The high dispersion of results leads to characteristic values, i.e. 5% fractile, that are far away from the average values of FRC tensile strength parameters. This may even lead to a complete neglect of the effect of fibres [41]. However, the behavior of real structural elements with high degree of redundancy in which larger crack surfaces are involved in the failure process, is governed by the average material properties [52]. Substantial difference between characteristic and average values of residual tensile strength parameters lead to design of overly safe structures. This difference is shown by the results obtained from notched beam specimens and structural tests on full-scale slabs on grade made from the same material.

Parmentier et al. [150] tested FRC samples of hooked-end fibres with different testing modalities in which the plate tests showed less than 10% of variation and the beam test up to 24% of variation. Fig. 2.10 shows the variation in results obtained in this work. They also point out that different fibres show different scatter in the results which also depends on the type of experiment carried out. Some fibres that show lower scatter in beam test, show higher scatter in panel test and vice versa. Using correlations between results of different test methods at the same cracking level is suggested in order to reduce the number of tests required. Bernard [25] showed that FRC concrete plates show a coefficient of variation in the range of 6% to 9%. Minelli and Plizzari [139] compared the scatter of results between beam tests (according to UNI 11039 [117] and EN 14651 [86]) and round panel tests (according to ASTM C1550-10 [8] and small panels proposed by the authors) and showed that larger crack surfaces and internal redundancy reduces the coefficient of variation of results. The coefficient of variation for the UNI and EN tests were 23% and 41%, while for the ASTM round panel and the proposed small round panel test, the scatter was 16% and 8% respectively. Kooiman [124] has shown that the coefficient of variation of fracture energy is higher for a stronger matrix while fibre aspect ratio has marginal effect on coefficient of variation. Also investigating the effect of beam width tested in 3 point bending test on scatter of results, Kooiman points out that under a controlled casting scheme for beams with three widths of 150, 300, and 450 mm, while the fracture energy does not vary, wider specimens show lower scatter of results. This is shown in Fig. 2.11. The large scatter of results in a three-point bending test is not specific to FRC, and the determination of fracture energy of plain concrete also suffers from this effect, although to a smaller degree [110]. A thorough discussion will be given

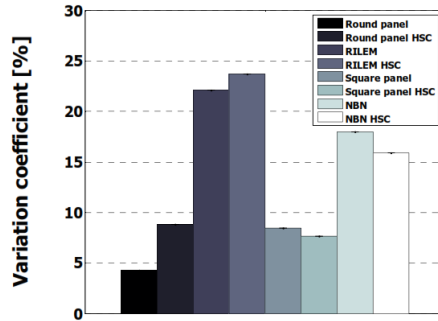


Figure 2.10: variation of the results of the bending test according to four different methods and two concrete types (NC-HSC) [150].

in Chapter 7.

## 2.7 Fibre orientation

While a perfect fibre alignment in the direction of stresses gives the highest efficiency of fibres in crack bridging, fibres oriented perpendicular to the stress direction, theoretically speaking, fail to contribute in strength increase [138]. Edgington and Hannat [81] in 1972 showed very nicely how the distribution of fibres can affect concrete behavior. They had the assumption that fibres tend to orient perpendicular to the direction of vibration. Hence they tested two concrete prisms under compression in two different direction, as shown in Fig. 2.12(a), while measuring horizontal strains. Fig. 2.12(b) clearly exhibits and confirms their assumption on anisotropy in FRC. Qing et al. [160] tested

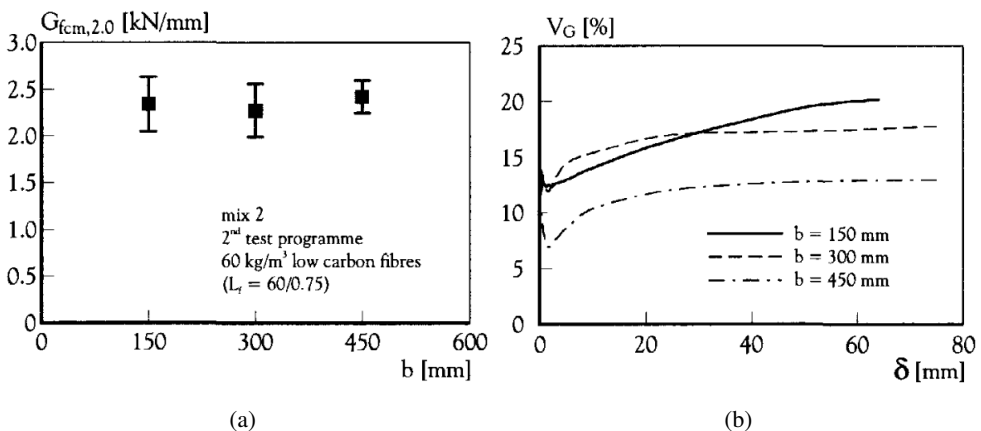


Figure 2.11: Effect of increasing beam width on (a) fracture energy and (b) coefficient of variation [124].

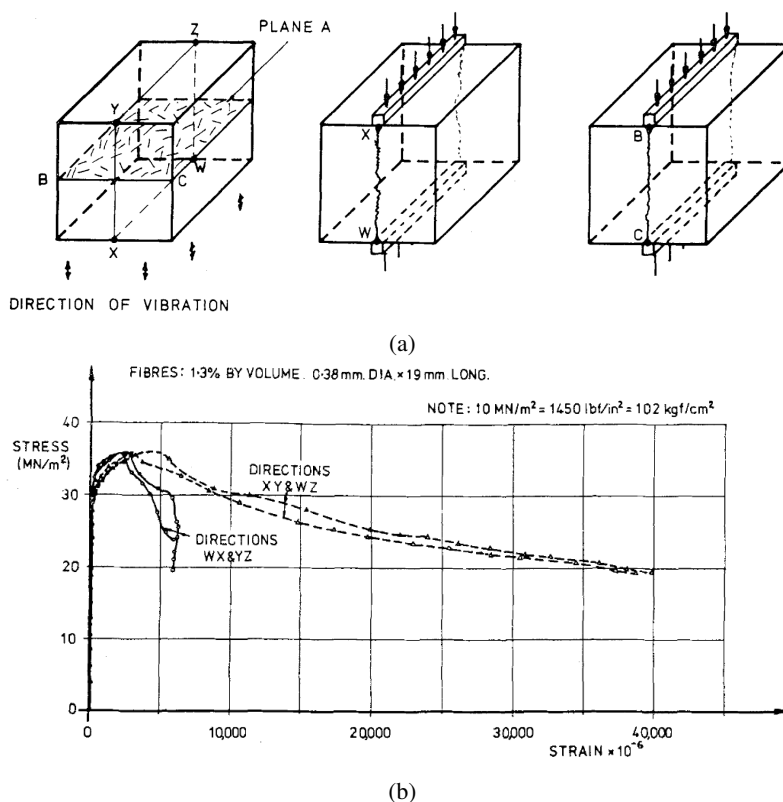


Figure 2.12: (a) Alignment of fibres in a plane perpendicular to the direction of vibration and the two two directions for the compression test (b) The stress versus lateral strain of the tested specimens in two directions [81].

and aligned SFRC (ASFRC) in which through the application of a magnetic field, the fibres were aligned in the direction of principal stresses leading to an orientation factor of 0.9. Comparison of the uniaxial tensile behavior of this specimens with the normal SFRC companions in three matrices with a w/c ratio of 0.42, 0.36, and 0.32, evidently underlines the importance of fibre orientation. Fig. 2.13 shows these results.

The effectiveness of the application of SFRC is strongly dependent on the uniform distribution of fibres within the structural element, as areas with reduced number of fibres will work as flaws in the structure affecting its overall behavior. While fibre orientation is affected by dosage of fibre, size of specimen, workability of the mixture, and method of compaction, it has been seen that fibres tend to orient perpendicular to concrete flow [13]. Vandewalle [198] shows that in SCSFRC beams, due to velocity profile and wall effect, fibres tend to orient along the direction of flow. They also carried out X-ray

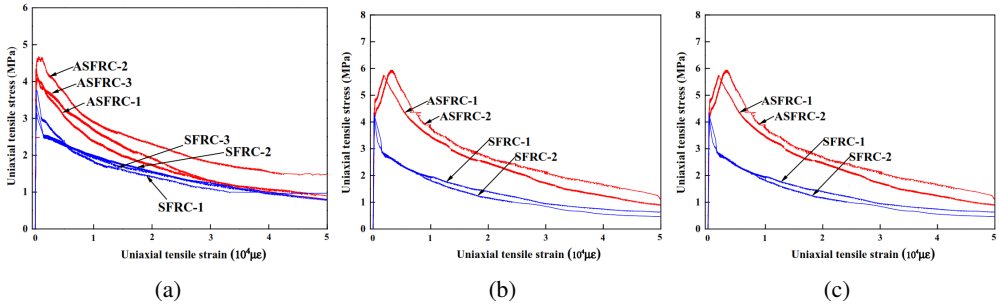


Figure 2.13: Direct tension test on specimens with aligned fibres (ASFRC) and normal SFRC in a mixture with a w/c of (a) 0.42 (b) 0.36, and (c) 0.32 [160].

imaging of SCSFRC and traditional SFRC beams and showed the better orientation of fibres in the self-consolidating mix design, along the direction of the beam. As expected, higher residual strength values were obtained for the SCSFRC beams. Higher stress values in stress-strain relationship fitted for FRC slabs were reported for sample of a larger size which was due to the tendency of fibres to orient perpendicular to concrete flow, while in smaller slab samples, the wall effect hindered better orientation of fibres with respect to crack planes [31]. Fig. 2.14 shows this phenomenon which was called fibre network effect by the authors.

In another work [33], a non-destructive magnetic method is used to assess

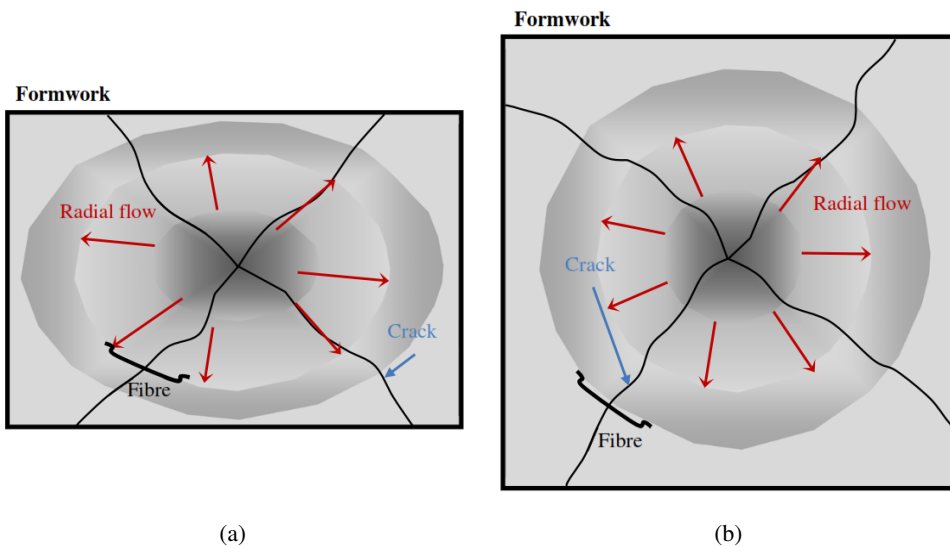


Figure 2.14: fibre orientation in a (a) smaller rectangular slab (b) larger square slab [31].

fibre orientation in concrete slabs in which concrete is cast from the center of the slab. The results show the orientation of fibres to be parallel to the sides of the formwork due to the wall effect. The results obtained in this work demonstrate that while in the central part of the slab that concrete is poured the orientation of fibres is almost equal in both directions, going further away from the slab center, fibres tend to orient perpendicular to the direction of flow. Three regions of central, intermediate and external are recognized based on fibre orientation. Furthermore, an orientation factor is derived based on the results of the inductive method, whose application gives much better numerical results in modeling of the load deflection of slabs. An iterative fitting procedure is also carried out to find the orientation factor which gives values of around 2 to 3.2. In [157], a 14% increase in  $\sigma_3$  value (stress at maximum strain in the assumed trilinear  $\sigma - \epsilon$  relationship) is observed for square slabs compared to slabs with a width to length ratio of 0.5 which is assumed to be due to better orientation of fibres with respect to the cracks, based on which a geometrical coefficient is introduced to be applied to  $\sigma_3$  provisioned by the code. Orientation and distribution of fibres in square concrete slabs cast from the center is also studied in a work by Zhou and Uchida [209]. A slab of 1200 mm diameter and 50 mm of thickness was cast from the center and beams were cut from the slab with  $0^\circ$ ,  $30^\circ$ ,  $60^\circ$ , and  $90^\circ$  inclination with respect to the radial direction and tested under a three-point bending test with a 10 mm deep notch. Effect of inclination and distance from the casting point were studied and the results show that while the distance from the casting point does not affect the flexural behaviour of beams at  $90^\circ$ , it has a considerable effect on other cutting angles. Also fibres tend to align perpendicular to the flow. The results are shown in Fig. 2.15.

Barnett et al. [13] studied the effect of casting modality on fibre orientation through resistivity measurement of concrete in two perpendicular directions on circular concrete panels which was able to show the tendency of fibres to orient perpendicular to the direction of casting. The electrodes were arranged in a square array in two sizes of 5 cm and 10 cm. The larger probe was more influenced by deeper layers of concrete. There were indications that close to the bottom of the mold, fibres were less inclined to be oriented perpendicular to flow direction which was also confirmed through X-ray image analysis. Boulekbache et al. [34] considered the effect of rheological parameters on orientation of fibres. To this aim, a translucent polymeric material was adjusted for two different yield stresses of 25 Pa and 70 Pa, and observations were made on the distribution of fibres in the two materials. Dispersion of fibres in the fluid with lower yield stress led to better distribution of fibres perpendicular to the flow direction, while in the material with higher yield

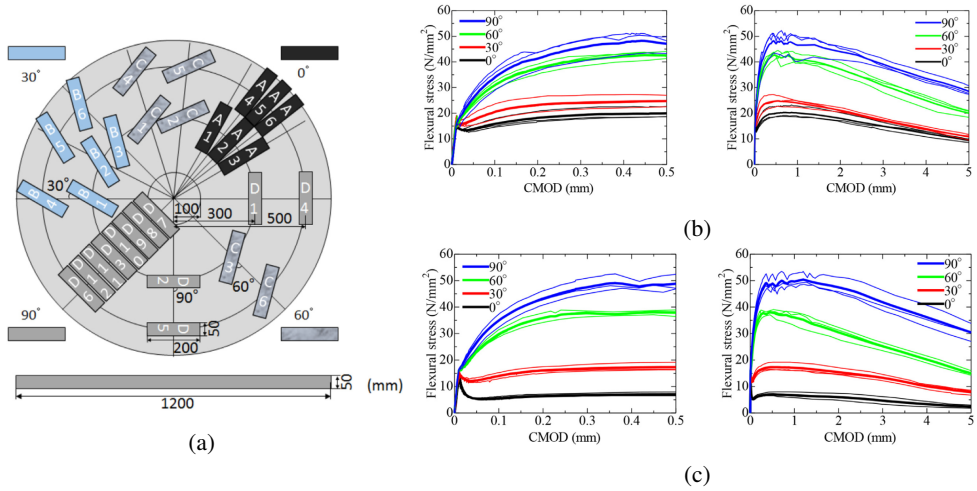


Figure 2.15: Effect of fibre orientation on flexural behaviour of FRC, (a) slab cast from the center (b) Specimens cut from 30 cm distance from the center and (c) from 50 cm [209].

stress distribution was more random with balling-up of the fibre clusters. This is shown in Fig. 2.16. Afterwards, a normal concrete, a high strength concrete, and a SCC together with their fibre incorporated mix designs were made and the rheological parameters of the mixtures were assessed. Increasing the yield stress of the mixtures, with the lowest for the SCC with 36 Pa and highest for the HSC with 261 Pa, led to a decrease in the orientation factor [185], from 0.57 for the fibre reinforced self compacting concrete to 0.30 for the high strength fibre reinforced concrete.

In case of channel flow of concrete, the orientation of fibres is highly affected by the wall effect due to which, fibres tend to orient in the direction of flow [34]. Stähli et al. [187] cast concretes with the same mix design with the only difference being the dosage of superplasticizer, in a U-shaped box with a  $70 \times 70$  mm cross section. CT-scan of beams cut from the three branches of the box showed that the higher the flowability of the concrete, the more they are aligned in the direction of flow. The results of bending tests on the beams cut from the box were affected by enhanced fibre orientation for more workable concrete, the inability of the workable concrete to carry fibres in the vertical branch flowing upwards and the effect of segregation.

Ferrara et al. [94] tested beams cut from two slabs, one with a 1-D casting direction parallel to the longer side of the slab, and the other following a radial flow of concrete poured from the longer side. The beams cut from the slabs were in two set of orthogonal direction as shown in Fig. 2.17. The results of

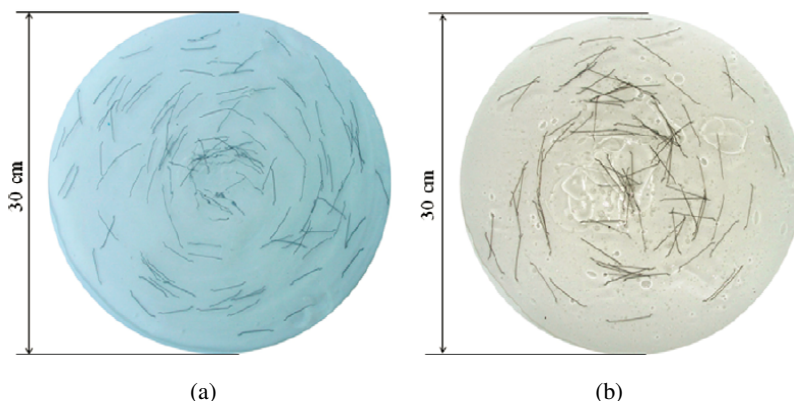


Figure 2.16: Fibre orientation in polymeric material with yield stress of (a)  $\tau_0=25$  Pa (b)  $\tau_0=70$  Pa [34].

4 point bending tests carried out on the specimens show that in slab A fibres are preferentially oriented in the direction of flow while, the results of slab B show more comparable results. The fibre orientation factor driven from a fibre counting procedure from micrographs also confirm the better alignment of fibres in specimens cut from slab A parallel to the direction of the flow, with an orientation factor of  $\alpha=0.85$  compared to  $\alpha=0.442$  for the specimens cut in the other direction. Direct correlations were observed between number of fibres and orientation densities with residual strength of the samples tested. Moreover, Švec et al. [190] have reported the effect of formwork roughness on orientation of fibres. Lower roughness increases the fluid shearing rate and consequently the tendency of fibres to be oriented according to the flow. The effect of rebars on the orientation of fibres is studied in the work by Žirgulis et al [210]. They cast SFRC slabs without rebars, with rebars in one direction, and with a grid of rebars. They demonstrated that while in the unreinforced slabs, fibres tend to orient following the radial flow of concrete, in the presence of rebars, flow of concrete is mostly parallel to the rebars which affects the orientation of fibres. Fibres tend to be parallel to the rebars in front of the rebar (relative to the flow direction), and perpendicular to the rebar at the back of the rebars. Furthermore, they observed the largest number of fibres above the grid of rebars depicting the effect of rebars on the vertical flow of concrete. Vibration also affects the orientation of fibres and promotes a planar positioning of the fibres [98]. Laranjeira et al. [126] argue that isolated treatment of different influencing factors on fibre orientation is inconclusive and gives very limited insight on the collective effect of different factors, i.e. flow, vibration, casting method, fresh-state properties, and formwork geometry. They attempt to give a framework in which different aspects can be integrated.



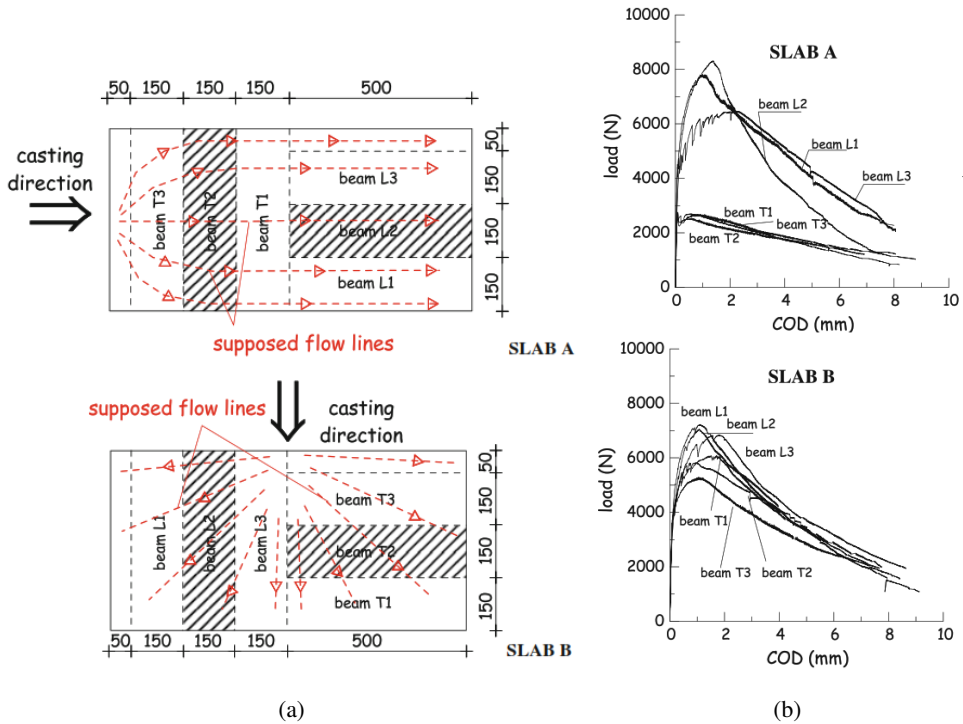


Figure 2.17: (a) slab and specimen geometries and casting direction (b) results of 4 point bending test on specimens cut from the slabs [94].

### 2.7.1 Orientation factor

The effect of orientation of fibres is formally quantified through the *orientation factor*. This factor represents the ratio of average projected fibre length in the direction of tensile stresses for all possible orientations of fibre, to the fibre length. For example, in 3D space, and for equal chance of orientation in any direction we have  $\alpha_0=0.405$  [185] (shown in Eq. 2.1).

However, the presence of boundaries, fresh state properties, and casting modality of the FRC can substantially affect the orientation of fibres. Different codes approach this issue in more or less different and at times similar manners. Here, a few of these approaches are explained.

#### 2.7.1.1 Model Code

In MC2010, not much explanation was given on how to deal with the orientation effect in FRC. The orientation factor,  $K$ , was suggested to be taken as 1 assuming an isotropic fibre distribution. For favorable and unfavorable effect of orientation,  $K < 1$  and  $K > 1$  may be applied upon experimental

$$\alpha_0 = \frac{\int_0^{\pi/2} \int_0^{\pi/2} l_f \cos(\theta) \cos(\phi) d\theta d\phi}{(\pi/2)^2 l_f} \quad (2.1)$$

$$= 0.405$$

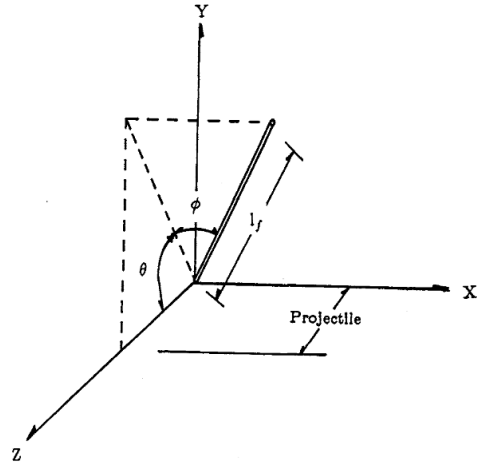


Figure 2.18: 3D fibre orientation [185].

verification. The residual tensile strength values are divided by  $K$ . On the contrary, in MC2020 draft, the orientation factor,  $\kappa_0$ , is being multiplied to the residual tensile strength values of  $f_{Fts,ef}$  and  $f_{Ftu,ef}$ . Similar to MC2010, a quasi-isotropic distribution is presumed for fibres with  $\kappa_0=1$ . The orientation factor is defined as the ratio of orientation factor in the structure under study to the orientation factor in a standard specimen tested according to EN 14651. This is,  $\kappa_0 = \alpha_0/0.58$  [80]. A maximum value of  $\kappa_0$  is bounded to 1.5, and in case a  $\kappa_0 > 1$  is applied in one direction, the other direction needs to be penalized with a  $\kappa_0 < 1$ . Furthermore, it is suggested to implement a  $\kappa_0=0.5$  when local checks are to be done. A new addition to this standard, adopted from the Danish guideline [178], that can be of practical interest is that in two separate tables, the  $\kappa_0$  values for slab and wall elements are given. For slabs, for the longitudinal and transversal directions  $\kappa_0=1$  is given, while for wall elements different values are given for the middle and end portions, as well as top, center and bottom sections.

### 2.7.1.2 Norwegian guideline [122]

In the Norwegian guideline by the effort of Kanstad, fibre orientation factor is applied for two goals. One, is for the computation of residual tensile strength of FRC in a structure, and the other is for theoretical computation of residual tensile strength. For the FRC cast in a structure, this guideline reads:

$$f_{ftk,res,2.5,struct} = f_{ftk,res,2.5,norm} (4\alpha_{struct} - 1) \nu_{f,struct} / \nu_{f,nom} \quad (2.2)$$

where  $\alpha_{struct}$  is the orientation factor in the structure,  $\nu_{f,struct}$  and  $\nu_{f,nom}$  are the volumetric ratio of fibres in the structure and the nominal one. For the

computation of the residual strength this guideline suggests:

$$f_{ftk,res,2.5} = \eta_0 \nu_f \sigma_{fk,mid} \quad (2.3)$$

in which  $\nu_f$  is the volume of fibres,  $\sigma_{fk,mid}$  is the mean stress in the fibres crossing the crack with the assumption that they all carry an equal stress, and  $\eta_0$  is the capacity factor which is the ratio of resultant force in the fibres with the current distribution to the condition that they are all unidirectionally oriented. If fibre orientation is not known, this value is taken as 1/3, otherwise:

$$\eta_0 = 4/3\alpha - 1/3 \quad \text{for } 0.5 < \alpha < 0.8 \quad (2.4a)$$

$$\eta_0 = 2/3\alpha \quad \text{for } 0.3 < \alpha < 0.5 \quad (2.4b)$$

### 2.7.1.3 German [56] code, and Danish guideline [178]

In both documents the orientation factor,  $\kappa_F^f$ , which is multiplied to the residual tensile strength values, a general value of 0.5 is suggested and for horizontally cast, plane structures in which width  $> 5 \times$  height,  $\kappa_F^f = 1$  is proposed. The Danish guideline gives further suggestions for the orientation factor of SCFRC in beams, slabs, and wall element (for slab and wall elements the same values are proposed in MC2020 first draft). Also, in Annex-L of this document, the fibre orientation factor is given as  $\kappa_F^f = \alpha_0 / 0.6$  where  $\alpha_0$  is the fibre orientation in a structure and 0.6, is the reference value for a characterization beam. Determination of the  $\kappa_F^f$  is to be done through simulation, CT scanning, visual inspection, and based on experience when sufficient data are available.

### 2.7.1.4 French recommendation [2]

This recommendation introduces the reduction factors of  $K_{local}$  and  $K_{global}$ , which are determined through suitability tests under circumstances that properly represent the real structure under investigation. The former is applied when local effects are of interest and the latter is considered when overall structural responses are examined. They are introduced to the post-cracking tensile parameters. The determination is carried out based on sawn beams from real structure. If results are not available, a  $K_{global} = 1.25$ , and  $K_{local} = 1.75$  are recommended for design situation. Although the recommendation is for ultra high performance fibre reinforced concrete, its approach on fibre orientation is not significantly different from other guidelines for FRC.

## 2.8 Slab testing

### 2.8.1 Flat slabs

One of the most efficient applications of FRC, is the construction of slab elements. Propagation of multiple cracks in these elements allow for a better

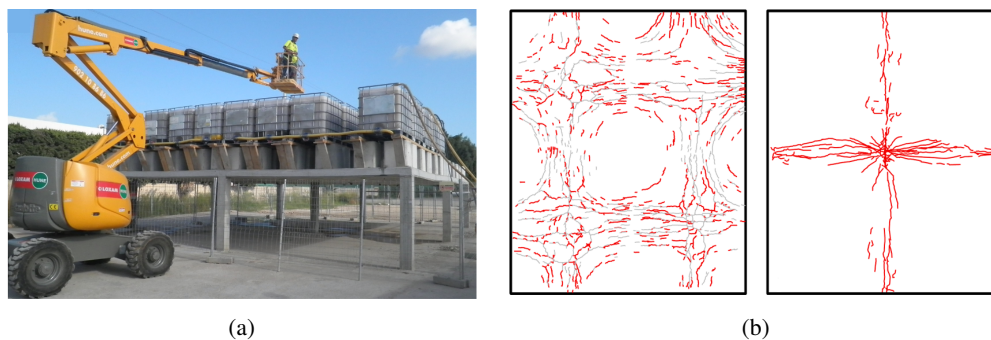


Figure 2.19: (a) The overall configuration of the flat slab and loading condition and (b) formation of yield lines on top and bottom of the slab panels [3].

exploitation of the effect of fibres. This is specifically the case for two-way statically redundant slabs. A two-way action in slabs allows for a better redistribution of stresses and propagation of much higher number of secondary cracks [33]. These applications consist of slabs on grade, pile supported industrial floors, elevated slabs, etc. Some examples of laboratory tests and full-scale experiments are discussed. More examples can be found elsewhere [3, 107, 134].

### 2.8.1.1 Aidarov et al. [3]

A full-scale four-panel SFRC flat slab with  $70 \text{ kg/m}^3$  of double-hooked fibres with aspect ratio of 65 is tested under a uniformly distributed load. Anti progressive rebars are utilized. Span length is 5 m and 6 m in the two directions and the depth of the slab is 0.2 m. The slab is loaded gradually in multiple steps starting from a load level that is lower than the SLS and surpassing the design load in the last stage. At each stage of loading, the load is kept for a duration of time so that the response is stabilized. Deflection, length and width of cracks are evaluated. Also, orientation of fibres is assessed by means of an inductive test.

At SLS, deflection and crack widths were much smaller than requirements. Although the maximum reached load was more than the design load, still more strength capacity was left in the slabs. It was shown that the orientation of fibres was in the plane of the slab which enhances the in-plane behaviour of these elements. Furthermore, plastic hinges were fully formed on the top and bottom sections of the slabs. Fig. 2.19(a) and (b) show the overall testing conditions and the formation of plastic hinges at the expected position of the yield lines.

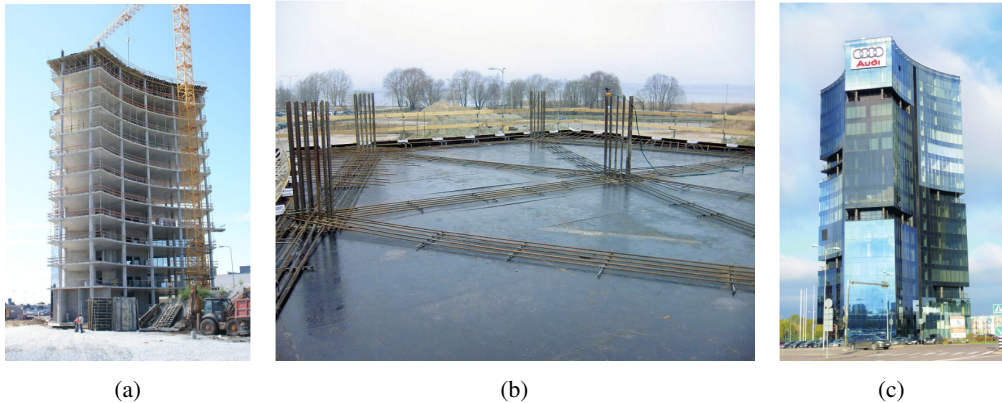


Figure 2.20: (a) The column-slab system [68] (b) SFRC slab and the APC rebars [134] and (c) the finished structure [134].

### 2.8.1.2 Destrée & Mandl [69]

They report the results of four full-scale tests on suspended slabs made only of SFRC. All the tested structures have nine fields resting on sixteen columns. In two of them the span length is 3.1 m in each direction which is typical of pile supported suspended industrial floors, and the other two structures have 5 m and 6 m of span which is a common value for elevated slabs in residential and commercial buildings. The first two examples are reinforced with  $45 \text{ kg/m}^3$  of fibres and the two latter with  $100 \text{ kg/m}^3$ . They report the load at first cracking and the ultimate load for the tested slabs, and demonstrate that common methods in computation of resisting bending moment for SFRC sections underestimate real values. Fig. 2.20 shows the structure made of suspended flat slabs of the Rocco al Mare building in Tallinn, Estonia, in which  $100 \text{ kg/m}^3$  of fibres were utilized and only anti-progressive collapse, or continuity rebars [172] were adopted.

### 2.8.1.3 Fall et al. [91]

Fall et al. [91] tested octagonal concrete slabs of 2.4 m wide and approximately 80 mm of thickness supported on 20 steel pipes. Nine slabs were tested, three of which were reinforced only with rebars, three were reinforced with steel fibres, and three of the slabs had both rebars and fibres.  $\phi 6$  rebars were used with two different spacing in each direction and the steel fibre used in the study was double-hooked with a length of 60 mm and a diameter of 0.9 mm. The support reaction forces were measured during the test to study the redistribution effect of steel fibres. The load-deflection results of the tested slabs are shown in Fig. 2.21. Higher numbers of cracks were observed for the R/FRC slabs and for the SFRC slabs almost no additional crack was formed after the development

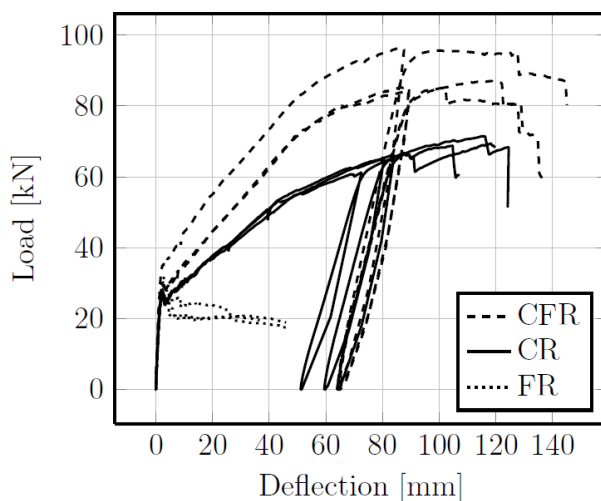


Figure 2.21: load deflection results of the slabs reinforced with rebar (CR), reinforced with rebar and fibres (CFR), and reinforced with only fibres (FR) [91].

of the ultimate crack pattern which was soon arrived after the first crack. It was observed that addition of fibres to the slab, leads to a more homogeneous traversal distribution of forces along the support. While in the RC slabs all supports in the strong direction were compressed, only 57% of supports of the weak side were in compression on average. However in the R/FRC slab, the average engagement of the supports were respectively 90% and 73% for the strong and weak directions. Following these results, the authors point out that in FRC structures the smearing effect of the fibres increases the effective support width [91].

#### 2.8.1.4 Facconi et al. [89]

They tested eleven thin concrete plates of  $4.2 \times 2.5 \times 0.08$  m. Two slabs were made from  $25 \text{ kg/m}^3$  of a double-hooked steel fibre with a length and diameter of 60 mm and 0.9 mm respectively (SD25), and  $20 \text{ kg/m}^3$  and  $25 \text{ kg/m}^3$  of a single hooked fibre with a length and diameter of 32 and 0.4 mm were incorporated to cast six slabs, three with each of them (SG20 and SG25). Two slabs were cast with an opening. One of them was reinforced with  $91 \text{ kg/m}^3$  of rebar and the other was reinforced with an optimized configuration of  $43 \text{ kg/m}^3$  of rebar and  $25 \text{ kg/m}^3$  of fibres (overall  $68 \text{ kg/m}^3$ ). They point out that high slenderness of the plates with the application of SCC may promote the 2D in plane orientation of fibres which can help increase ductility of these elements which is a significant parameter to be checked when rebar are completely excluded. The slabs are simply supported on all sides and are loaded with two loading knives of 1000 mm long in the direction of the longer

axis.

All the SFRC plates show an almost plastic, or hardening behaviour after cracking with a maximum deflection that is more than 30 times the first cracking deflection. In the R/FRC slabs with opening, much narrower cracks propagated, from 0.4 mm to 1.6 mm as opposed to 0.8 mm to 5.2 mm for the conventionally reinforced plate despite of roughly 20% less steel employed. Fibres were very effective in mitigating the disturbed stress field due to the presence of the opening.

#### **2.8.1.5 di Prisco et al. [73], Parmentier & Van Itterbeek [151] (Limelette slab)**

A full-scale frame structure made of a column-slab system was erected in Limelette, Belgium. The structure was made of a SFRC mixture with  $70 \text{ kg/m}^3$  of steel fibres as the sole reinforcement. Each panel of the structure is  $6 \times 6 \times 0.2 \text{ m}$ . Some panels were tested for their behaviour in SLS and some were tested up to ULS. Of significance is the plastic response of the central panel under a concentrated load with more than 40 mm of deflection. Moreover, the development of plastic hinges at the supports of the central panel are worth of noticing. Proper characterization of the SFRC material make this test a suitable benchmark for modeling.

#### **2.8.1.6 Hedebratt & Silfwerbrand [108]**

A flat slab with sixteen panels with a 3 m span between the columns and a thickness of 130 mm were cast and tested. Two dosages of  $40 \text{ kg/m}^3$  and  $80 \text{ kg/m}^3$  of fibres with  $l_f/d_f=60/0.9$  are adopted, each incorporated in half of the slab. Also, in half of the flat slab, column to column rebars of  $3\phi 12$  is placed at the top and bottom sections with a spacing of 100 mm. Overall, four configurations of rebars and fibre dosages were examined. Moreover, panels vary in their boundary conditions in that some of them are clamped to a sandwich wall and some have free edges. Panels are tested under concentrated load and crack patterns and openings are recorded. Yield line analysis is implemented to predict the bearing capacity of the slabs.

#### **2.8.1.7 Døssland [76]**

In her PhD thesis she tested 13 simply supported slabs of  $3.6 \times 1.2 \times 0.15 \text{ m}$  under a concentrated load in the middle of the specimens. In all tests fibres and rebars were combined as reinforcement. In the first series of the tests a low reinforcement ratio of  $\rho=0.07\%$  and  $0.15\%$  were adopted along with  $0.7\%$  of fibres of two lengths of 65 and 35 mm with the same aspect ratio. In a second series of the tests higher reinforcement ratio with different kinds of fibres and

dosages were tested. The results highlighted the importance of fibre length in enhancement of the load bearing capacity of the slabs. Also, a reduction in ductility of the slabs was observed as softening occurred for all slabs.

#### **2.8.1.8 Pujadas et al. [158]**

Eighteen slabs of  $3 \times 1 \times 0.2$  m were tested under a four-point bending setup. Two steel fibres and two polypropylene fibres were adopted in 0.25% and 0.50% by volume, and in all cases these fibres were accompanied by reinforcing rebars to cast the slabs. Two slabs were tested for each configuration and two reference slabs reinforced only with rebars were also made. The FRC was characterized in a three-point bending tests according to MC 2010, and for each slab test, deflection and crack width and spacing was measured. Effect of fibres, specifically for the SLS region, in reducing crack opening and deflection is praised. It is interesting to notice that up to a 40-50 mm of deflection that is reported in their work, there is no trace of softening in the slab response.

#### **2.8.1.9 Blanco et al. [33]**

They tested six concrete slabs with a thickness of 20 cm and length of 3 m. The width of the slabs were 1.5, 2, and 3 m. Two specimens were tested for each size. The elements were simply supported on all sides and they were loaded with a concentrated load in the center.  $40 \text{ kg/m}^3$  of steel fibres with an aspect ratio of 80 and a length of 50 mm were adopted. The bearing capacity of the smaller slabs is only 16% more than the resistance of the slabs that are twice as large. This has been attributed to the effect of fibres that diminish the influence of geometrical differences. Furthermore, they investigate the orientation of fibres by a magnetic method applied to specimens cored from the slabs. They showed that fibres were mostly oriented in the plane of the slabs and at the edges of the slabs fibres tended to be directed parallel to the formwork. Afterwards they showed that without taking into account the effect of orientation of fibres, a nonlinear numerical model may considerably overestimate the bearing capacity of the slabs. However, in their choice of the tensile constitutive law for the SFRC material, the tensile law given in MC2010 was adopted, which is suitable for practical design situations. This may justify the substantial overestimation of the bearing capacity of the slabs.

### **2.8.2 Slab on grade**

In one of the most prominent works on application of SFRC in slab construction, this material was used in the underwater slab construction in Postdamer platz in Berlin, where the slabs were loaded by very high water



pressure. In this project 30000 m<sup>3</sup> of SFRC was cast in a 10h shift. Falkner and Henke [90] tested SFRC slabs of 3×3 m with a thickness of 280 mm to study the deformation and load bearing capacity of these slabs. One plain concrete slab and two SFRC slabs with 40 kg/m<sup>3</sup> of 50/0.6 fibres and 60 kg/m<sup>3</sup> of 60/0.8 fibres were tested with 9 hydraulic jacks and a cork plate was placed under the slab to simulate the high water pressure. While the load bearing capacity of the plain concrete slab was reached by the tensile stresses reaching the tensile stress of concrete, the SFRC slabs were able to sustain much higher loads and four to five times higher deformations.

Roesler et al. [169] tested five concrete slabs of 2.2×2.2 m and a thickness of 12.7 cm on a clay soil layer, two with two different steel fibres, two other with a synthetic macro-fibre at two dosages and a plain concrete. They observed a 25% to 55% improvement in the flexural cracking load for of the fibre reinforced slabs over the slab made with plain concrete while the flexural tensile strength of almost all mixtures were comparable. As expected, the ultimate load-bearing capacity of the slab made with plain concrete was considerably increased by addition of fibres which mainly depended also on the fibre type. Barros and Figueiras [14] found similar results in terms of effectiveness of fibres in reinforcing soil supported slabs. In [183], Sorelli et al. testing concrete slabs of 3×3×0.15 m on ground, observed a better behavior in terms of load deflection for shorter fibres with a length/diameter of 30/0.6 with respect to the slabs made with fibres of 50/1 with the same content of fibres. It was also shown that the application of a hybrid combination of shorter and longer fibres can substantially reduce the crack opening of the slabs when compared to slabs containing just the 50 mm long fibres. Cominoli [52] tested three slabs of 3×3×0.15 m reinforced with a with 0.38% by volume of hooked-end steel fibres having a length of 50 mm and a diameter of 0.75 mm. The slabs were supported by an array of steel springs with a distance of 400 mm to replicate a Winkler soil effect. The three slabs demonstrated very close response with a long branch of plastic behaviour. Fig. 2.22 shows the load-deflection response of the slabs and the experimental configuration.

## 2.9 Durability

Extensive research has been carried out over decades on durability and transport properties of concrete. Existence of cracks significantly affects the transport properties of concrete and makes the nature of the percolating fluid of a second importance compared to the crack pattern. With this regard, the geometry (crack width and roughness), connectivity and different scales of the cracks needs to be considered. It has been observed that the relation

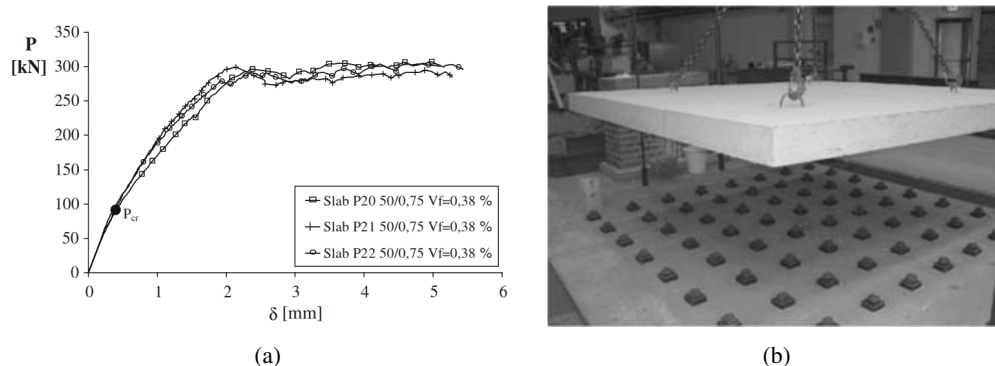


Figure 2.22: (a) load-deflection response and (b) the experimental configuration [52].

between permeation and crack opening can be easily developed considering a reduction factor taking into account the tortuosity of the crack surfaces [97]. While most studies investigate concrete properties in uncracked phase, the almost permanent presence of cracks in concrete structures which may lead to instantaneous initiation of corrosion, makes these results unsound and unreliable in real applications. Therefore, a sound study of service life of RC structures needs to consider as a component, the crack characteristics as well [148]. In their work, Ottieno et al. [148], pre-cracked concrete beams of  $100 \times 100 \times 500$  mm to three crack opening levels: 0.4, 0.7 mm, and incipient cracking that was identified visually by a lens which upon unloading would not be recognizable. Exposed to pounding and drying cycles of 5% NaCl solution they measured corrosion rates for two w/c ratios and two cement types at different ages. As expected, wider cracks width led to higher corrosion rates and even at incipient cracking they observed considerably higher corrosion rates compared to uncracked specimens. At older ages these specimens together with those pre-cracked to 0.4 mm showed reduction in corrosion rate due to self-healing. They concluded that no universal crack width threshold could be considered for all concrete types for the initiation of corrosion. However Wang et al. [203] and Rapoport et al. [162] mention a COD of 0.05 and 0.1 mm as the threshold below which the permeability of concrete is not affected. Water permeability test on 50 mm thickness circular specimens which were pre-cracked to different CMODs in a Brazilian splitting test, showed that application of steel fibres can reduce the permeability coefficient for the same CMOD. This was due to smaller crack widths as a result of multiple cracking in the SFRC specimens compared to the unreinforced specimen as the permeability coefficient is related to the cube of the crack width [162]. It was also observed that the rate of increase of permeability with CMOD decreased with fibre volume. While there are reports concluding that the presence of

fibres can lead to an increase in the chloride migration coefficient due to weakened fibre-matrix interface, [28] have reported that fibres in uncracked concrete does not affect the chloride migration coefficient. Berrocal et al. [26] have also demonstrated that fibres delay the formation of corrosion-induced cracks and improve the bond behaviour of corroded rebars. Slight corrosion of fibres themselves may increase the post-peak tensile properties of the mixture due to a slight expansion of the fibre and an enhanced bond with concrete. This can lead to embrittlement of SFRC and changing the failure mode [21]. However, presence of wide cracks can lead to severe corrosion of the fibres [102].



---

## EXPERIMENTAL PROGRAM

---

### 3.1 Introduction

In this chapter we are presenting the extensive experimental program carried out within the scope of this thesis in which thirty two plates of  $2000 \times 2000 \times 150$  mm are tested. The tests carried out on the plate specimens are divided in two parts: *Part A*, and *Part B*. In *Part A* we try to give a self-evident and comprehensive comparison between the structural response of SFRC, RC, and R/FRC (combination of both rebars and fibres) plate elements under a concentrated load. Twenty specimens are tested in this series with three different boundary conditions. In *Part B*, twelve nominally identical SFRC plates are tested with the same boundary condition in order to gain insight into the scatter of structural resistance of SFRC plates in a redundant scheme, where the failure process consists of a stable multi-cracking phase with involvement of considerable volume of material. In addition to the plate elements, six shallow beams of  $350 \times 150 \times 1500$  mm are also tested under a four-point bending setup. Three beams are reinforced only with fibres, while in the remaining three beams the combination of fibres and rebars is adopted. In each part, the tensile properties of the SFRC material is properly characterized through three-point bending tests. In the following sections, first the test set-up and tested specimens in each category is described and afterwards, the details

of the testing conditions will be explained.

## 3.2 Experiments

### 3.2.1 Part A; RC, SFRC, and R/FRC plates

In this section we are describing the experimental program pertaining to the first phase of the study. The complete overview of the *Part A* of the experimental campaign is depicted in Fig. 3.1. The experiments designed in this part try to materialize a solid ground for a comparison between RC, SFRC, and R/FRC plate elements with dimensions of  $2000 \times 2000 \times 150$  mm. To do so, twenty specimens are tested with three distinctive boundary conditions in terms of load and support positions. These three boundary conditions consist of S1 configuration, where the concentrated load is applied in the center of the plates and the specimens are supported at the mid-length of each side, S2 in which the load is imposed in the center with the supports being positioned at the four corners, and the S3 configuration in which the load is applied at the mid-edge of one side of the plates with the supports being in the four corners. Different boundary conditions are chosen to trigger different failure mechanisms. The RC plates are reinforced only at the bottom with 12  $\phi$  12 reinforcing rebars in each direction (in both axis of the plates) with a minimum cover of 30 mm, the SFRC plates are reinforced with  $35 \text{ kg/m}^3$  of Dramix<sup>®</sup> 4D 65/60 BG steel fibres ( $l_f/d_f=65$ ,  $l_f=60$  mm), and the R/FRC specimens are reinforced with a combination of both of the reinforcing solutions. Furthermore, a special case is studied under the S2 configuration where  $35 \text{ kg/m}^3$  of steel fibres are combined with reinforcing rebars that run only on the outer rig of the plates. The reinforcing rebars in these specimens are half the reinforcing rebars in the R/FRC plates and comprise only of six rebars closer to the edges of the plates in each direction. This solution which is an alternative to the R/FRC specimens is labeled as R/FRC-Alt. In terms of weight of steel, the RC plates are reinforced with  $70 \text{ kg/m}^3$  of steel and accordingly, the R/FRC and R/FRC-Alt specimens are reinforced with 105 and  $70 \text{ kg/m}^3$  of steel respectively. Given that the overall weight of steel in the RC and R/FRC-Alt plates are equal, comparison of these two reinforcing solutions underlines the effect of partial replacement of rebars with fibres.

Fourteen notched prismatic beams of  $600 \times 150 \times 150$  mm were tested in a three-point bending test to characterize the tensile properties of the SFRC material at three different ages, and six cubes of 150 mm side are examined for the assessment of the compressive strength of the SFRC. The plain concrete cast for the RC plates is not separately tested for compressive strength and it is assumed that the moderate dosage of fibres does not alter the compressive strength of the concrete.

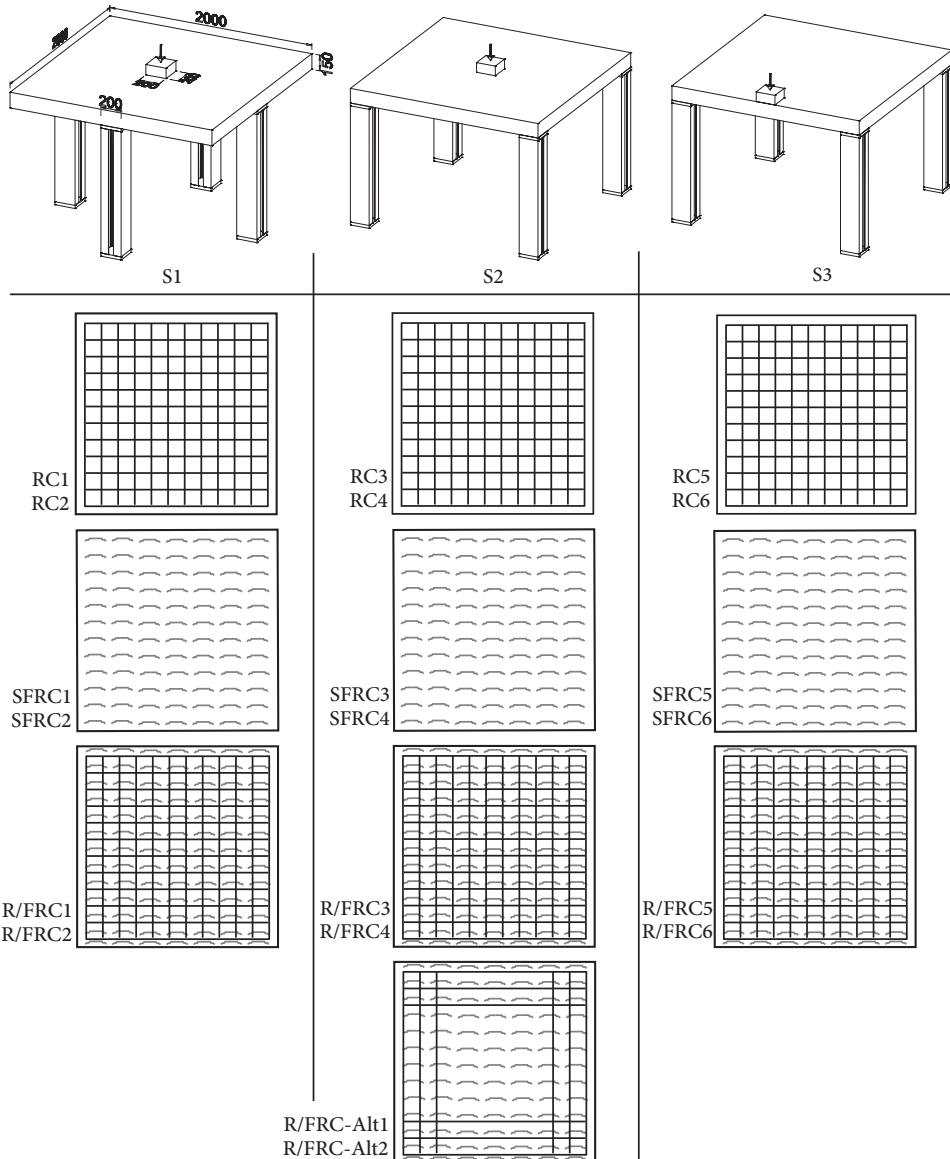


Figure 3.1: Experimental program of *Part A*. Twenty plates are tested in three testing configurations of S1, S2 and S3. RC, SFRC, R/FRC and R/FRC-Alt reinforcing solutions are implemented. Two specimens are tested for each reinforcing type.

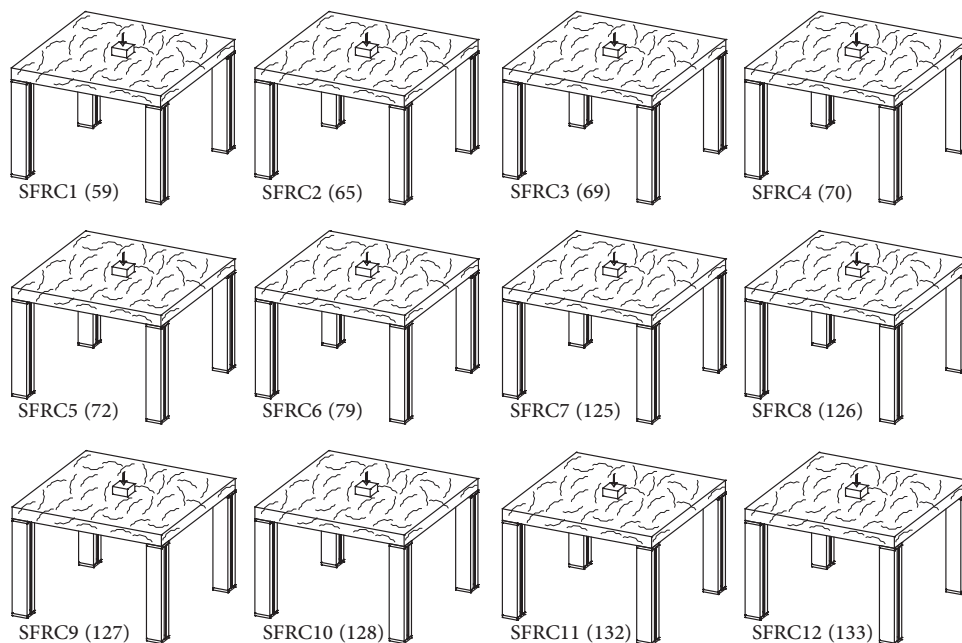


Figure 3.2: Experimental programme of *Part B*. Twelve SFRC plates were tested along with eleven notched beams. The number in parenthesis is the age, expressed in days, at which the test was carried out.

### 3.2.2 *Part B*; Scatter of strength of SFRC plates

The second phase of the experimental program is vis-à-vis the dispersion of the structural resistance of SFRC plates. To this end, twelve nominally identical SFRC plates with the same dimensions as those specimens mentioned in *Part A* were tested under the S2 configuration. Together with each of these twelve structural elements, notched specimens were also tested in a three-point bending setup. Of specific interest in this part is the difference in the dispersion of results obtained from testing the plate elements versus the notched prismatic beams. The compressive strength of the SFRC is determined testing six cube specimens of 150 mm side: three were tested with the first tested plate and three were tested with the last plate. The overview of the *Part B* of the experimental program is schematized in Fig. 3.2. The numbers in parenthesis shows the age of the specimen at testing.

### 3.2.3 Shallow beams

Six shallow beams of  $350 \times 150 \times 1500$  mm were tested under a four-point bending setup with 1350 mm of clear span. Three of the beams were reinforced



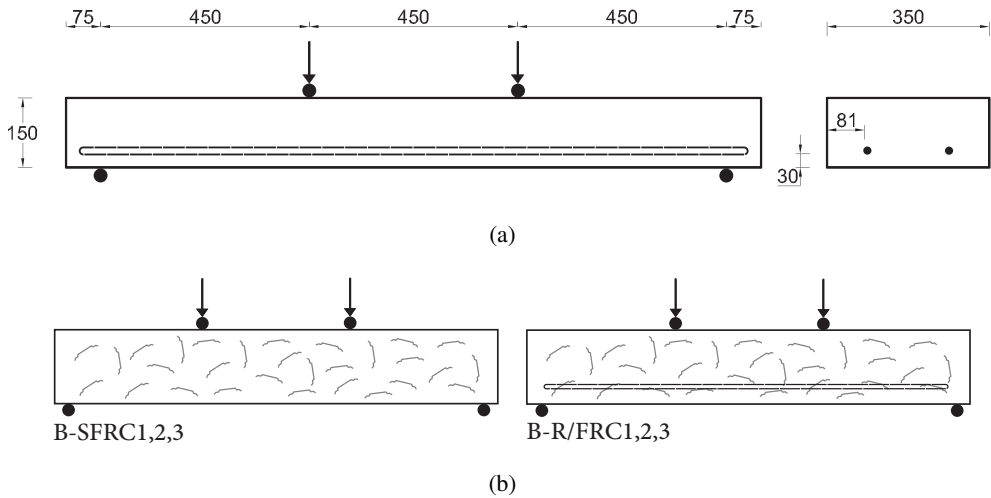


Figure 3.3: (a) The dimensions of the shallow beams and the loading condition (b) three SFRC (B-SFRC) and three R/FRC (B-R/FRC) beams were tested.

with  $35 \text{ kg/m}^3$  of the same 4D steel fibres (B-SFRC), and three beams were reinforced with  $2\phi 12$  rebars in the longitudinal direction and  $35 \text{ kg/m}^3$  of fibres (B-R/FRC). The spacing of the rebars and the geometric reinforcement ratio is the same for the shallow beams and the plates. The experimental setup and tested shallow beams are shown in Fig. 3.3.

### 3.3 Material and casting

The mix design of the SFRC material used to cast the plates and shallow beams is given in Table 3.1. The plain concrete used to cast the RC specimens has the same mix design, except for the steel fibres which were excluded. The steel fibres are Dramix<sup>®</sup> 4D 65/60 BG steel fibres, double hooked with a length of 60 mm and a diameter of 0.9 mm. According to the manufacturer the tensile strength and the Young's modulus of the fibres are respectively 1600 MPa and 200 GPa. The compressive strength of the SFRC material is determined in both *Part A* and *B* on six 150 side cube specimens. In *Part A* the cubes are tested at 34 days of age while in *Part B* three cubes are tested with the first plate test at 59 days of age and three cubes are tested with the last one at 134 days of age. The concrete cast for the shallow beams is the same as of the *Part A*. The obtained values are given for each specimen tested within each of the two phases and the characteristic values are reported in Table 3.2. The coefficient of variation of the compressive strength values obtained for *Part A* show a remarkably high scatter, the origin of which is not clearly known.

Table 3.1: Mix design of the SFRC material used in the study.

Constituent	Dosage
Cement (Cem IV 42.5R) [kg/m <sup>3</sup> ]	380
Sand 0/4 [kg/m <sup>3</sup> ]	1008
Sand 0/8 [kg/m <sup>3</sup> ]	504
Gravel 4/14 [kg/m <sup>3</sup> ]	171
Carbonate filler [kg/m <sup>3</sup> ]	100
w/binder	0.33
Fibre [kg/m <sup>3</sup> ]	35
Superplasticizer [% of cement weight]	1.5

The tensile properties of the rebars that were utilize in the study were characterized in a direct tensile test on four specimens. Fig. 3.4 depicts the tensile stress-strain curve for the four specimens, and the mean yield strength  $f_{y,m}$ , mean tensile strength  $f_{t,m}$ , and the ultimate strain  $\epsilon_{u,m}$  are shown on

Table 3.2: Determination of the compressive strength of the SFRC material for both *Parts A* and *Part B*.

<b>Part A:</b>	
$f_{c,cube}$ [MPa]	age [days]
51.29	
73.16	
51.00	
76.15	34
46.52	
50.42	
$f_{cm,cube}=58$ (V=22%)	
$f_{cm}=48.14$	
$f_{ck}=40.14$	
<b>Part B:</b>	
49.04	
46.89	59
46.27	
$f_{cm,cube}=47.4$ (V=3%)	
61.81	
56.78	134
60.94	
$f_{cm,cube}=59.8$ (V=4.5%)	
$f_{cm,cube,6specimen}=53.75$	
$f_{ck}=36.6$	

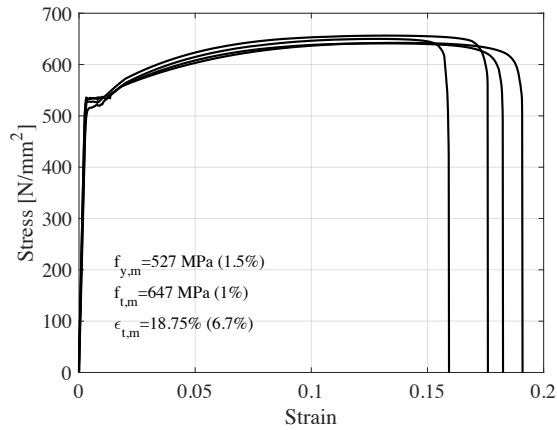


Figure 3.4: Direct tensile test on four rebar specimens.

the figure. All the specimens were cast in a job-site from a concrete that was delivered by truck mixers. Plate specimens of *Part A* and the shallow beams, were cast on May 9th and the specimens of *Part B* were cast on February 13th. Wooden frameworks were prepared and the concrete was pumped from the truck into the molds. Fig. 3.5 shows images of casting and the molds. The concrete was self-compacting and no vibration was needed for placement of concrete into the molds. Attention was given to cast the SFRC mixture from the center of plates to allow concrete to radially flow to fill the frameworks. Effort was made to follow the same casting modality for all the specimens. It is shown that fibres tend to orient perpendicular to the direction of flow, hence a radial flow would lead to a favorable alignment of fibres.

After casting, the plates were covered with wet burlaps for a couple of days after which they were transferred to the laboratory. In the laboratory, the plates and the prismatic beams were kept in atmospheric conditions, while the cubes were kept in a room with controlled temperature of 25°C and a relative humidity of around 90%.

## 3.4 Testing methods

### 3.4.1 Three-point bending test

For both *Part A* and *Part B*, the prismatic beams of 600×150×150 mm were tested according to a three-point bending test, following the recommendations of EN 14651 [86], to characterize the tensile properties of the SFRC material. Specimens were notched in the mid-length to a depth of 25 mm with a cutting machine. The tests were carried out with a servo-hydraulic machine controlling



Figure 3.5: (a) The job-site (b) placement of the anchorage device (c) casting of the plates (d) prismatic beams and cubes for compressive strength measurement (e) casting of the shallow beams.

the displacement of the loading head. During the test the Crack Mouth Opening Displacement (CMOD) was measured at the notch with a clip gauge attached to two knife edges that were glued to the bottom of the beams. With the assumption of linear stress distribution at the cross section, the results of the tests are reported as nominal stress-CMOD. The results obtained from the characterization tests will be discussed in the next chapters together with the corresponding plate elements.

### 3.4.2 Plate tests

#### 3.4.2.1 Loading

The load was applied by means of an electro-mechanical jack with maximum capacity of 1000 kN by adopting a displacement control. A constant displacement rate equal to  $20 \mu\text{m/s}$  was imposed to the loading head. The loading head has a cross section of  $200 \times 200 \text{ mm}$ . A piece of neoprene with

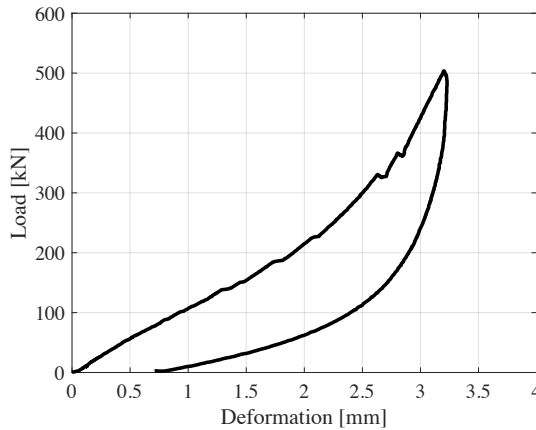


Figure 3.6: The load-deformation of the neoprene sheet which was placed between the loading head and the plate surface.

dimensions of  $220 \times 220 \times 25$  mm was placed under the loading point. The behavior of this neoprene sheet was examined by loading it and measuring the variation of its thickness. The obtained load-displacement curve obtained is shown in Fig 3.6.

### 3.4.2.2 Support condition

The plate was supported on four  $200 \times 200$  mm steel plates of 25 mm thickness, welded on the top of two UNP200 profiles of 1200 mm high. A neoprene sheet, of 5 mm thick, was placed on the steel plate to prevent direct contact of the slab with the steel plate. The slab was fastened to the support by a 16 mm grade 8.8 bolt screwed inside an anchorage system located in the center of the plate, with the goal to provide a bilateral constraint. The anchorage device is a T-FIXX GV<sup>®</sup> by Halfen. The bolt was fastened manually through the clearance between the UNP sections by a wrench. The anchorage device was designed for a tensile load of 35.3 kN and a shear load of 21.2 kN in a C45/55 concrete. The details of the support, the anchorage device, placement of the anchorage device, and the sizes are given in Fig. 3.7.

**3.4.2.2.1 Anchorage behaviour** In order to examine the behavior of the anchorage system, the vertical displacement of the corner of the slab was measured on two supports (NW and SE supports) on a SFRC plate from S2 series. The displacements are recorded on the external edge and the internal edge of the support on concrete surface with an offset from the support corner that is taken into account. The positions where the measurements were carried out are shown on the top right inset of Fig. 3.8 with transparent gray circles.

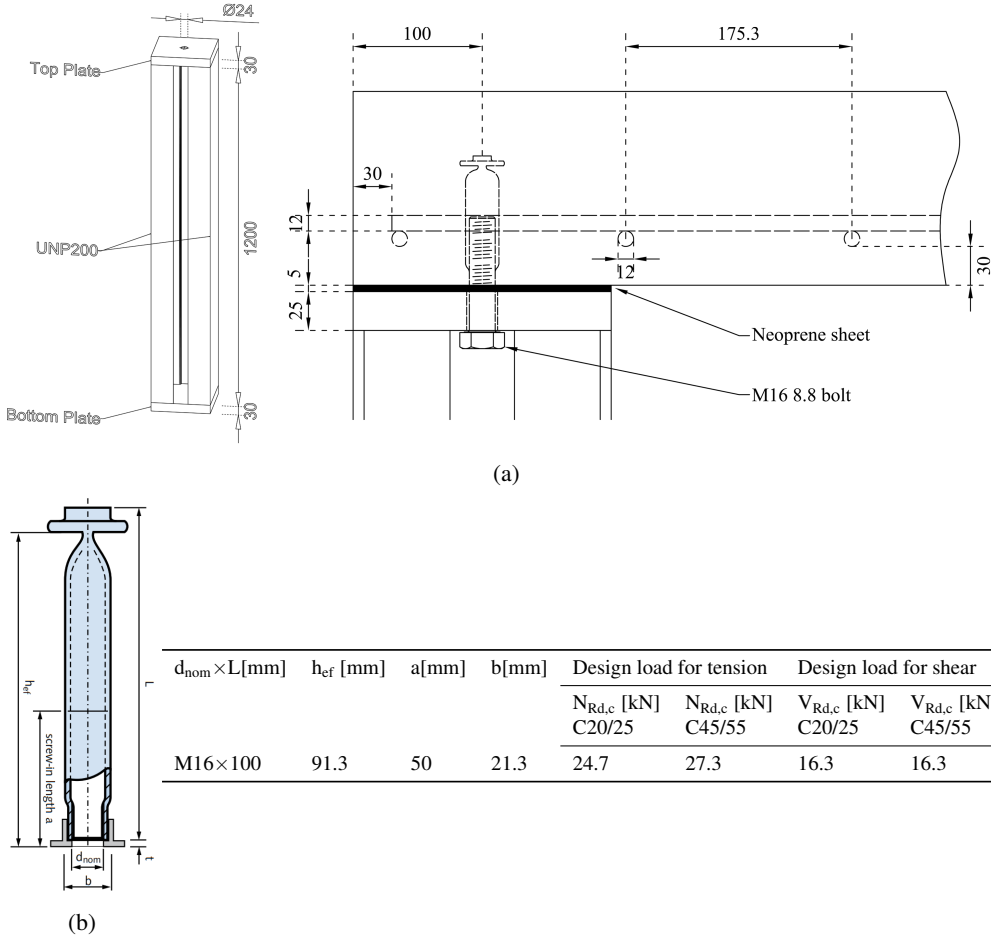


Figure 3.7: (a)left- Detailing of the support and, right- positioning of the support and dimensions related to the placement of rebar (b)The anchorage device adopted to create a bilateral support for the plate elements and its specifications.

In Fig. 3.8, the as-measured results for the external and internal instruments (the effect of the offset of the instrument from the corner of the support is not excluded) are shown with dark gray and light gray curves, which regard the deflection of the inner corner and uplift of the outer corner of the plate, respectively. Assuming a linear deformation, the displacement of the plate at the position of the anchorage is computed for both supports, which is shown by thicker black curves in the center of the graph. It is observed that the anchorage is compressed almost up to the maximum load reached in the plates. This is due to the presence of the thin neoprene sheet that was placed between the plate and the support. Therefore, it is reasonable to assume that for the SFRC plates, the support works in compression. This will not hold true for plates with other

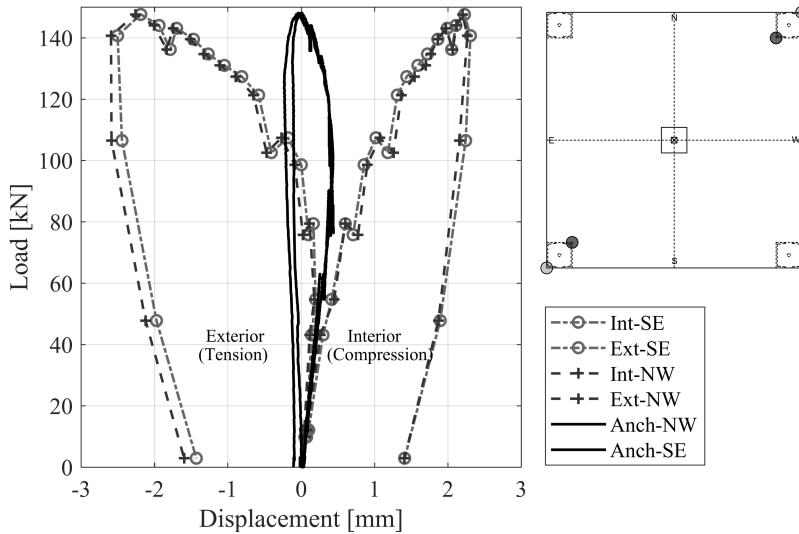


Figure 3.8: The measurements regarding the corner displacement of the slabs and the deformation of the anchorage.

reinforcement solutions, however, no measurement was carried out for these elements.

### 3.4.2.3 Measurements

For each specimen the deflection was measured from the bottom surface of the plate and below the loading point with a potentiometer. Furthermore, some displacement measurements were carried out to monitor the opening of the cracks with Linear Variable Differential Transducers (LVDTs). The position, label, and nominal gauge length of instruments utilized to measure the Crack Opening Displacements are shown in Fig. 3.9. For the S1 and S2 series, eight instruments were positioned below the plates to capture the opening of the positive cracks, and four instruments were applied on the top surface at the supports to capture possible opening of negative cracks. Four of the instruments at the bottom were in square configuration with a nominal length of 300 mm. The actual length of the gauges excluding the thicknesses of the supports used for the placement of the instruments is around 270 mm. These instruments are labeled as “COD<sub>b</sub>” indicating that the instrument was at the bottom surface of the specimen, which is followed by another set of letters showing the position of the instruments in cardinal directions. In addition, there were two longer instruments that recorded the COD further away from the loading point, hence being less affected by the local damage caused by the concentrated load. These two instruments were placed 500 mm away from the concentrated load and have a gauge length of approximately 950 mm. The

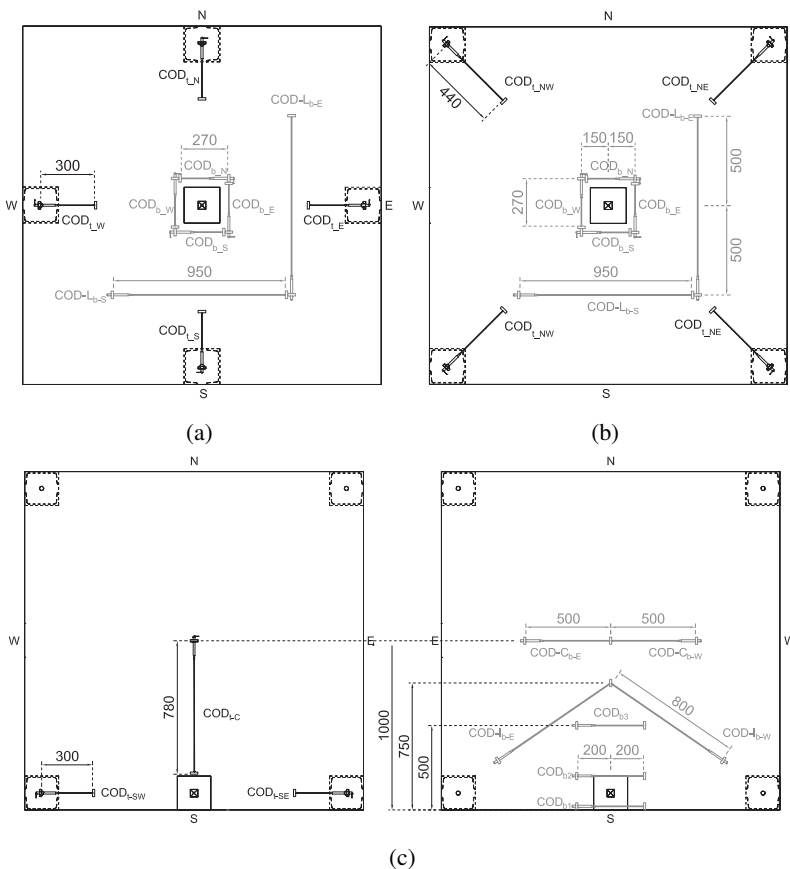


Figure 3.9: The position and label of instruments adopted to measure the opening of positive and negative crack on plates in series (a) S1, (b) S2, and (c) S3.

longer instruments are designated with "COD-L", the L letter specifying their longer length. In the same manner, the instruments on the top surface of the plates are marked as "COD<sub>t</sub>" preceded by the cardinal directions.

In S3 series, given that the expected crack pattern was very different from the S1 and S2 series, the position of instruments was modified to better capture the crack propagation. In this series, three instruments were positioned on the top of the plates and seven LVDTs were located at the bottom. At the bottom of the plates, COD<sub>b-1,2,3</sub> recorded the opening of the cracks that propagated close to the loading point, COD-C<sub>b-E,W</sub> were positioned along the central x-axis of the plates, and COD-I<sub>b-E,W</sub> were arranged with an inclination to capture the opening of the cracks that branched out from the loading point. The three measurements carried out on the top surface of the plates try to record possible propagation of a circular negative fan.



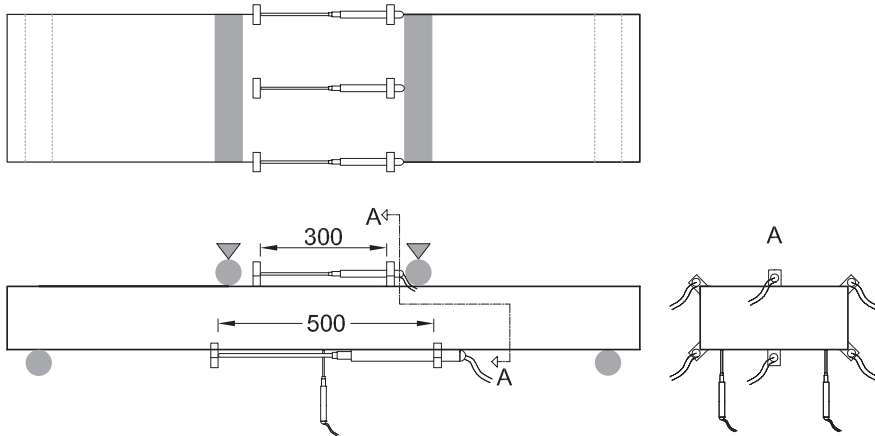


Figure 3.10: The position and gauge length of the instruments.

### 3.4.3 Shallow beams

For the tested shallow beams, deflection, and deformations on the top and bottom chords were measured with eight LVDTs. The position and length of these instruments are shown in Fig. 3.10. Two LVDTs were applied to measure deflection, and three instruments were utilized to measure deformations on top and bottom face of the beams.

Up to 10 kN of load, the load was applied in load-control, and from that point on, a displacement control scheme with a rate of  $150 \mu\text{m}/\text{min}$  was implemented. In all cases the specimens were unloaded after some softening behaviour was observed. Then specimens were removed from the loading machine and the cracks at the bottom of the specimens were marked with a marker.



---

## ***PART A: COMPARISON BETWEEN SFRC, R/C, AND R/FRC PLATES***

---

### **4.1 Introduction**

In this chapter the results of the experimental programme carried out in *Part A* of the campaign are presented. The goal is to investigate the effect of fibres on the structural response of plates in a self-explanatory manner. We report the results of twenty plate elements that were tested in three configurations for the load and support positions: S1 (support in the middle of each side and loaded in the center), S2 (supported in the four corners and loaded in the center), and S3 (supported at the four corners and loaded on the edge of one side). In each configuration three reinforcement solutions are investigated; RC plates in which the plates are reinforced with  $12\phi 12$  rebars at the bottom in each direction ( $70 \text{ kg/m}^3$  of steel overall), SFRC plates that are reinforced with only  $35 \text{ kg/m}^3$  of 4D steel fibres ( $l_f=60 \text{ mm}$ ,  $d_f=0.9 \text{ mm}$ ), and R/FRC plates in which both previous solutions are combined ( $105 \text{ kg/m}^3$  of steel overall). In the S2 configuration a reinforcement solution with reduced number of rebars and  $35 \text{ kg/m}^3$  of fibres is also investigated. In this type of plate,  $6\phi 12$  that are placed closer to the sides of the plates are utilized in each direction. This layout is labeled as R/FRC-Alt. What is noteworthy about these plates is that the overall amount of steel used in them equals  $70 \text{ kg/m}^3$  which is as much steel

as adopted in the RC plates. For each of the specimens in each configuration, two identical plates are tested.

## 4.2 Experimental results

### 4.2.1 Tensile characterization of the SFRC

The SFRC material that was cast for the SFRC, R/FRC, and R/FRC-Alt plates in *Part A* were tested in a three point bending test at different ages. Five specimens were tested in 34 days for a standard characterization of the SFRC material, five specimens were tested at 167 days of age at the beginning of the plate tests, and four specimens were examined at 220 days when the last plate was tested. In this manner, a proper evaluation of the gradual increase of, specifically, the post-peak residual tensile strength of the SFRC could be attained. Given that S1, S2, and S3 series were tested in chronological order, the tensile properties obtained at 167 and 220 days are better representatives of the SFRC material cast for S1 and S3 series respectively, and the average of the two ages would better illustrate the tensile mechanical properties of the S2 series. Consequently, the results of the flexural tests are categorized accordingly: 34 days results as standard characterization tests, results obtained at 167 days, 220 days of age, and the average of the two. Fig. 4.1 shows the stress-CMOD results based on these categories. It is clearly evident that age of specimens has a considerable effect on the tensile mechanical properties of the SFRC material which is specifically visible in the post peak region. The difference is much more visible when going from 34 days to 167 and 220 days, while there is not as much difference between the results of 167 and 220 days. The results pertaining to 167 and 220 days are shown together in Fig. 4.1(b) for the sake of easier comparison. This could also be due to the presence of the carbonate filler in the mix design which leads to delayed strength gain of the concrete. It is also noteworthy to highlight the fact that the improvement in the residual strength values is limited only to the CMODs of up to approximately 1.4 mm, while for wider CMODs, there seems to be no change in the post-peak strength values among different ages. This observation deserves more attention as the partial enhancement of residual strength values up to 1.4 mm, is equivalent to a reduced ductility of the SFRC material. Similar observation has been reported by Naaman and Al-Khairi [141] in a study where they tested high strength fibre reinforced concrete. They reported much faster residual tensile strength gain for smaller crack openings for hooked-end fibres when comparing 1 day results to 28 days. Bernard [23] in a study on age-dependant properties of fibre reinforced shotcrete tested round panels from 1 day of age to 5 years where a clear reduction in ductility was observed. Based on these results he emphasizes that a satisfactory result at 28 days does not

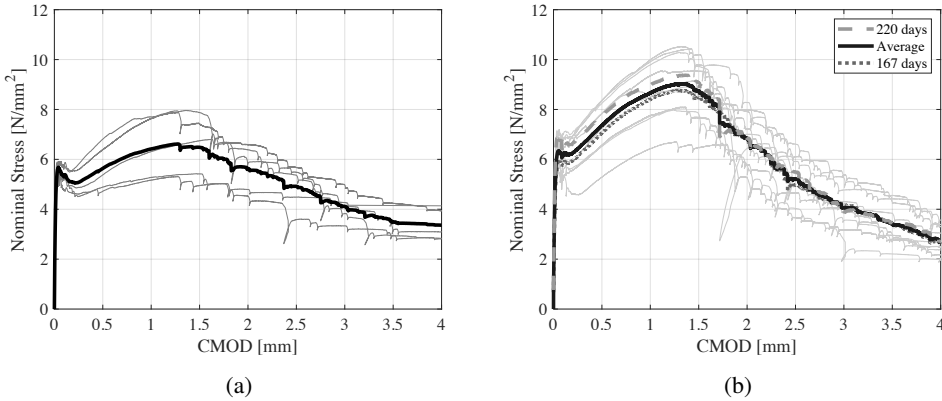


Figure 4.1: Nominal stress-CMOD results obtained at (a) 34 days and (b) 167, 220, and the average of 167 and 220 days.

guarantee the same performance at later ages. Similar results were obtained by Buttignol et al. [37]. The increasing slope of the softening branch compromises ductility of the material which can jeopardize its capacity for redistribution of stresses and maintaining stability. Within the FRC community, researchers suggest to test FRC not only at 28 days but also at 90 days of age. According to the results reported here and elsewhere, this seems to be a sensible proposition.

Following the recommendations of the MC 2010 the residual tensile strength values,  $f_{Ri}$ , at CMODs of 0.5, 1.5, 2.5, and 3.5 mm together with the flexural tensile strength,  $f_{ct,fl}$ , are reported in Table 4.1. What is remarkable in the results depicted in this table is the significant difference between the coefficient of variation of  $f_{ct,fl}$  and  $f_{Ri}$  values. The large coefficient of variation of the residual tensile strength values can have serious consequences on design of FRC elements. This topic will be briefly discussed in Section 4.3.2 of the present chapter, and Chapter 7 is dedicated to this argument. Classification of the SFRC material at different ages is given in Table 4.2. In time, the SFRC goes from a “3c” class material to a “5a” at 220 days, which underlines the reduction of ductility in time. Also, the ratios of  $f_{R1}/f_{Lk}$  which for structural purposes should be more than 0.5, is always respected.

#### 4.2.2 Plate results

In this section the experimental results concerning the failure mode of the plates, and their structural response in terms of deflection and crack opening displacements are presented and discussed. Discussions starts with the overall failure pattern of the plates followed by load-deflection and load-COD measurements at the bottom and top of the specimens. Given the similarities between the S1 and S2 series, these two configurations are discussed together

Table 4.1: The tensile strength parameters of the three-point bending tests carried out on the notched specimens divided in four categories based on their testing age.

Specimen category	number of specimens		$f_{ct,fl}$	$f_{R1}$	$f_{R2}$	$f_{R3}$	$f_{R4}$
34 days	5	$f_m$ [MPa]	5.7	5.64	6.49	4.92	3.48
		std [MPa]	0.21	.92	1.27	0.87	.65
		V [%]	0.04	0.16	0.2	0.18	19
		$f_k$ [MPa]	5.22	3.82	3.99	3.1	2.24
167 days	5	$f_m$ [MPa]	5.97	7.06	8.48	4.97	3.37
		std [MPa]	0.39	1.19	1.38	0.89	0.8
		V [%]	0.06	0.17	0.16	0.18	0.24
		$f_k$ [MPa]	5.13	4.6	5.61	3.16	1.94
167 & 220 days	9	$f_m$ [MPa]	6.32	7.36	8.73	5.2	3.39
		std [MPa]	0.53	1.05	1.22	0.96	0.88
		V [%]	0.08	0.14	0.14	0.18	0.26
		$f_k$ [MPa]	5.34	5.39	6.48	3.5	1.97
220 days	4	$f_m$ [MPa]	6.77	7.75	9.06	5.5	3.43
		std [MPa]	0.28	0.87	1.09	1.11	1.11
		V [%]	0.04	0.11	0.12	0.2	0.32
		$f_k$ [MPa]	6.07	5.66	6.53	3.07	1.34

Table 4.2: Classification of the SFRC material following the MC 2010 approach and the check of the allowable limits for a structural FRC.

Specimen category	Class	$f_{R1,k}/f_{L,k}$	$f_{R3,k}/f_{R1,k}$
34 days	3c	0.73	1.03
167 days	4b	0.9	0.79
167+220 days	5b	1	0.70
220days	5a	0.93	0.61

and S3 results are explained separately.

#### 4.2.2.1 Crack patterns

Fig. 4.2 shows the crack patterns of all the tested plates which gives an overall view of the behaviour and extent of stress redistribution in these specimens. The positive cracks at the bottom of the plates are depicted with gray lines and negative cracks formed on top surface of the plates are displayed with thicker black lines. As explained in Chapter 3, due to the peculiar behavior of the anchorage device utilized to create bilateral restraint at the supports, specifically for the S1 and S3 series plates, the failure mode may change during the test at increased deflections.

For the S1 plates, the positive cracks tend to be similar to the case of a

slab simply supported on all edges with unrestrained corners, in which strong torsional moments in the corner regions tend to lift up the corners, and if not held down, leads to forking of the yield lines. Two bands of diagonal cracks are formed which are more visible for the SFRC plates where the individual cracks can be detected. The extent of cracks are much higher for the RC and R/FRC plates compared to the SFRC plates. While negative cracks did not propagate on the top surface of the SFRC plates (other than a very short stretch of crack at bottom edge) the RC and R/FRC plates exhibit the formation of a negative fan. The limited ductility of the SFRC plates deters the formation of a failure mechanism that consists of also the negative crack. The ramifications of limited ductility of these specimens will be discussed in 4.3.5.

Failure pattern of S2 plates comprises of two orthogonal band of cracks. Clearly, the band width and the extension of the cracks are much wider for the RC and R/FRC plates when compared to their SFRC companions. In few cases, an inclined negative crack is formed at the position of the support for RC and R/FRC plates. Furthermore, some compressive crushing was also observed for the R/FRC plates.

In the S3 series plates there are some positive cracks that go from the loading point almost straight to the other side of the plate, and two bands of inclined cracks. Similar to the S1 series in which the SFRC plates lacked the required ductility to accommodate the propagation of negative cracks, the SFRC plates in S3 series also did not show cracks on the top surface. It is also remarkable that the failure of the SFRC plates occurred only after propagation of very few cracks.

#### 4.2.2.2 Load-deflection

**4.2.2.2.1 S1 and S2** The load-deflection curves related to the plates tested in S1 and S2 series are displayed in Fig. 4.3(a) and 4.3(b). The influence of steel fibres on the behaviour of the plates is readily appreciated. For the S1 series, the load-deflection curve for RC1 specimen was not registered due to technical errors and is not shown. In both cases at a certain load level, the RC plates undergo a sudden reduction in the stiffness, while the plates that are reinforced with steel fibres do not show any change in the behavior at this load level. Due to the loss of stiffness, the plates that are solely reinforced with reinforcing bars go through much greater deflection compared to the companion specimens that benefit from the presence of steel fibres. For instance, in the S1 configuration, at a load of 150 kN, the maximum deflection among SFRC1, SFRC2, R/FRC1 and R/FRC2 plates is 1.8 mm while RC2 displays a 2.85 mm of deflection. For the S2 series, at 75 kN of load which is around one-third of the maximum

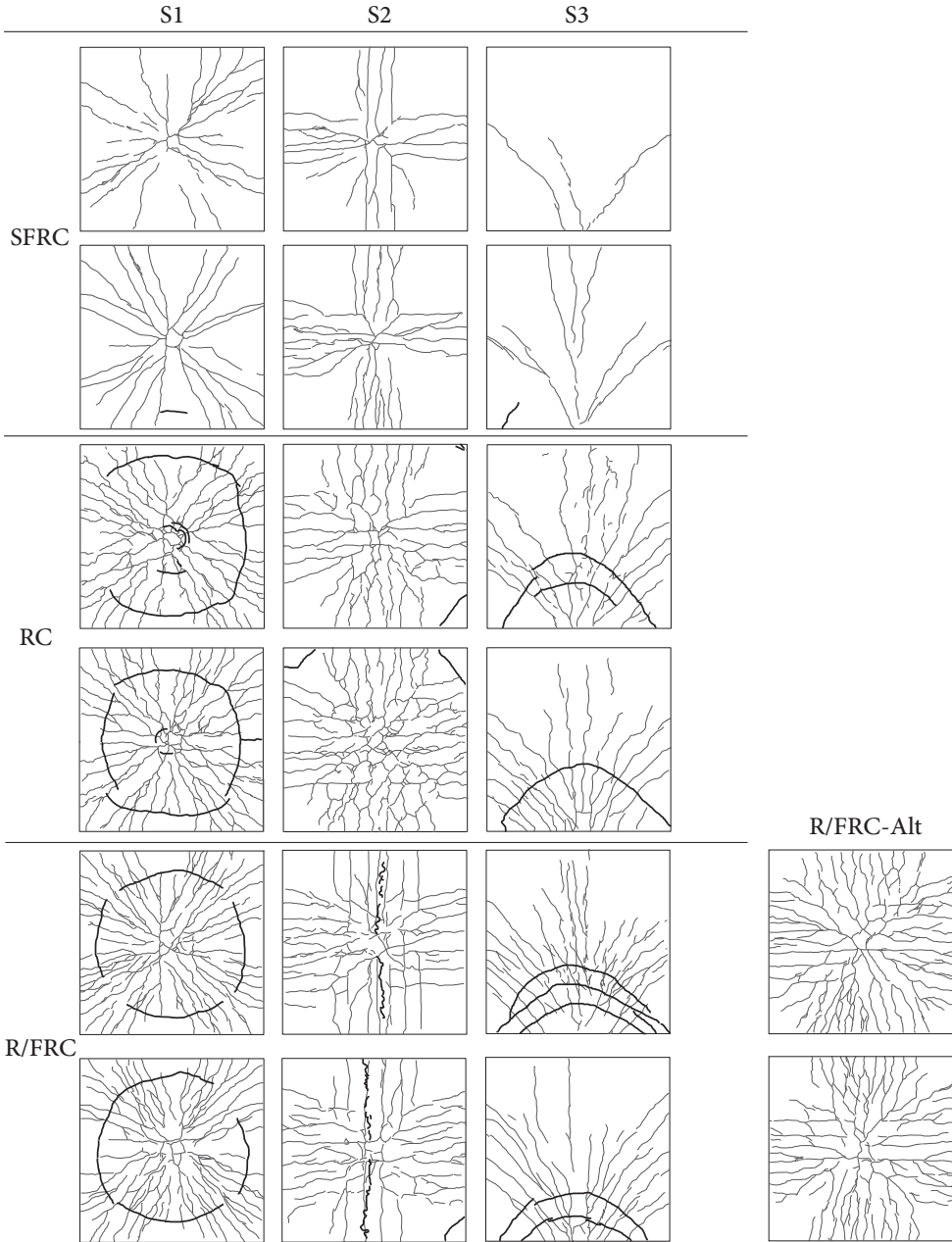


Figure 4.2: Crack pattern of SFRC, R/C, and R/FRC plates tested in S1, S2 and S3 configurations. Bottom cracks are shown with gray lines and the top cracks are shown with black lines.

load reached in the RC plates, the maximum deflection among the plates that incorporate steel fibres is for R/FRC3 plate with 1.65 mm compared to the



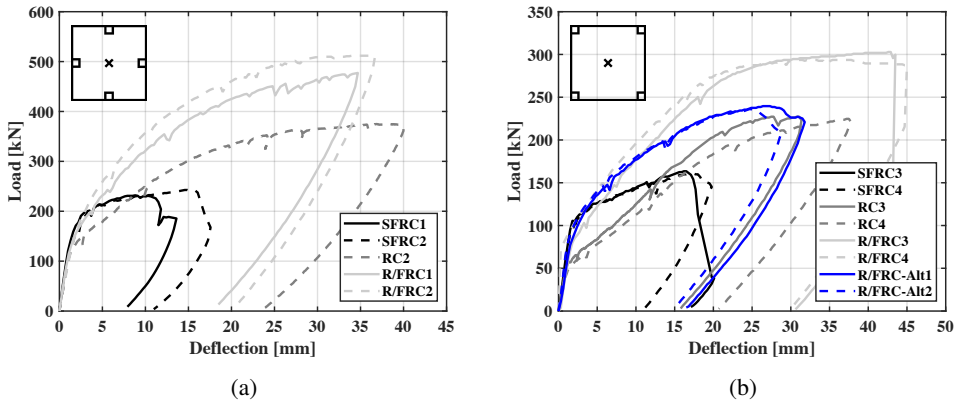


Figure 4.3: Load-deflection curve for (a) S1 and (b) S2 series.

average deflection of 4 mm for the R/C specimens.

When a major crack propagates in the RC plates, a substantial loss of stiffness occurs which at greater deflection is to some extent compensated through the tension-stiffening effect, however, the presence of fibres at the location of the cracks in the SFRC keeps concrete involved throughout the overall response of the plates. The influence of fibres in enhancement of tension-stiffening effect has been studied on tensile members [1, 30]. Although no measurements were carried out, the earlier cracking of the RC plates could to some extent be due to shrinkage effects.

Focusing on the response of the SFRC plates, it is quite noteworthy that the structural response of these specimens is very closely repeated for the two specimens in each configuration. It is only the initiation of the softening phase that differs for the SFRC1 and SFRC2 plates in S1 configuration. This is despite of the significant dispersion in the tensile characterization of the results shown earlier. Greater volume of the material involved in the failure process of the plates due to sizable redistribution capacity of the plate elements, leads to a structural behavior that is much less affected by the local heterogeneities of the material. The effect of structural size, volume involved in fracture, and stress redistribution on behavior of SFRC members will be further discussed in Chapter 7.

The overall response of the SFRC plates in S1 series consists of a first linear branch, a short stretch of a non-linear phase, and a hardening behavior. The S2 companions, however, demonstrate an almost bilinear behaviour, with an initial linear branch, followed by a hardening behaviour. It is quite

noteworthy to observe that the initiation of the non-linearity in the SFRC1 and SFRC2 plates, and the end of the linear branch of the SFRC plates in S2 series, start slightly after that of the R/FRC companions. This may indicate that the absence of reinforcing rebars and the diffused spatial distribution of fibres allows for a more smeared distribution of stresses which delays the accumulation of damage. Eventually, the SFRC plates go through a softening branch which in some cases has been rather abrupt. For the SFRC3 and SFRC4 plates from S2 series the deflection at maximum load is around 16.5 mm, however for SFRC1 and SFRC2 there is a substantial difference between the deformation capacity of the specimens that can be quantified by approximately 11 and 15.5 mm respectively. Clearly, the SFRC plates can not provide as much deformation capacity as the plates that are reinforced with rebars.

The final stage of loading of the RC and R/FRC plates gets close to a plateau corresponding to the yielding of the rebars. Table 4.3 depicts the maximum load reached for the specimens of each configuration. The presence of steel fibres in the R/FRC plates of the S1 and S2 series accounts for an increase of 131 kN and 70 kN in the load bearing capacity with respect to their RC companions. The maximum load attained in the SFRC plates of series S1 and S2 are 237 and 162 kN respectively. Comparison of the contribution of fibres in load bearing capacity of the SFRC and R/FRC plates suggest that when fibres work as secondary reinforcement, their full potential in terms of load resistance can not be mobilized. Addition of steel fibres increases the depth of the neutral axis and a shorter lever arm at the cross section explains to some extent such difference. However, the reduction is more than the sole effect of this parameter. It is evident that in the prediction of the resisting load of the R/FRC specimens the reinforcing bars and fibres can not be decoupled.

The load-deflection response of the R/FRC-Alt plates deserve to be scrutinized separately. What makes the results of these plates significant, is that the overall amount of steel utilized to reinforce these plates is equal to the amount of steel used in the RC plates; both are reinforced with 70 kg/m<sup>3</sup> of steel. The extent to which substitution of half of the rebars in RC plates with 35 kg/m<sup>3</sup> of fibres has changed the structural response of these elements can not be overstated. Two features of the R/FRC-Alt plates makes them distinctive from the RC companions: first is the much smaller deflection of these specimens, and second is the reduced ductility of the R/FRC-Alt plates when compared to the RC ones. In terms of deflection, the R/FRC-Alt plates are more similar to the R/FRC companions than to the RC ones. On the other hand, both R/FRC-Alt plates show some loss of load at a deflection of around 25 mm, which highlights the importance of presence of rebars in imparting a

ductile behavior to the plates.

In some sense, the RC and R/FRC-Alt plates demonstrate how the same amount of steel can be utilized to serve two different purposes without changing the load bearing capacity. The RC plates exhibit a ductile response which is a favorable feature when having ULS in mind, but at the same time show much less resistance in face of deformation and experience larger deflections. And the R/FRC plates display much smaller deflection values, a praiseworthy quality when considering SLS condition, yet failing to provide a ductile behavior. It should be reminded that the R/FRC-Alt reinforcement solution was obtained only by excluding some rebars from the R/FRC plates and the goal was not to find an optimized solution. One can assume that a optimized design can bring about an improved behavior to the R/FRC-Alt plates. Altogether, these results show that adoption of fibres as partial replacement for rebars in structures whose behaviour in the SLS region is of main concern is very well justified.

**4.2.2.2.2 S3 plates** Fig. 4.4 regards the load-deflection response of the S3 series specimens. Due to the close response of some specimens, few markers are shown to make them distinguishable. What stands out in the load-deflection curves, is that the results for the plates with the same reinforcement are not as close as they were for the S1 and S2 series. There is a discernible difference between the results obtained for SFRC5 and SFRC6 specimens and between RC5 and RC6 plates. For SFRC5, at 90 kN there is a slight reduction of load which is then recovered to the same level at a greater deflection after which the softening phase is initiated. Unlike this specimen, SFRC6 plate displays a non-linear hardening branch which goes up to 103 kN followed by the softening phase. Nevertheless, the R/FRC specimens illustrate a similar behaviour. It is emphasized that the specimens were not loaded up to their failure, and specifically the RC plates could have reached higher loads. However, for the R/FRC plates, it is observed that at some load levels they start to lose the effect of fibres and undergo some reduction in the sustained load. The R/FRC5 experiences a reduction of 10 kN at 20 mm of deflection, and the R/FRC6 goes from the maximum load of 207 kN to 180 kN at a vertical displacement of 17 mm. The reason for this should be sought in the cracking behavior of these plates at the top surface, which will be discussed later on.

### 4.2.2.3 Positive cracks

**4.2.2.3.1 S1 and S2** Fig. 4.5 illustrates the results obtained from COD<sub>b</sub> and COD-L<sub>b</sub> instruments on the S1 and S2 plate specimens. The figures on the left

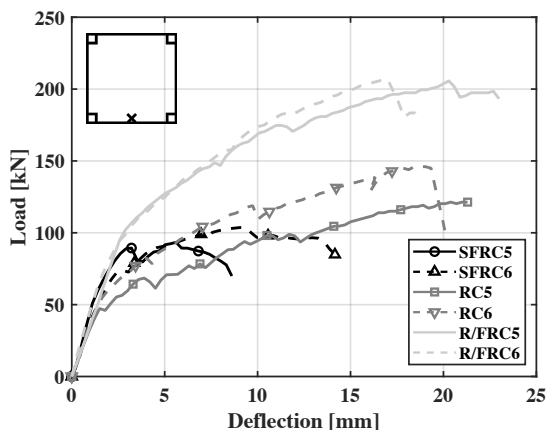


Figure 4.4: Load-deflection curves of S3 plates.

Table 4.3: Maximum load reached in each of the plates from S1, S2 and S3 series in kN.

Series	SFRC			RC			R/FRC			R/FRC-Alt		
	1	2	Ave	1	2	Ave	1	2	Ave	1	2	Ave
S1	231	243	237	366	374	365	476	512	494			
S2	163	161	162	227	225	226	302	294	298	236	240	238
S3	90	103	96	121	146	133	205	207	206			

regard S1 and those depicted on the right regard the measurements recorded for S2 plates. The curves shown are the average results of those instruments that have recorded increasing values for the cracks the are covered by those instruments. Specifically for the SFRC plates, at some point, deformation is concentrated in a few cracks while the rest of the cracks whether slightly close down, or show constant opening. To be able to take the average of the measurements, only those cracks that dominate the late stage of behavior are taken into account. The curves related to  $COD_b$  and  $COD-L_b$  measurements are very similar, however, given the distance of the longer instruments from the loading point, they are less affected by the local damage due to the presence of the concentrated load.

It is remarkable to discover that virtually throughout the whole range of behavior of the SFRC plates, they show less deflection and crack opening when compared to the RC companions. For the SFRC1 and SFRC2 plates the softening phase occurs at the same  $COD$  measured by both the  $COD_b$  and  $COD-L_b$  instruments, while in the case of SFRC3 and SFRC4 plates there is some difference on the  $COD$  at which the softening unfolds.

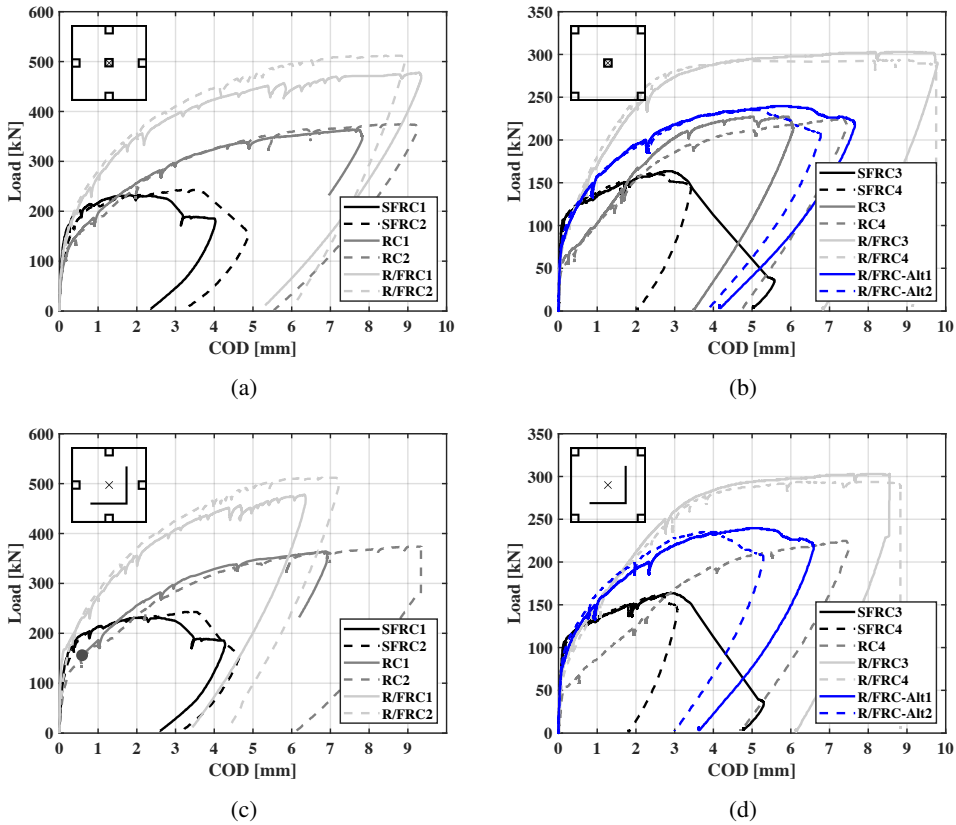


Figure 4.5: Load-COD measurements carried out on (a) COD<sub>b</sub> instruments on the S1 series (b) COD<sub>b</sub> instruments on S2 series (c) COD-L<sub>b</sub> measurements on S1 series and (d) COD-L<sub>b</sub> measurements on S2 series.

A similar comparison elaborated for the deflection behaviour of the RC and R/FRC specimens could be extended to the cracking behaviour. After the point where a substantial stiffness loss is observed for the RC plates, the COD values of these specimens very soon measure more than twice of the values measure on the SFRC and R/FRC plates. For instance with reference to the COD<sub>b</sub> measurements (Fig. 4.5(a) and (b)), at a load of 150 kN in the S1 series, COD of SFRC and R/FRC plates are around 0.17 mm, while for the RC plates the COD measurement reads 0.47 mm. At 75 kN on the plates tested in S2 configuration, the difference is even much more remarkable, with the SFRC, R/FRC, and RC plates demonstrating an average COD of 0.04, 0.07, and 0.36 mm. At this load, the R/FRC-Alt plates replicate the behaviour of the R/FRC companions.

The influence of fibres on limiting COD can have appreciable consequences

on durability of structures. It is shown that there might be a threshold for opening of a crack, below which concrete permeability is not affected. While according to Otieno et al. [148] this threshold depends on concrete properties, a crack opening of 0.05 and 0.1 mm are reported by Wang et al. [203] and Rapoport et al. [162], and Berrocal et al. [28] recognize a range between 0.06 and 0.1 mm for this threshold value. Here a threshold value of 0.1 mm is considered for further comparison of the specimens. On the COD<sub>b</sub> instruments for S1 configuration, Fig. 4.5(a), at 0.1 mm of crack opening the SFRC plates sustain the average load of 127 kN, the RC plates carry an average load of 92 kN, and the R/FRC specimens take 120 kN of load. In S2 configuration, Fig. 4.5(b), SFRC plates significantly outperform the RC plates. In these specimens the SFRC, RC, R/FRC, and R/FRC-Alt plates carry an average load of 103 kN, 54 kN, and 75 kN, and 82 kN. Surprisingly, the SFRC plates carry almost twice the load that the RC companions carry with half of the total amount of steel (in terms of weight), which is quite an impressive observation.

A notable observation that is in common for both testing configurations is that the R/FRC plates do not show any sign of load loss even at great values of COD. Even though the localization occurs at a COD between 2-3 mm for all SFRC plates in the S1 and S2 series, the R/FRC plates do not show a softening behavior even at COD values of more than 8 mm measured in the center of the specimens and a COD of more than 6 mm measured at the position of COD-L<sub>b</sub> instruments. Higher extent of cracking for the R/FRC plates due to a higher capacity for redistribution of stresses, reduces the opening of each single crack. Therefore, fibres remain active during larger deformations. Accordingly, the combination of fibres and reinforcing rebars leads to a better exploitation of the capacity of fibres.

For the R/FRC-Alt plates, similar to their overall structural response, they show a very distinctive behaviour in comparison to their RC companions despite of being reinforced with the same amount of steel by weight. The recorded crack opening  $s$  for the R/FRC-Alt plates are much smaller than those of the RC ones. The softening of these plates occurs when the COD<sub>b</sub> and COD-L<sub>b</sub> measurements are around 4-5.5 mm. It should be taken into account that a concentrated load is a rather extreme case of loading for a plate element. A larger loading footprint facilitates a better redistribution of stresses in which case, the softening of the R/FRC-Alt plates could have happened at a later stage of loading. By and large, these results indisputably underline the advantages of fibres for SLS behaviour.

**4.2.2.3.2 S3** seven LVDTs were applied to capture the bottom cracking of the S3 series. Here, the results of four of these instruments will be shown and explained given the similarity between the measurements. Fig. 4.6 illustrates the measurements recorded by the COD1, COD2, and the two inclined instruments. For RC5 plate, the result of COD1 is not recorded completely and they are shown up to the last recorded value, on Fig. 4.6.

For SFRC5 plate the COD2 measurement is considerably smaller w.r.t to the COD1 measurement as the final localized crack is captured by COD1 and not by the COD2. Looking at the results obtained from the inclined instruments in Figs. 4.6(c) and 4.6(d), it is clear that the presence of reinforcing rebars secures a symmetrical response in the RC and R/FRC plates which is unlike the response of the SFRC plates. For RC and R/FRC plates the COD measured by both inclined instruments is almost equal. Also a glance at the crack patterns in Fig. 4.2 demonstrates that these inclined cracks are more closely spaced for the R/FRC plates when compared against the RC companions. For the SFRC plates, the opening of the cracks registered by the inclined LVDTs are very different with much larger values recorded for the instrument shown in Fig. 4.6(c). A glance at the crack pattern of these SFRC plates shows that each of these instruments is capturing the propagation of one or two cracks. Sizable difference between the COD measured by these two instruments is an indication of lack of redistribution in this setting of load and boundary conditions. Therefore, very different from the S1 and S2 series where a substantial and rather symmetrical redistribution of stresses were observed, in the SFRC5 and SFRC6 plates few cracks with very different openings are observed. Similar to the deflection results, there are more discrepancy among the specimens with the same reinforcement in this configuration of testing as compared to the S2 and S3 testing layouts. Nevertheless, the influence of fibres in reducing the COD in the R/FRC specimens is easy to recognize.

#### 4.2.2.4 Negative cracks

The propagation of the negative cracks are investigated in light of the deflection of the plates. Fig. 4.7 shows the def-COD measurements of the negative cracks measured on the top surface of the tested plates. In Fig. 4.7(a) COD is the average measurement of the instruments that have recorded the propagation of a crack. SFRC1 plate did not show any negative crack and is not shown on the figure. In Fig. 4.7(b), given that very few crack propagated overall, the result of each instrument that has captured a crack is shown separately. In R/FRC3 no negative cracks propagated, therefore, it is not shown on the figure. There are two curves corresponding to the RC4 plate as negative cracks appeared on two of the supports for this specimen. In Fig. 4.7(c) the deflection

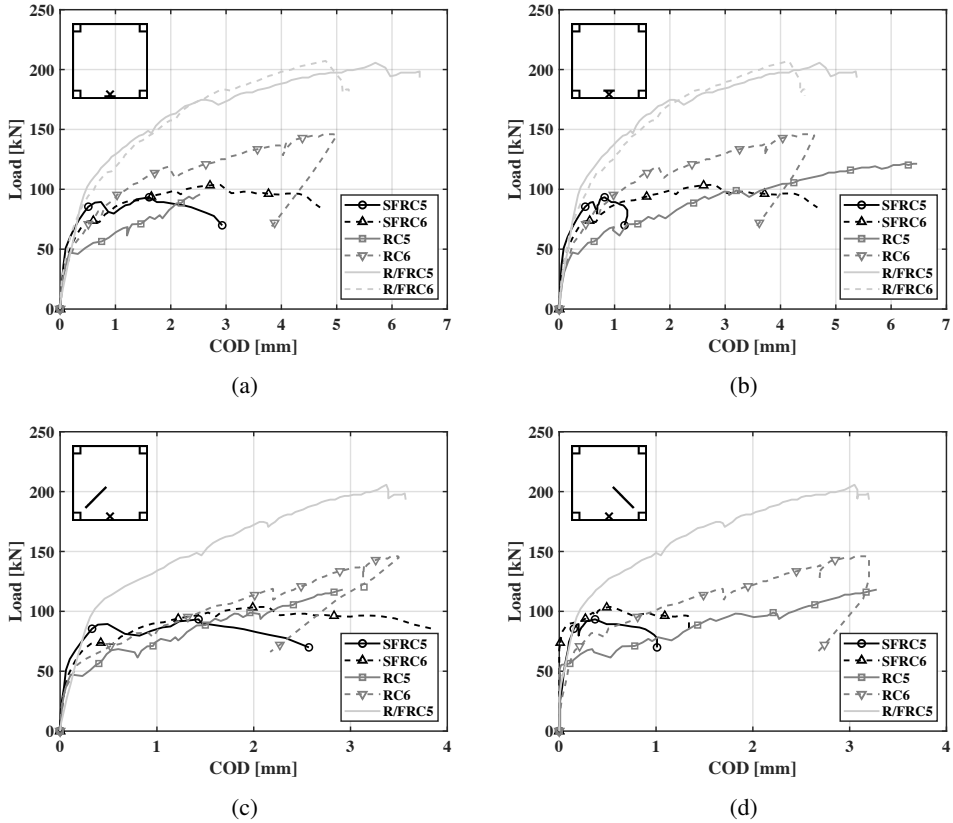


Figure 4.6: Load-COD measurements for the S3 plates at different positions.

measurement for R/FRC6 was lost and is not shown on the figure. Except a very short crack on SFRC2 plate, no other negative cracks propagate for the SFRC plates. The failure of the SFRC plates occurs before any negative cracks can appear.

For the S1 plates, Fig. 4.7(a), the negative cracks start to appear for the RC and R/FRC plates when the deflection of the center of the plates reach around 15 mm. However, after the propagation, higher slope of the curves for the R/FRC plates indicates a greater resistance against further opening of the cracks at increasing deformation, which owes to the presence of fibres. For the S2 plates, the propagation of negative cracks is abrupt and right after propagation, large openings are recorded, specifically for the RC ones. The R/FRC4 plate displays much smaller crack opening in comparison to the RC ones which can be solely attributed to the presence of fibres. Moreover, the rate at which this crack opens up is substantially smaller than the rate at which the negative cracks in the RC plates widen. In these series of plates the negative



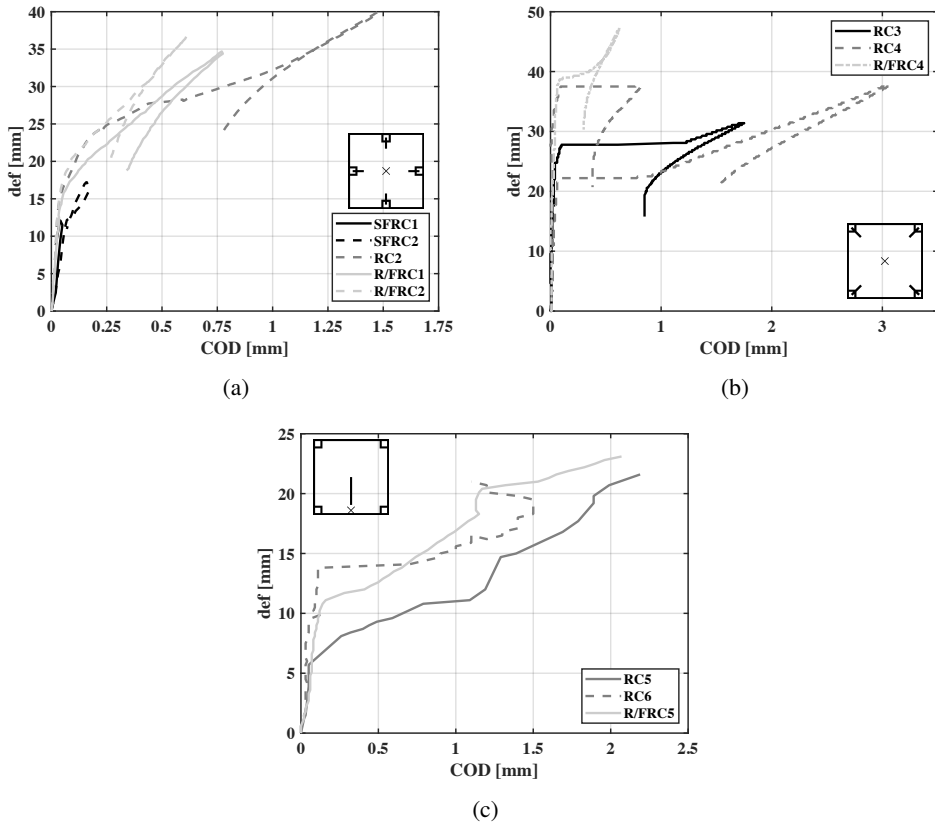


Figure 4.7: def-COD measurements on the top surface of the plates for (a) S1, (b) S2, and (c) S3 series.

crack in the R/FRC plate propagated at much larger deflection with respect to the RC companions. Looking at the results for the S3 plates, RC5 plate cracks at a small value of deflection while the RC6 plate after cracking shows no resistance against its opening and reaches close to 1 mm of COD. Negative cracking for R/FRC5 starts at a deflection of around 11 mm, a second crack propagates at around 18 mm of deflection, and the third negative crack show up at the end of the test. Nevertheless, the R/FRC5 plate records smaller COD values and higher number of cracks which can be easily translated to much narrower opening of individual cracks. Overall, for the present testing configuration, in all cases the propagation of negative cracks occurred in the ULS region of the response and still in the absence of negative reinforcement the advantage of fibres in controlling the opening of cracks is conspicuous.

## **4.3 Design resistance and prediction of load bearing capacity of plates**

### **4.3.1 Yield lines**

The expected bearing capacity, and the design resistance of the plates are computed by the yield line method [121]. In this approach, it is assumed that the failure of a slab occurs with the formation of lines of plastic hinges, or yield lines, where the resisting bending moment is the ultimate bending resistance of the section (or commonly yielding moment). Yield lines are in fact comprised of bands of multiple cracks and the overall rotation of the yield line would be the sum of the rotation that takes place at each single crack. The position of these yield lines should be compatible with the boundary and loading conditions. Such admissible collapse mechanism will give an upper bound for the load bearing capacity of the slab. The formation of a collapse mechanism may entail considerable redistribution of stresses, therefore, enough ductility reserve is required at critical sections to allow for formation of plastic hinges that need to be activated before a full failure pattern can form. In the presence of rebars in lightly reinforced slabs, enough ductility is assured. However, for FRC slabs this can pose some concerns. If rebars are completely excluded, ductility is considerably reduced. Such substantial reduction in deformation capacity may sacrifice the possibility of formation of a presumed yield line pattern. This is evident in Fig. 4.2 in which for some SFRC plates, negative cracks did not propagate, while for the RC and R/FRC companions a complete failure mechanism is formed with both positive and negative cracks. This shortcoming of the SFRC plates can lead to an overestimation of their load bearing capacity.

Yield line method is based on an assumption of rigid-plastic response with a constant resisting bending moment all along the crack lines. This assumption can be accommodated for RC slabs, however, when the only reinforcement is fibres, the adoption of a yield line method depends on some conditions, assumptions, and prerequisites. The moment-curvature diagram of a FRC cross section should not be softening or at least for a range of CMODs needs to show a hardening response. The width of a long line of crack will not be constant. For FRC, this would be translated to a variable resisting bending moment along the crack. If a yield line has to be applied to a FRC slab element, it should be taken into account that the adopted resisting bending moment will represent a sort of average bending moment along the crack. For instance, the SFRC material under study after cracking demonstrates a hardening behavior up to a CMOD of around 1.4 mm, Fig. 4.1.

---

Experimental evidence suggests that the opening of cracks in the tested SFRC plates fall in the range that is characterized by a hardening response, narrower than 1.4 mm. This means that along the crack length, cross sections are in the hardening portion of the moment-curvature diagram. A hardening behaviour at the cross section justifies the adoption of a yield line method with a bending moment in a curvature range that can represent the average response of the yield line. In practice, yield line analysis has been widely applied to FRC plate and slabs [3,69,73,151,173,174] with satisfactory results.

Among the assumptions of the yield line method proposed by Johansen, there is one, which can lead to conservative predictions in determining the ultimate load bearing capacity of slabs. In Johansen's version of the yield line method, he assumes that the reinforcing bars retain their original direction when crossing a crack. A yield line is considered as the limiting case of a "stepped" line in which the rebars meet the infinitesimal steps at right angle and keep their direction while plastic curvature occurs. The plastic moment,  $m_n$ , at the fracture line with inclination  $\alpha$  relative to the rebar direction gives:

$$\frac{m_n}{m} = \cos^2 \alpha + \sin^2 \alpha = 1 \quad (4.1)$$

In the most optimistic condition for the computation of the ultimate resisting moment, full benefit of the complete kinking of the rebars at the crack is postulated. Although this assumption which was proposed by Wood [206] is kinematically permissible, it disregards the crushing of concrete that resists straightening out of the rebars. Nevertheless, the ultimate bending moment at the yield line with this assumption would be:

$$\frac{m_n}{m} = \cos \alpha + \sin \alpha \quad (4.2)$$

For a common case of  $\alpha = 45^\circ$ , the resisting bending moment at the crack will be 40% larger than the bending resistance perpendicular to rebar directions,  $m_n = \sqrt{2}m$ .

The more realistic condition allows for partial kinking of the rebars at inclined yield lines. Kwiecinski [125] formulates such yield criteria in which the rebars rotate as much as  $\gamma$  and  $\delta$  compared to when complete kinking is allowed. Fig. 4.8 depicts the circumstances under which he formulates his assumptions.  $\chi$  is the degree of orthotropy.

With this assumptions the flexural and torsional bending moments at the

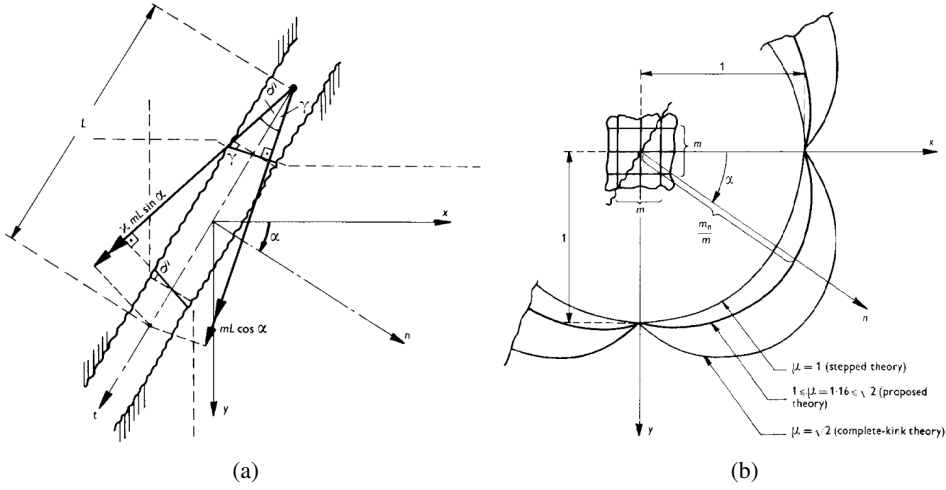


Figure 4.8: (a) Assumptions made by Kwiecinski in formulating a yield line criteria with partial kinking of rebars at inclined crack (b) Graphical representation of ultimate resisting moment at different inclination angles of yield line for different assumptions [125].

crack are found as:

$$\frac{m_n}{m} = \cos \alpha \cos \gamma + \chi \sin \alpha \sin \delta \quad (4.3a)$$

$$\frac{m_{nt}}{m} = \cos \alpha \sin \gamma - \chi \sin \alpha \sin \delta \quad (4.3b)$$

This general formulation yields Eq.4.1 for  $\gamma = \alpha$ ,  $\delta = \pi/2 - \alpha$  and for  $\gamma = \delta = 0$  Eq.4.2 is obtained. With the most simplifying assumptions of an isotropic rebar layout, an inclined crack with  $\alpha = 45^\circ$ , and  $\delta = \gamma = \theta^\circ$ , Eq.4.3b reduces to  $m_n/m = \sqrt{2} \cos \theta$ . For  $\theta = 45^\circ$  this gives the Wood's assumption and for other values, gives smaller resisting bending moment at the crack. Kwiecinski depicts the condition where  $m_n = \mu m$  with  $\mu = 1.16$  which is represented in Fig. 4.8. This case might be applicable to the results obtained for S1 series plates in which the crack pattern was inclined relative to the rebars direction.

### 4.3.2 SFRC tensile law

Derivation of tensile constitutive law for FRC in terms of stress-CMOD is carried out through inverse analysis of the results of a bending test. A certain form is considered for the tensile law, and equations of equilibrium are written for certain crack openings to find the residual tensile strength parameters. As an example, in both the MC2010 and EC2-Annex L draft, these benchmark CMODs at which the residual tensile strength values are obtained are assumed to be 0.5 mm and 2.5 mm. The Italian code, *Guide for the Design and*

*Construction of Fiber-Reinforced Concrete Structures (CNR-DT 204-2006)* adopts the same assumptions as of the MC2010 for the tensile constitutive law of FRC. The narrower CMOD of 0.5 mm is chosen to represent SLS condition, and the wider 2.5 mm of CMOD is chosen to express the situation at ULS. Fig4.9 shows the bilinear tensile laws that are given in both MC2010 and EC2 for FRC. The equations and the solution of the tensile law given in MC2010 are explained in [71]. The distinction between the two tensile laws come mainly from their assumption in the first elastic branch. Apart from this bilinear tensile law, both standards suggest also a rigid-plastic tensile law with the  $f_{ftu}$  value being equal to  $f_{R3}/3$  for MC2010 and  $0.37f_{R3}$  in EC2-Annex L draft. The post-peak tensile parameters of  $f_{R1-4}$  for the tested notched beams were given earlier in Table 4.1. A quick glance at the coefficients of

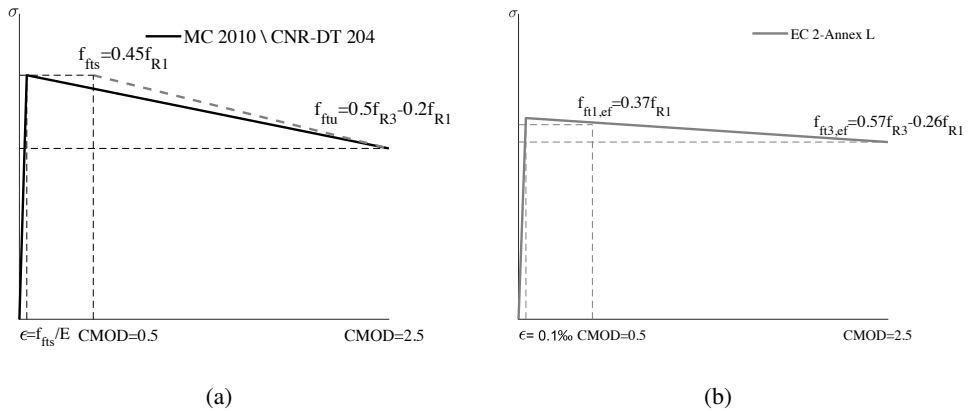


Figure 4.9: The bilinear  $\sigma - CMOD$  tensile constitutive law given in (a) MC2010 and CNR-DT 204 and (b) in EC2-annex L.

variation,  $V$ , given in Table 4.1 for the post-peak strength parameters, shows that these values are much larger than common variation obtained for strength parameters of concrete, like the flexural tensile strength,  $f_{ct,fl}$  reported in the same table. The coefficient of variation for  $f_{ct,fl}$  reported for these specimens is between 4% to 8%. Similar values are often obtained for variation of compressive strength of concrete. For the specimens tested here, the average coefficient of variation of  $f_{R1}$  and  $f_{R3}$  value is around 15% and 18%. Larger coefficient of variation means that the 5% fractile, or the characteristic values of these parameters will be further away from the average values. It has been shown [75] and will be discussed further in chapter 6, that redundant structural elements in which the failure process consists of a stable phase of multi-cracking with large crack areas do not exhibit such high scatter in their behaviour. Design of such structural elements with characteristic values that are obtained from the highly dispersed curves of a notched three-point

bending test lead to very safe designs. To compensate for this shortcoming different standards propose different remedies. This topic shapes the core of the discussion in chapter 6, therefore, the details are not mentioned here and only the formulations and methods are briefly explained.

MC2010 introduces a magnification factor,  $K_{Rd}$ , which is multiplied to the design load:

$$P_{Rd} = K_{Rd} \times P(f_{Fd}) \quad (4.4)$$

where  $P_{Fd}$  is the resistant load computed taking into account the design strength of FRC. In fact, the  $K_{Rd}$  coefficient should be multiplied only to the contribution of FRC in the resistant load, i.e. in R/FRC structures the  $K_{Rd}$  should not affect the contribution of rebars in load bearing. In this manner, it is suggested to multiply the  $K_{Rd}$  directly to the design/characteristic values of residual tensile strength parameters. This will be different from what is suggested in Eq.4.4, in that it assumes a linear relationship between residual tensile strength values and the resistant load. However, the error introduced will not be considerable. To compute the  $K_{Rd}$  factor a probabilistic non-linear structural analysis is needed in which material heterogeneity is taken into account. The  $K_{Rd}$  factor is computed as:

$$K_{Rd} = \frac{P_{max,k}}{P_{max,m}} \times \frac{f_{Ftum}}{f_{Ftuk}} \leq 1.4 \quad (4.5)$$

where  $P_{max,m}$  and  $P_{max,k}$  are the average and characteristic maximum loads obtained from numerous structural analysis taking into account material heterogeneity.

In EC2, the maximum value for the residual tensile strength parameters is  $0.6f_{R,m}$ , meaning that it can not surpass 60% of the average values. This standard suggests the adoption of a  $\kappa_G$  factor which magnifies the characteristic value of residual tensile strength properties. It is computed as:

$$\kappa_{G,max} = 0.9 \frac{f_{fts/u,m}}{f_{fts/u,k}} \quad (\text{if the notched beam results are available}) \quad (4.6a)$$

$$\kappa_G = 1 + A_{ct} \times 0.5 \leq 1.5 \quad (\text{for redundant slabs}) \quad (4.6b)$$

The approach proposed in CNR-DT 204 is different from the MC2010 and EC2, in that it does not give a factor to magnify the characteristic values, but instead, it allows to chose a larger characteristic value with respect to what would be obtained from the results of the notched beams by introducing a

reduction factor that reduces the standard deviation obtained in a test. The formula to obtain the characteristic value of residual tensile strength parameters for FRC reads:

$$f_{Ftk} = f_{Ftm} - \alpha ks \quad (4.7)$$

$k$  is assumed to be equal to 1.48 for log-normal distribution, and  $\alpha$  depends on the volume involved in the failure process of the structure and the capacity of the structure in redistribution of stresses. Here,  $\alpha = 0.5$  is adopted.

Following these methods, all the parameters related to the fourteen notched specimens whose curves were shown in Fig. 4.1 are given in Table 4.4. The results are given for different groups of specimens based on the age of testing. In the table the characteristic values that are designated with an asterik,  $f_{R,k^*}$ , are those which are modified to yield a larger characteristic value. As we did not have a probabilistic nonlinear model to have the distribution of the resisting load of the plates, the provision of MC2010 was not considered here, and the  $\kappa_G$  factor from the EC2-annex L, and the  $\alpha$  coefficient from CNR-DT 204 were taken into account. The  $K_{Rd}$  factor from MC2010 will be discussed in Chapter 7 in details, and the sample of twelve identical plates will give the distribution of the resistance. The assumptions of MC2010 and CNR-DT 204 for the tensile law of FRC are the same other than how they compensate for the small characteristic values from a bending test. So the values given in Table 4.4 under CNR-DT 204 hold also for MC2010, other than the  $f_{k^*}$  values.

### 4.3.3 Average and design resisting bending moment

In order to find the actual load bearing capacity and the design resistance of the plates, different sets of values are adopted to compute resisting bending moments. Prediction of a realistic value for the load bearing capacity of the plates is undertaken with the average material properties. For the rebars the yield strength of  $f_{ym}=527$  MPa is adopted, which was found from the tensile test on four rebar specimens. once a rigid-plastic behavior is considered for the rebars neglecting hardening, and once the ultimate tensile strength of the rebars are accounted for in the computation. Compressive strength of concrete was evaluated on six concrete cubes at the age of 34 days, Table 3.2. Evolution of compressive strength in time was taken into account by adopting the  $\beta$  factor,  $f_{cm}(t) = \beta \times f_{cm}$ , as given in the MC2010. The average daily temperature of city of Lecco, where our laboratory is located, was considered for the computation of the  $\beta$  coefficient. In this manner, the  $f_{cm}$  at 167 and 220 days of age (the age at which the S1 and S3 plates were tested), was found to be 53.5 MPa and 53.8 MPa. For simplicity it was taken as  $f_{cm} = 54$  MPa

Table 4.4: All strength parameters related to the fourteen tested notched beams. Average and characteristic values of  $f_{fts}$  and  $f_{ftu}$  are given following the provisions of CNR-DT 204 [50] and EC2-Annex L draft [43].

Parameter/Age (days)	34	167	167 & 220	220
<b><math>f_{R1}</math></b>				
$f_{R1,m}$ [MPa]	5.64	7.06	7.36	7.75
$f_{R1,k}$ [MPa]	3.82	4.60	5.39	5.66
V [%]	16.00	17.00	14.00	11.00
$\min(f_{R1,k}, 0.6f_{R1,m})$ [MPa]	3.38	4.24	4.42	4.65
<b><math>f_{R3}</math></b>				
$f_{R3,m}$ [MPa]	4.92	4.97	5.20	5.50
$f_{R3,k}$ [MPa]	3.10	3.16	3.50	3.00
V [%]	18.00	18.00	18.00	20.00
$\min(f_{R3,k}, 0.6f_{R3,m})$ [MPa]	2.95	2.98	3.12	3.30
<b>Class</b>				
	3c	4b	5b	5a
<b><math>f_{fts}</math></b>				
<b>CNR-DT 204</b>				
$f_{fts,m}=0.45f_{R1,m}$ [MPa]	2.54	3.18	3.31	3.49
$f_{fts,k}=0.45f_{R1,k}$ [MPa]	<b>1.72</b>	<b>2.07</b>	<b>2.43</b>	<b>2.55</b>
$f_{fts,k}^* = f_{fts,m} - \alpha_{ks}$ [MPa]	<b>2.24</b>	<b>2.78</b>	<b>2.97</b>	<b>3.20</b>
<b>EC2-Annex L</b>				
$f_{ft1,m}=0.37f_{R1,m}$ [MPa]	2.09	2.61	2.72	2.87
$f_{ft1,k}=0.37f_{R1,k}$ [MPa]	<b>1.25</b>	<b>1.57</b>	<b>1.63</b>	<b>1.72</b>
$f_{fts,m} = 0.4f_{R1,m}$ [MPa]	2.26	2.82	2.94	3.10
$f_{fts,k} = 0.4f_{R1,k}$ [MPa]	1.35	1.69	1.77	1.86
$\kappa_G=0.9 f_{fts,m}/f_{fts,k}$	1.50	1.50	1.50	1.50
$f_{ft1,k}^*=\kappa_G \times f_{ft1,k}$ [MPa]	<b>1.88</b>	<b>2.35</b>	<b>2.45</b>	<b>2.58</b>
<b><math>f_{ftu}</math> [MPa]</b>				
<b>CNR-DT 204</b>				
$f_{ftu,m}=0.5f_{R3,m} - 0.2f_{R1,m}$	1.33	1.07	1.13	1.20
$f_{ftu,k} = 0.5f_{R3,k} - 0.2f_{R1,k}$ [MPa]	<b>0.79</b>	<b>0.66</b>	<b>0.67</b>	<b>0.37</b>
std [MPa]	0.32	0.37	0.36	0.40
$f_{ftu,k}^* = f_{ftu,m} - \alpha_{ks}$ [MPa]	<b>1.10</b>	<b>0.80</b>	<b>0.86</b>	<b>0.90</b>
<b>EC2-Annex L</b>				
$f_{ft3,m} = 0.57f_{R3,m} - 0.26f_{R1,m}$ [MPa]	1.34	1.00	1.05	1.12
$f_{ft3,k} = 0.57f_{R3,k} - 0.26f_{R1,k}$ [MPa]	<b>0.80</b>	<b>0.60</b>	<b>0.63</b>	<b>0.67</b>
$f_{ftu,m} = 0.37f_{R3,m}$ [MPa]	1.82	1.84	1.92	2.04
$f_{ftu,k} = 0.37f_{R3,k}$ [MPa]	1.09	1.10	1.15	1.22
$\kappa_G = 0.9f_{ftu,m}/f_{ftu,k}$	1.50	1.50	1.50	1.50
$f_{ft3,k}^* = \kappa_G \times f_{ft3,k}$ [MPa]	<b>1.20</b>	<b>0.90</b>	<b>0.95</b>	<b>1.01</b>



---

for all cases. For the plain concrete, tensile strength is neglected. For the SFRC material, the  $f_{R,m}$  values are taken into account. The prediction of the load bearing capacity of the plates in which SFRC material was incorporated is performed with the average material properties that were obtained from notched beams that were tested closer in age to those plates. Therefore, for the S1, S2, and S3 series plates, the 167 days, 167 and 220 days together, and 220 days specimens were taken into account. All the related parameters are shown in Table 4.4.

For the design resistance of the plates two conditions are assumed. First the design load,  $P_d$  is found based on the material properties measured at 34 days of age. This is a normal procedure in which, commonly, the 28 days characteristic material properties are adopted for design. Second, the characteristic material properties at the age of testing the plates are taken as the basis for design. This is done so that the evolution of safety factor of the plates in which fibres are incorporated can be investigated. For RC plates, the design load depends on the yield strength of rebars, which does not change in time, and compressive strength of concrete whose evolution slightly changes the lever arm at the cross section. When fibres are added, the cross sectional behavior is highly dependent on the contribution of fibres in the tensile zone, and the evolution of the tensile properties of SFRC may have a sizable effect on the resisting bending moment and correspondingly on the factor of safety.

Computation of the design resistance is carried out with safety coefficients of  $\gamma_c=1.5$  and  $\gamma_s=1.15$  that are introduced to all characteristic values of material properties for rebars and concrete respectively. For the rebars a  $f_{yk} = 500$  MPa is considered. Characteristic compressive strength of concrete is taken as  $f_{ck} = 40$  MPa. For the SFRC material, once the characteristic values related to 34 days tests are adopted and once the characteristic values derived from three-point bending tests that were carried out at a age close to the plate test is adopted. In each case, for the  $f_{R,k}$  parameters of the SFRC, two series of values are considered. One are those related to the 5% fractile obtained from Stress-CMOD curves of the notched specimens, and the other is the magnified version of the characteristic values, which are obtained separately according to the provisions of CNR-DT 204 (through  $\alpha$  coefficient) and EC2 ( $\kappa_G$  factor).

To find the resisting bending moment, a plane-section multi-layer approach is implemented at the cross section. For a maximum curvature which is set by introducing the ultimate crack opening,  $w_u$ , equations of equilibrium are solved and the resisting bending moment is found. A linear strain distribution over the cross-section is assumed and the cross-section is discretized into

several layers, each one characterized by a proper constitutive law. A constitutive parabola-rectangle model is adopted in compression [51]. Tensile behaviour of SFRC is introduced in terms of stress-strain by introducing a  $l_{cs}$  to the stress-CMOD relationship which is assumed to be equal to the depth of the plates. For plain concrete, tensile resistance of concrete is disregarded and only the rebars with a small effective depth create some resisting moment. The resisting bending moments for different cases are given in Table 4.5. Four different design moments are reported. “Design” values which are based on the  $f_{R,k}$  values obtained at 34 days, “Design-Aged” values which are based on the  $f_{R,k}$  values obtained at the age of the plate test, “Design\*” values which are based on  $f_{R,k}^*$  values corresponding to 34 days notched beam results, and finally, “Design\*-Aged” values which are based on  $f_{R,k}^*$  values at the age of the plate tests. However, the values with asteriks were not adopted for the plates in the S3 series. This configuration exemplifies a case in which the capacity of the structure in redistribution of stresses is limited. Therefore, in such a case the characteristic values should not be altered and their original values should be adopted.

For the R/FRC-Alt plates the yield line passes through cross sections which are reinforced only with fibres, and those which are reinforced with both fibres and rebars. For simplicity, it is assumed that half of the length of the yield line is characterized by the SFRC material and along half of its length the R/FRC cross section provides resistance. As such the resisting bending moment is the average of the bending moments of the SFRC and R/FRC cross sections. These values are reported in Table 4.5.

Table 4.5: Resisting bending moment for design and prediction of the load bearing capacity of plates of different series.

		$m^+$ [kN.m/m]		$m^-$ [kN.m/m]							
	Mean	Design <sup>1</sup>	Design-Aged <sup>2</sup>	Design* <sup>3</sup>	Design*-Aged <sup>4</sup>	Mean	Design	Design-Aged	Design*	Design*-Aged	
<b>RC</b>											
S1, S2, S3	34.7	27.7	-	-	-	8.8	5.8	-	-	-	
<b>SFRC</b>											
S1	CNR-DT	18.0	7.4	7.7	9.9	9.9	9.9				
	EC2	17.0	7.1	7.5	10.4	11.0					
S2	CNR-DT	18.8		8.6	10.5	10.5	same				
	EC2	17.7	same	7.8	11.4	11.4					
S3	CNR-DT	19.9		7.7	same	same					
	EC2	18.7		7.6							
<b>R/FRC</b>											
S1	CNR-DT	50.6	33.8	34.1	35.9	36.0	22.4	10.9	11.1	12.8	
	EC2	49.6	33.5	33.9	36.4	36.8	21.6	10.7	10.9	13.2	
S2	CNR-DT	51.4		34.8	36.5	36.5	23.0		11.7	13.2	
	EC2	50.4	same	34.1	same	37.3	22.2	same	11.1	13.8	
S3	CNR-DT	52.4		34.1			23.9		10.9	same	
	EC2	51.3		33.9			23.0		10.9		
<b>R/FRC-AIt</b>											
S2	CNR-DT	35.1	20.6	21.7		23.5	20.9	9.1	10.1	11.3	
	EC2	34.0	20.3	20.9		24.35	19.9	8.9	9.4	11.8	
1-Design resisting bending moments that are obtained based on $f_{R,k}$ values of 34 days results											
2-Design resisting bending moments that are obtained based on $f_{R,k}$ values at the age of the plate test											
3-Design resisting bending moments that are obtained based on $f_{R,k}^*$ values of the 34 days results											
4-Design resisting bending moments that are obtained based on $f_{R,k}^*$ values at the age of the plate test											

#### 4.3.4 Failure mechanism

To adopt the yield line method, some failure mechanisms are considered for the plates in each series. Table 4.6 demonstrates these failure mechanisms and the corresponding ultimate load,  $P_u$ . Due to the peculiar behavior of the support, prediction of the exact failure mode before carrying out the tests could be difficult. The crack patterns are chosen to be close to the experimental failure modes in accordance with the discussion given earlier on experimental crack patterns, Section 4.2.2.1.

For the S1 plates, the pattern of the positive cracks may suggest that the rotation of the unrestrained edges of the plates occurs along the axes that passes through the supports parallel to the edges of the plates. Concerning the negative cracks, the RC and R/FRC plates showed the formation of a negative fan on the top surface which did not propagate for the SFRC plates due to limited ductility. With this explanation, the mechanism with a negative fan may better represent the RC and R/FRC plates and the one with diagonal positive cracks may picture the failure mode of the SFRC plates of the S1 series.

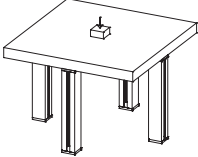
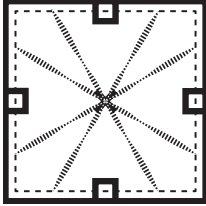
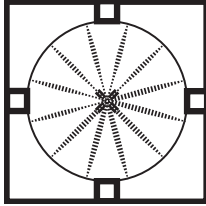
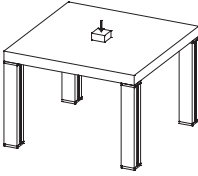
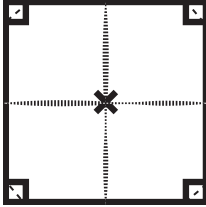
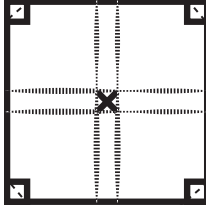
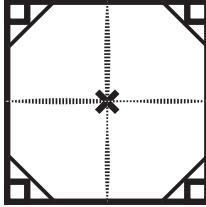
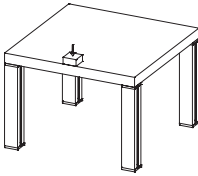
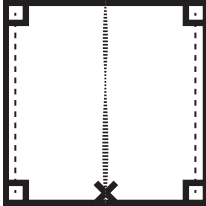
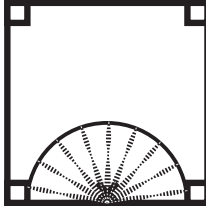



The failure mechanism of the S2 plates exhibits two band of orthogonal cracks going from the middle of each side to the other. Few negative cracks have also propagated at the supports. Three failure patterns are postulated for the S2 series plates. The first consists of two orthogonal yield lines in the form of a plus sign. While this might be the most obvious mechanism to think of, such failure pattern holds that the load is exerted on a point and disregards the loading head footprint. Elstner and Hognestad [85] have shown that under concentrated loads, the mechanism consists of a different pattern which in Table 4.6 is shown as mechanism B for the S2 plates. For the computations, a mechanism C is also taken into consideration consisting of both positive and negative cracks.

For the S3 series, detection of a clear failure mechanism is more difficult. The early part of the response of the S3 plates may be similar to a plates with simple supports on the sides, and upon larger deflections, it moves towards a plate with fixed supports which facilitates the propagation of negative cracks. Due to this complication, both mechanisms are considered.

#### 4.3.5 Design resistance and expected load bearing capacity

Table 4.7 reports the average experimental maximum load obtained for the two identical tested plates for each configuration  $P_{Exp}$ , and values obtained

Table 4.6: kinematic mechanisms considered for the yield line analysis of the plates and the maximum load for each case.

Configuration	Mech. A	Mech. B	Mech. C
	 $8m^+ \left( \frac{1}{1-a/L} - 3 + 2\sqrt{2} \right)$ [85]	 $2\pi(m^++m^-)$	
	 $4.44m^+$	 $4m^+ \left( 1 + \frac{4}{L/a-1} \right)$ [85]	 $5m^++2m^-$
	 $4m^+$	 $\pi(m^++m^-)$	
	$m^+$  $L =$ Length of plate $m^-$  $a =$ dim. of loading plate axis of rotation 		

for the design resistance, and the expected bearing capacity of the plates  $P_m$ , through the yield line analysis. The design resistance found out with the  $f_{R,k}$  and  $f_{R,k^*}$  values are reported as  $P_d$ , and  $P_{d^*}$  respectively. Under  $P_d$  and  $P_{d^*}$  the computations made with 34 days material properties and those made with the properties at the age of testing are shown. None of the RC and R/FRC plates were loaded to the ultimate load, hence the actual load bearing capacity of some of these plates could have been slightly larger than the values given in Table 4.7. The hardening of the rebars was not taken into account in the computations made with the yield line method. Due to considerable hardening of the rebars, complying with class C bars according to EC2,  $f_t/f_y=1.22$ , the estimations are still on the safe side. If instead of yield stress of rebars, the ultimate strength,  $f_t$ , is plugged in the yield line formulations, the expected load bearing capacity of the RC and R/FRC plates would be as depicted in Table 4.8.

For both the RC and R/FRC plates, Mechanism B is closer to the experimental evidence. For the S1 plates, looking at estimation of the capacity obtained for RC plate in the upper part of Table 4.7, the  $P_m$  value obtained is very conservative. The ratio between the experimental load, and the computed expected load bearing capacity, is  $\gamma_m = P_{Exp}/P_m = 1.37$ . Part of this underestimation can be attributed to the adoption of  $f_{ym}$  in the rigid-plastic behavior presumed for the rebars. When  $f_t$  is adopted in the yield line, closer results are obtained,  $\gamma_m = 1.18$  (Table 4.8). The rebars are certainly far from ultimate strain during the tests, but in any case, overlooking the hardening of rebars is in part responsible for the very safe predictions made in Table 4.7. It was discussed earlier, Section 4.3.1, that with Johansen's assumptions for the yield line theory, if the crack lines are inclined relative to the rebars, can lead to safe prediction of the ultimate load. This effect will be at its maximum when the cracks and rebars make a  $45^\circ$  angle, which is almost the case for the S1 plates. Therefore, some contribution from the rotation of rebars at the crack surfaces which is neglected here, could offer another source of strength that is overlooked. For the R/FRC plates the predictions are closer to the experimental values and the adoption of  $f_t$  for the rebar strength gives almost exact results. It can be reckoned that for the R/FRC plates, the effect of partial kinking of rebars has less influence on the overall load bearing capacity as kinking only affects rebars and not the fibres.

For the SFRC plates of the S1 series, the choice of the failure mechanism underlines a significant argument. To apply a yield line method to slabs, ductility of critical cross sections should be assured so that a postulated kinematic mechanism can be developed. The SFRC plates of the S1 series very vividly manifest this shortcoming of FRC elements. For both SFRC1 and SFRC2 plates, the softening of the plates unfolded before the activation of mechanism B, which might be the most likely mechanism to choose for such boundary condition under a concentrated load. With this regard, application of a minimum reinforcement to guarantee ductility seems to be necessary. One may argue that the predictions made by adopting mechanism B, is very close to the experimental results. It will be shown in the next section that the underlying reason for this observation is not the capability of this mechanism in explaining the failure pattern of SFRC plates of S1 series. Mechanism A gives a  $\gamma_m = 1.76$  and  $1.86$  for CNR-DT 204 and EC2 assumptions.

For the S2 plates mechanism B properly pictures the failure pattern of the plates. The ratio of experimental load to predictions are 1.13, 1.48/1.59 (for CNR-DT 204/EC2), and 1.00/1.02 (for CNR-DT 204/EC2) for the RC, SFRC,

---

and R/FRC plates respectively. Fig. 4.3 shows that the RC plate of the S2 series could have reached to higher load levels if the test was not stopped. Indeed, if hardening of the rebars were taken into account a  $\gamma_m$  value closer to 1 could be achieved.

For the S3 plates, similar to S1 series, the SFRC plates did not have enough ductility to assure the attainment of mechanism B, which consists of negative cracks. Adoption of this failure mechanism leads to unsafe prediction for the bearing capacity of these plates. Nevertheless, with this mechanism, for RC and R/FRC plates, satisfactory results are achieved with  $\gamma_m$  close to 1.

Table 4.7: Design resistant load and estimated actual bearing capacity of the plates computed through a yield line analysis with the bending moments reported in Table 4.5.

RC plates	$P_{E_{PR-Ave}}$ [kN]	Mechanism A				Mechanism B				Mechanism C						
		Pm [kN]	Pd [kN]	Test Age	Pd* [kN]	Pm [kN]	Test Age	Pd [kN]	Test Age	Pd* [kN]	Pm [kN]	Test Age	Pd [kN]	Test Age	Pd* [kN]	Test Age
S1	370	261 (1.42)	209 (1.77)		274 (1.35)	210 (1.76)				191	150					
S2	226	154 (1.47)	123 (1.84)		200 (1.13)	160 (1.41)										
S3	133	140 (0.95)	111 (1.20)		137 (0.97)	105 (1.26)										
SFRG																
S1	CNR-DT	135 (1.76)	56 (4.25)	58 (4.10)	75 (3.17)	74 (3.21)	226 (1.05)	93 (2.56)	97 (2.45)	125 (1.90)	124 (1.92)					
	EC2	128 (1.86)	54 (4.41)	56 (4.25)	79 (3.01)	83 (2.87)	214 (1.11)	90 (2.64)	94 (2.53)	131 (1.82)	138 (1.72)					
S2	CNR-DT	84 (1.93)	33 (4.91)	38 (4.26)	44 (3.68)	47 (3.45)	109 (1.48)	43 (3.77)	50 (3.24)	57 (2.84)	61 (2.65)			69 (2.35)		
	EC2	79 (2.05)	32 (5.06)	34 (4.76)	46 (3.52)	51 (3.17)	102 (1.59)	41 (3.95)	45 (3.6)	60 (2.70)	66 (2.45)			79 (2.05)		
S3	CNR-DT	79 (1.24)	30 (3.27)	31 (3.16)			125 (0.78)	47 (2.09)	48 (2.04)							
	EC2	75 (1.31)	29 (3.38)	30 (3.26)			118 (0.83)	45 (2.18)	48 (2.04)							
R/FRC																
S1	CNR-DT	381 (1.30)	254 (1.97)	256 (1.93)	270 (1.83)	271 (1.82)	459 (1.07)	281 (1.76)	284 (1.74)	306 (1.61)						
	EC2	373 (1.32)	254 (1.94)	255 (1.94)	273 (1.81)	277 (1.78)	448 (1.10)	278 (1.78)	282 (1.75)	311 (1.58)	316 (1.56)					
S2	CNR-DT	228 (1.30)	150 (1.98)	155 (1.92)	159 (1.87)	162 (1.83)	297 (1.00)	195 (1.52)	201 (1.48)	207	211 (1.41)			205 (1.45)		
	EC2	224 (1.32)	149 (1.99)	152 (1.95)	161 (1.84)	165 (1.8)	291 (1.02)	194 (1.53)	197 (1.51)	210 (1.41)	215 (1.38)			208 (1.43)		
S3	CNR-DT	210 (0.98)	135 (1.52)	137 (1.51)			240 (0.86)	141 (1.46)	142 (1.45)							
	EC2	205 (1.00)	134 (1.54)	136 (1.51)			234 (0.88)	139 (1.48)	141 (1.46)							
R/FRC-AIT																
S2	CNR-DT	152 (1.56)	91.59 (2.59)		102 (2.33)		198 (1.20)	117 (2.03)		132 (1.8)				137 (1.73)		
	EC2	150 (1.58)	90 (2.64)		104 (2.28)		195 (1.22)	117.5 (2.02)		135 (1.76)				140 (1.7)		



Table 4.8: Estimated actual load bearing capacity of the RC and R/FRC plates with the tensile strength of the rebars,  $f_t=640$  MPa.

		$P_{Exp-Ave}$ [kN]	$P_u$ [kN]		
			Mechanism A	Mechanism B	Mechanism C
<b>RC</b>					
S1		370	311 (1.19)	312 (1.18)	
S2		226	183 (1.23)	239 (0.94)	223 (1.01)
S3		133	166 (0.80)	156 (0.85)	
<b>R/FRC</b>					
S1	CNR-DT	494	425 (1.16)	492 (1.00)	
	EC2		419 (1.18)	482 (1.02)	
S2	CNR-DT	297	254 (1.17)	331 (0.90)	331 (0.90)
	EC2		250 (1.18)	326 (0.91)	325 (0.91)
S3	CNR-DT	206	233 (0.88)	256 (0.80)	
	EC2		229 (0.90)	250 (0.82)	

#### 4.3.5.1 Conservative $P_d$ for SFRC and R/FRC plates

To better investigate the reliability of the adopted method and the material model utilized for tensile behavior of the SFRC material to predict the load bearing capacity and to obtain the design load of the plates, Fig. 4.10, depicts  $\gamma_d/\gamma_m$ .  $\gamma_d$  is the ratio  $P_{Exp}/P_d$ , and  $\gamma_m$  is  $P_{Exp}/P_m$ . In other words  $\gamma_d/\gamma_m = P_m/P_d$  ratio. This ratio is shown for the design resistance obtained at 34 days of age, and at the test age, obtained based on the original  $f_{R,k}$  values as well as for  $f_{R,k^*}$  values. The red line is related to the RC plates which is taken as reference value. Given that the number of notched beam specimens based on which  $f_{R,k}$  values were obtained for S1, S2 and S3 series were different, the  $\gamma_d/\gamma_m$  values can not be compared among the three configurations.

For the RC plates the  $\gamma_d/\gamma_m$  ratio varies between 1.25 and 1.3. The difference between design resistance and the average load comes from adoption of characteristic values instead of average ones, and the safety factor of 1.15 introduced to the rebars yield strength and the safety factor of 1.5 applied to concrete compressive strength. For the R/FRC plates, design condition gives more conservative values with  $\gamma_d/\gamma_m$  ranging between 1.5 and 1.7. The increased margin of safety is mainly due to the large coefficient of variation of the tensile parameters of the SFRC material which leads to small characteristic values for residual tensile strength parameters of the SFRC material. Adopting larger characteristic values according to CNR-DT 204, and applying the  $\kappa_G$  factor following EC2, help reduce the overly conservative design while still providing enough safety.

For the SFRC plates, design condition leads to overly safe values with substantial gap between the average predictions and the design resistance. The least value of  $\gamma_d/\gamma_m$  is 2.2 for the S2 condition. It is important to notice that the values shown by “+” marker are affected by the number of specimens tested. To compute the  $P_d$  value,  $f_{R,k}$  parameters for the S1, S2, and S3 series are obtained from 5, 9, and 4 specimens respectively. If we assume that for the S1 and S3 series, without changing the coefficient of variations, the  $f_{fts/u}$  parameters were derived based on 9 test results (similar to S2), the  $\gamma_d/\gamma_m$  ratio would be reduced to 2.18 and 2.25 (with CNR-DT 204 material law) which are close to the value acquired for S2. Implementation of corrective measures based on CNR-DT 204 and EC2 considerably compensates the conservative computed design loads. The approach given in CNR-DT 204 leads to safer values in comparison to the EC2 method.

#### 4.3.5.2 Conservative $P_m$ prediction for the SFRC plates

Fig. 4.10 demonstrated the large gap between the computed design resistance and the average prediction for the load bearing capacity of the R/FRC, and SFRC plates. However, another aspect that needs to be investigated is the incapability of the adopted method to predict the actual bearing capacity of, specifically, the SFRC plates. Fig. 4.11 depicts the ratio between the experimental maximum load to the realistic prediction of the bearing capacity of the plates,  $\gamma_m = P_{Exp}/P_m$ . With the explanations given earlier, the predictions made for the RC and R/FRC plates seem to be acceptable, however, for the S1 and S2 series, the predictions made for the SFRC plates are too small compared to the experimental load.

In order to look into the origin of this shortcoming, the cracking behavior of the SFRC plates in S1 and S2 series are scrutinized. A quick look at Fig. 4.5(c) and (d) reveals that at maximum load, the COD measured by the instruments that are positioned halfway between the loading point and the side of the plates, measures a maximum value in the range of 2.5 to 3.5 mm. This value is the sum of the opening of multiple cracks. Having the number of cracks that are captured by each of these instruments, Fig. 4.12 displays load versus the overall COD registered by these instruments divided by the number of cracks. This value can be regarded as an average CMOD, therefore, it is labeled as  $CMOD_{Ave}$ . It is easily noticed that the average opening of a single crack at the maximum load for the SFRC plates is somewhere between 0.4 to 0.8 mm which is different in the two directions. The ultimate limit state for these plates corresponds to an ultimate crack opening,  $w_u$ , which is significantly smaller than the code provisions, in which a  $w_u = 2.5$  mm is

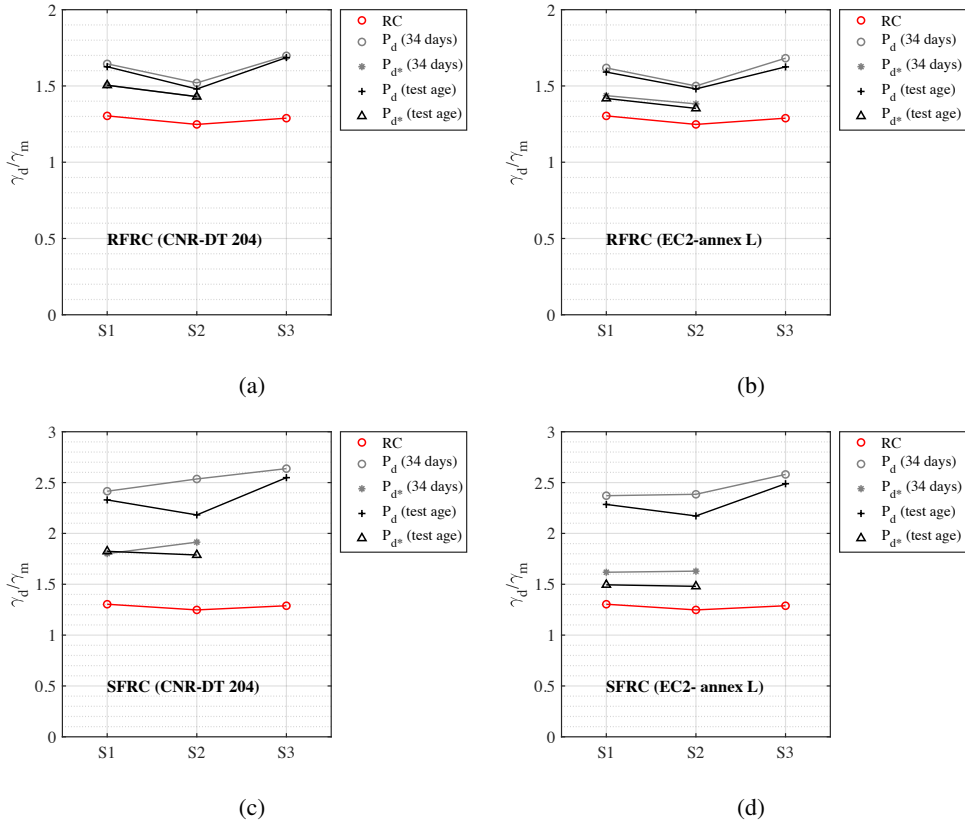


Figure 4.10: The ratio of the safety factor corresponding to the design resistance  $\gamma_d = P_{Exp}/P_d$ , to the safety factor corresponding to the realistic prediction of the load bearing capacity of the plates  $\gamma_m = P_{Exp}/P_m$ , for the (a) R/FRC plates with CNR-DT 204 tensile law, (b) R/FRC plates with EC2-Annex L draft tensile law (c) SFRC plates with CNR-DT 204 tensile law, and (d) SFRC plates with EC2-Annex L tensile law. The computation of design resistance is carried out with design value of tensile parameters from tests carried out at 34 days, or at an age close to the plate test with the original or magnified values. magnified values are shown with  $P_{d^*}$ .

presupposed. According to the experimental results presented in this work, the failure of the SFRC plates unfolds much earlier than a wide 2.5 mm crack can form. In reality and on average, the resisting bending moment that acts at each single crack, is very different from the initial assumption based on a tensile law as depicted in Fig. 4.9. Of course, this situation holds for the S1 and S2 series due to the propagation of multiple cracks. For the S3 series in which few cracks propagate, failure coincides with wide cracks, whose width is not far from the adopted tensile model with  $w_u = 2.5$  mm. It should also be noticed that the  $CMOD_{Ave}$  is obtained by dividing the overall COD by the number of cracks, however, the presence of a very narrow crack in the band

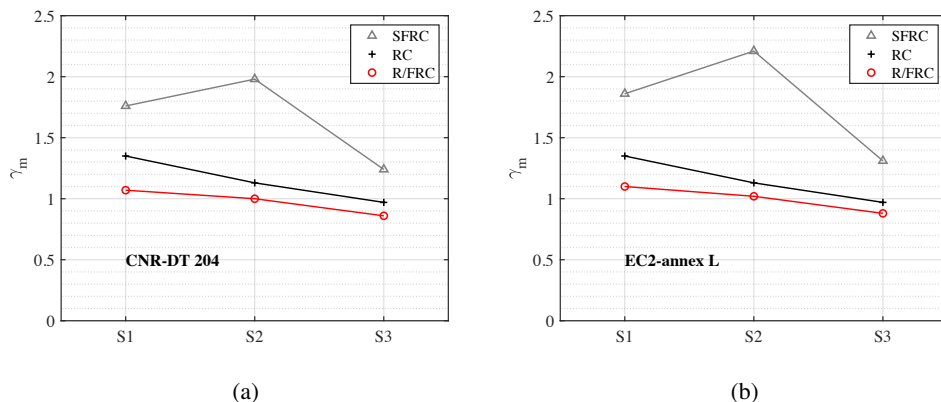


Figure 4.11: The ratio of the experimental maximum load to the predicted average load bearing capacity of the plates,  $\gamma_m = P_{Exp}/P_m$ , based on a yield line method, and adopting the tensile constitutive law according to (a) CNR-DT 204 and (b) EC2- Annex L draft.

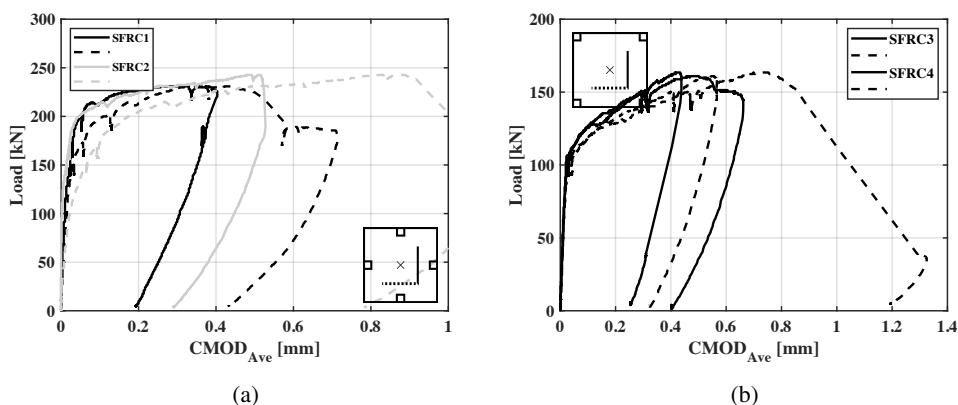


Figure 4.12: Load-CMOD<sub>Ave</sub> for the SFRC plates of the S1 and S2 series. CMOD<sub>Ave</sub> is the COD measured by each of the COD-L<sub>b</sub> long instruments divided by the number of cracks that are captured by these instruments.

of cracks can considerably change the average values. So, the absolute values given as CMOD<sub>Ave</sub> depend very much on the scatter of crack widths which is not available. That said, still the overall argument is valid as the COD readings are in the range of 2.5 mm to 3.5 mm for multiple cracks.

To apply this experimental evidence in the computation of resisting bending moments, the direct tensile law for a chosen ultimate crack opening needs to be found. An inverse analysis is carried out with different assumptions for  $w_u$ . The chosen values for  $w_u$  are 0.4, 0.6, 0.8, and 1 mm. The tensile laws that were obtained are shown in Fig. 4.13. In the absence of a direct

---

tensile test result, a certain shape and a simplifying assumption of a bilinear behavior were made for the stress-CMOD profile. The first elastic branch and the drop that follows the tensile strength were adopted according to the tensile model given in MC1990 [53]. This is shown in Fig. 4.13 with a gray line. In practical terms, the first elastic branch of the tensile constitutive law is not of much importance. The contribution of the elastic part of the tensile law in resisting bending moment is negligible when compared to the contribution of the post-cracking region with wide cracks. Hence, attempt is made here to keep it as close as possible to the provisions of EC2-annex L. Nonetheless, even assumption of a rigid-multilinear tensile law will do fine and the choice of the initial branch is more a matter of formality. The stress of the first point of the tensile law is fixed at a fraction of the flexural tensile strength, 70% or 50% of  $f_{ct,fl}$ . It is shown in the next chapter, that with 70% of  $f_{ct,fl}$  as a fixed position for the knee-point on the falling branch of the plain concrete direct tensile response, the stress-CMOD curve from the three-point bending test on the SFRC material under study can be replicated with high accuracy through a multi-layer plane section approach. Yet, most likely, the position of the knee-point is at smaller stress levels. Hence, in case D of the tensile laws shown in Fig. 4.13, 50% of  $f_{ct,fl}$  is adopted as the position of the knee-point. The strain corresponding to this point is fixed at  $\epsilon = 0.0001$ , which is in accordance with EC2- annex L tensile law. A second point is chosen at the  $w_u$ . The characteristic length is chosen as the depth of the notch,  $h_{sp} = 125$  mm.

The yield line analysis is repeated for these tensile laws and the results are given in Table 4.9. As expected and similar to previous results, the mechanisms that agree with experimental failure mechanism yield closer results. Mechanism A properly explains the failure pattern of SFRC plates in S1 series and Mechanism B is in agreement with the failure mechanism of S2 plates.

The  $\gamma_m = P_{Exp}/P_m$  for the SFRC plates with different assumptions on the ultimate crack opening,  $w_u$ , is demonstrated in Fig. 4.14. For  $\gamma_m$  related to  $w_u = 0.8$  mm two values were obtained from Case C and D tensile laws given in Fig. 4.13. In Fig. 4.14 the two values are averaged for this crack opening. Further, for  $w_u = 2.5$  mm, the average  $\gamma_m$  related to computations based on CNR-DT 204, and EC2 is reported on the figure. For both cases of S1 and S2 series, a  $w_u = 2.5$  mm gives the safest results. The SFRC material under study shows hardening up to a CMOD of around 1.4 mm. Therefore, there is no surprise that adoption of a  $w_u$  which approaches 1.4 mm results in higher predictions for the load bearing capacity and smaller  $\gamma_m$ . A crack opening of 2.5 mm is a wide crack and for a broad spectrum of SFRC classes

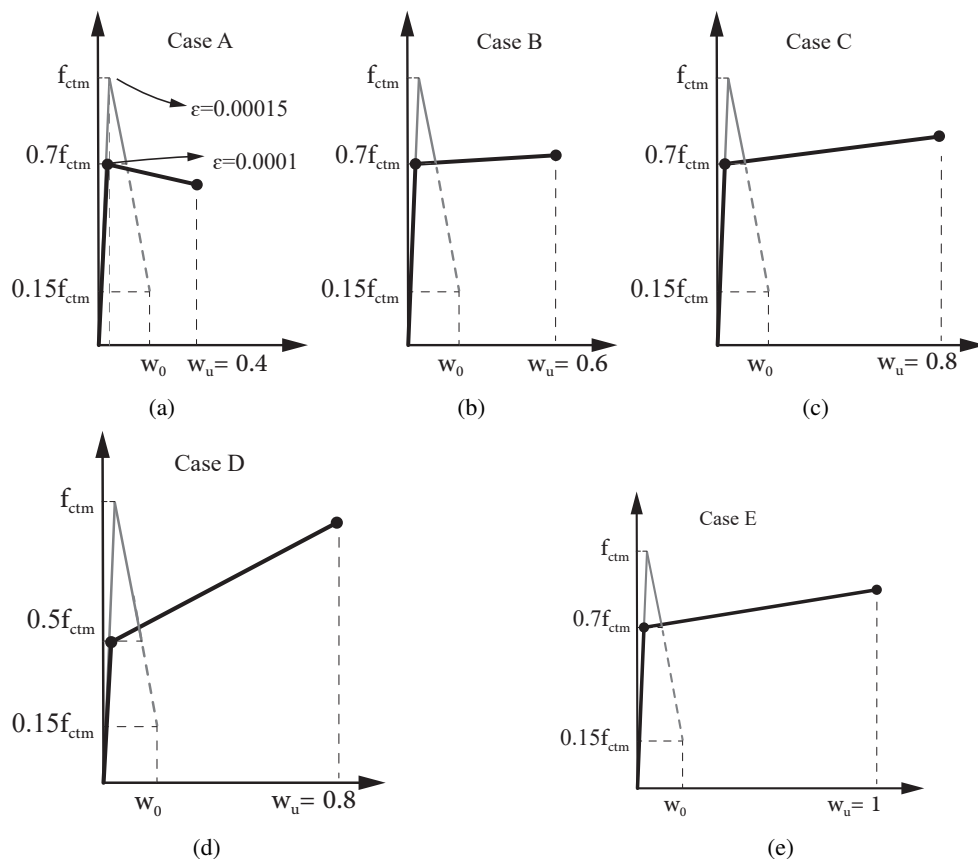


Figure 4.13: Assumptions for a direct tensile law driven for different values of  $w_u$ .

Table 4.9: The results of the yield line method using the average material properties for different assumptions on  $w_u$  for the SFRC plates in S1 ad S2 series.

Series	$w_u$ [mm]	Mech. A		Mech. B		Mech. C	
		$P_m$ [kN]	$\gamma_m$	$P_m$ [kN]	$\gamma_m$	$P_m$ [kN]	$\gamma_m$
S1	0.4	149	1.60	250	0.95		
	0.6	170	1.40	285	0.84		
	0.8 (Case C)	186	1.28	312	0.76		
	0.8 (Case D)	185	1.29	310	0.77		
	1	198	1.20	332	0.72		
S2	0.4	92	1.76	120	1.35	145	1.12
	0.6	104	1.56	136	1.19	164	0.99
	0.8 (Case C)	109	1.49	142	1.14	172	0.94
	0.8 (Case D)	113	1.43	147	1.10	178	0.91
	1	121	1.34	157	1.03	190	0.85

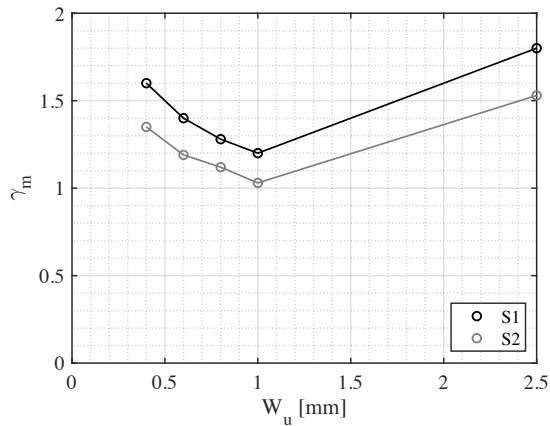


Figure 4.14: The ratio  $\gamma_m = P_{Exp}/P_m$ , with variation of  $w_u$ .

with moderate dosage of fibres, softening behavior initiates at narrower crack openings. A better redistribution capacity, is translated into more number of narrower cracks. As suggested by the experimental results obtained here, the resisting bending moment offered by these narrow cracks surpass the prediction made by the tensile law proposed in the codes which are based on a fixed  $w_u = 2.5$  mm. This is certainly a considerable source of safety that can be exploited only for structures that can undergo a stable stage of multiple cracking. For instance, the SFRC plates from S3 series (SFR5, and SFR6) in which the load was applied on their edge, failed with only few cracks (Fig. 4.2), few cracks that were much wider than those in the S1 and S2 series (Fig. 4.6). This is why when the tensile law with  $w_u = 2.5$  mm was adopted to predict the load bearing capacity of SFRC5 and SFRC6 plates, the prediction was not very far from experimental load. For mechanisms A and B approximately a  $\gamma_m = 1.3$  and  $0.8$  was achieved. As the failure mechanism could not be detected distinctly for this boundary condition (due to the fact that the support provided only partial restraint), a realistic  $\gamma_m$  would be smaller than  $1.3$  and larger than  $0.8$ .





# CHAPTER 5

---

## MODELLING

---

### 5.1 Introduction

In this chapter the behaviour of the notched beams and the plates are subjected to NLFE modeling with *Abaqus*. The focus is on the modelling of the SFRC material at two levels of standard notched specimens and large scale plate specimens. However, the RC, R/FRC, and R/FRC-Alt plates from the S2 configurations are also modelled.

To model the SFRC material, the tensile constitutive law is derived based on an inverse analysis. The SFRC material under study, shows considerable hardening behaviour after the initial post-peak softening. Seemingly, this behaviour poses some difficulties in regularization of the model. The importance of controlling the dissipated energy in the model is underlined and the choice of a proper internal parameter for fracture energy regularization of the SFRC plates is discussed. Overall, the experimental structural response of the plates and their load-COD behaviour is captured with satisfactory precision.

## 5.2 Background

### 5.2.1 Concrete tensile constitutive law

It is possible to derive a complete tensile stress-strain curve for small concrete specimens tested with stiff machines. In a direct tensile test, concrete shows a first linear elastic branch. At a certain stress level micro-cracking phase starts which leads to nonlinearity in the stress-strain curve. While at the outset micro-cracks are distributed in the specimen, at a certain point there would be a concentration of micro-cracks in the direction of principal strains which depends on the geometry and boundary conditions [170]. This zone which is characterized by damage and microcracks is called the Fracture Process Zone (FPZ). At a certain load, deformations localize in a small volume of material in the form of a macro-crack which leads to instability of the system. This transition is shown in Fig. 5.1. From this point on, deformations are concentrated in this small region while the material outside of this region will elastically unload [42]. While before the propagation of an unstable crack a stress-strain relationship can well express the deformation field in the specimens, upon the propagation of a macro-crack, strain will depend on the length of the gauge applied to measure deformations. Hence, upon reaching the tensile strength of the material, strain can not be considered anymore as a material property. A better way to illustrate deformations after localization of a crack is through stress versus the absolute deformation of the fracture zone [155]. There are clear evidence on this phenomenon as early as 1969 [109] where uniaxial tensile test under an eccentric load was carried out and

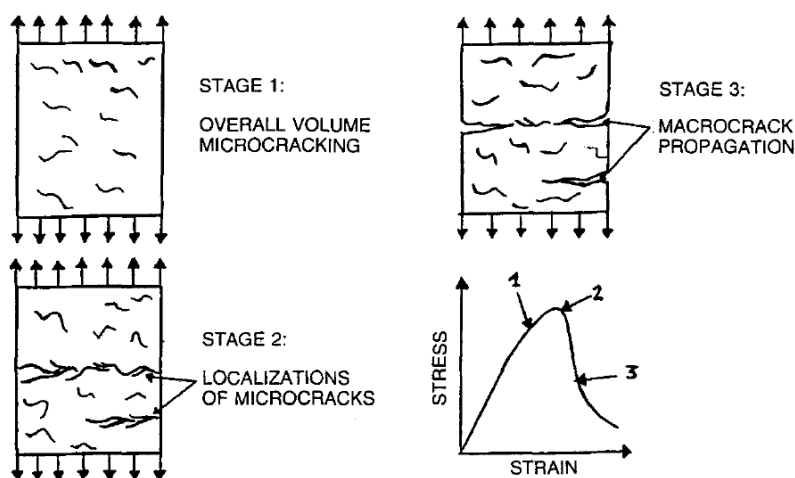


Figure 5.1: Process of cracking in plain concrete [170].

deformations were measured along the specimen with multiple gauges. These results are shown in Fig. 5.2(a) and (b) as local strains versus the mean strain of the specimen. It is observed in this figure that at a stress below the tensile strength of the material the gauges 2 and 3 keep recording elongation of the specimen while gauges outside of this region start to retract. According to Petersson [155] this observation can be better depicted with a model in which stresses are transferred within a slit, (Fig. 5.2(c)), which is how the Fictitious Crack Model (FCM) [112] is arranged.

Hillerborg and his coworkers in 1976 introduced the landmark FCM [112], which was able to take into account the crack initiation and propagation in concrete. In their model which was inspired by the works of Dugdale for yielding materials [77] and the Cohesive Crack Model of Barenblatt [12], which is almost equivalent to the FCM, crack initiation or propagation of existing cracks depend on realization of tensile strength,  $f_{ct}$  at a point. Upon this condition, stress does not fall to zero, but decreases with increasing crack width,  $w$ . In their model, the zone in which the crack opening is less than a limiting value of  $w_l$  represents a region of micro-cracking ahead of the crack tip characterized by a softening curve expressed in terms of  $\sigma - w$ . There are two very important aspects to the FCM model: first is that it is in accordance with extensive experimental results that show the presence of a FPZ ahead of a crack whose behavior can be explained by a softening behavior, and second is that unlike linear elastic fracture mechanics

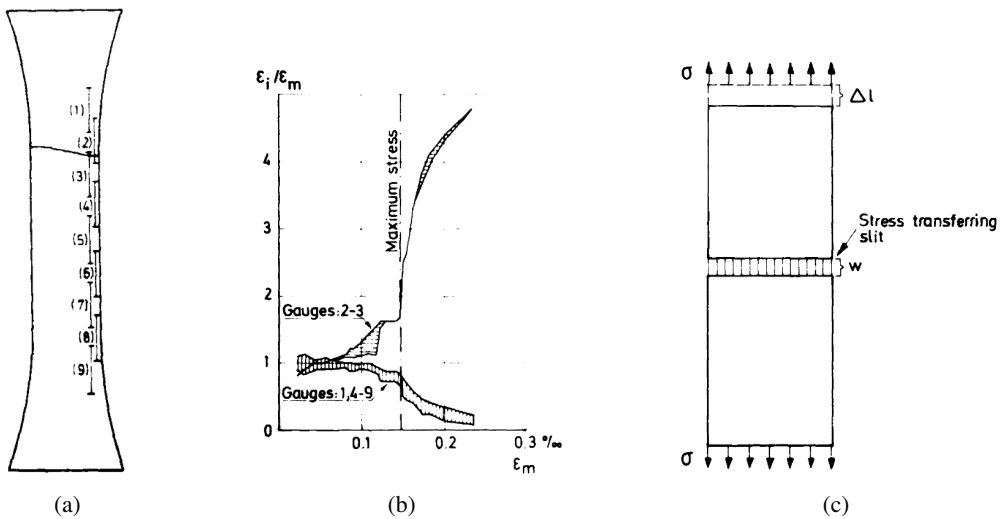


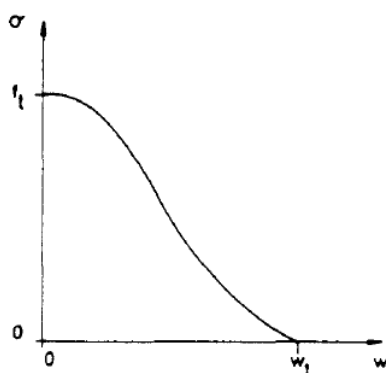
Figure 5.2: (a) Position of strain gauges and (b) the experimental results for gauge 2 and 3 in the fracture zone and for gauge 1, 4 and 9 outside of this zone [109] (c) simple model for tensile fracture where stresses depend on the width of a slit [155].

that can be solely applied to existing cracks and flaws, this model sets a clear condition for creation of a crack. This model assumes that there is no energy dissipation outside of the cohesive crack [16]. Therefore, the area under the  $\sigma - w$  curve which is the energy absorbed to create a unit area of crack is the fracture energy,  $G_f$ , Fig. 5.3. This, is indeed, different from the surface energy, which is defined as the energy needed to create a unit area of smooth surface. The fracture of concrete as a quasi-brittle material consists of dissipation in micro-cracks and friction due to slip of tortuous surfaces which requires much more energy than creating a smooth surface [16].

Similar and yet different to the FCM, Bažant and Oh introduced the Crack Band Theory [19] in which micro-cracking occurs within a certain length in the continuum, and crack opening and strain are directly correlated based on this length. This is in agreement with the fact the in concrete cracks are not slit-like and that micro-crack coalescence, zigzag cracks, crack branching and aggregate interlock occurs in the vicinity of a main crack [114].

### 5.2.2 Fracture energy and characteristic length

Toughness of concrete is a very important feature of this material which makes it different from a perfectly brittle material that would catastrophically fail upon the presence of a small crack or flaw. Toughness comes in fact from the dissipated energy by the softening cohesive stresses in the FPZ [114] and from this perspective, *softening* may be a misnomer for a behaviour that imparts *toughening* to material fracture [96]. According to Hillerborg [111],  $f_{ct}$ , modulus of elasticity  $E$ , and fracture energy  $G_f$  suffice to determine the strength, fracture, and deflection properties of structures. Hillerborg [111]



$$\int_0^{w_1} \sigma(w)dw = G_f \quad (5.1)$$

Figure 5.3: A general case for the variation of stress with crack opening [112].

highlights the significance of fracture energy demonstrating some examples and showing that the sensitivity of structural strength to  $f_{ct}$  is sometimes in the order of the sensitivity to  $G_f$ , normally however the sensitivity is less than three times of the normal strength values. Given the difficulties in carrying out a direct tensile test due to load instability, specimen misalignment, etc, the determination of the  $G_f$  is commonly undertaken through a test on a notched specimen in an indirect manner [36, 111], very often in a three point bending test. In the Rilem recommendation of 1985 [111] the work of fracture was suggested for determination of  $G_{fa}$ ; i.e. the area under the load-deflection curve divided by the area of ligament, and if the material follows the cohesive crack model the  $G_f = G_{fa}$ . Guinea et al. [104] inspected and highlighted the considerable influence of the support condition in a three-point bending test setup and pointed out the dissipation by the rolling friction of the support is not negligible.

Indeed,  $G_f$  increases with specimen size and the maximum aggregate size  $d_{max}$ . Elices, Guinea, and Planas in three consecutive works studied the influence of energy dissipated at the support, the energy dissipated in the bulk of the material and the influence of cutting the tail of the  $P - \delta$  to examine the source of the size effect [83, 104, 156]. They observed that these factors affect the measured fracture energy, but still cannot justify the 50% increase in  $G_f$  for a threefold increase in specimen size. Trunk and Wittmann [193] assume a functional form for the width of the FPZ and by developing a relationship between  $G_V$ , as the fracture energy for unit volume (a material property), and fracture energy  $G_f$ , show the dependence of  $G_f$  on a characteristic length of the structure which for large structures reaches to an asymptotic value. In another work, Hu and Wittmann [114] explain the size dependent nature of  $G_f$  by defining a local fracture energy  $g_f(x)$  for a thin strip of material as shown in Fig. 5.4. They presume that the width of the softening zone,  $W_{sf}$ , depends on the width of the macro-fracture zone  $W_f$ , and that the critical crack opening,  $w_c$ , will in turn depend on the width of  $W_{sf}$ . As the local  $w_c$  values along the FPZ can vary so does the  $g_f(x)$ . With the assumption that the micro-fracture zone is delimited by the stress contour showing  $0.9f_{ct}$  in Fig. 5.4(b), it is clear that the local fracture energy has a non-uniform distribution along the ligament area with a decreasing trend as it approaches the back of the specimen. In fact,  $G_f$  for a certain notch depth ( $a/W$  ratio) is the average of the  $g_f$  along the surface. Then, writing the variation of fracture energy,  $G_f$ , for an extension of the crack, it becomes clear that the local fracture energy at the tip of the crack depends on the variation of fracture energy with the notch depth ratio. According to Fig. 5.4(c) they conclude that the size dependency of  $G_f$  lies in the distribution of  $g_f$ .

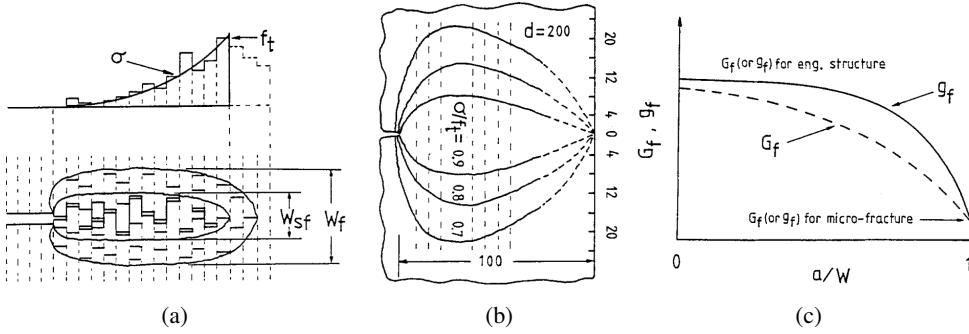


Figure 5.4: (a) the FPZ comprised of a inner softening zone and an outer micro-fracture zone with strips of material having different local fracture energy  $g_f(x)$  (b) the contour of the maximum tensile stresses and the fact that the extent of the FPZ contracts approaching the back of the specimen (c) the decrease of  $g_f$  along the ligament and the size dependency of  $G_f$  [114].

The presence and extent of the FPZ which is due to the inhomogenous nature of concrete [18] has been the subject of extensive studies. Unlike ductile materials for which the majority of the fracture front is taken up by a hardening or yielding zone, for concrete, there is negligible plasticity and this zone is filled up by a softening FPZ whose length is around 0.5 m for normal concrete [17] and depends on a characteristic or material length,  $l_{ch}$ . Cedolin et al. [42] explored the FPZ in plain concrete for single notched, double notched and un-notched specimens with moire interferometry where they remark the presence of large FPZ compared to the dimensions of the specimens. Slowik and Wittmann point out that the FPZ also depends on the strain gradient. The greater the strain gradient the more confined the FPZ [181]

The existence of a  $l_{ch}$  as a material property can be inferred from  $G_f$  and  $f_{ct}$  as two independent material parameters that can be related through a length. Hillerborg [112] introduces a critical length as  $l_c = EG/f_t^2$ , and shows that the ratio of bending strength to tensile strength depends on the ratio  $H/l_c$ , where  $H$  is a structural dimension. Larger values of this ratio leads to smaller bending strength relative to tensile strength. According to Gustaffson [106], if only strength is of concern, the only parameters needed are the  $f_{ct}$ , and a measure of the ratio between the slope of the  $\sigma - \epsilon$  and  $\sigma - w$  branches in a tensile behaviour.  $f_{ct}/(G_f/f_{ct})$  being a measure of the slope in  $\sigma - w$  relationship, the parameter  $EG_f/f_t^2$  having the dimensions of length, is referred to as characteristic length,  $l_{ch}$ , which determines the brittleness of a material and is a material property. As Petersson puts it [155], the brittleness of a material that can be determined by the  $\sigma - \epsilon$  and  $\sigma - w$  curves can be represented by a single characteristic parameter. A specimen of stiffness  $k = AE/L$

that experiences the maximum load of  $F_c$  under a deformation of  $\delta$ , has a energy of  $F_c^2 L / 2AE$  available for crack creation, and can absorb as much energy as  $G_f A$  by propagation of a crack. Equating these two terms will give  $l^* = 2G_f A^2 E / F_c^2 = 2G_f E / f_t^2$  that is a length of the specimen at the instant of crack propagation. Smaller values of  $l^*$  represent more brittle material. Half of this length is taken as the characteristic value defined as  $l_{ch} = G_f E / f_t^2$ .

Bažant points out that the fracture energy which controls the maximum structural strength is not the whole area under the  $\sigma - w$  curve, but its the portion of this area which is below the first branch of the curve, and demonstrates this hypothesis by FE modeling of notched specimens in various sizes, and showing the steep fall of stress value at the notch tip. He tends to label the complete fracture energy as  $G_F$  and the area under the initial branch of the stress-separation relationship as, initial fracture energy,  $G_f$ . This is schematically shown in Fig. 5.5. Beside the definition already given for the  $l_{ch}$ , a characteristic length,  $l_1 = EG_f / f_{ct}^2$  is defined that corresponds to this initial part of the fracture energy.

There are conflicting reports on the effect of maximum aggregate size on concrete tensile fracture energy. However, there is more evidence showing that larger maximum aggregate size increases fracture energy. Cedolin et al. [42] investigated the effect two maximum aggregate size of 6 and 10 mm and they point out that the aggregate size does not affect the extent of the fracture process zone. Chen and Liu [46] studied the effect of four different maximum aggregate size on fracture energy through acoustic measurements under a three-point bending test. They also carried out X-ray inspection to better capture the extent of the cracked zone. Unlike Cedolin and colleagues, they point out that increasing the maximum aggregate size leads to an increase of the width of the cracked zone and a more tortuous crack surface. More twist

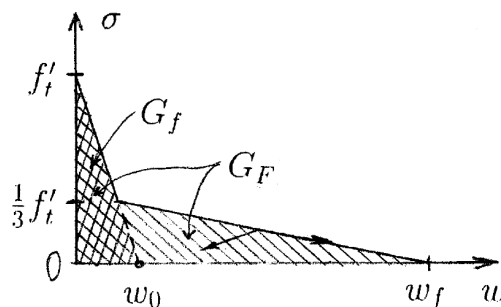


Figure 5.5: Bilinear cohesive law and the designation of fracture energy  $G_F$  and the initial fracture energy  $G_f$  [17].

in the crack path requires overcoming larger interfacial bond and consequently larger fracture energy and more acoustic activity. The increase of fracture energy with maximum aggregate size is further shown by Elices and Rocco [84] where they use spherical aggregates with three different maximum size in a weak and a strong matrix. They also treat the surface of the aggregates to impart strong and a weak interfacial zone. They cite many other works in the literature, where increasing the maximum aggregate size led to increasing fracture energy and fracture process zone [154, 161, 175, 192].

### 5.2.3 Post-peak tensile behaviour

To describe the post-peak behaviour of plain concrete, it might be sufficient to know the value of  $G_f$ . The softening curve can be estimated by some linear or non-linear degradation relationship on the basis of numerous available experimental results, which have shown that the softening branch is almost independent of the concrete type [54]. A bilinear curve with a break point (knee point) and a long tail is commonly adopted for the post-cracking region which is also supported by extensive experimental observations [181]. The first branch is specified by a sharp slope. It falls down to a stress level for which different values are given. Petersson [154] recommended  $f_t/3$ , the CEB-FIB MC 1990 [53] gives a value of  $0.15f_{ct}$ , MC 2010 [116] suggests  $0.2f_{ct}$ , but in any case, the value remains between  $0.15f_{ct}$  and  $0.33f_{ct}$ . The second branch goes up to a critical crack opening that depends on the width of the FPZ. The wider the FPZ, the wider the critical crack opening [181].

Roelfstra and Wittmann [168] adopted the bilinear softening branch proposed by Hillerborg [111] in a finite element model and varied the position of the break point in the post-peak tensile relationship keeping the  $G_f$  constant, to investigate its influence on the response of three-point bending results. To find the post-peak response they, for the first time, used an inverse analysis method minimizing the difference between the calculated and experimental load-deflection response at two crack opening values. Fig. 5.6 shows their results. They underlined the fact that tensile strength and fracture energy are necessary parameters, but not sufficient for a proper calculation. Hence toughness,  $G_f$ , is not a useful tool in material characterization and a proper  $\sigma - w$  relationship is needed [189]. Uchida et al. [195] also showed the influence of different parameters on the load-displacement response of three-point bending test and among them highlighted the effect of the tension-softening law (Fig. 5.7).



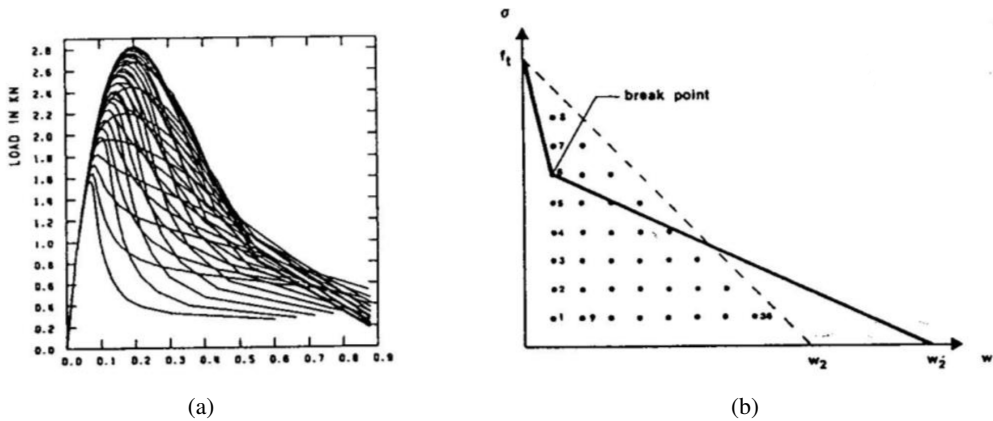


Figure 5.6: (a) Calculated load-displacement diagrams for a three-point bending test for (b) 36 different strain-softening diagrams with the same fracture energy,  $G_f$  [168].

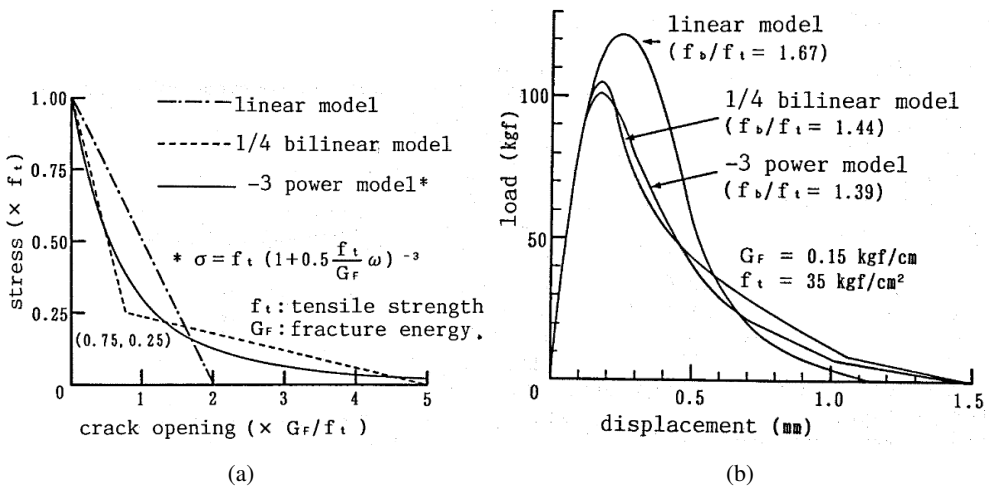


Figure 5.7: Effect of (a) different tension softening models on the (b) load-displacement curve of three-point bending test [195].

## 5.2.4 Fracture energy regularization

Concrete cracking is modeled in a discrete manner or within the assumptions of continuum mechanics. In discrete modeling of cracks, which for the first time was suggested by Ngo and Scordelis in 1967 [144], cracks are modeled in the form of discontinuities in the FE mesh. Yet in smeared crack modeling, continuity is preserved and the evolution of material properties and the propagation of the cracks are considered based on the state of strain or stress [163]. The smeared crack models depending on whether the Plane of Deterioration (POD) [205] retains its initial direction upon further loading, or

rotates to remain orthogonal to the current major principal stress is divided in to *fixed* and *rotating* crack approaches. In fixed crack models shear is taken into account by introducing a retention factor which couples shear resistance with crack opening displacement, while there is zero shear resistance for rotating crack models as they coincide with the principal axis of material isotropy. The easier implementation of smeared crack models in that they do not suffer from topology change and the need to rearrange the mesh in one way or another has made them the most common approach for concrete modeling.

For a strain softening material like concrete, upon cracking, strains localize in a narrow band of one element width regardless of the element size and the energy is dissipated within this elements. As such, energy dissipation depends on the size of the elements giving rise to non-objectivity of results, i.e. upon mesh refinement and for infinitesimally small elements, no dissipation would take place. A numerical length parameter is introduced to regularize the model to assure that the dissipated energy in a finite element is consistent with the fracture energy of the material. Fracture energy,  $G_f$  being a material property, is the energy required to create a unit area of crack and is expressed as:

$$G_f = \int \sigma_{nn} dw \quad (5.2)$$

where  $\sigma_{nn}$  is the stresses normal to the crack, and  $w$  is the sum of all micro-cracks within the fracture zone. In smeared crack approach, crack opening is represented as strains over a certain length, the *crack band*, or the *characteristic length*, which is shown with  $h$  following [19, 171], or with  $l_{cs}$ . This is schematically shown in Fig. 5.8. If a uniform distribution of micro-cracks along the crack band is presumed, we have:

$$w = h \times \epsilon_{nn}^{cr} \quad (5.3)$$

with  $\epsilon_{nn}^{cr}$  being the crack strain in the direction of principal tensile stresses. The energy dissipated within a single element would be:

$$g_f = \int \sigma_{nn} d\epsilon_{nn}^{cr} \quad (5.4)$$

From Eq. 5.2 to Eq. 5.4 it is inferred that :

$$G_f = h \times g_f \quad (5.5)$$

meaning that for the energy dissipated in one element,  $g_f$ , to be equal to the fracture energy of the material,  $G_f$ , the softening branch of its constitutive

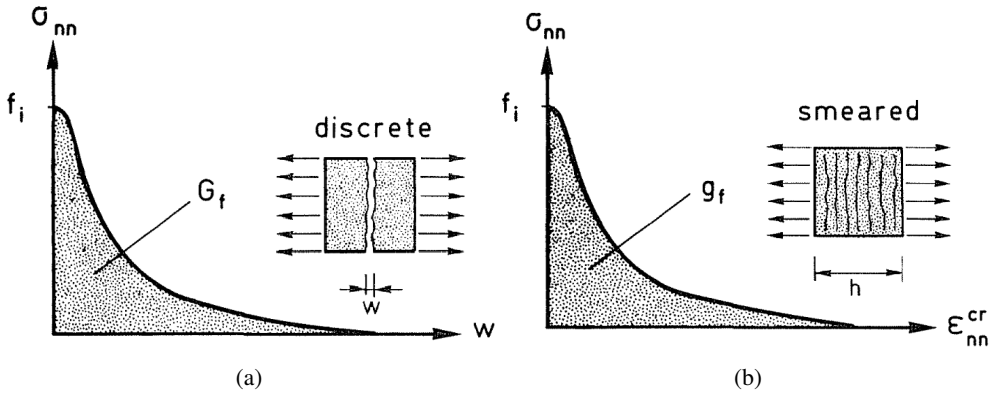


Figure 5.8: (a) Tensile stress-w diagram versus (b) tensile stress-strain diagram [171].

behavior should be scaled by the numerical length. Fig. 5.9 shows a schematic representation of how this length affects the local tensile law for a computation point. Clearly, there is a maximum to the value of  $l_{cs}$  that does not lead to snap-back. This regularization which is based on fracture energy, is the most common regularization technique that is very often implemented for modeling concrete in FE software packages like *Abaqus*, *DIANA*, *ATENA*, etc. Accordingly, the local tensile softening law does not just depend on fracture energy and the cohesive law, but also on the features of discretization and integration scheme.

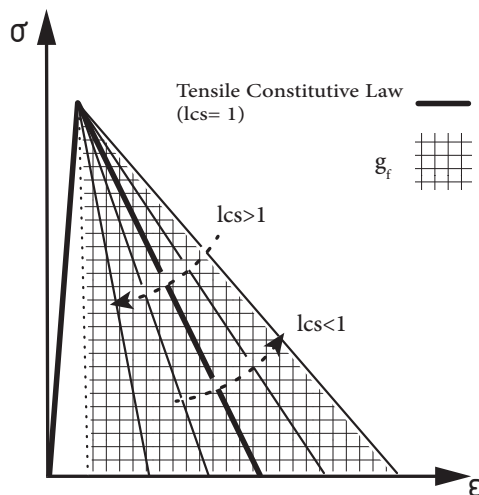


Figure 5.9: Introduction of a numerical characteristic length to adjust the softening branch of the tensile constitutive law to regularize the fracture energy.

According to Rots et al. [171] for quadratic elements where the crack is parallel or almost parallel to the finite element, the choice of the crack band will be as shown in Fig. 5.10. In Fig. 5.10(a) the crack will pass through two or three Gauss points for full or reduced integration respectively, and for Fig. 5.10(b), in reduced integration scheme, it is assumed that the cracks passes through one integration point and given that the Gauss point is close to center of the element, the width will almost be equal to half of the length of the element.

### 5.3 Derivation of FRC tensile constitutive law

The derivation of FRC tensile constitutive law through inverse analysis, by minimizing the difference between the calculated and experimental load-CMOD of a three-point bending test result, is very often done based on the assumption that the  $l_{ch}$  equals the ligament depth of 125 mm. This is how design tensile constitutive law for FRC is formulated in codes, when a plane section (Bernoulli-Navier) model is assumed. For design purposes, two crack openings of 0.5 mm and 2.5 mm are considered as benchmark values for which the residual tensile strength values are obtained. Given that concrete structures are designed with the assumption of presence of cracks, this is a realistic assumption. However, such method fails to give a proper tensile constitutive law that can well demonstrate the overall uniaxial tensile response of a FRC. Some limitations and examples of inverse analysis for determination of the tensile constitutive law for FRC are given in [131]. Among these limitations are the sizable effect of fiber distribution on the results of a three-point bending test. A bundle of fibres close to the notch can substantially affect the result of a flexural test, while in a direct tensile test this may not be of great concern. Löfgren et al. add that conducting the inverse analysis on a curve that is averaged among some specimens may cancel out this effect and well agrees with the assumption of a homogeneous material. Furthermore, they point out the fact that the determination of the tensile strength,  $f_{ct}$  is better to be carried out on a splitting test on a mix design without fibres, or taken based on experience. Similarly, yet for normal concrete, Uchida and Barr [194] point

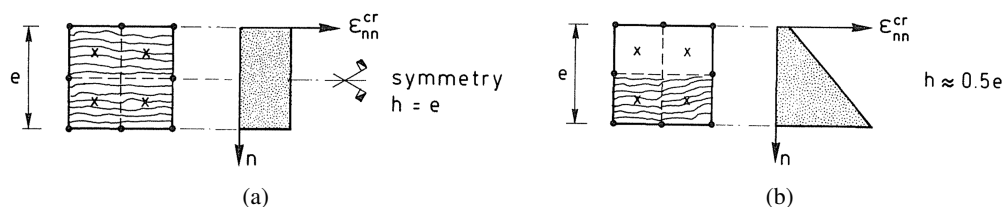


Figure 5.10: Estimate of the crack band width,  $h$ , in (a) symmetric mode I problem and (b) non-symmetric problem [171].

out that the derivation of the tensile strength from an inverse analysis in the absence of any further data is very unreliable. Dupont [78] in his PhD thesis, suggests that the flexural tensile strength might be a better indicator of true tensile strength due to many influencing factor that affect a direct tensile test. He chose the relationship available in the Rilem recommendation reading

$$f_{ct} = f_{ct,fl} \times \frac{1600 - h}{1600 - h_{sp}} \quad (5.6)$$

with  $h$  being the effective depth of the beam, and  $h_{sp}$  being the ligament length, 125 mm for Rilem beam. For a three-point bending test on a notched beam according to EN 14651 [86], it is assumed that  $f_{ct} = f_{ct,fl}$ . However, the determination of  $f_{ct}$  from a flexural test does not seem to be straightforward. The ratio of  $f_{ct,fl}$  values derived from a three-point bending test to  $f_{ct}$  values derived from a direct tensile test for FRC specimens with 60 mm long hooked-end fibers with a dosage between 0.4% to 1% ranged from 0.54 to 0.84 in tests carried out by Amin and Foster [7], indicating that the relationship between tensile strength and flexural tensile strength might be heavily affected by the stabilizing action of fibers. Fig. 5.11 shows the average nominal stress-CMOD results up to a CMOD of 0.2 mm for the notched beams tested in *Part A* at two different ages. Following the provisions of the EN 14651 [86], the  $f_{ct,fl}$  value would be the maximum stress up to a CMOD of 0.05 mm. As such, for the average results obtained at 167 days and 220 days of age, the  $f_{ct,fl}$  will be 6.32 MPa and 6.84 MPa respectively. This is a very large value for a C40 concrete. The fibers used in this study with a length of 60 mm and a diameter of 0.9 mm at the moderate dosage of 35 kg/m<sup>3</sup> would not be able to affect micro-cracking behavior that leads to the propagation of macro cracks. Hence, the  $f_{ct,fl}$  obtained from these three-point bending tests does not seem to be a good indicator of the  $f_{ct}$ .

After reaching the tensile strength, the tensile constitutive law is followed by a steep slope. Olesen et al. [147] studied the split cylinder test and the parameters of the tensile softening law on the response of such test method. They point out that the location of the knee point in the post-peak tensile constitutive law is the parameter that is most directly affected by the addition of fibers. The main bridging effect of commonly adopted long fibres is activated only after the propagation of macrocracks in the extent of a couple of tens of micrometers [184]. In the Variable Engagement Model (VEM) by Voo and Foster [202], it is assumed that for mechanically anchored fibres, some slip is needed for the fibres to be effectively engaged in carrying tension and the COD for which fibres start to work is called the engagement length,  $w_e$ . Voo and Foster adopted a CMOD corresponding to 50% of the  $f_{ct,fl}$  as the engagement

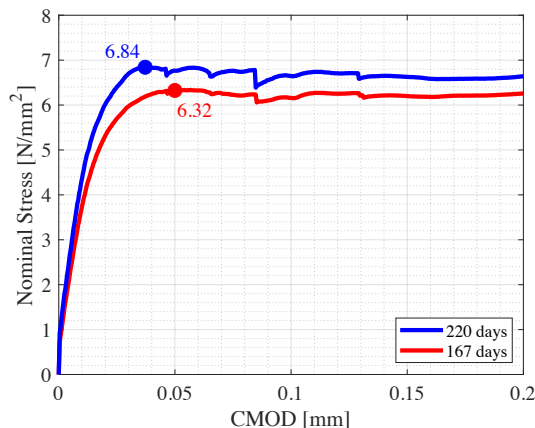


Figure 5.11: The  $f_{ct,fl}$  values for the notched beams tested in *Part A* of the campaign at two different ages.

length and verified their model on the test results of Banthia and Trottier [11] for single fibre pull-out results.

In the present work, having in mind the earlier works on the derivation of a justifiable direct tensile constitutive law, a simplified method is devised and adopted. This tensile law performs well also in a NLFEA. Before macro-cracking, a linear elastic law is assumed, overlooking the initiation of micro-cracking phase. The tensile strength, in the absence of direct measurement, is determined so that the cracking point of three point bending test can be captured in with a non-linear hinge model. The softening branch after the peak, is built upon the provisions of the Model Code 1990 [53]. In our previous experience, adoption of the tensile constitutive law of concrete from MC 1990 gave much better results in NLFEM for plain concrete when compared to the MC2010 tensile law. In MC1990, fracture energy,  $G_f$ , and the maximum crack opening after which, supposedly, no stress is transmitted,  $w_c$ , depend also on the maximum aggregate size,  $d_{max}$ , which agrees with experimental observations. However, in MC2010, these parameters only depend on concrete strength. Hence the post-cracking slope, and consequently the fracture energy under the first branch of the softening response that dominate the response of concrete differs considerably between the two. Fig. 5.12(a) shows the difference between the tensile constitutive law for the two codes. In the figure, the ratios between the values are realistic. The position of the break point on the softening branch is chosen so that the experimental results of the three-point bending test can be replicated within an acceptable range by a non-linear hinge model. For the fibres used in this study, that are characterized by a long extension of the hook which favors the

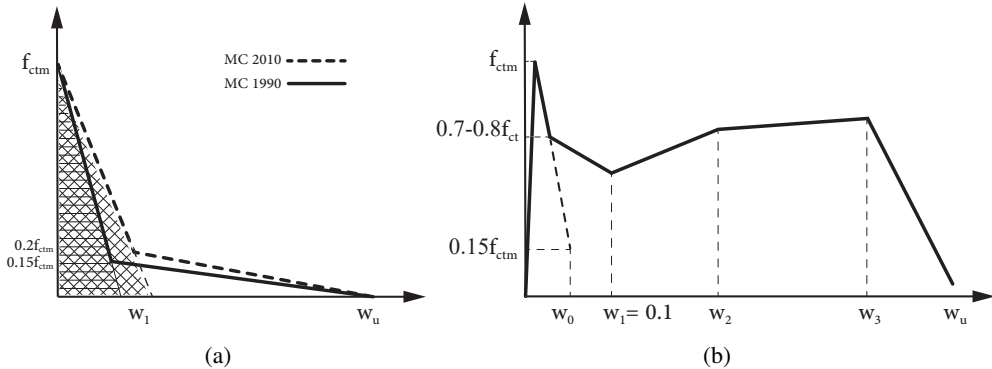


Figure 5.12: (a) comparison of the post-cracking tensile constitutive law given in MC 1990 and MC 2010 (b) Tensile constitutive law devised and adopted for FRC.

mechanical anchorage of the fibres, a break point at 70% to 80% of  $f_{ct}$  gave satisfactory results. Afterwards, to keep the procedure as simple as possible, four values of CMODs are chosen for which the residual tensile values are obtained by imposing force and bending moment equilibrium. The first CMOD is 0.1 mm, and the other ones are chosen so that a proper representation of the experimental nominal stress-CMOD curve can be reproduced. The passage between CMOD to strain, for this kinematic model, is by adopting a  $l_{ch} = 125mm$ . For sake of simplicity, nonlinearity in compression is neglected and a linear stress-strain relationship is considered.

There are certain simplifying assumptions to such method that can affect the results of its application to different extent. First being the assumption of a linear elastic behavior up to the onset of macro-cracking. A heterogeneous medium like concrete, goes through considerable nonlinearity before the appearance of macro cracks. The presence of fibers, in a three-point bending test can bring about stabilization to the failure process which can increase the stretch of nonlinear response before emergence of a macro crack. This can also be inferred from Fig. 5.11 in which sizable nonlinearity is observed. In this manner, assumption of a linear elastic behavior leads to an overestimation of the  $f_{ct}$  [78]. Second, is the presumption of a constant characteristic length,  $l_{cs}$ , equal to the depth of the ligament. The ligament depth being 125 mm, is almost twice the length of a single fiber in this study, 60 mm, which may justify the assumption of  $l_{cs}=125$  mm to some extent. Yet there is a whole dynamic to the extent of the  $l_{cs}$  comprising its sudden expansion in the beginning of the damage process and later, its contraction due to large strain gradients. Obviously, the assumption of a constant length is for the sake of simplicity and in the absence of valid experimental data for the material under study, no

effort is made here to examine the influence of variation of the characteristic length on the tensile constitutive law.

Fig. 5.13(a) displays the tensile constitutive law that is obtained for the SFRC used in *Part A* of the study and tested at 167 and 200 days in a three-point bending test. These tensile laws are also checked in a nonlinear hinge model with a plane section, multilayer approach to replicate the complete experimental curves. In the author’s knowledge, the first analytical treatment of the bending behaviour of concrete within the framework of a fictitious crack model was developed by Ulfkjaer et al. [196], and later adopted and modified also for FRC [40]. Here, a parabola rectangular behavior for concrete in compression and the multi-linear constitutive law in tension is adopted. Figs.5.13(b) and 5.13(c) compare the experimental results with the curve that is built with the multi-layer approach.

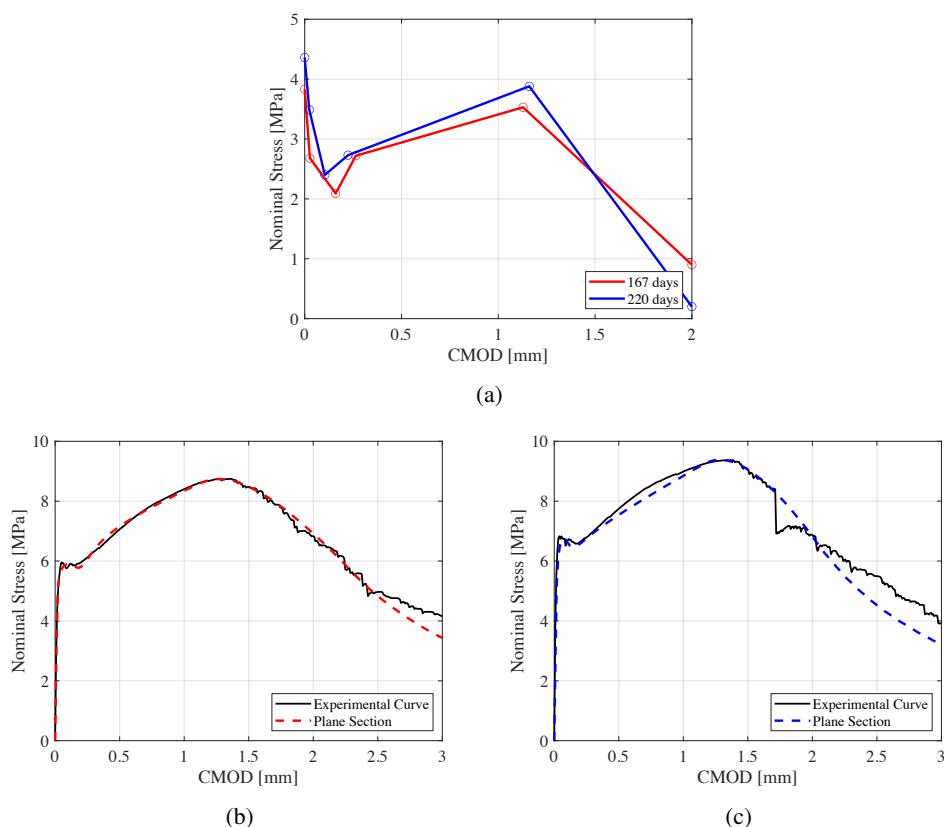


Figure 5.13: (a) The obtained direct tensile law for the SFRC material tested at 167 and 220 days through inverse analysis, and The comparison of the experimental nominal stress-CMOD curves with the curves obtained from a multi-layer plane section approach based on these tensile constitutive laws for (b) 167 days and (c) 220 days results of *Part A*.



## 5.4 Model details: constitutive law, elements, discretization

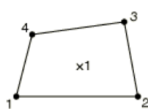
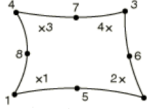
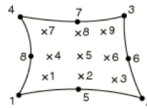
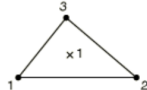
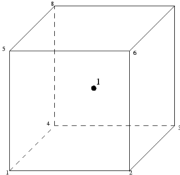
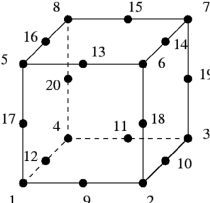
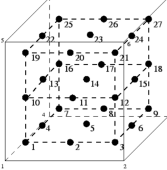
The Concrete Damage Plasticity (CDP) model, without the introduction of the damage parameter, is adopted to model concrete. The failure process of hooked-end FRC involves considerable plastic behavior of concrete around the hook. As such, the plasticity model has shown to perform well for modeling this type of fibers whose behavior is mostly controlled by the anchorage of the hook. The model is built upon the uniaxial constitutive law of concrete in tension and compression, and through some parameters builds up the flow rule, plastic potential, and hardening/softening behaviour. The parameters of CDP for the SFRC material are adopted from the work of Godde and Mark [100]. The CDP model, originally proposed by Lubliner [132] and later modified by Lee and Fenves [127] is a elasto-plastic damage theory model with isotropic damage, and a non-associated flow rule, which was developed for plain concrete. In this model, the flow rule  $F$ , and flow potential  $G$ , are defined as a function of hydrostatic pressure  $p$ , *von Mises* equivalent stress  $q$ , and the maximum principal stress  $\sigma_{max}$ . Evolution of flow rule depends on two parameters,  $\alpha$  which is a function of the ratio of biaxial to uniaxial compressive strength  $f_{b0}/f_{c0}$ , and  $\gamma$  which depends on the shape of the yield surface in deviatoric plane through parameter  $K_c$  that determines the ratio of tensile to compressive meridians. The flow potential  $G$ , defined in the  $p - q$  plane, depends on dilation angle  $\psi$  at high confining pressure, and eccentricity, that defines the rate at which plastic potential approaches the asymptote. For modeling the plain concrete and the SFRC, the following parameters are adopted:

Table 5.1: Parameters of the CDP adopted for modeling of plain and fibre reinforced concrete

Material	$\psi$	Eccentricity	$f_{b0}/f_{c0}$	$K_c$	Viscosity parameter
Plane concrete	37	0.1	1.16	0.66	$10^{-5}$
SFRC	15	0.1	1.27	0.66	0

Solid elements are utilized for modeling of the notched beams and plates. The notched beams are modeled with plane strain elements, and the plates are modeled with brick elements. The elements adopted and the corresponding Gauss points for these elements are shown in Table. 5.2. The CPE family of elements are general purpose plane strain elements, in which the displacement of all nodes in the z-direction is zero. Although they are used to model slices of long structures, they have shown to give better results in modeling three-point bending test when compared to the plane stress elements. The plates are modeled with general purpose bricks. The C3D8R element, unlike its

Table 5.2: The element types and their Gauss points adopted for modeling the notched beams and plates.

Notched beams	 <p>CPE4R</p>	 <p>CPE8R</p>	 <p>CPE8</p>	 <p>CPE3</p>
Plates	 <p>C3D8R</p>	 <p>C3D20</p>		

companion with full integration, does not show the locking problem, however, there are 12 spurious hourglassing modes. When these elements are adopted to model the plates, six elements in thickness of the plates are adopted to prevent hourglassing. The C3D20 elements can be too stiff in bending problems of thin element, yet, given that the tested plate are not thin, their application would not create problems.

When modeling the three-point bending tests, the whole specimen is modeled to investigate the numerical crack width at the notch. For the plates, symmetry is taken into account, and one-fourth of the specimen is modeled. This is shown in Fig. 5.14. For the plates, the neoprene sheet that was placed on top of the support, as well as at the interface between the loading head and the plate is also modeled (although it was observed that the effect is marginal). At the interface of the loading head with the plate and at the support, frictionless contact is defined.

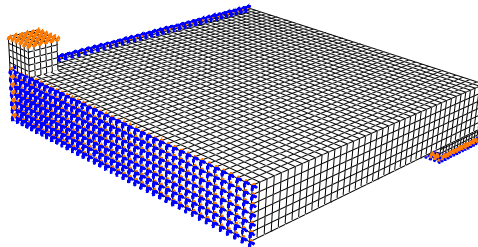


Figure 5.14: Boundary conditions and discretization of the models for plates when C3D8R elements are adopted. When C3D20 elements are utilized, element size is increased.

## 5.5 NLFEM of notched beams

To verify the constitutive law driven for the SFRC under study, the three-point bending tests on a notched specimen are modeled with the software *Abaqus*. The boundary conditions consist of two frictionless supports and the loading head whose horizontal movement is restraint to the contact surface. The load is applied in displacement control.

### 5.5.1 Element type, integration rule, and localization

#### 5.5.1.1 Quadrilateral element

Fig. 5.15 shows the results of the FEM for the notched beams for two element sizes of 5 mm and 2.5 mm. The cracking point of the beam is not captured by the model. As mentioned earlier, for the inverse analysis, the assumption of a linear elastic behavior up to the initiation of cracking may lead to an overestimation of the tensile strength. This is clearly reflected here in the results of the model, despite the fact that the overall nominal stress-CMOD response could be predicted.

Looking at Fig. 5.15(a) for a 5 mm mesh size, with nine and four Gauss points, the maximum of the curve can be nicely predicted, however, only one Gauss point in CPE4R element is not close enough to the notch tip and overestimates the maximum of the experimental curve. Although normally, for a quadratic element half of the diagonal of the element is taken as the internal length, here, the two curves that are close to the experimental curve are obtained with a characteristic length that equals the whole width of the element, 5 mm. When  $l_{cs}$  was reduced to half of the width of the element, the softening branch was not captured. For an element size of 2.5 mm, adopting quadratic elements that are shown with the blue and green curves, were not giving reliable results. The best result was for a single Gauss point in a linear element.

The main problem in modeling is related to the spread of localization to many Gauss point when two elements of higher order are used on top of the notch. Even introducing a flaw into the model was not enough to localize plastic strains in one band of elements. Fig. 5.16(a) and 5.16(b) show the distribution of maximum principal plastic strains for three points along the nominal stress-CMOD curve of the three-point bending tests shown on the curves as “a”, “b”, and “c”. When there are two elements on the notch, Fig. 5.16(a), at point “a” on the curve, the plastic strains are mostly concentrated on two rows of Gauss points on the band of elements on the left. The crack width might be assumed to be around  $2/3$  of an element size then.

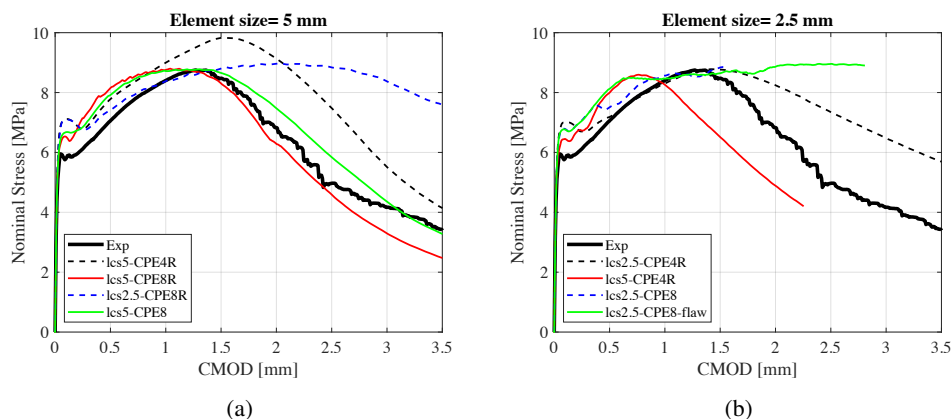


Figure 5.15: Results of FEM with different elements with an element size of (a) 5 mm and (b) 2.5 mm.

This condition holds also for point “b” on the curve. However, later on, at point “c”, there is a substantial expansion of plastic strains. The elements on the left show plastic strains on all nine Gauss points and the elements on the right of the notch also are involved in the dissipation up to almost one-fourth of the depth of the beam. The *flooding* of dissipation to many points brings about a plastic behavior on the stress-CMOD response. This effect can not be controlled by a pseudo-regularization method which assumes a constant crack width during the whole failure process. Adopting one element on the notch, Fig. 5.16(b), mitigates the problem to some extent. Here, the crack width varies slightly between two and three Gauss points depending on the position of the element along the height of the beam, and always, on the elements that dissipate most energy, all the nine Gauss points are involved. With this regard, adoption of a characteristic length equal to the width of an element may do well. Looking at the blue dashed line in Fig. 5.15(a), indicates that a  $l_{cs}=2.5$  mm is an underestimation of the crack band.

### 5.5.1.2 Triangular element

To evaluate the performance of constant strain triangle elements in plane strain (CPE3), the notched beam is modeled with fine triangular elements close to the notch. The mesh is shown in Fig. 5.17(b). In this model a  $\sigma - w$  relationship is introduced for the tensile behaviour of the SFRC material. The results obtained for this model are shown in Fig. 5.17. Fig. 5.17(a) compares the experimental curve obtained for the nominal stress-CMOD of the notched beam and the result obtained from the model. Up to the peak load, the fine mesh gives very satisfactory result, however, reaching to point “1” on the curve a sudden softening occurs which is followed by a hardening behaviour starting at point

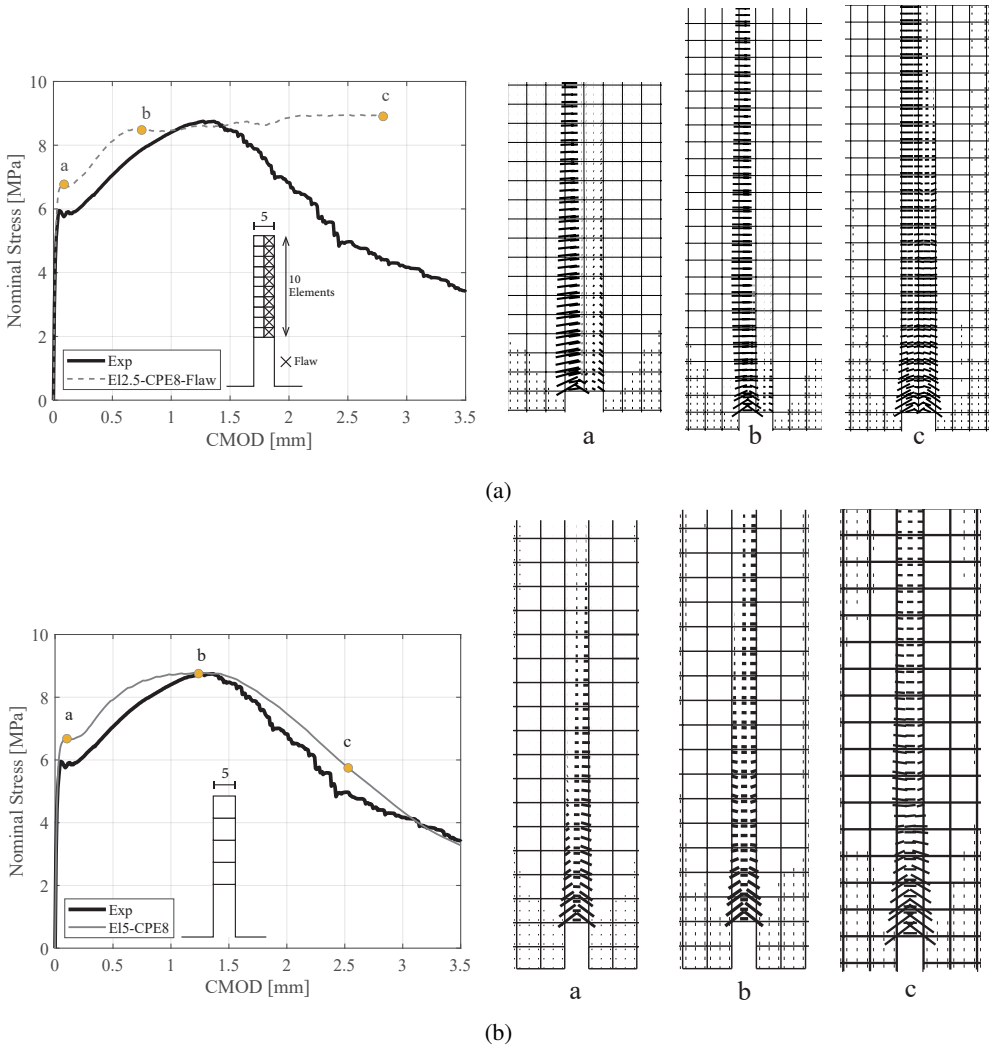


Figure 5.16: Comparison of spread of plastic strains on three points on the nominal stress-CMOD curves of the notched beams for two element sizes of (a) 2.5 mm in which a flaw is also introduced in the model, and (b) 5 mm.

“2”.

To examine this phenomena from a closer perspective, distribution of maximum principal plastic strains at points “1” and “2” on the numerical curve is shown in Fig. 5.17(c) for the elements on top of the notch. At point “1”, dissipation is localized on the elements on the right of the notch. Plastic strain values are in the range of 1.5-2. The localization parameter for plane elements is the square root of the element area. For the triangular elements

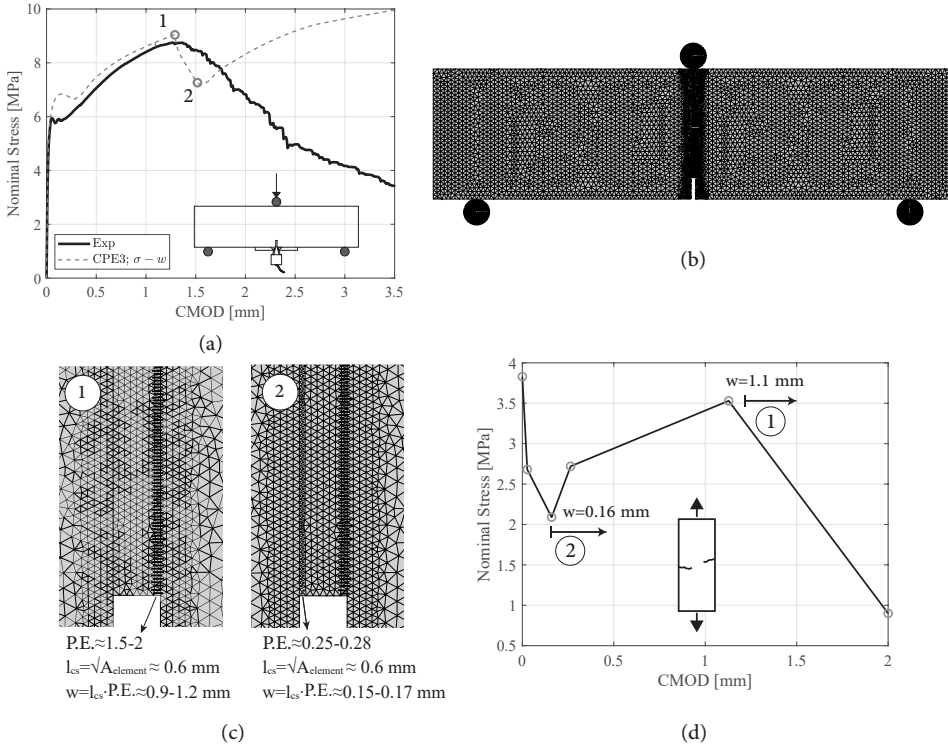


Figure 5.17: (a) comparison of experimental nominal stress-CMOD result with the result of the model with constant strain triangular elements (CPE3) (b) mesh of the notched beam (c) distribution of maximum principal plastic strain (P.E.) on the elements on top of the notch for points 1 and 2 on curve related to the model result with transformation of the P.E. values to crack opening and (d) the crack opening corresponding to the elements on top of the notch at points 1 and 2 on the model curve.

utilized this value is around  $l_{cs} \approx 0.6$  mm. Therefore, such plastic strain can be translated into a crack opening of around  $w \approx 0.9-1.2$  mm. On the direct tensile constitutive law adopted as the input for the model, which is obtained from inverse analysis of the notched beam results, such crack opening is on the verge of the softening response of the material, shown in Fig. 5.17(d) and highlighted with an arrow numbered as “1”. After the initiation of this softening response, at point “2” on the numerical response curve, elements on the left of the notch reach to crack opening values of around  $w = 0.16$  mm, which is the starting point for the post-crack hardening response of the material. This leads to restoration of stresses and an increase in the nominal stress values which is not realistic. Hence, modeling of such material that exhibits an extended stretch of hardening after some crack opening is reached, needs to be done with caution and the dissipated energy at the computation points needs to be checked.

## 5.6 NLFEM of plates

For the SFRC plates, the three configurations of S1, S2, and S3 are modeled. For the RC and R/FRC plates only the S2 series are subjected to modeling. The plates are modeled with either eight node linear brick elements with reduced integration (C3D8R), or with quadratic bricks with full integration scheme (C3D20). A uniform element size of 25 mm is adopted through out the whole plates other than one case which will be discussed. Artificial strain energy is compared to total strain energy to make sure that hourglassing was not affecting the results when linear bricks with reduced integration are adopted.

For the rebars an elastic-linear hardening behaviour complying with the tensile test on the rebars are implemented. They are modeled as embedded beam elements with cubic shape function. The tensile stress-crack opening relationship for plain concrete is defined according to the findings of Cornelissen et al. [54]. They found out that the stress-crack opening for a given concrete is a unique behavior which does not depend on stress strain history. The smoothness of this relationship suits its application in numerical modelling. According to these authors:

$$\sigma/f_t = f(\delta) - \delta/\delta_0 f(\delta = \delta_0) \quad (5.7a)$$

$$f(\delta) = (1 + (C_1\delta/\delta_0)^3 \exp(-C_2\delta/\delta_0)) \quad (5.7b)$$

The values of  $\delta_0$ ,  $C_1$ , and  $C_2$  are found to be respectively 160  $\mu\text{m}$ , 3, and 6.93. The relationship is shown in Fig. 5.18(a). Stress-strain relationship in compression is derived from MC2010, Eq.5.8, and depicted in Fig. 5.18(b).

$$\frac{\sigma_c}{f_{cm}} = - \left( \frac{k.\eta - \eta^2}{1 + (k - 2).\eta} \right) \quad (5.8)$$

where

$$\eta = \epsilon_c/\epsilon_{c1};$$

$$k = E_{ci}/E_{c1}$$

with  $\epsilon_{c1}$  being the strain at maximum compressive stress,  $E_{c1}$  being the secant modulus from the origin to the peak compressive stress, and  $k$  is the plasticity number.

### 5.6.1 RC plates

The RC plates of the S2 series are modeled with eight node brick elements with reduced integration (C3D8R). Fig. 5.19 displays the result of the model for load-deflection response and load-COD for the instruments shown on the figure

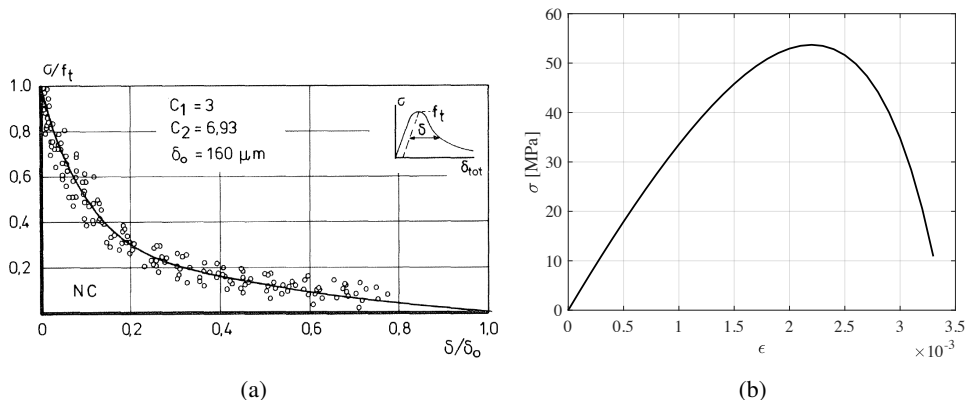


Figure 5.18: (a) Stress-Crack opening relation according to the model of Cornelissen et al. [54] and (b) Compressive stress-strain relationship adopted for modeling of the plates according to Eq.5.8.

inlet. The cracking point is not captured by the models which is a common observation when shrinkage effects are not taken into account in the model.

### 5.6.2 SFRC plates

There is some distinction between modeling the SFRC plates of the S1 and S2 series with those of the S3 series, therefore the results are given and explained separately. For the S1 and S2 configurations, SFRC plates are modeled with linear brick elements with reduced integration (C3D8R). The results of the models obtained for the SFRC plates are shown in Fig. 5.20. The black curves display the experimental results, the red curve is the model in which the tensile

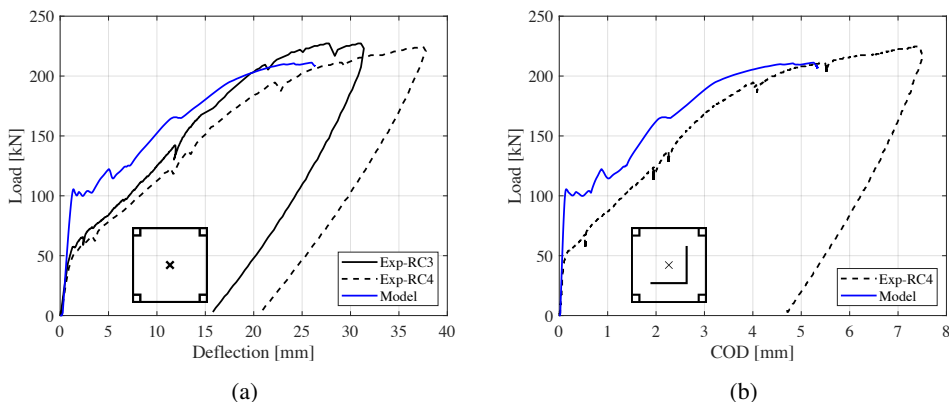


Figure 5.19: Results of the NLFEM for the (a) load-deflection response and (b) load-COD behaviour of the RC plates of the S2 series.



law is give as  $\sigma - w$  and the ragularization is implemented by the software; i.e. taking an internal length equal to the diagonal of one element for C3D8R, and the blue curve regards a model in which a characteristic length equal to the width of four elements ( $l_{cs}=100$  mm) is adopted and a scaled  $\sigma - \epsilon$  relationship is given to the software. It is evident that the numerical internal length can substantially alter the result of the numerical model.

To investigate the rationality of choosing an internal length which encompasses more than the dimension of a single row of elements, Fig. 5.21 highlights a point on the load-deflection curve of the models for SFRC plates of the S1 and S2 series, and depicts the contour of the maximum principal strain (PE max. Principal) mapped on the crack pattern of the corresponding plates. It is evident that each crack is represented by a band of elements consisting of a few elements. It should be pointed out that this band is not constant and at different stages of loading shrinks and expands to some extent. However, almost throughout the entire analysis, the crack band consists of few elements. In the present analysis a width consisting of four elements, 100 mm, is taken as the band of the numerical crack.

Fig. 5.22 illustrates the result of the numerical model on crack opening of the same SFRC plates. The COD values regard the longer instruments whose position is illustrated on the inlet of the figures. In Fig. 5.22(a) the model gives the same result in both directions, therefore, only one line represents the measurement for both instruments, while for the SFRC plates in S2 series, there is some difference between the displacement in the two directions. The solid and dashed blue curves correspond to linetype of the instruments shown on the

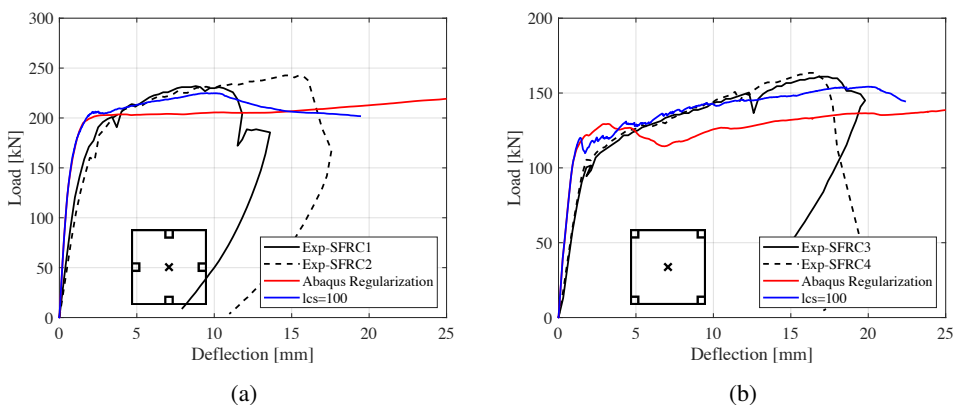


Figure 5.20: Comparison of NLFEM results with the experimental load-deflection curves of SFRC plates, and the effect of the regularization for (a) S1 and (b) S2 plates.

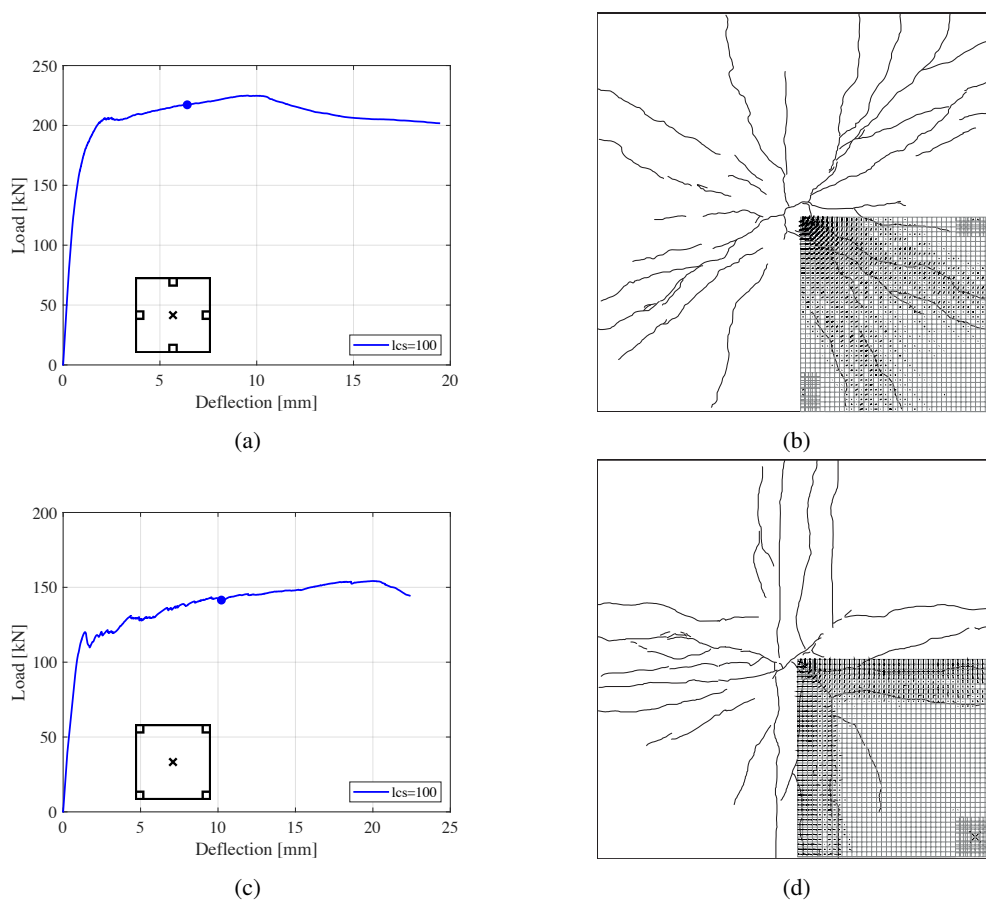


Figure 5.21: Extent of numerical crack width shown by mapping maximum principal plastic strain on the crack patterns of the plates for a point shown on the load deflection behaviour of the S1 SFRC plates in (a) and (b), for S2 SFRC plate in (c) and (d).

inlet. Although the maximum crack opening is not exactly captured with the models, still a valid estimation for the ultimate crack opening can be made.

For the SFRC plates from the S3 series, where the load is applied on the edge of the plates, it is likely that two different factors affect the results. One is that the damage due to thermal stresses is in any case larger on the crust of the plates, and given that in this configuration load is applied on the edge, this effect can influence the results. Moreover, as the zone involved in the failure of the plates is more confined as opposed to the S1 and S2 series, local heterogeneity of the FRC can play a major role and a deterministic model with the average material properties may overestimate the real capacity of the plate. With this in mind, the SFRC5 and SFRC6 plates are modeled and the load-deflection results of these plates are depicted in Fig. 5.23.

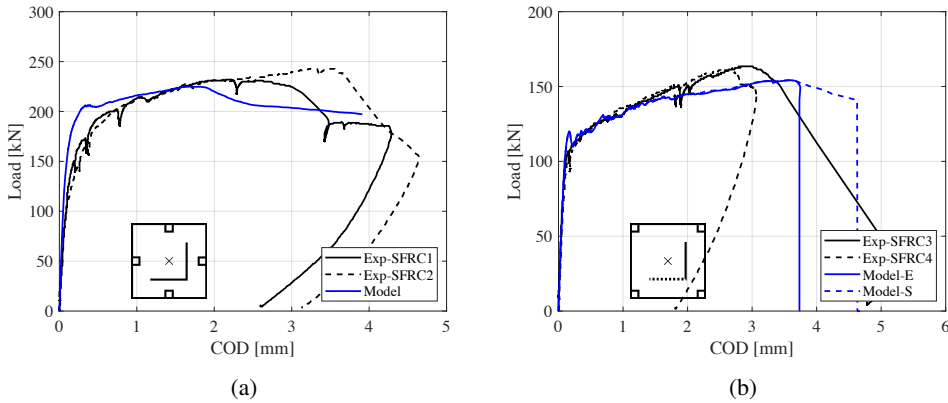


Figure 5.22: Comparison of NLFEM results with the experimental load-COD response of the SFRC plates in (a) S1 and (b) S2 series.

As the failure zone is more limited, the tensile law is introduced as  $\sigma - w$ . The plates are first modeled with the linear bricks with reduced integration (C3D8R) and a dimension of 25 mm, similar to what was done for the SFRC plates from S1 and S2 series. The corresponding curve is shown with a solid blue line. The prediction overestimates the bearing capacity of the plates and at the end of the behaviour some spurious energy seem to affect the results with an unrealistic hardening in the behaviour. Therefore, the model is repeated with C3D20 elements with two elements sizes of 50 mm and 75

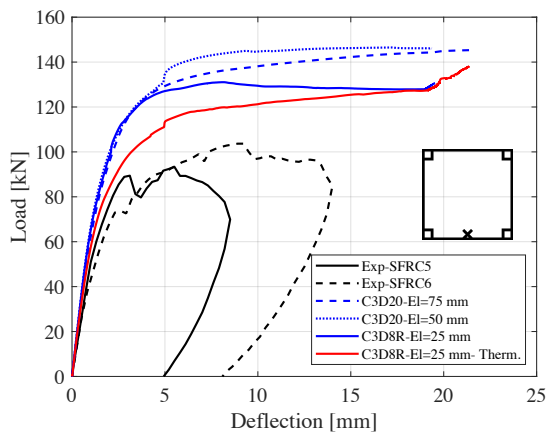


Figure 5.23: Comparison of the experimental load-deflection response for the SFRC plates of the S3 series with different element types and in one case, with introduction of a realistic temperature profile.

mm, shown respectively with the dotted and dashed blue lines. Both curves fall above the the one with 25 mm element size. In an attempt to introduce thermal stresses, an exponential temperature profile with a 15°C temperature difference between the core of the plate and its surface is given as a predefined field. This is done on the model with C3D8R elements with 25 mm element size (C3D8-EI 25 mm-Therm. curve). Although the curve gets closer to the experimental measurements, specially in terms of the initial slope, still its an overestimation to the experimentally measured values.

The results depicted here may show how the modeling of FRC elements may face challenges for cases where the very local properties of the material which is very much affected by the heterogeneity may dominate the problem. On the contrary was modeling of the SFRC plates of the S1 and S2 series in which the only challenge was the choice of the  $l_{cs}$  for the softening phase of the material. In those specimens, the average tensile properties of the SFRC gave very reliable outcome.

### 5.6.3 R/FRC plates

Modeling of the R/FRC plates with the C3D8R elements and a 25 mm of size faced convergence problems. Therefore, 50 mm, C3D20 elements were adopted and the tensile constitutive law of the SFRC was given as  $\sigma - w$  relationship. Fig. 5.24 illustrates the modeling results for the R/FRC plates of the S2 series for the load-deflection and load-COD responses. Still convergence was not reached easily and very small increments were made. Finally it was decided to stop the model. The predicted curve overestimates the bearing capacity of the plates with some 10%. The first cracking is again not captured, similar to the model for the RC plates. When concrete shrinks, the presence of rebars may act as an internal restrain the may promote cracking. This can be the reason for the overestimation of the first cracking point.

### 5.6.4 R/FRC-Alt plates

The plates of this type of reinforcement solution are modeled with C3D8R elements of 25 mm side. Fig. 5.25 shows the results of the model for the R/FRC-Alt plates. Interestingly, the experimental results are captured by the model almost exactly. Unlike the models for the RC and R/FRC plates, here, the smooth nonlinear stiffness decay is properly captured. This is in line with the assumption stated earlier, that the presence of rebar may accentuate the shrinkage effect. The R/FRC-Alt plates do not have rebars below the loading point, hence, this effect may be diminished. The obtained results show the strength of NLFEM for prediction of load bearing capacity of the

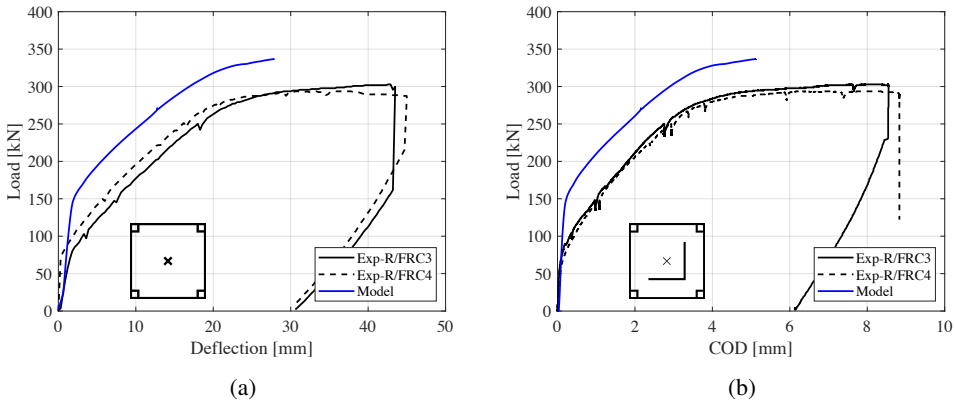


Figure 5.24: Comparison of NLFEM results with the experimental curves of (a) load-deflection and (b) load-COD, for the R/FRC plates.

reinforcement solutions for which the application of limit analysis may be questionable.

### 5.6.5 Comparison of failure patterns

Eventually, in order to illustrate the differences in the numerical crack widths among the different models, Fig. 5.26 depicts the distribution of maximum principal plastic strain for the plates specimens of the S2 series for one-quarter of the plate. While the model for the RC plates cast with plain concrete successfully show the multiple cracking with a distance of 150-200 mm, for the plates in which the SFRC material was cast, localization does not occur and

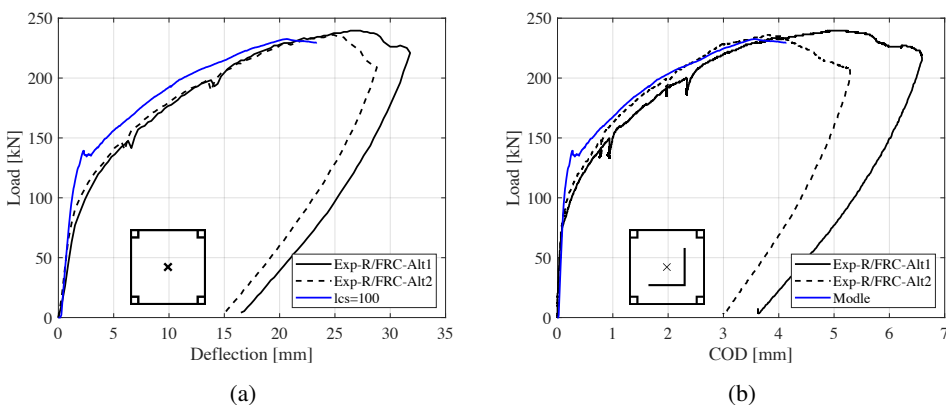


Figure 5.25: Comparison of NLFEM results with the experimental curves of (a) load-deflection and (b) load-COD, for the R/FRC-Alt plates.

rather than single cracks, regions of dissipation is observed. When rebars are present, the consequence of such difference may not be significant, however, in the absence of rebars, such behaviour requires more attention to the choice of the numerical characteristic length.

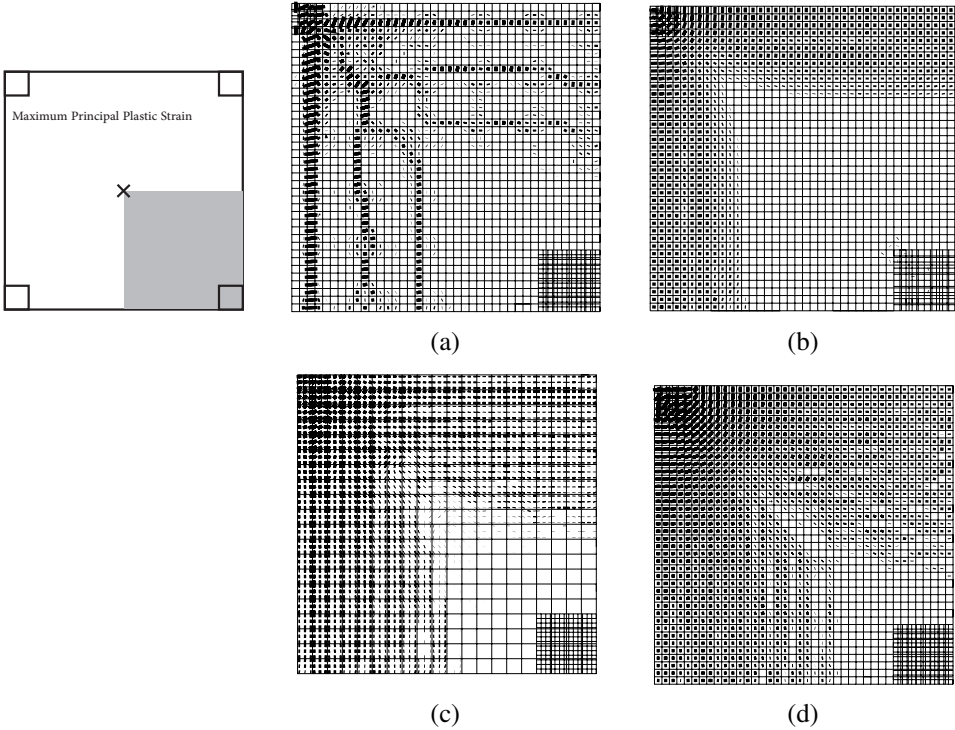


Figure 5.26: Distribution of maximum principal plastic strain for the (a) RC, (b) SFRC, (c) R/FRC, and (d) R-FRC-Alt plates of the S2 configuration.

# CHAPTER 6

---

## SHALLOW BEAMS

---

### 6.1 Introduction

In this chapter the results of six shallow beams that were tested under a four-point bending setup are presented. The beams are 1500 mm long and are tested on a 1350 mm span, with a cross section of 350×150 mm. Three specimens are reinforced with only 35 kg/m<sup>3</sup> of 4D steel fibers (B-FRC) and the other three have two reinforcing bars of  $\phi$ 12 in addition to 35 kg/m<sup>3</sup> fibers (B-R/FRC). During the tests, deflection and crack openings are recorded.

### 6.2 Experimental results

In the outset it is pointed out that mistakenly, the rotation of the loading head was blocked during the test on B-FRC2 beam which makes it hard to compare the results obtained from this specimen with other companion beams. Due to this experimental error, it is likely that during the test one of the loading knives may have lost its contact with the specimen which changes the loading condition. Nevertheless the results of this specimen is displayed through out this chapter. Before presenting the experimental measurements on deflection and crack opening of the beams, the crack patterns at the bottom of the specimens are depicted in Fig. 6.1. These cracks are detected and marked

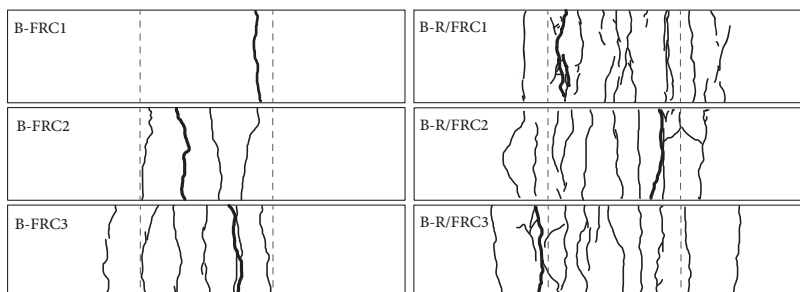


Figure 6.1: Crack pattern of the tested beams. The localized crack is shown with a thick line, and the dashed lines show the length of the gauge by which the COD is measured.

manually after each test. The localized crack is shown with a thick line and the length of the gauge over which COD is measured is shown with dashed lines. Figures on the left are related to the B-FRC beams and those on right regard the B-R/FRC beams. As expected, much more diffused cracks propagated on the B-R/FRC beams with a more or less similar pattern. Noteworthy is the difference between B-FRC1 and B-FRC3 beams. Despite of multiple cracks for the B-FRC3 beam, only a single crack appeared on B-FRC1 beam. Such considerable difference leads to very distinctive response for the two specimens.

Fig. 6.2 shows the load-deflection curves of the six tested beams. As expected, looking at Fig. 6.2(a), the B-FRC1 and B-FRC3 beams exhibit a strikingly different response. Load-deflection response of B-FRC1 beam is characterized by a sharp cracking point followed by a steep fall, a hardening behavior, and eventually softening, while B-FRC3 shows a hardening behavior up to maximum load. Unlike the B-FRC beams, the response of the three B-R/FRC beams is almost exactly repeated. Attention is drawn to the loss of some load at a deflection of around 12.5 mm in all three B-R/FRC specimens which sets a limit to their ductility. Some [208] relate the occurrence of localization in only one crack for the FRC element, to the scatter of fibre content along the length of the specimen. The repetition of localization at almost the same COD for the three B-R/FRC beams in this study, cast doubts on this hypothesis. If this was due to the randomness in the content of fibres at different cross sections, more scatter in these results should have been obtained.

The results of load-COD of the tested beams are demonstrated in Fig. 6.3. The COD values are averaged between the three instruments that are positioned at the bottom on the two sides and at the center line of the beams. Except for B-FRC2 beam in which an improper boundary condition for the loading head was adopted, for the other five beams, the reading of the three instruments



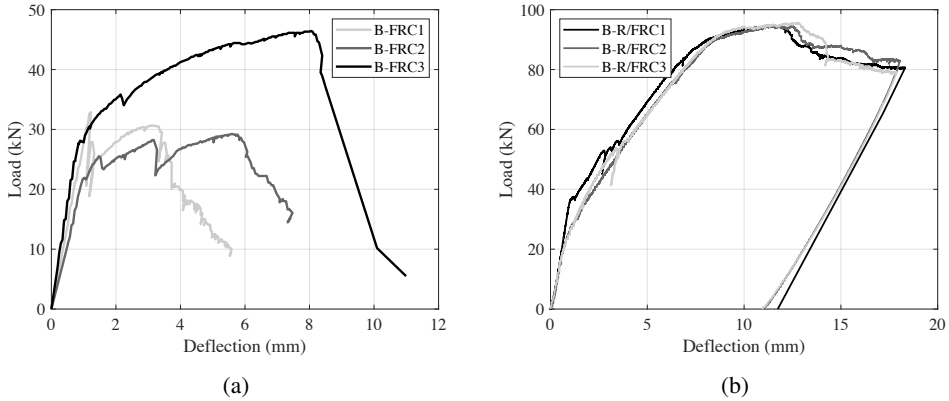


Figure 6.2: Load-deflection curves of the (a) B-FRC and (b) B-R/FRC beams.

recording COD are the same for each specimen (These results are shown in Appendix 9.1). For B-R/FRC3 beam the localized crack fell out of the gauge, therefore, smaller crack openings are recorded for this specimen when compared to the two other companion beams, Fig. 6.3(b).

The shape of the load-COD curve of B-FRC1 beam whose response is characterized by a single crack is very similar to that of the notched beams from the same material batch, which after cracking, show a hardening behavior up to a CMOD of around 1.4 mm (Fig. 4.1). As only one crack propagated for the B-FRC1 beam, its nominal stress-COD can be compared to the nominal stress-CMOD of the notched beams that were tested closer in age to these beams. The nominal stress for the beams is obtained with the assumption of linear elastic distribution of stresses along the cross section. The B-FRC1 beam

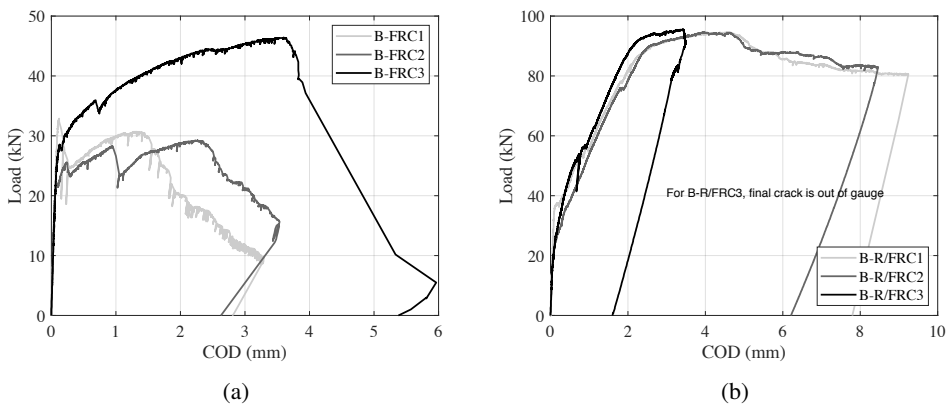


Figure 6.3: Load-COD curves of the (a) B-FRC and (b) B-R/FRC beams.

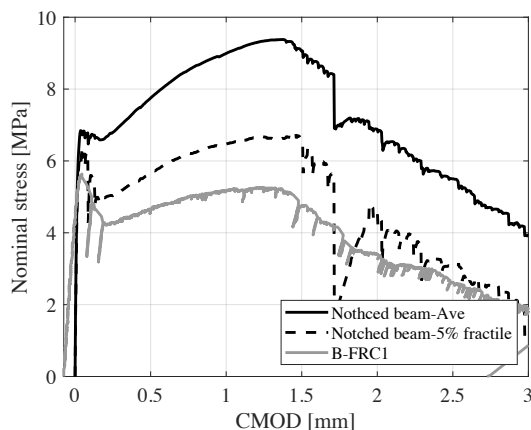


Figure 6.4: Comparison of the nominal stress-CMOD of the B-FRC1 shallow beam with the average and 5% fractile curve of the nominal stress-CMOD of the tested notched beams. The elastic part of the tensile deformation for the shallow beam is removed from the readings, therefore, the curve corresponding to this specimen starts from negative values.

was tested at 225 days of age, and the results of the notched beams tested at 220 days are compared with it. Fig. 6.4 shows the average and the characteristic curves of the four notched specimens tested at 220 days and the nominal stress-COD for the B-FRC1 beam. For B-FRC1, the elastic deformation is removed from the reading of the 500 mm gauge assuming that the bottom fiber was on the verge of cracking with  $\epsilon=0.00015$ , which is an overestimation of the deformation of the bottom fibres, yet its effect is marginal on the comparison made. The curve for the shallow beam falls even below the characteristic curve of the three-point bending results. The number of tests carried out are not enough to make solid conclusions, however, cautiously, it can underline the shortcoming of application of FRC in structures that do not allow for a proper redistribution of stresses.

For the B-R/FRC beams, crack opening and spacing is very much controlled by the presence of rebars and the transfer length. As such, a very similar behavior is observed for the three specimens both in terms of the overall structural response and also in terms of the cracking behavior. Interestingly, the localized crack in B-R/FRC3 beam being out of the gauge length, may give some indication of the opening of this crack in juxtaposition to the other two B-R/FRC beams. From the similarity between the load-deflection response of the three B-R/FRC beams and the closeness of the load-COD behavior of the B-R/FRC1 and B-R/FRC2, it can reasonably be concluded that the load-COD of B-R/FRC3 would have been similar to the two companion beams had the localized crack been properly captured by the LVDTs. The difference between

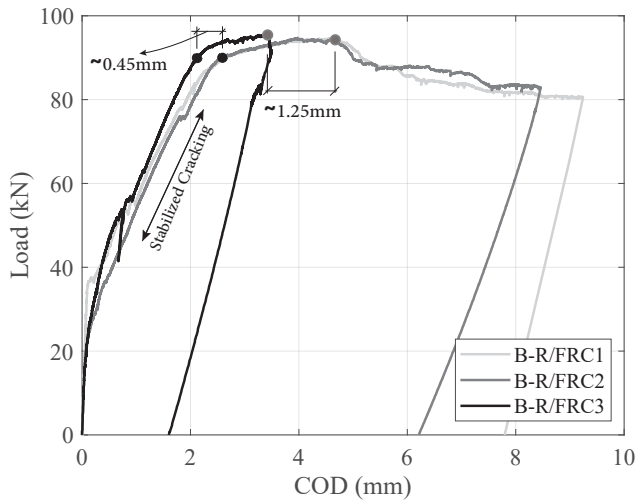


Figure 6.5: Comparison of the load-COD curves of the B-R/FRC beams taking into account that the localized crack was out of the gauge length for the B-R/FRC3 beam.

the maximum COD for B-R/FRC1 and B-R/FRC2 beams and the B-R/FRC3 beam before the initiation of load loss is 1.25 mm. This is shown in Fig. 6.5. According to Fig. 6.1, this value is the sum of openings of four cracks out of the gauge for B-R/FRC3 beam. However, it is very likely that the major portion of this opening is related to the crack that eventually becomes the localized crack. So the opening of the localized crack at the instant of softening might be close to 1 mm, which is considerably different from the provisioned value of  $w_u = 2.5$  mm for ULS condition in different standards.

### 6.3 Estimation of load bearing capacity

Estimation of the load bearing capacity is carried out benefiting from the experimental observations. The B-FRC2 beam is not taken into account due to the experimental error related to the rotation of the loading head.

A very important aspect in prediction of load bearing capacity of the B-FRC beams lies in the cracking behavior of these specimens. The propagation of only one crack in the B-FRC1 beam led to a response that was examined in Fig. 6.4. Clearly, using the average residual tensile strength values derived from the black solid curve in this figure will result in a considerable overestimation of the bearing capacity of this specimen. Even using the 5% fractile values will lead to predictions which would be larger than the bearing capacity of this shallow beam. This highlights the importance of multiple

cracking in FRC structural elements and the fact that utilization of average values of post-peak tensile properties is very much dependent on the cracking response of the element. For a heterogeneous material like FRC, a single crack can propagate at a cross section, whose strength is much smaller than the average values and in such a circumstance, the structural response of this element can not be predicted reliably. Unlike for B-FRC1, average residual strength properties should be able to explain the behaviour of B-FRC3 beam which goes through multiple cracking.

For the B-R/FRC beams, it was shown that at the maximum load, the ultimate crack opening is much smaller than the value commonly adopted in the codes. This is similar to the case of the plates that was discussed in Section 4.3.5.2. As it was done for the plates (Fig. 4.12), the overall reading of the LVDT measuring COD at the bottom of the beams is divided by the number of cracks, to have an average estimate of the opening of a single crack ( $CMOD_{Ave}$ ) for the beams. Fig. 6.6 demonstrates these results. It is observed that at maximum load, the average opening of a single crack for B-FRC3 plate is around 0.7 mm. For B-R/FRC plates this value is around 0.9 mm. This is also in accordance with the rough observation that was made for B-R/FRC3 plate in which the localized crack was out of the gauge length. For this specimens it was concluded that  $w_u < 1.25$  mm and most likely close to 1 mm which is close to the 0.9 mm obtained here.

The multi-layer approach that was adopted earlier to estimate the load bearing capacity of the plates is again adopted. Once the tensile constitutive

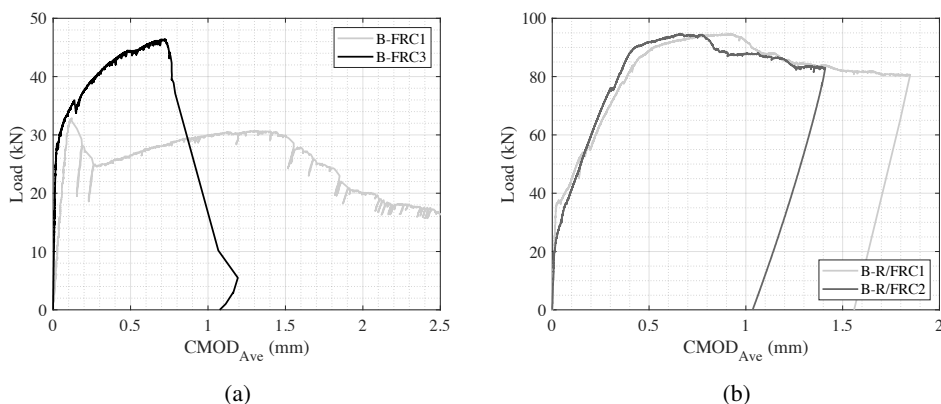


Figure 6.6: The load- $CMOD_{Ave}$  curve for the (a) B-FRC and (b) B-R/FRC specimens.  $CMOD_{Ave}$  is obtained by dividing the overall reading of the gauge by the number of cracks as shown in Fig. 6.1.

law as per EC2-annex L is utilized and once the tensile law is obtained through back analysis of the results of the three-point bending test considering a  $w_u=0.7$  mm for the B-FRC3 beam, and  $w_u=0.9$  mm for the B-R/FRC beams. The tensile laws are given in Fig. 6.7. The general shape of the constitutive law adopted in the inverse analysis is shown in the figure inset. For the B-R/FRC beams, when the tensile constitutive law of the EC2-annex L is implemented, the characteristic length is taken as the calculated average crack spacing for the R/FRC elements,  $l_{cs} = S_{r,m,cal}$ . According to EC2 1992:2020, when spacing of rebars are larger than  $10\phi$ , which is the case here, the average crack spacing for RC elements is  $S_{r,m,cal} = 1.3(h - x)$ . It is assumed that when fibres are introduced, a reduction factor of  $(1 - f_{fts,ef}/f_{ctm})$  is multiplied to this expression to take into account the effect of stress transmission at the cracks due to presence of fibres. Hence,  $S_{r,m,cal} = 1.3(h - x)(1 - f_{fts,ef}/f_{ctm}) = 89$  mm. However, when the realistic conditions with the  $w_u = 0.9$  mm is taken into account, the experimentally obtained average crack spacing of 86 mm is considered. It is worth mentioning that the calculated and experimental average crack spacing are almost equal. For the B-FRC3 beam, the characteristic length is always taken to be equal to the depth of the beams.  $h = 150$  mm. The topic of crack spacing in beams and plates will be thoroughly discussed in Chapter 8.

The results related to the computation of the bearing capacity of the beams are given in Table 6.1. When the tensile constitutive law given by the EC2 is applied, for both B-FRC and B-R/FRC beams safe results are obtained. The predicted load bearing capacity for the B-RFC3 beam is overly safe. For both cases, modification of the tensile constitutive law with an assumption of a

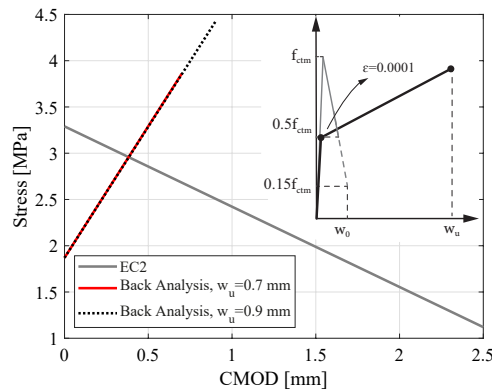


Figure 6.7: The tensile constitutive laws adopted for prediction of the load bearing capacity of the beams. Once the tensile law given in EC2 is selected and once the tensile law is found through back analysis of the stress-CMOD results with an assumption of  $w_u=0.7$  mm for B-FRC beam and  $w_u=0.9$ mm for B-R/FRC beams.

Table 6.1: Computation of the load bearing capacity of the beams and the safety factor  $\gamma_m = P_{Exp}/P_m$ .

Specimen	EC2			$w_u=0.7$ [mm] ( $l_{cs}=h$ )		$w_u=0.9$ [mm] ( $l_{cs} = S_{r,m,Exp} = 86mm$ )	
	$P_{Exp}$ [kN]	$P_m$ [kN]	$\gamma_m$	$P_m$ [kN]	$\gamma_m$	$P_m$ [kN]	$\gamma_m$
B-FRC3	46	29.00 ( $l_{cs} = h$ )	1.59	39.70	1.16		
B-R/FRC	95	82.40 ( $l_{cs} = 1.3(h - x)(1 - f_{fts,ef}/f_{ctm})$ )	1.15			94.00	1.01

narrower ultimate crack opening which is compatible with the experimental evidence, leads to better predictions. For the B-R/FRC beams the bearing capacity is almost exactly predicted, and for the B-FRC3 beam a 16% of safety margin is retained. It is worthwhile to mention that in this study the effect of possible settlement of fibres was not considered. It is likely that the settlement of fibres in the bottom layer of the beams would impart an enhanced residual tensile strength which is an effect that is overlooked here, while it may have significant influence depending on the fresh state properties of the SFRC material [173].

---

***PART B: STRUCTURAL PLATES VS.  
NOTCHED BEAM SPECIMENS; THE  $\kappa$   
FACTOR***

---

### **7.1 Introduction and background**

In the present chapter, the results regarding the second phase of the experimental campaign are presented. In an unprecedented work, twelve nominally identical SFRC plates of  $2000 \times 2000 \times 150$  mm were tested under a concentrated load. The goal is to study the effect of volume involved in the failure process of SFRC structures and their stress redistribution capacity, on the scatter of structural response of these elements. For each of the plates a companion notched beam of  $150 \times 150 \times 600$  mm was tested in a three-point bending test as well. The results of one of the specimens tested in three-point bending scheme was not saved, hence, the results of eleven notched beams are presented.

Inclusion of large fibres in a concrete mixture makes it more heterogeneous compared to plain concrete. While for plain concrete aggregates are the main source of heterogeneity, long fibres of high aspect ratio that can be oriented in any direction in space render a rather peculiar aspect to FRC. Apart from the

innate heterogeneity of FRC that comes from conglomeration of ingredients of different sizes and shapes, placement and casting modality can further affect the properties of a FRC material by favorably or unfavorably facilitating a preferential direction for the orientation of fibres.

Acquisition of tensile properties of a FRC material from a bending test on a notched specimen, as it is very often done, suffers from wide dispersion of results. Coefficients of variation ranging between 15%-20% for laboratory cast specimens and higher values, e.g. 30%, for specimens cut from cast in-place elements are common. In such test, failure occurs at a predefined cross section at which, the number, position and orientation of fibres are virtually random (disregarding the fact that flowing along the formwork, fibres may tend to orient in the direction of flow). In fact, properties of a FRC in a 600 mm long beam with a relatively small 150×150 mm cross section may be considerably different from one section to another. A large enough specimen consisting of many representative volumes allowing the formation of large crack areas and large failure volumes makes a characterization test impractical and unfeasible.

Dispersion of results of a three-point bending test is not limited to FRC. It was in the 1980s, and within the activities of the *Rilem Technical Committee 50, Fracture Mechanics of Concrete (TC50-FMC)*, that applicability and suitability of a three-point bending test on a notched beam for  $G_f$  measurement of plain concrete was studied in an extensive round robin [110]. The first issue that was brought up in the discussion of the results of the round robin was the scatter of the tests results, which on average was in the range of 10%-15%, reaching to 25% in some cases. It was indicated that the coefficient of variation of the results depends to some extent on the ratio of the size of the ligament,  $A_{lig}$ , to maximum aggregate size  $d_{max}$  (Fig. 7.1). In another publication of the Rilem Technical Committee by Hillerborg [110] from the same year, he demonstrates the significance of  $G_f$  on the structural resistance of structures, which answers also the question of required accuracy of the testing method for its measurement. With reference to Fig. 7.2, for the notation he adopts,  $d$  being the beam depth,  $l_{cs} = EG_f/f_t^2$ , and for the tangent of a small part of the curve he writes:

$$\ln \frac{f}{f_t} = A - B \ln \frac{d}{l_{ch}} \quad (7.1a)$$

$$\ln f = A \ln d + B \ln E + B \ln G_f + (1 - 2B) \ln f_t \quad (7.1b)$$

$$\frac{df}{f} = -B \frac{dd}{d} + B \frac{dE}{E} + B \frac{dG_f}{G_f} + (1 - 2B) \frac{df_t}{f_t} \quad (7.1c)$$



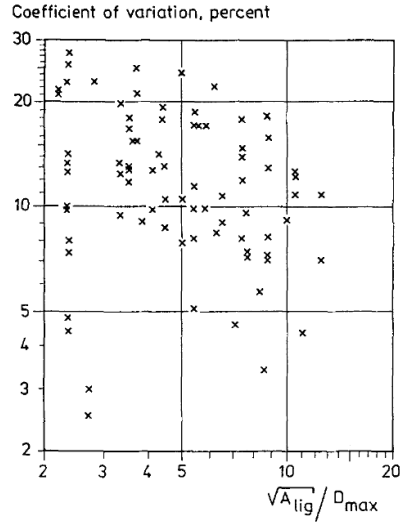


Figure 7.1: Variation of the coefficient of variation of the measured fracture energy,  $G_f$  with the ratio of ligament size,  $A_{lig}$ , to the maximum aggregate size,  $D_{max}$ .

From Eq.7.1(c) the sensitivity of structural strength,  $f$ , to variation of different parameters is found. Sensitivity of  $f$  to changes of  $G_f$  and  $f_t$  is respectively  $B$  and  $1 - 2B$ . From Fig. 7.2,  $B$  varies between 0.15 and 0.35 which is the sensitivity of  $f$  with reference to changes of  $G_f$ . The sensitivity w.r.t to  $f_t$  would be between 0.3 and 0.7. To give an example, Hillerborg adds that sensitivity of structural strength to the strength of reinforcing bars or concrete compressive strength may be close to 1, as opposed to a maximum of 0.35 for  $G_f$  in usual applications. As such, an acceptable standard deviation for

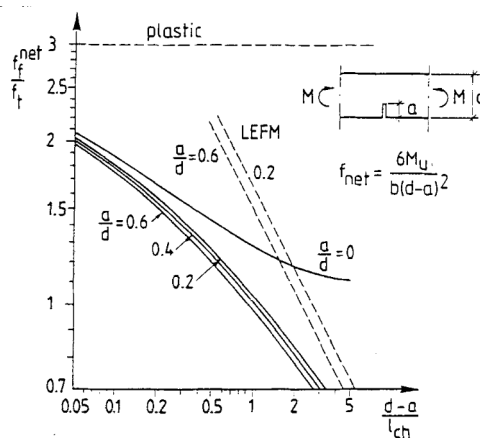


Figure 7.2: Theoretical flexural strength of notched and unnotched concrete beams [110].

determination of  $G_f$  can be about 3 times as large as in most strength tests. With this in mind, a 15% of scatter in determination of  $G_f$  may lead to a 5% change in structural resistance, which is smaller than the normal scatter in determination of concrete strength. To conclude the discussion on the substantial scatter in determination of  $G_f$  through a three-point bending test on a notched beam he writes:

“Thus it will seem that the uncertainty in the determination of  $G_f$  by means of the proposed method has no greater influence on the calculated maximum loads than the corresponding uncertainties in the determination of the compressive strength of concrete according to standardised methods. As a matter of fact the uncertainty in the determination of the tensile strength is a greater problem.”

For FRC this discussion follows a different path. Strength of FRC structures, specifically those that can accommodate a stable phase of multiple cracking, i.e. redundant slabs, significantly depends on the post-cracking behavior of the material. Here the question would be, how much does the uncertainty in determination of post-peak residual tensile strength values for FRC affect the calculated design resistance? The answer is clearly, very much! This is the starting point of two arguments. *First*, one may argue that design of a FRC structure with a material with such high dispersion in its tensile properties requires larger safety factors to guarantee the same target reliability index as of RC elements. However, based on limited experimental evidence, there is consensus that structures of large volume demonstrate a repeatable behavior and do not suffer from the substantial dispersion obtained for the material. In fact, it has been shown that the behavior of a FRC structure in which the bulk of the material is involved in failure can be explained with acceptable accuracy by the average tensile properties derived from the highly dispersed results of a flexural test (Chapter 4 and 6). This has been highlighted lately, in the work of Aidarov et al. [3] in which they adopted the design value of residual strength parameters of a SFRC material to compute the design resistance of a full-scale flat slab. The computed uniformly distributed load that they obtained with design properties of the material was less than half of the design load. This was due to the fact that the coefficient of variation of post-peak tensile strength parameters obtained from a three-point bending test in their study was more than 25%. Yet, with the average properties of the SFRC, they were able to predict the load bearing capacity of the flat slabs with good accuracy through a limit state analysis.

The *second* viewpoint may suggest that the high scatter in the results of a three-point bending test, and given the high dependency of structural resistance on residual tensile parameters, makes such test unfit for FRC. There

are already other testing methods for FRC, explained in Section 2.6.1, on specimens of much larger size, which clearly, show much less scatter in the results. The limitation is that even a so-called small beam tested in flexure, is large enough to be handled by one person, and adoption of any larger specimen only hinders testing and application of FRC. Besides, a three-point bending test on a notched specimen is a relatively common method with long history of successful application.

The remedy to this problem lies in recognizing that while the average tensile parameters obtained from a three-point bending test can reliably describe the structural response of a FRC structure capable of redistributing stresses, the large dispersion of the  $f_R$  values in a test on a small specimen is not a definitive attribute of such parameter, and if for instance, a panel test would be carried out instead, a scatter would be obtained that could be much closer to what is expected from a real structure. In practice, the ramification of large scatter of tensile parameters is that the characteristic values of tensile parameters,  $f_{R,k}$ , become overly small and fail to represent the characteristic response of the real structure. This is why in standards and guidelines methods are given to compensate for the large gap between the measured  $f_{R,k}$  values based on a flexural test and a characteristic value that would represent the characteristic response of a structure. It should indeed be emphasized, that this argument can be accommodated for structures that possess a high capacity in redistribution of stresses, and the behaviour of those structural elements that is governed by the propagation of small crack areas might be very affected by the heterogeneity of FRC.

In this chapter, a sufficiently large sample of identical structural elements reinforced only with steel fibres are tested. This enables us to draw meaningful conclusions on how the difference between the scatter of results of a SFRC in material testing and the scatter of the structural strength of a redundant plate made of the same material can affect the design of these elements.

### 7.1.1 Reliability analysis of structures

A structure shall remain fit for the use which is required and should sustain all actions and influences that may occur during its execution and use [113]. In the context of EC 1990 [188] the definition of reliability that passes through the failure probability,  $p_f$ , and the reliability index  $\beta$ , includes four elements of, performance requirement, the required service life  $T$ , assessment of probability of failure, and condition of use. According to the reliability classes defined based on consequence of failure (RC1,RC2,RC3), and for ultimate, fatigue and serviceability limit states, different reliability indices are given for 1 and 50

year reference periods. For a 1 year and 50 years period for a normal structure, the target reliability index for ULS is given as 4.7 and 3.8 respectively. Given that the effect of loads and resistance are dealt with separately, a sensitivity factor is introduced,  $\alpha_R=0.8$  (obtained from a first or second order reliability method). The outcome of  $(\alpha_R = 0.8) \times (\beta = 3.8) = 3.04$  which corresponds to a failure probability of 0.1% for a 50 year period, which is the basis for design.

In the partial safety factor commonly adopted for design of structures, effect of load and resistance are dealt with in a rather inconsistent manner. The analysis of the structure is carried out assuming linear elastic behavior of the materials, while sectional resistance is computed based on material nonlinear response, cracking of concrete and yielding of rebars. Indeed, such method provides no information concerning the overall structural safety. The increasing popularity of nonlinear finite element method and its application by engineers, opens up new possibilities in accounting for the overall structural behavior which gives information about redundancy, robustness and structural safety and leads to more economical solutions by exploiting reserves [44].

In 1995 König et al. [123] introduced a global safety factor for hyperstatic structures taking into account only the overall structural behavior uncertainty considering that the material scatter and uncertainties regarding the actions are known. This safety factor was expressed as:

$$\gamma_G G + \gamma_Q Q \leq \frac{F_m}{\gamma_{Gl}} \quad (7.2)$$

Where the left hand side contains the external actions and the corresponding partial safety factors, while  $F_m$  shows the load bearing capacity obtained in the non-linear analysis carried out with realistic material properties of  $f_{cm}$  and  $f_{ym}$  for concrete and reinforcing steel.

Cervenka [44] discusses the following reliability formats within a global perspective based on non-linear analysis:

- Full probabilistic analysis
- E-COV method; estimation of coefficient of variation
- EC2 1992-2
- Partial Safety Factor (PSF)

**Full probabilistic method** is based on a non-linear model that defines the resistance function  $r(\mathbf{r})$  with input variables (material properties, dimensions,

boundary conditions, etc.) following a random distribution. The randomization can be introduced either in different models, keeping the inputs constant for each sample and changing them between different models, or through creation of *random fields* within a single model. The random parameters can be generated by a Latin Hypercube sampling method and the determination of the design resistance is based on a reliability index of  $\beta$ . Pukl et al. [159] point out the appropriateness of a full probabilistic approach for reliability, safety and performance analysis of FRC structures. To this procedure a model uncertainty factor  $\gamma_{Rd}$  can also be added to give the global design resistance:

$$R_d = \frac{1}{\gamma_{Rd}} R(\alpha\beta) \quad (7.3)$$

**ECOV** method, estimates the coefficient of variation of structural resistance based on two non-linear models, one with the average material properties and one with the characteristic material properties. Thence:

$$V_R = \frac{1}{1.65} \ln\left(\frac{R_m}{R_k}\right) \quad (7.4)$$

where  $R_m$  and  $R_k$  are the mean and characteristic value of structural resistance obtained from NLFEM. Having found the coefficient of variation of structural resistance, the required safety factor, and the design resistance is found:

$$\gamma_R = \exp(\alpha_R \beta V_R) \quad (7.5a)$$

$$R_d = \frac{R_m}{\gamma_R \gamma_{Rd}} \quad (7.5b)$$

where  $\alpha_R$  is the sensitivity factor [116],  $\gamma_R$  is the global resistance factor, and  $\gamma_{Rd}$  is the model uncertainty that for a well validated numerical model may be assumed as 1.06, or as 1.1 when higher uncertainties prevail.

**EC 1992-2** introduces a method for a global reliability check based on non-linear analysis. In this method, a model is made with rebars strength as  $f_{ym} = 1.1f_{yk}$  and concrete strength is taken as  $\tilde{f}_{cm} = 0.843f_{ck}$ . A global factor of resistance of  $\gamma_R=1.27$  gives the design resistance:

$$R_d = \frac{R(f_{ym}, \tilde{f}_{cm})}{\gamma_R} \quad (7.6)$$

**PSF** method is based on the fact that for a log-normal distribution a certain fractile of the probability distribution function can be approximately written as:

$$x_p \simeq x_m \exp(u_{norm,p} \times V) \quad (7.7)$$

where  $u_{norm,p}$  corresponds the fractile of a standardized random variable with a normal distribution, and  $V$  is the coefficient of variation of the variable  $X$ . In this manner, the safety factor,  $\gamma_c$ , for concrete is found as:

$$\gamma_c = 1.15 \frac{f_k = f_m \exp(-1.64V_m)}{f_d = f_m \exp(-\alpha\beta V_R)} \quad (7.8)$$

The coefficient of 1.15, is just to take into account that due to different curing conditions, on-site structural strength is very often smaller than lab cured specimens.  $V_m$  is variation of material properties which is assumed to be 15%, and  $V_R$  is the coefficient of variation of structural resistance, which includes the effect of material ( $V_m=15\%$ ), geometry ( $V_g=5\%$ ), and modeling ( $V_\theta=5\%$ ) uncertainties and is :

$$V_R = \sqrt{V_m^2 + V_g^2 + V_\theta^2} = 16.5\% \quad (7.9)$$

With these values  $\gamma_c=1.5$  is derived. For steel, the 1.15 coefficient is excluded and the material, geometry, and modeling uncertainty is taken as 4%, 5%, and 2.5% [176] to give  $\gamma_s=1.15$ . Of course, adopting the very small design values of material properties for modeling a structure, may lead to unrealistic results and may also alter the failure modes.

In this chapter, the PSF and E-COV methods will be implemented and their applicability for the tested SFRC plates will be examined. The factors utilized to magnify the characteristic values of FRC residual tensile strength parameters will be investigated, and a proper representation of a  $\kappa$  coefficient will be discussed.

## 7.2 Tensile characterization of the SFRC

Fig. 7.3 shows the results of the tests carried out on the notched beams in terms of nominal stress-CMOD, and Table 7.1 reports the parameters obtained from these tests. On the figure, the gray area shows the scatter of the results, the black solid line is the average of the curves, and the solid gray line is the characteristic curve for eleven specimens considering a lognormal distribution. To get the characteristic values for a log-normal distribution, the values are first transformed to a normal distribution, the coefficients for different fractiles for a normally distributed variable is applied, and they are transformed again to a

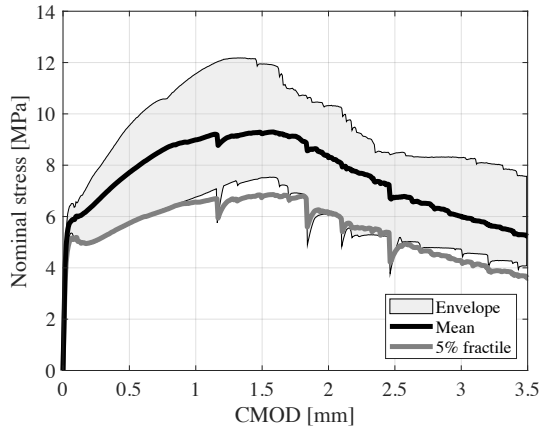


Figure 7.3: Nominal stress-CMOD curve for the eleven notched prismatic beams. The thick black and grey lines show the average and the characteristic curves.

Table 7.1: Flexural tensile strength and residual strength values and their statistical parameters.

	Average [MPa]	Characteristic [MPa]	Class	V [%]
$f_{ct,fl}$	5.7	4.9		7
$f_{R1}$	7.6	5.6	5c	15
$f_{R2}$	9.3	6.7		17
$f_{R3}$	7.7	5.4		16
$f_{R4}$	5.8	4		19

log-normal distribution. It reads :

$$f_{R,k} = \exp(f_{R,m} - k_n s) \quad (7.10a)$$

$$f_{R,m} = 1/n \sum \ln(f_{R,i}) \quad (7.10b)$$

$$s = \sqrt{1/(n-1) \sum (\ln(f_{R,i}) - f_{R,m})^2} \quad (7.10c)$$

with  $f_{R,m/k}$  being the average and characteristic residual tensile strength parameters,  $k_n$  being a coefficient from Table 7.2,  $s$  being the standard deviation of the sample of  $n$  specimens. The  $k_n$  coefficient depends on the number of specimens through:

$$k_n = t_p(1/n + 1)^{0.5} \quad (7.11)$$

with  $t_p$  being the P-fractile of the generalized Student's t-distribution for  $\nu=n-1$  degrees of freedom.

Table 7.2: Coefficients  $k_n$  for a 5% characteristic value.

coefficient	number of specimens										
	1	2	3	4	5	6	8	10	20	30	inf
$u_p(1/n + 1)^{0.5}, \sigma$ known	2,31	2,01	1,89	1,83	1,80	1,77	1,74	1,72	1,68	1,67	1,64
$t_p(1/n + 1)^{0.5}, \sigma$ unknown	–	–	3,37	2,63	2,33	2,18	2,00	1,92	1,76	1,73	1,64

### 7.3 Plate results

Fig. 7.4 shows the main experimental measurements obtained from the twelve tested plates. Fig. 7.4(a) shows the load-deflection results of each of the twelve tested plate elements with the unloading phase, Fig. 7.4(b) depicts the load-deflection response only up to the maximum load for each plate, and Fig. 7.4(c) and 7.4(d) regard the average measurements of crack opening recorded at the bottom surface of the specimens. It is emphasized that the average COD results presented relate only to the instruments that captured the localized cracks, registering increasing values all throughout the test. The tests were stopped and the specimens were unloaded upon demonstration of substantial softening behaviour. Given that the main argument of the present chapter is to view these results within a reliability analysis framework, the focus of the remainder of the chapter will be on the dispersion of results and the fractiles of the distribution which are of interest in the design of structures.

Fig. 7.5 shows the dispersion of the load-deflection curves of the twelve tested plates with the curves corresponding to certain fractiles of interest. All the curves and related fractiles are for a given value of deflection. These curves extend up to the deflection at maximum load for the plate with the lowest ductility so that at each deflection value a population of twelve samples could be considered. In this figure, the black line is the average response of the twelve plates, the gray curve is the 5% fractile of the response, or in other words, the characteristic curve of the sample of twelve plates following a lognormal distribution, and the dashed gray line is the 0.1% fractile of the experimental measurements of the load-deflection curve, which corresponds to the experimental design curve. Furthermore, the design curve corresponding to a target reliability index,  $\beta = 3.8$  for a 50 year period for a RC2 class structure, with a sensitivity factor  $\alpha_R = 0.8$ , and a coefficient of variation of 16% for structural resistance, which is the default value assumed for concrete structures and explained in Eq.  $\text{refeq:Vr}$ , is given with a dotted blue line.

The maximum load on the average, 5% fractile, and 0.1% fractile experimental response curves are respectively, 127.6 kN, 113.5 kN, and 97.5



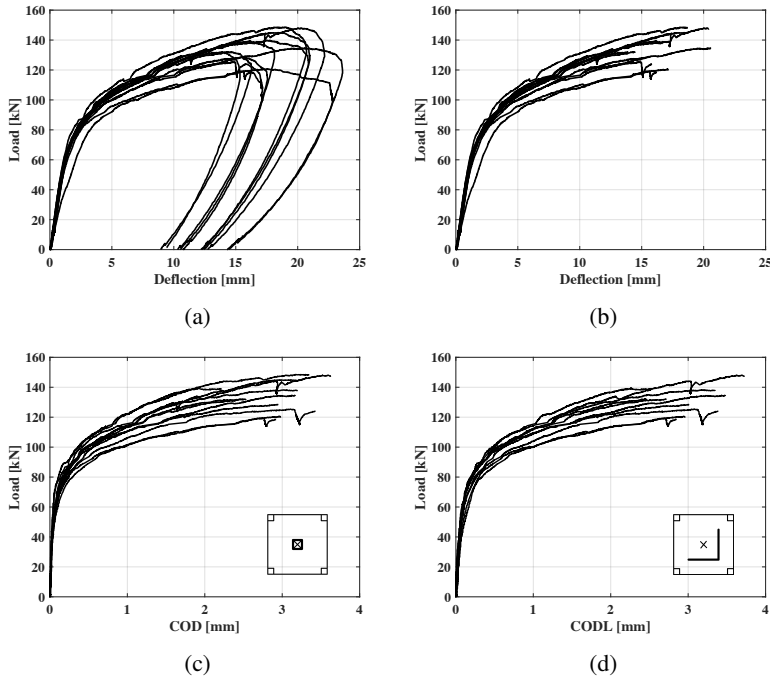


Figure 7.4: (a) complete load-deflection response of the twelve plates, (b) load-deflection response up to the maximum load, (c) and (d) average load-COD<sub>b</sub> and load-COD-L<sub>b</sub> measured those of instruments shown on the figure which record the final crack.

kN. For such distribution of structural response, the provision of the code requires a design resistance of 78.5 kN, the maximum on the blue dotted line. With this respect, there is a 24% safety margin, which stems from the smaller coefficient of variation of the structural response of the SFRC plates with respect to the foreseen value in the EN 1990,  $V=16\%$ .

Yet, it should be taken into account that these plate elements were not all tested on the same day and the tests spans between 59 days for the first test, to 133 days for the twelfth one. Consequently, the dispersion observed in the experimental measurements of the plates is not solely the intrinsic scatter of the response, mainly coming from the heterogeneity of the SFRC. Hence, attempt was made to cancel out the influence of the improvement of strength of the SFRC material in time. To this end, the load-deflection curves are normalized with respect to the expected tensile strength at the age of testing of each specimen. According to the MC 2010, with the curing condition applied in this study, it is reasonable to assume that the development of tensile strength is similar to that of compressive strength. Hence, the compressive strength values measured at 59 days with the first plate and at 133 days of age with the

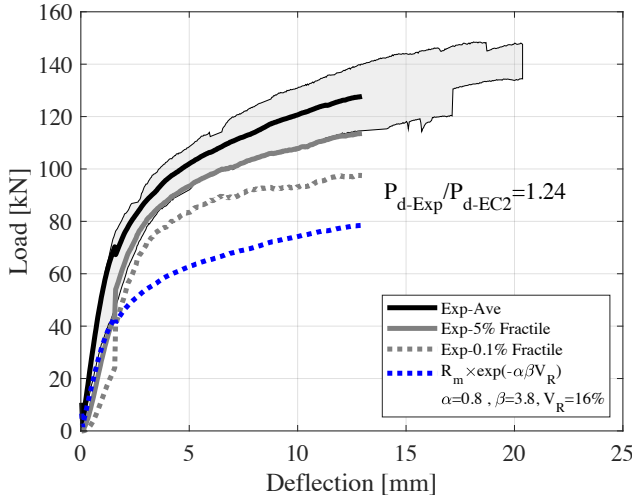


Figure 7.5: Dispersion, average, 5% fractile corresponding to the characteristic response of the plates, 0.1% fractile corresponding to the design response of the plates, and the curve corresponding to the design resistant of the plates according to the requirements of the EC2.

last plate were considered as the reference. Taking into account the average daily temperature that the plates were exposed to, the compressive strength at 28 days was found out as the average of the value obtained by taking back in time the compressive strength values from 59 and 133 days. The formula given in the MC 2010 for development of compressive strength reads:

$$f_{cm}(t) = \beta_{cc}(t) \cdot f_{cm} \quad (7.12)$$

with

$$\beta_{cc}(t) = \exp\left\{s \cdot \left[1 - \left(\frac{28}{t}\right)^{0.5}\right]\right\} \quad (7.13)$$

where  $f_{cm}(t)$  is the mean compressive strength at time  $t$ ,  $f_{cm}$  is the mean compressive strength at 28 days of age,  $\beta_{cc}(t)$  is a function to describe the development with time,  $t$  is the concrete age in days adjusted according to:

$$t_T = \sum_{i=1}^n \exp\left[13.65 - \frac{4000}{273 + T(\delta t_i)}\right] \quad (7.14)$$

Finding the compressive strength at 28 days, it was again corrected for the development of strength at the age of testing the plates, from which the expected tensile strength value of the SFRC was found as :

$$f_{ct} = 0.3 \times (f_{cm})^{2/3} \quad (7.15)$$

To normalize the results, the load-deflection curves are divided by the expected tensile strength at the age of testing, and finally they are all multiplied by the average of the tensile strength among all the twelve specimens. In this manner, it is as though they were all tested at the same time at an age in the middle of 59 and 133 days. The normalized load-deflection response of the twelve plates are displayed in Fig. 7.6. Needless to point out that the dispersion of the normalized results narrows down. In this case, the experimental characteristic and design loads are respectively 118.2 kN, and 106.8 kN. The safety margin increases to 36%.

Fig. 7.7(a) shows the improvement of the bearing capacity of the plate elements with time. Given the clear shift in the structural resistance of the plates, we decided to divide the tested plates in two groups based on the testing age. In this manner, the first six plates together with the corresponding notched beams tested within 59 to 79 days after casting were grouped together as G1, and the other six plates and notched beams that were tested from 125 to 133 days of age were categorized as G2. The tested plates in each of these two series are shown in Fig. 7.7(b). We remind that the data of the first notched beam specimen was lost, therefore, the G1 group consists of six plates and five beam elements.

Fig. 7.8 shows the stress-CMOD results of the notched beam specimens

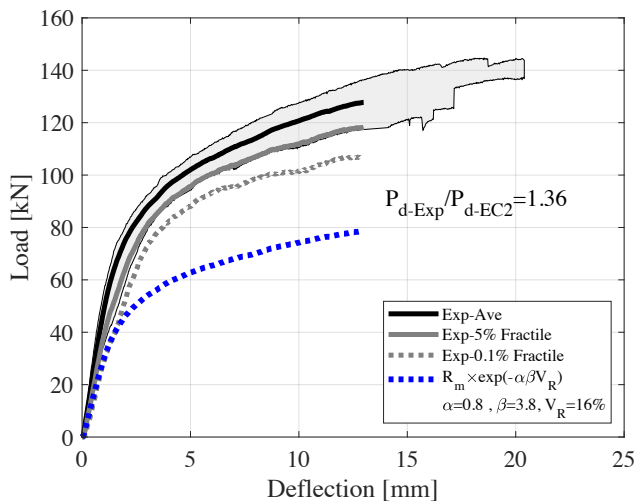


Figure 7.6: Normalized load-deflection response of the twelve SFRC plates. The measured results are normalized by the expected tensile strength at the testing age of each plate considering the curing temperature.

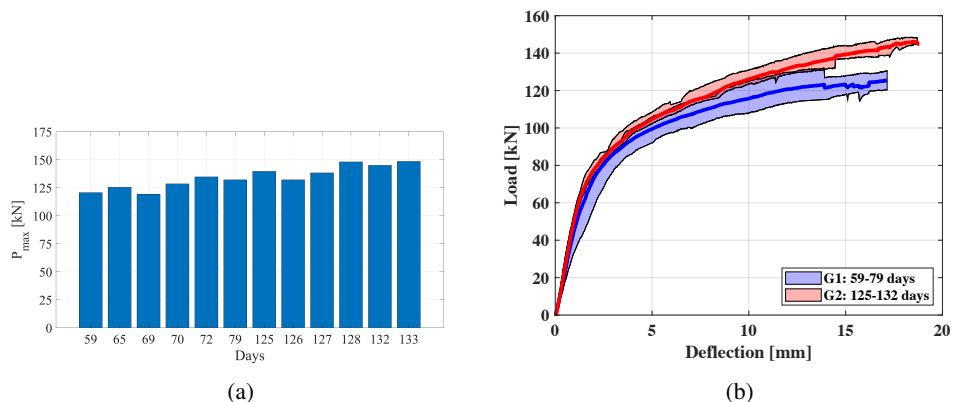


Figure 7.7: (a) Variation of the load-bearing capacity of the plates in time and (b) categorizing the twelve plates in two groups of six plates based on the age of testing.

and the load-deflection results of the G1 and G2 groups. From these results considerable observations can be made. The stress-CMOD results of the G2 group shows a considerably higher dispersion compared to the companion specimens in the G1 group, while for the plate elements, the contrary holds. Larger dispersion of plate results in G1 group as opposed to those of the G2, could be reasonably attributed to the longer duration in which the tests were carried out for G1 group. The G1 plates were tested in twenty days, while the G2 plates were tested within a week. But, still, the notched beams of the G1 series show narrower dispersion. Fig. 7.9 compares the average and characteristic experimental results obtained from the three-point bending tests of the G1 and G2 series. Although the average curves are very similar for both groups, the wider scatter of the older specimens led to a lower characteristic curve for the G2 series. This is despite of the fact that in the G1 group five specimens were tested and therefore a larger distance from the average curve was considered compared to the G2 group with six specimens (with reference to Eq.7.10). In a design situation based on characteristic tensile values derived from a three-point bending test, this implies a larger safety margin for the G2 series compared to G1.

The residual tensile values of the G1 and G2 notched beams with the parameters related to the dispersion of the results are given in Tables 7.3 and 7.4, and a summary of the results pertaining to the dispersion of the load-deflection curves of the plates for the as-measured results, the normalized curves, and the G1 and G2 groups separately are given in Table 7.5. The average maximum load,  $P_{max}$ , the deflection at maximum load,  $Def-P_{max}$ , and the sustained load at two deflection values of 5 mm and 10 mm,  $Load@Def=5$  mm and  $Load@Def=10$  mm, together with the coefficient of variation of the

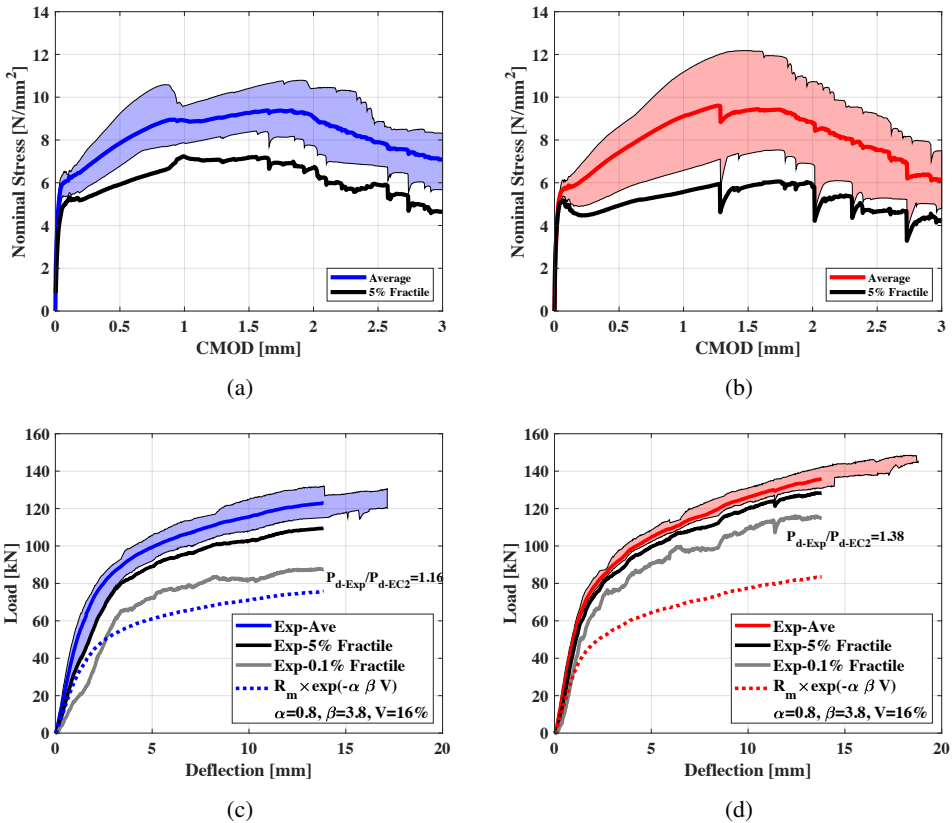


Figure 7.8: The results of the nominal stress-CMOD for the notched beams of (a) G1 and (b) G2 groups, and the load-deflection response of the plates for the (c) G1 and (d) G2 groups of specimens.

results are given for each case. It is important to notice that the  $P_{max}$  value reported in table occurs at different deflection values for the twelve plates and is not the same as of the average curves that were shown earlier.

For the three-point bending tests, the coefficient of variation of the residual tensile strength values range between 11% for  $f_{R,2}$  in G1 group, which is a rather low value, to around 20% for  $f_{R,2}$  and  $f_{R,3}$  values for G2 group of specimens, which are very often observed for this type of material. Before normalization, the bearing capacity of the plates show a coefficient of variation of 7.4%. With normalization this value is surely reduced, which results a  $V=5.3\%$ . For G1 and G2 groups that were tested during a time span of 20 days and 7 days respectively, the coefficient of variation is 4.8% and 4.5%. Had we tested all the twelve plates on the same day, the bearing capacity of the plates would have shown a variation of less than 5%. It is also interesting to observe

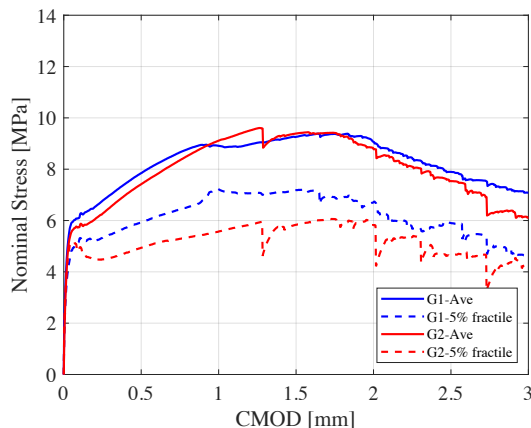


Figure 7.9: Comparison of the average and characteristic curves of the stress-CMOD response of the notched beam specimens for G1 and G2 groups.

that while the scatter of the sustained load at a certain deflection for the G1 series is more than twice of the scatter for the G2 plates, in terms of maximum load  $P_{max}$ , the difference between the scatter of results for the two series is very small.

The wide dispersion in the post-peak strength values of SFRC materials is a very common observation. In the draft of the Annex L of EC2 on SFRC, the minimum assumption for the coefficient of variation of the residual strength values is chosen to be 20% which sets a roof on the maximum allowable characteristic value that can be taken for the residual strength values.

Table 7.3: Results of the three-point bending test for G1 series

Specimen	$f_{ct,fl}$	$f_{R,1}$	$f_{R,2}$	$f_{R,3}$	$f_{R4}$	
1	6.3	8.11	10.24	8.86	8.08	
2	6.24	7.2	8.37	6.78	6.04	
3	6.32	7.91	10.41	8.23	6.38	
4	5.3	9.23	8.9	8.59	7.01	
5	5.38	6.78	8.38	7	5.06	
$f_m$	5.91	7.85	9.26	7.9	6.51	
V(%)	9	12	11	12	17	
$f_k$	4.78	5.92	7.19	5.91	4.29	class 5c

Table 7.4: Results of the three-point bending test for G2 series.

Specimen	$f_{ct,fl}$	$f_{R1}$	$f_{R2}$	$f_{R3}$	$f_{R4}$	
1	5.56	6.14	7.36	6.4	4.61	
2	5.36	8.54	8.41	7.76	5.83	
3	5.28	5.61	7.48	5.27	4.53	
4	5.89	8.62	12.18	9.18	4.81	
5	5.66	7.43	9.75	9.08	6.35	
6	5.62	8.15	11.17	7.55	5.33	
$f_m$	5.56	7.42	9.39	7.54	5.24	
V(%)	4	17	21	20	14	
$f_k$	5.1	4.93	5.83	4.65	3.86	class 4c

Table 7.5: Parameters of the load-deflection curves for the plate elements.

	$P_{max}$		Def- $P_{max}$		Load@ Def=5 mm		Load@ Def=10 mm	
	Ave (kN)	V (%)	Ave (kN)	V (%)	P (kN)	V(%)	P(kN)	V(%)
All	134.4	7.4			102	4.5	120.8	5.8
All-Normalized	134.2	5.3	16.7	12.9	102	3.3	120.8	3.9
G1	126.8	4.8	16.28	14.3	99.4	4.9	115.7	5.3
G2	148.8	4.5	17.56	11.8	104.7	2.2	126	2.2

## 7.4 Magnification of 5% fractile values; the $\kappa$ factor

In an economical design, the design value of resistance equals the design value of load effects [105]. Looking at resistance alone, this would be achieved if one can predict the characteristic structural response with the characteristic material properties. In such case, introduction of provisioned safety factors guarantees the attainment of required reliability index. Hypothetically speaking, if the average material properties is capable of predicting the average structural response in a precise manner, equal coefficients of variation of the material properties and structural strength leads to a precise prediction of the characteristic structural strength using the characteristic material properties. In this hypothetical explanation we disregard the fact that determination of characteristic values of material properties on limited number of specimens depends on confidence levels which brings about larger safety margins. With the assumption that  $f_{R,m}$  values can nicely predict the response of a FRC element, the debate over the small 5% fractile of  $f_{R,k}$  of a FRC material, which is due to the testing method, can be boiled down to the determination of the scatter of structural strength of a member made of the same FRC. For instance, the magnification factor,  $K_{Rd}$ , given in MC 2010 to be multiplied to  $f_{R,k}/d$ , assumes that the scatter of material can be taken equal to the scatter of the

structural strength, which needs to be estimated through stochastic non-linear modeling. This relationship is repeated here which reads:

$$K_{Rd} = \frac{P_{max,k}}{P_{max,m}} \times \frac{f_{Ftum}}{f_{Ftuk}} \leq 1.4$$

When multiplied to  $f_{ftu,d} = f_{ftu,k}/\gamma_c$  value, the second term in the multiplication cancels out the effect of scatter of results of a three-point bending tests, and sets the starting point to be the average material properties,  $f_{Ftum}$ . Then the average properties are multiplied by the ratio of  $P_{max,k}/P_{max,m}$  of the structural strength. For a log-normal distribution with a lower bound at zero, this ratio, as expressed in Eq. 7.7, is equal to:

$$P_{max,k}/P_{max,m} = exp(-1.65V_R)$$

which only depends on  $V_R$ , the scatter of structural strength. Obtaining this ratio from a probabilistic NLFEM in which material heterogeneity is properly accounted for, should give a reliable estimation of the theoretical scatter of the structural strength. Hence, the  $K_{Rd}$  factor is entirely based on the assumption of an equal scatter for the material properties and structural strength, which is a straightforward and reasonable approach when dealing with structures with high redistribution capacity. It is not easy to exactly determine what would be the dispersion of structural resistance for a given structural scheme without generating a sufficiently large sample through a probabilistic model, however, looking at available results in the literature where large FRC specimens were tested, we can expect a scatter in the range of 5%-8% [150, 183]. Fig. 7.10 depicts the  $K_{Rd}$  factor as defined in the MC2010 for two coefficients of variation for structural resistance of  $V_{P_{max}}=5\%$  and  $8\%$ . While for the structural strength the theoretical probability distribution is taken into account, the ratio of  $f_{R,m}/f_{R,k}$  is obtained based on experimental results on a few specimens with corresponding coefficients for 5% fractile (4, 6, and 12 specimens). With  $V_{P_{max}}=5\%$ , and with six tested beams, the maximum value of  $K_{Rd}=1.4$  occurs if the tested specimens show approximately a  $V=19\%$ . For  $V_{max}=8\%$ , a  $K_{Rd}=1.4$  would be obtained if the scatter of the experimental results is  $V=21\%$ .

This approach is in fact based on the adoption of a *reduced coefficient of variation*,  $V_{red}$ , for post-peak tensile strength values of FRC. In line with this idea, a different view point is to assume that the three-point bending test has a scatter equal to  $V_{red}$ . To check the implications of this method  $V_{red}=5\%$  and  $8\%$  are chosen again. Depending on the number of tested specimens in a flexural test (here 4, 6 and 12 specimens), and the scatter of test results characterized by  $V$ , a  $\kappa$  factor is found. The  $\kappa$  factor is the



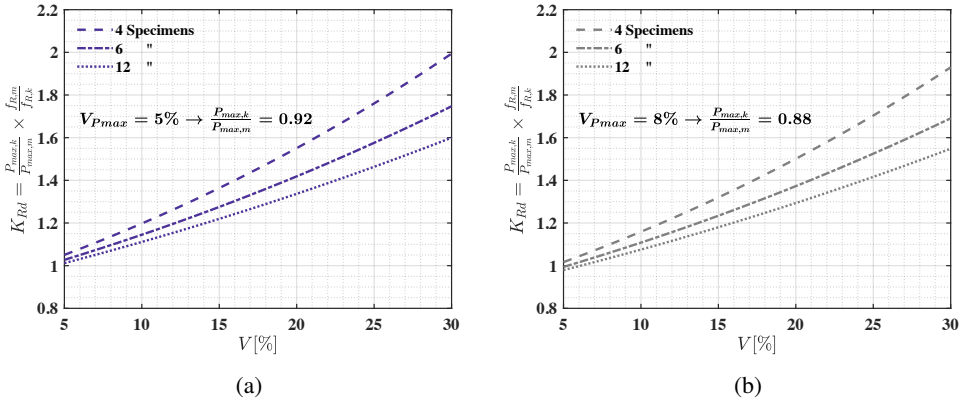


Figure 7.10: The  $K_{Rd}$  factor according to MC2010 depending on the number of tested specimens in a three-point bending test and for two coefficients of variation of (a) 5% and (b) 8%, for the structural resistance.

ratio of  $f_{R,k}$  with the reduced coefficient of variation,  $V_{red}$ , to the  $f_{R,k}$  found in a three-point bending test with the coefficient of variation,  $V$  (Here up to 30% is shown). Fig. 7.11 depicts these results for (a)  $V_{red}=5\%$  and (b)  $V_{red}=8\%$ . In addition to the case of limited number of specimens, the case for the theoretical probability distribution is also shown with a solid line. For instance if derivation of tensile properties of a FRC is carried out on six specimens with a coefficient of variation of 15%, with an assumption of  $V_{red}=5\%$  (Fig. 7.11(a)), the magnification factor will be  $\kappa=1.3$ . For four, six, and twelve specimens and a  $V_{red}=5\%$ , a  $\kappa=1.4$  is justified for a  $V$  of 18%, 21%, and 23% respectively. Or for instance, for a common coefficient of variation of 20%, which is the minimum acceptable  $V$  proposed in EC-annex L, for six specimens,  $\kappa=1.38$  and  $\kappa=1.3$  is obtained for  $V_{red}=5\%$  and 8% respectively. The only difference between Fig. 7.11 and Fig. 7.10 is that in Fig. 7.10 the  $P_{max,k}/P_{max,m}$  is obtained based on the theoretical lognormal distribution, while in Fig. 7.11, the initial and the magnified characteristic values are found for the same number of specimens with corresponding confidence levels.

To better investigate the effect of large scatter of a flexural test on  $f_{R,k}$  value, it is compared to the characteristic values of other strength parameters of concrete, namely  $f_c$  and  $f_{ct}$ . Fig. 7.12 depicts the ratio between characteristic values and mean values for these parameters. The left and bottom axes are related to  $f_c$  and  $f_{ct}$  values, and the top and right axes regards the results of  $f_R$  of a FRC. The same color is used for the axes and the corresponding curves. For different classes of concrete, C20 to C50, the  $f_{ck}/f_{cm}$  is shown with a solid black line. For normal strength concrete  $f_{cm} = f_{ck} + 8$ . The dashed black line

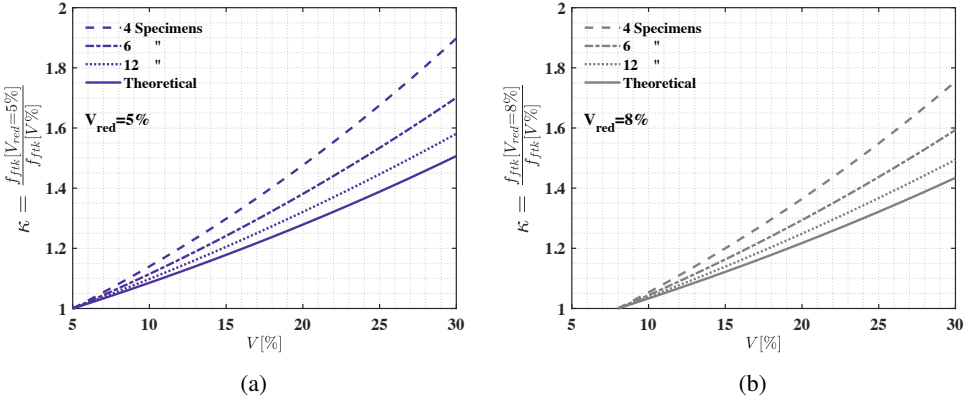


Figure 7.11: The magnification factor,  $\kappa$  defined as the ratio between the characteristic value of residual strength with the assumption of a reduced coefficient of variation,  $V_{red}$  of (a) 5% and (b) 8%, to the experimental characteristic values based on the number of tested specimens.

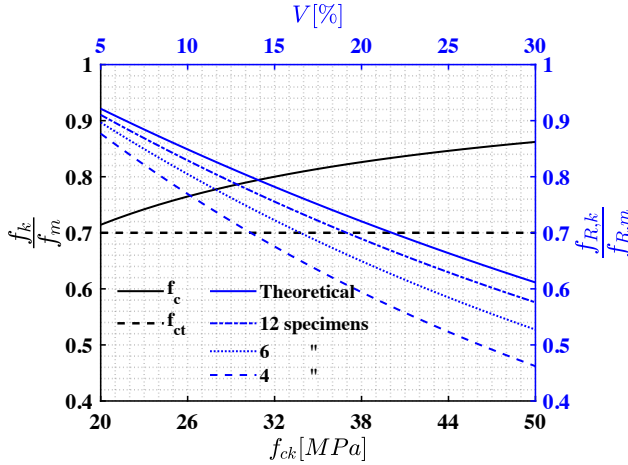


Figure 7.12: Comparison of ratio between the characteristic value and average value of compressive and tensile strength (bottom and left axes) and for the residual tensile strength value for FRC depending on the number of tested specimens (top and right axes).

is the lower limit of  $f_{ctk} = 0.7f_{ctm}$ . The blue curves display the  $f_{R,k}/f_{R,m}$  for  $5\% \leq V \leq 30\%$  based on four, six, and twelve tested specimens. It is evident that for a  $V=17\%$  on six specimens,  $f_{R,k}$  values fall even below the lower limit of  $f_{ctk}$  w.r.t the average values. For structures that demonstrate a highly repeatable ductile response, such low value for the characteristic properties leads to unjustified extra design costs.

### 7.4.1 Magnification factor in EC2 and CNR-DT 204

MC 2010 is not the only code in which suggestions are given for magnification of the characteristic values. In this section two other methods given in the EC2-annex L, and CNR-DT 204 are explained and discussed.

#### 7.4.1.1 EC 2-Annex L

Annex L of the new version of EC2 is attributed to fibre reinforced concrete and design rules are given for this material. In this document, certain limitations are imposed for the maximum value of the characteristic value of the residual strength properties that can be adopted, and then, it is allowed to introduce a magnification factor to the characteristic value of the residual strength properties. Regarding the maximum value for characteristic residual strength values this standard reads:

$$\begin{aligned}\kappa_{k,max} &= 0.6 \\ f_{R,1k} &= \min(f_{R,1k}; \kappa_{k,max} f_{R,1m}) \\ f_{R,3k} &= \min(f_{R,3k}; \kappa_{k,max} f_{R,3m})\end{aligned}\tag{7.16}$$

Then some passages are followed to transform the characteristic nominal residual strength values obtained from a three-point bending test,  $f_{R,1}$  and  $f_{R,3}$ , to the design values of tensile resistance for serviceability and ultimate limit states,  $f_{Ft1d}$  and  $f_{Ft3d}$ . These passages are as follows:

- multiplication of relevant coefficients to pass from the nominal residual tensile strength measured from three-point bending test to the direct tensile law of the FRC to get  $f_{Ftsk}$  and  $f_{Ftuk}$ .
- multiplication of the  $\kappa_0$  factor to take into account the fibre orientation effect which results in the effective residual tensile strength values of  $f_{Fts,ef}$  and  $f_{Ftu,ef}$ .
- At the end, to get the design value of the residual tensile strength values,  $f_{Ftsd}$  and  $f_{Ftud}$ , safety coefficient is applied to the effective residual tensile strength values, and a magnification factor,  $\kappa_G$ , is introduced which aims to compensate for the small characteristic values obtained for the residual tensile values.

It is mentioned that the maximum value of  $\kappa_G$  corresponds to the maximum value of  $\kappa_k$  factor through the relationship:

$$\kappa_{G,max} \leq \frac{0.9}{\kappa_{k,max}} = 1.5\tag{7.17}$$

It is further pointed out that in the availability of results for  $f_{Fts/um}$ ,  $\kappa_G$  factor can be increased up to :

$$\kappa_{G,max} = 0.9 \times \frac{f_{Fts/um}}{f_{Fts/uk}} \quad (7.18)$$

For statically indeterminate slabs, the values of  $\kappa_G$  is obtained from the following formula in line with DafStb Guideline [56]:

$$\kappa_G = 1 + 0.5 \times A_{ct} \leq 1.5 \quad (7.19)$$

with  $A_{ct}$  being the area of the tension zone (in  $m^2$ ) of the cross-section involved in the failure of an equilibrium system. In 2012 version of DafStb, the maximum value for  $\kappa_G$  is 1.7.

**7.4.1.1.1 comments** With reference to Eq.7.16, the maximum value for  $f_{R,k}$  is considered to be  $0.6 \times f_{R,m}$ . For a log-normal distribution and for a sample of six specimens this corresponds to a coefficient of variation of more than 20%. From the inequality of Eq.7.17, It might be inferred that there is a logical relationship between the variables  $\kappa_G$  and  $\kappa_k$ , through this formula, in the sense that smaller values of  $\kappa_G$  would be obtained for larger values of  $\kappa_k$ . However, this is not the case and in this relationship  $\kappa_k$  can not take any larger values to yield a smaller  $\kappa_G$  factor, because it has assumed already its maximum value of 0.6. What this inequality conveys is that even if the  $f_{R,k}$  value obtained from three-point bending tests is smaller than  $0.6f_{R,m}$ , the value of  $\kappa_G$  can not be higher than  $0.9 \times \frac{1}{\kappa_{k,max}=0.6} = 1.5$ .

Although the  $\kappa_G$  is multiplied to the effective residual tensile strength values, i.e. after the direct tensile strength values are obtained and the effect of fibre orientation is taken into account, here we introduce it at an earlier stage to check its applicability and to control its validity w.r.t to certain fractiles. We assume that the  $\kappa_G$  is multiplied to the  $f_{R,k}$  values, namely, the specifiers of FRC class (table L.2 of the Annex L of EC 2). Assuming the maximum value of  $\kappa_G$  corresponding to maximum value for  $f_{R,k}$  we have:

$$\begin{aligned} f_{R,k} &= 0.6 \times f_{R,m} \times (\kappa_{G,max} = 0.9/0.6) \\ &= 0.9 \times f_{R,m} \end{aligned} \quad (7.20)$$

According to this standard the 0.9 coefficient is to “allow for the lower mean of the average”. The adoption of  $f_{R,k} = 0.9f_{R,m}$  is equivalent to the assumption of a coefficient of variation of around 5% for the material properties. This can be seen looking at Fig. 7.12.

#### 7.4.1.2 CNR DT 204-2006 (Italy)

Appendix D of CNR-DT 204 [50], *Guide for the Design and Construction of fibre-Reinforced Concrete Structures*, regarding the characteristic value of FRC structural elements reads:

“In statically undetermined structures, wide cracked regions and significant redistributions occur at failure. Consequently, the characteristic values obtained from small size specimens do not represent the lowest ones. As a result, the effect of the structural redundancy on the topological inhomogeneities of fibre reinforced concrete may be experimentally evaluated by means of qualification tests, carried out on proper structures reproducing the real ones. Without suitable experimental tests, the strength increase may be taken into account by using

$$f_{Ftk} = f_{Ftm} - \alpha k s \quad (7.21)$$

$k$  is assumed to be equal to 1.48, and  $\alpha$  is

$$0.5 \leq \alpha = \left[ 1 - 0.1 \left( \frac{\nu}{2\nu_0} - 1 \right) \left( \frac{\alpha_u}{\alpha_1} \right) \right] \leq 1 \quad (7.22)$$

In Eq. 7.22,  $\nu/\nu_0$ , is the ratio of volume of structure involved in the cracking process to a reference volume, the volume of zone of cracking in the tested specimen for derivation of the residual tensile properties. And  $\alpha_u/\alpha_1$  is the ratio between the maximum load and the one corresponding to the elastic limit. A table is given in this standard for different types of structural elements and for which these values are given. With this regard,  $\nu$  depends on the failure mechanism of the structural element and on the characteristic length,  $l_{cs}$ .

**7.4.1.2.1 comments** In this standard, design of FRC structures that posses two features is allowed to be realized with augmented characteristic values of the residual tensile strength parameters. First, is the size of the volume involved in the cracking process, and second is the ability of the structure to go through a stable multi-cracking phase. Although the influencing factors are properly acknowledged, the parameters in Eq.7.21 may not be coherent with derivation of characteristic values from a few specimens. The  $k=1.48$  coefficient, corresponds to a theoretical 5% fractile of infinite number of specimens that are log-normally distributed and have a coefficient of variation of approximately 17% (or a skewness value,  $\alpha_X=0.5$ , This is obtained by

Table 7.6: Coefficients  $k_n$  for a 0.1% design value

coefficient	number of specimens										
	1	2	3	4	5	6	8	10	20	30	inf
$u_p(1/n + 1)^{0.5}, \sigma$ known	4,36	3,77	3,56	3,44	3,37	3,33	3,27	3,23	3,16	3,13	3,09
$t_p(1/n + 1)^{1/2}, \sigma$ unknown	–	–	–	11,4	7,85	6,36	5,07	4,51	3,64	3,44	3,09

the assumption of a linear variation of  $t_p$  with  $\alpha_x$  from Table 7.7). For six specimens which is often tested for classification of a FRC, the characteristic value has a distance of  $1.77s$  from the mean. So adoption of a  $k=1.48$  does not respect the required confidence to obtain characteristic values based on a sample of data.

## 7.5 Normal or Log-normal?

The common approach for estimation of characteristic properties of concrete, passes through coefficients determining the 5% fractile for limited number of tested specimens. The current approach that is implemented for both conventional and fibre reinforced concrete passes through the coefficients in Tables 7.2 and 7.6 for estimation of characteristic and design values respectively. The values given in these tables are for a normal distribution.

Concrete properties are very often considered to follow a log-normal distribution and the transformation needed to pass from a normal to a log-normal distribution is given in Eq 7.10. Nevertheless, a log-normal distribution with a low skewness, is very similar to a normal distribution and the adoption of the values given in Tables 7.2 and 7.6 without log-normal transformation would not lead to a sizable deviation of the characteristic and design values from a log-normal distribution. Hence with these circumstances, the coefficients for estimation of 5%, 0.1% fractile are almost equal for the normal and log-normal distributions. For a log-normal distribution with lower bound at zero, the skewness is:

$$\alpha_X = 3V + V^3 \quad (7.23)$$

with  $V$  being the coefficient of variation. JCSS [118] suggests a coefficient of variation of 6% for concrete behavior related to compression, which leads to a skewness value of around 0.18. For FRC, where coefficient of variation is often between 15%-30%, the skewness will be in the range of  $\alpha_X=0.45 - 0.9$ . Therefore, for these large values of skewness, the difference between a normal and log-normal distribution can be significant. Table 7.7 gives the values of  $t_p$  coefficient (according to Eq.7.11) for different skewness values

Table 7.7: Coefficient  $-t_p$  from equation for  $p = 0,05$  and a log-normal distribution with the skewness  $\alpha_X$ 

skewness	Coefficient $t_p$ for $\nu = n-1$ degrees of freedom								
	3	4	5	6	8	10	20	30	inf
$\alpha_X = -1$	2,65	2,40	2,27	2,19	2,19	2,04	1,94	1,91	1,85
$\alpha_X = 0$	2,35	2,13	2,02	1,94	1,86	1,81	1,72	1,70	1,64
$\alpha_X = 1$	1,92	1,74	1,64	1,59	1,52	1,48	1,41	1,38	1,34

and for different degrees of freedom. For instance, according to Table 7.7, for a  $\alpha_X = 0$ , and for six specimens for characterization of a FRC material, the  $t_p$  value would be 2.02. Multiplication of this value with  $(\frac{1}{n} + 1)^{0.5}$ , according to Eq. 7.11, gives 2.18, which is the same coefficient if a normal distribution was assumed. Yet, for larger skewness values the story will be slightly different. For a positively skewed distribution, like the log-normal distribution, the 5% fractile of the variable will be slightly larger than that value disregarding skewness. Fig. 7.13(a) shows a comparison between the characteristic stress-CMOD curves for the G2 notched beams, with and without the consideration of skewness. Fig. 7.13(b) demonstrates the ratio between the characteristic value in case skewness is taken into account and the case of a normal distribution with zero skewness. The choice between a normal and a log-normal distribution can lead to considerable differences for large values of  $V$ . For a coefficient of variation of  $V=24\%$ , the assumption of a normal distribution for  $f_R$  values brings about 15% smaller values compared to an assumption of log-normality. To the knowledge of the author, not much research has been done in this area. However, in a major work comprising of few thousand test results on specimens tested according to ASTM C1550 [8] and ASTM C1609 [39], it is shown that while a log-normal distribution better explains the distribution of within-batch results, Central Limit Theorem holds for multiple batches and for different batches a normal distribution better represents the distribution of post-peak tensile strength parameters of a FRC. This can have consequences, specially for large casting volumes that are produced in multiple batches.

## 7.6 Anomaly in experimental results of plates

Fig. 7.14 demonstrates the results of SFRC notched beams and plates tested within *PartA* and *PartB* of the experimental campaign. The SFRC plates from *PartA* were tested on 185 and 189 days of age, and therefore the companion beams are chosen from the five specimen tested on 167 days from the same batch. For the twelve identical plates of *PartB*, the tests were carried

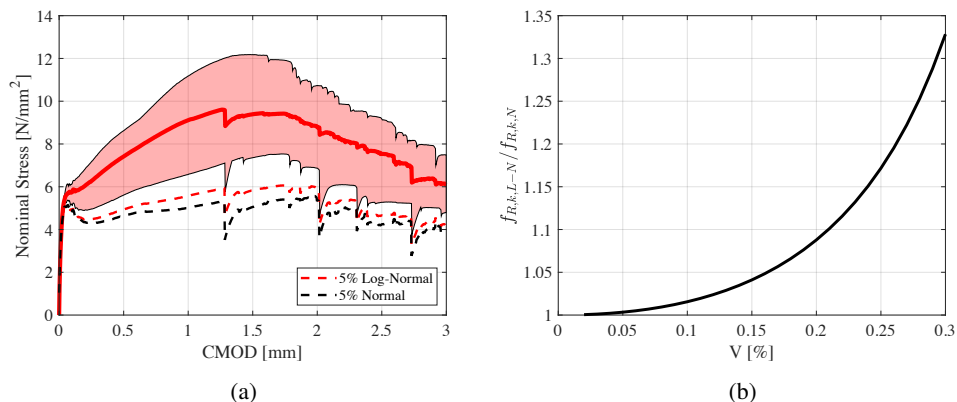


Figure 7.13: Effect of considering the unsymmetry in the log-normal distribution.

out from 59 to 133 days of age. The peculiarity of these results is that while the notched beams of *Part B* demonstrate higher residual strength values, the plates of the same series, display a lower bearing capacity. Given that the casting modality was closely monitored to make sure that all the plate elements were cast from the center, without moving the discharge pipe, fibre distribution should not be the reason for this anomaly. In Chapter 4, the load bearing capacity of the plates from *Part A* were predicted by the average residual tensile parameters of the companion beams with success. Therefore, evidently, the bearing capacity of the plates in *Part B*, can not be predicted by the properties derived the their companion beam elements. The underlying reason for this observation is explored and a rational explanation is given.

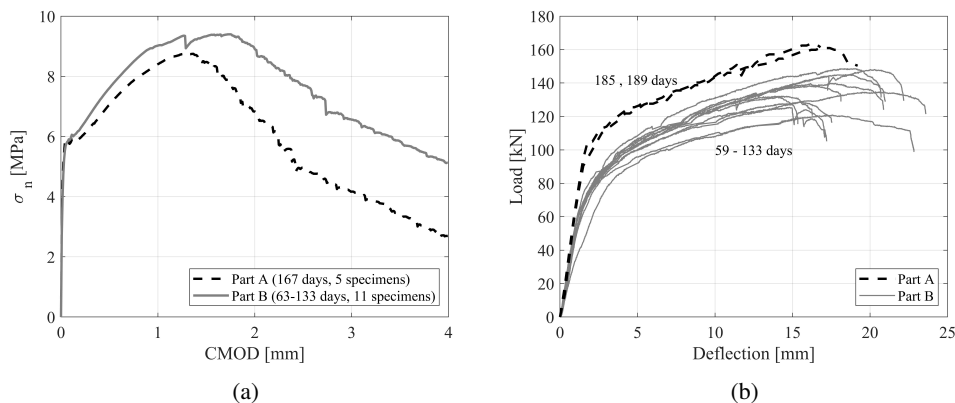


Figure 7.14: Comparison of SFRC plates and notched beams of *Part A* and *Part B* of the experimental campaign.



The first hypothesis would be that the younger age of the *Part B* plates might be the reason for their weaker performance. The results of these plates are divided by the tensile strength that might be expected for the FRC material at the age of each test and then is multiplied by the tensile strength of the same material that would have been obtained at 186 days of age, considering the average daily temperature given that the plates were cured in atmospheric condition. In this way, the results of plates for *Part B* are hypothetically transferred to 186 days of age. Fig. 7.15 displays these results in solid black curves. It is evident that the age of the specimens can not alone explain the considerable difference between the *Part A* and *Part B* results.

Specimens of *Part A* were cast in May, and the *Part B* specimens were cast in February and were cured in atmospheric temperature. Fig. 7.16 shows the average daily temperature of the the city of Lecco, during the curing time of the specimens of the two series. The harsh temperature during which the specimens of *Part B* were cast and cured can not be neglected. It is very likely that the cold weather has incurred damage to the plates mainly due to thermal stresses. However, this does not apply to the results of the notched beams. A glance at time variation of residual tensile strength values of the beams tested in *Part B*, Fig. 7.17 shows no specific trend. Any enhancement of strength in time for these beams is lost in the intrinsic scatter of the results. Had we tested multiple specimens at each age, enhancement of the post-peak results in time could have been observed on the average results.

The reason for larger post-peak residual strength values for specimens of

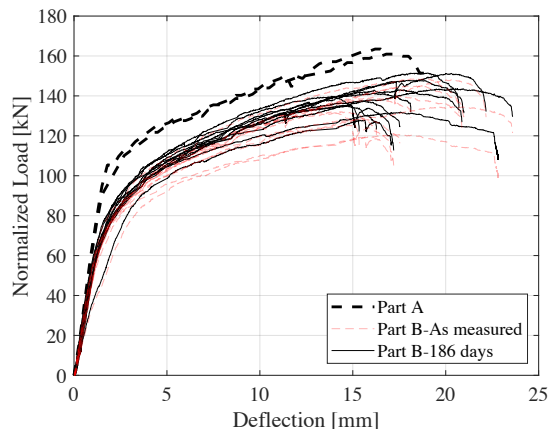


Figure 7.15: Shifting the results of the plates tested in *Part B* to 186 days of age to be compared with the plates of *Part A*.

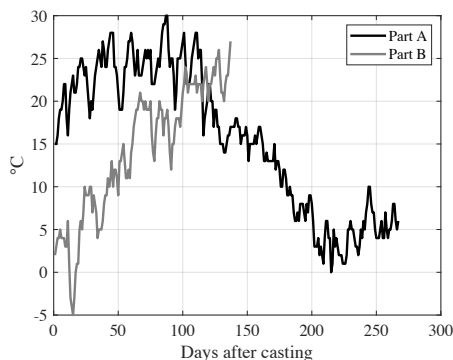


Figure 7.16: Average daily temperature for the whole curing period for the plate elements tested in *Part A* and *Part B*.

*Part B* that were cured in a colder temperature can be searched elsewhere. First, this is a matter of number of fibres. After each test, the number of fibres at the failed cross-section are manually counted and, Fig. 7.18 shows the effect of number of fibres on the residual tensile strength values for both series of specimens. In Fig. 7.18(a) to Fig. 7.18(d), the plot on the top is related to the notched beams tested in *Part A* and the plot on the bottom regards the

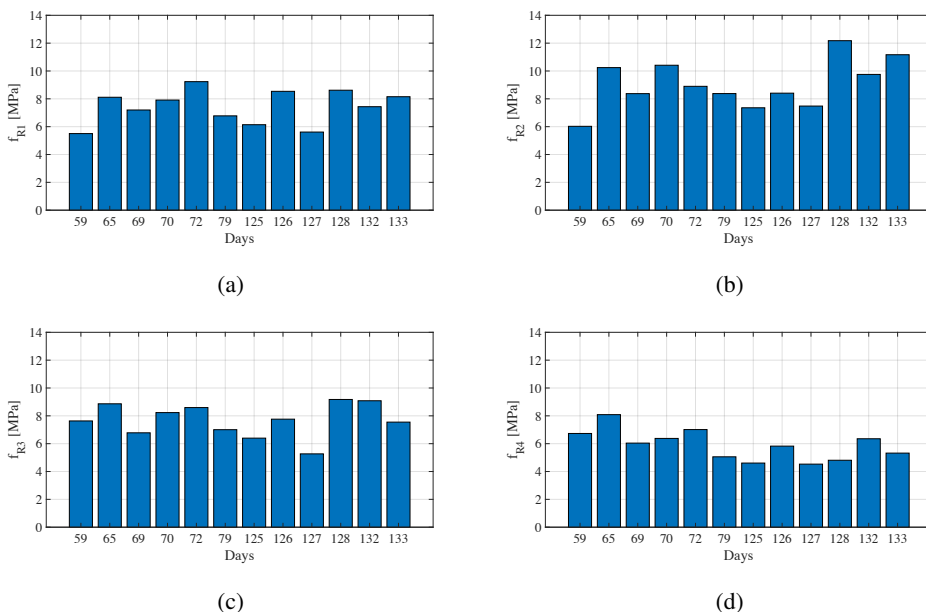


Figure 7.17: Variation of nominal residual strength values of eleven tested notched beam specimens in *Part B* with time for (a)  $f_{R1}$  (b)  $f_{R2}$  (c)  $f_{R3}$ , and (d)  $f_{R4}$ .

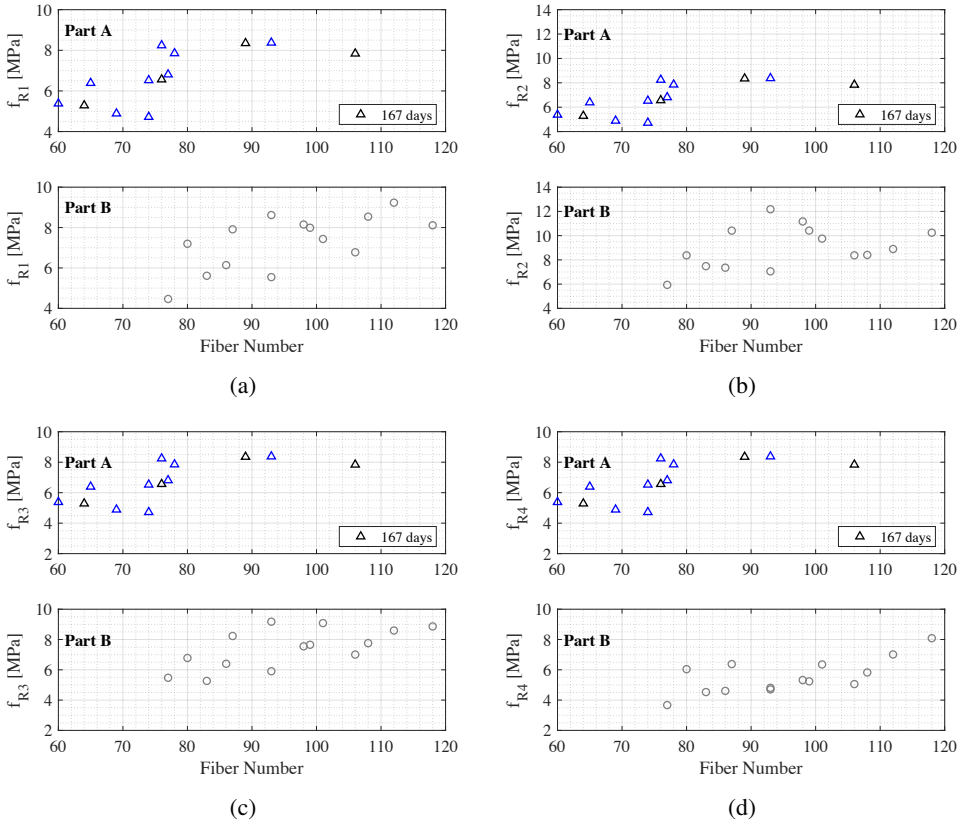


Figure 7.18: Number of fibres at the failure plane for notched beams of *PartA* and *PartB* and its effect on residual-tensile strength values.

*Part B* results. Here, the number of fibres in thirteen notched beams tested in *Part A* are shown. Out of the five tested notched beams at 167 days, four of them are depicted with black triangles, and the rest of specimens are shown in blue (the number of fibres were not counted on one specimen tested at 167 days). Although the mix designs are nominally the same, specimens of *Part A* seem to have lower number of fibres. Given the very limited failure surface in a three-point bending test, this difference in the number of fibres can play a major role in the post-peak results.

Second, the reason which may explain why lower curing temperatures affected the plates and did not affect the three-point bending results, may lie in the presence of the notch. The region which is mostly affected by the curing temperature is the surface layer of concrete, which is directly in contact with the atmosphere. When the notch is sawn in the beams, the damaged part of the specimen is removed, and internal layers which have experienced relatively

higher temperatures will come into play. Therefore, the creation of the notch may be able to alleviate the effect of thermal damage. All in all, higher number of fibres, and the reduction of effect of thermal damage by sawing the notch for the *Part B* notched beams, has led to an increase in the post-peak response of these specimens.

With this explanation, the lower bearing capacity of the twelve identical slabs in *Part B* compared to their companion plates tested in *Part A* might be due to thermal damage. Had we cast these twelve plates in the same time of the year as *Part A* plates, most probably, similar results were obtained.

In the remainder of this chapter, NLFEM is implemented within a reliability analysis framework to check the adequacy of the safety factors adopted in RC structures for the case of FRC plates. However, it should be taken into account that based on the discussion made, the tensile constitutive law driven from the notched beams will not be able to represent the behaviour of the twelve identical SFRC plates.

## 7.7 Derivation of $\kappa$ factor through a global safety format

In an overall safety format based on E-COV method compatible with NLFEA, two models are required. One model with the 5% fractile properties of the material, and one with the average material properties. With these two models, the probability density function of the structural resistance can be built, based on which, proper safety coefficient for fulfillment of a target reliability index can be derived. This was explained earlier in Section 7.1.1. To do so, in this section, first the tensile constitutive law of the SFRC material is obtained through inverse analysis, the tensile law is checked within a non-linear hinge model, the tensile law is adopted to model the three-point bending tests, and eventually these tensile laws are utilized for modeling the SFRC plates with average and characteristic material properties.

The obtained tensile laws are depicted in Fig. 7.19(a). These tensile laws are also introduced in a multilayer non-linear hinge model with plain section approach to replicate the nominal stress-CMOD results of the corresponding curves. The curves obtained are shown with dashed line in Fig. 7.19(b).

The same tensile laws are utilized in a NLFEM in *Abaqus*, to predict the results of the bending tests. These results are shown in Fig. 7.20 which give satisfactory results. With these well-founded tensile constitutive laws that proved adequate both in a non-linear hinge model and NLFEM, the

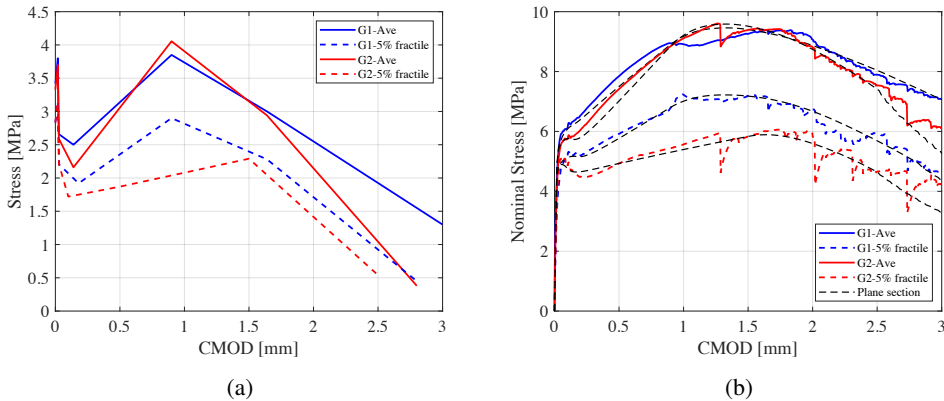


Figure 7.19: (a) Tensile constitutive law of the SFRC material obtained through the back analysis of the average and 5% fractile of stress-CMOD response of the notched beam specimens for G1 and G2 groups and (b) comparison of the experimental nominal stress-CMOD curves with the simulated results with a non-linear hinge model.

characteristic and average behavior of the plates in the G1 and G2 series are modeled.

Fig. 7.21 depicts the results of NLFEM for the plates in G1 and G2 series. As discussed earlier, unfortunately, the notched beams cast with the plates in the G1 and G2 series fail to properly represent the behavior of the plates. It was explained that this is very likely due to the cold curing temperatures and more damage to the plates as opposed to the notched beams. Furthermore, the difference in the slope of the first branch between the experimental and numerical results is due to thermal stresses in the plates that were not taken into account in the model. In a trial model, a realistic temperature profile was added to the model in which the slope was almost accurately captured. Nevertheless, for the sake of computational time, this is neglected in the model as it is not the main topic and only the dispersion of results is of interest.

Very significant conclusions can be drawn from these results. Building the probability distribution of structural strength for the SFRC plates based on two models, one with the average, and one with the characteristic material properties, does not even remotely give an image of reality. As expected, with assumption of homogeneity, the coefficient of variation that is obtained for structural strength is close to the coefficient of variation of the adopted SFRC material. While experimental results give a  $V=4.8\%$  and  $4.5\%$  for resistance of the G1 and G2 plates, the scatter of structural strength estimated based on the two models is  $16.8\%$  and  $25.7\%$ . In [159], Pukl et al. investigated the

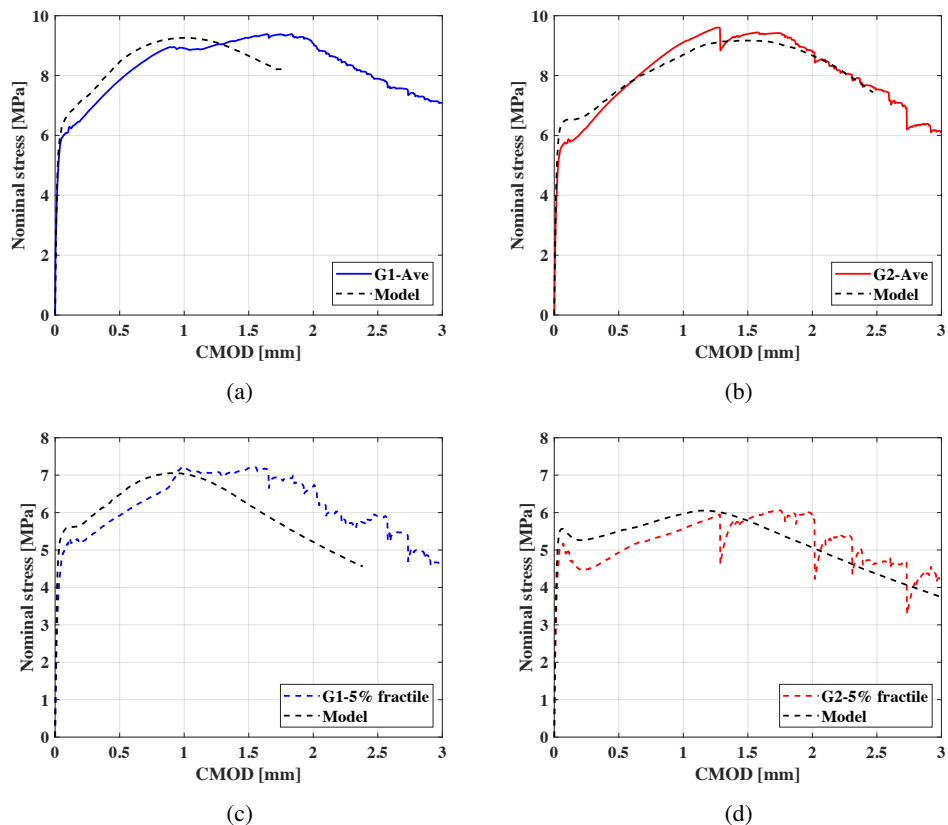


Figure 7.20: Comparison of experimental curves and modeling for nominal stress-CMOD results for the average curves of (a) G1 , and (b) G2 specimens and the characteristic curves of (c) G1, and (d) G2 series.

applicability of the available safety formats on different FRC structures. They found out that the calculated design resistance based on different methods is not significantly different from each other, with the E-COV method resulting in design resistance values that are slightly higher than the partial safety factor method. They attributed this difference to the fact that in the E-COV method the model uncertainty is overlooked while being partially introduced in the partial safety factor. Eventually they add

“Due to high variability of FRC material properties it can be recommended to utilize preferably the stochastic analysis based methods, i.e. full probabilistic analysis or ECOV method, where the actual material variability can be accounted for the evaluation of structural performance, safety and reliability under severe conditions”

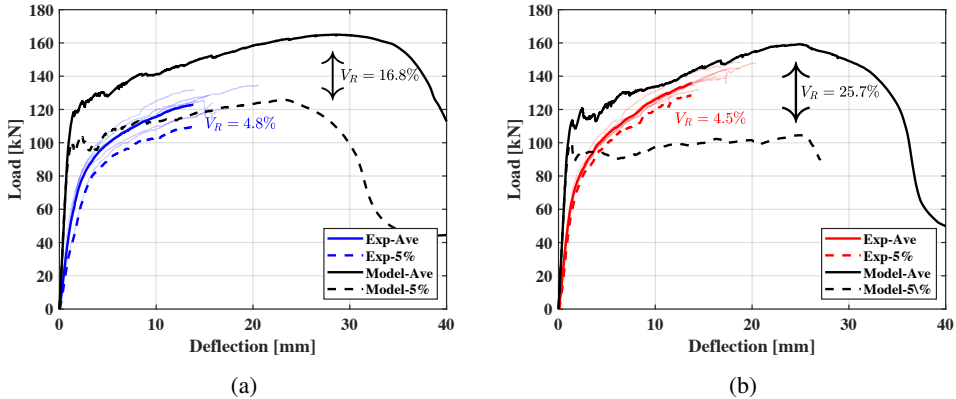


Figure 7.21: NLFE results of the plates based on average and 5% fractile material properties for the (a) G1 and, (b) G2 series, and derivation of the coefficient of variation of structural resistance for these elements. Results are compared with the structural resistance obtained from the experiments.

This may hold true when fibres and reinforcing bars are utilized together. In R/FRC structures only part of the resistance is provided by the fibres, hence, sensitivity of structural resistance to post-peak tensile parameters of the FRC is reduced. When fibres are the only reinforcing mechanism, the E-COV method can not represent the effect of material variability in structural performance and two deterministic models based on average and characteristic material properties lead to a scatter for structural strength that is closely related to material scatter.

The overall safety factor,  $\gamma_R = P_m/P_d$ , is obtained from three different methods and is compared to the required safety factor that is derived based on the experimental measurements. The design resistance is once found through PSF method with  $\gamma_c=1.5$  for concrete properties, with a yield line approach, similar to what was explained in Chapter 4. Both tensile laws given in EC2 and MC2010 are considered. Once, the  $\kappa_G$  and  $K_{Rd}$  factors are adopted to find magnified design resistance values, here referred to as PSF\*. For  $\kappa_G$  the maximum value of 1.5 is adopted and the  $K_{Rd}$  factor is obtained based on the experimental results of the notched beams and corresponding plates for the G1 and G2 series. Unlike the provisions of MC2010 in which the  $K_{Rd}$  is multiplied to the design resistance, here it is multiplied to the parameters of the tensile law. For  $f_{fts}$ , for G1 and G2 series the  $K_{Rd}$  is respectively 1.19 and 1.30, and for  $f_{ftu}$  it is 1.21 and 1.47. And once, following the coefficient of variation found for resistance of the plates through the E-COV method, the design resistance is found out and is compared to the average bearing capacity found through the

Table 7.8: The ratio of the average resistance to design resistance,  $\gamma_R = P_m/P_d$  based on PSF, PSF\* (partial safety factor with the introduction of magnification factors), E-COV method, and the required safety factor based on experimental measurements for maximum load on six specimens in each group.

Group	$\gamma_{req,Exp}$	$\gamma_{R,PSF}$		$\gamma_{R,PSF^*}$		$\gamma_{R,E-COV}$
		EC2	MC2010	EC2	MC2010	
G1	1.36	2.31	1.98	1.68	1.52	1.66
G2	1.35	2.29	2.35	1.74	1.59	2.18

NLFEMs. In the E-COV method,  $\gamma_R = exp(3.04 \times V_R)$  in which  $V_R$  is derived from the NLFEM results as  $V_R = 1/1.64 \times ln(P_m/P_k)$ . The required safety factor is derived according to the scatter of the experimental maximum loads. The design resistance is found in accordance with Eq. 7.10(c), and with the  $k$  coefficient of 6.36 for 0.1% fractile for six specimens, as given in Table 7.6. The overall safety factors obtained from different methods are illustrated in Table.7.8.

The required global safety factor is around 1.35 for both groups. For the PSF method very safe results are obtained with considerable safety margins. Introduction of the magnification factors is very effective in reducing the excessive safety. The E-COV method is very dependent on the  $V_R$  obtained through the non-linear model. For G1 plates the  $\gamma_R$  from this method is closer to the PSF\* and for the G2 group the safety coefficient is closer to the PSF method. However, there is a point of inconsistency in E-COV method that needs to be investigated. To do so, we repeat Eq. 7.8 for the partial safety factor method. According to this method the safety factor for concrete is obtained as:

$$\gamma_c = 1.15 \times \frac{f_k = f_m \times exp(-1.64V_m)}{f_d = f_m \times exp(-3.04V_R)} \approx 1.5$$

in which the coefficient of variation for material properties,  $V_m$  is assumed to be 15%, and the coefficient of variation of structural resistance,  $V_R$ , is around 16% (refer to Eq. 7.9). The 1.15 coefficient is not taken into account in the E-COV method. As this coefficient is to consider the difference in strength gain for lab-cured specimens and the concrete in real structure, the absence of this coefficient in the E-COV method can be justified when safety evaluation of existing structures is under study. Reliability analysis of existing structures is normally based on cores and samples taken from the structure and the material properties that are derived based on these specimens, represent the real structure. In the present study the notched beams and the plate elements



were both exposed to atmospheric curing regime. Consequently, the same strength development can be presumed for them. However, given that the computed  $\gamma_R$  values are compared with each other, and knowing that in the PSF and PSF\* methods the 1.15 coefficient is implicitly introduced in the computations of the  $P_d$  values, it should be taken into account that the  $\gamma_R$  from E-COV method naturally gives smaller value compared to the PSF method.

Eventually, having the overall safety format in mind, and in line with the proposal given for a  $\kappa$  factor in Section 7.4 which was based on the assumption of a reduced coefficient of variation for residual tensile strength parameters,  $V_{red}$ , the same approach can be implemented for the overall structural strength. The design resistance is expressed as  $P_d = P_m \exp(-3.04V_R)$ . If one carries out the E-COV method to find the scatter of structural resistance, a  $V_{E-COV}$  is obtained. For the plates tested in this study  $V_{E-COV}=16.8\%$  and  $25.7\%$  were found. However, the tested plates showed a  $V_R=4.8\%$  and  $4.5\%$  for the G1 and G2 groups. If the derivation of the magnification factor is based on a reduced coefficient of variation which is closer to the scatter of resistance of a real structure, the magnification factor can be written as:

$$\kappa = \frac{P_d = P_m \exp(-3.04V_{red})}{P_d = P_m \exp(-3.04V_{E-COV})} = \exp(-3.04(V_{red} - V_{E-COV})) \quad (7.24)$$

Similar to Section 7.4, where the  $\kappa$  factor was found for two  $V_{red}$  values of 5% and 8%, Fig. 7.22 illustrates this factor on the basis of the  $V_{E-COV}$  method. With an assumption of  $V_{red}=8\%$ , if the E-COV method gives a scatter of 19% for structural resistance, the  $\kappa$  factor will be 1.4.

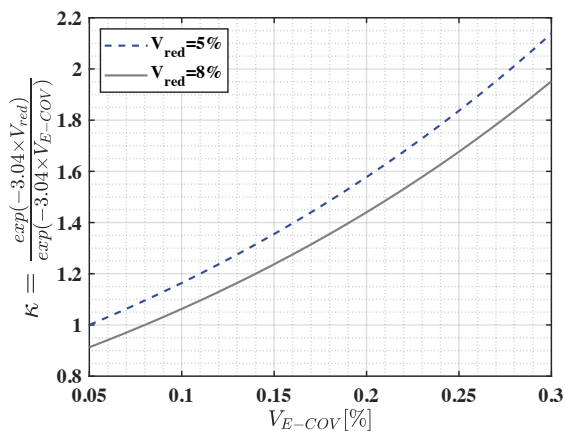


Figure 7.22: The magnification factor,  $\kappa$ , in light of the E-COV method defined as the ratio of design resistance considering a reduced coefficient of variation,  $exp(-3.04 \times V_{red})$ , to the design resistance based on the structural resistance scatter obtained from E-COV method,  $exp(-3.04 \times V_{E-COV})$ .

# CHAPTER 8

---

## CRACKING

---

### 8.1 Introduction

The realization of this thesis coincided with efforts made to revisit formulations related to prediction of crack spacing and width in RC and R/FRC elements within the activities of the EC2 and *fib* technical committees. At the time of writing this thesis these standards are not yet finalized and are still subjected to changes and modifications, therefore there could be discrepancies between the content found here and the final available versions of these standards available to the public. The arguments made are based on the latest available version of these documents to the technical committees. Although the experiments designed in this study were not aiming at a detailed study on the topic of crack spacing, the available experimental results for the plates and shallow beams were compared against the available formulations.

### 8.2 Crack spacing; state of the art and standards

The study of spacing and width of cracks in reinforced concrete members has been studied for long, with derivation of proper formulations based on classic theory of bond-slip for the transfer length in tie elements as early as 1943 [204]. In 1956, Clark [49] slightly modified the expression given by

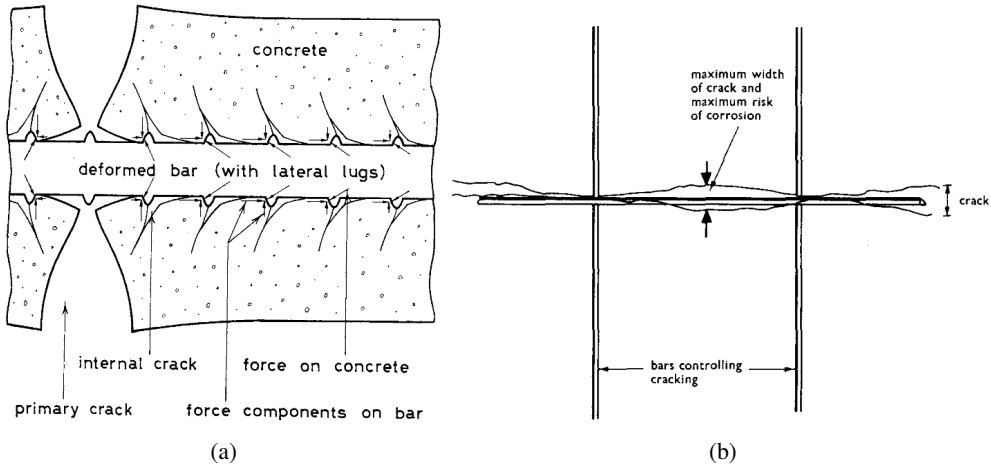


Figure 8.1: (a) Formation of internal cracks around reinforcing steel [101] (b) wider cracks at a distance from rebar [4].

Watstein and Parsons introduced an empirical coefficient consisting of the term  $(h - d)/h$  to account for the effect of cover on calculated crack width. He predicted crack width of beams and one-way slabs with satisfactory results. Goto [101] discusses the development of internal cracks at the concrete-rebar interface and mentions that crack width at the rebar level is much smaller than at the surface (Fig. 8.1(a)). In [15], effect of distance from rebars on crack pattern and spacing is illustrated and, Beeby [4] highlights the importance of measurement of crack width as far from the rebars as possible, normally mid-way between rebars, as widest cracks may form at largest distance from rebars (Fig. 8.1(b)). Caldentey et al. [152] attributes the wider crack widths away from the rebars, to the closing of secondary cracks which leaves a wider passing crack.

Leonhardt [129], referring to results of Goto [101], and also taking into account that crack width increases with increasing rebar spacing, suggested the following formula for minimum crack spacing:

$$S_{r,min} = l_0 + \underbrace{k_1(c, a) + k_2 k_3 \frac{\phi}{\rho_{t,ef}}}_{\text{transfer length}} \quad (8.1)$$

$l_0$  is the no bond region. Leonhardt gives two relationships for this parameter,  $\sigma_{sr}/45\phi$  and  $6\phi$  depending on the stress in rebars. Other relationships can be found for this length [165].  $k_1$  is an empirical coefficient taking into account the effect of cover and distance from rebar,  $k_2$  takes into account the ratio between tensile strength and shear along the rebar-concrete

interface, and  $k_3$  accounts for the distribution of stresses at the cross section with a value of 0.25 for pure tension and 0.125 for pure bending. Balázs and Borosnyói [10] list twenty four different formulations for estimation of crack spacing which may signify the extent of disagreement on the topic. Very often, the formulations take into account the effect of cover and the transfer length. Cover thickness affects the crack spacing due to some length required for diffusion of stresses [152], or equally by relating it to shear lag [20], and the effect of transfer length comes directly from the bond-slip phenomena. In EC2 the following relationships are given in chronological order from 1992 to 2021:

$$S_{r,max} = 1.7 (50 + 0.25k_1k_2\phi/\rho_{ef}) \quad (8.2a)$$

$$S_{r,max} = 1.7 (2c + 0.25k_1k_2\phi/\rho_{ef}) \quad (8.2b)$$

$$S_{r,max} = k_w \left( 1.5c + \frac{k_{fl}k_b}{7.2} \frac{\phi}{\rho_{ef}} \right); \quad (k_w = 1.7) \quad (8.2c)$$

Eq. 8.2(a) and 8.2(b) are the same other than the fact the effect of cover thickness is considered as a fixed value in Eq.8.2(a). In both equations  $k_1$  is related to bond properties and  $k_2$  represents the fact that in bending a triangular distribution of tensile strain leads to larger stress values in concrete to equilibrate the force transmitted from rebars through bond-slip. In the new version of EC2, Eq. 8.2(c), some modifications are applied to the formula. The effect of cover thickness is reduced in comparison to Eq.8.2(b). In comparison to Eq.8.2(a) and 8.2(b) the  $k_1$  coefficient is replaced by the direct introduction of  $f_{ctm}/\tau_{bms}=1.8$ , and  $k_{fl}$  replaces  $k_2$  to reflect that it is not actually the whole tensile zone that is responsible for taking the bond stresses, but rather the effective area around the bar [153]. The  $k_b$  coefficient is added to reflect the longer anchorage length needed due to “top bar effect” [120] which has been shown to affect cracking behavior of RC elements [153]. For bar spacing,  $s > 10\phi$ , the maximum crack spacing is limited to  $1.3(h - x)$ .

In MC2010 maximum crack spacing is formulated for a tie element:

$$S_{r,max} = 2 \left( kc + \frac{1}{4} \frac{f_{ctm}}{\tau_{bms}} \frac{\phi}{\rho_{ef}} \right) \quad (8.3)$$

with  $k=1$  and  $\tau_{bms} = 1.8f_{ctm}$  as commonly adopted. For long term loading for crack formation stage  $\tau_{bms} = 1.3f_{ctm}$  is proposed. Clearly this approach fails to capture the nature of a bent element. In the new edition of MC2020, this relationship is replaced by the following formula which is in line with the proposition of EC2:

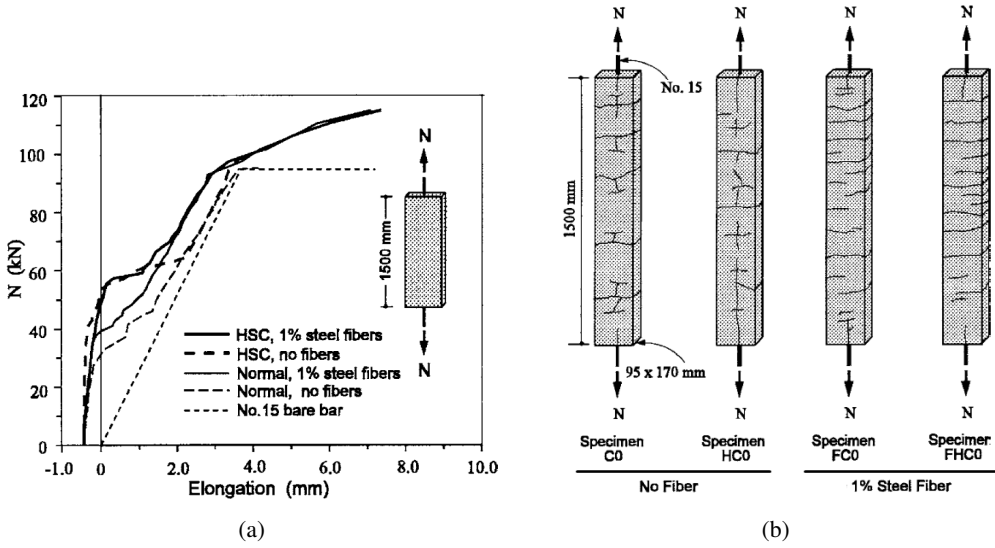


Figure 8.2: (a) Response of ties and (b) crack patterns [1].

$$S_{r,max} = \beta_w \left( k_c c + k_{\phi/\rho} k_{fl} k_b \frac{f_{ctm} \phi}{\tau_{bms} \rho_{s,ef}} \right) \quad (8.4)$$

Here,  $\beta_w=1.7$ ,  $k_c=1.5$ ,  $k_{\phi/\rho}=0.25$ , and  $k_{fl}$ , and  $k_b$  represent the same notion as of in Eq. 8.2(c), although the relationship given for  $k_b$  is slightly different.

Addition of fibres to concrete affects the cracking behaviour due to improved bond between rebars and concrete, and the post-cracking tensile strength of FRC [197]. Narrower and more closely spaced cracks are obtained with the addition of fibers [91, 146, 177, 191, 197] and for sustained loading, fibers stabilize the increase of the crack widths at an earlier age [191]. One of the first studies on the effect of fibres on tension-stiffening and cracking behaviour of R/FRC ties was carried out by Abrishami and Mitchell [1], the results of which is shown in Fig. 8.2. Smaller crack spacing was obtained for specimens in which 1% of fibres were added and splitting cracks were eliminated. Bischoff [30] tested plain concrete and SFRC ties and derived tension stiffening bond factor,  $\beta$ , as the ratio between average tensile force in concrete to the tensile force in concrete at first crack,  $P_{cm}/P_{cr}$ . Larger tension stiffening in SFRC specimens led to reduced crack spacing and crack width.

Of the first formulations for computation of mean crack spacing in FRC elements was the one suggested by Vandewalle [197] which was based on the original formula given in EC2:1992. This empirical formulation was relating

the average crack spacing to the inverse of fibre aspect ratio:

$$S_{r,m} = (50 + 0.25k_1k_2\phi/\rho_{ef}) (50/(L/\phi)) \quad (8.5)$$

with  $50/(L/\phi) \leq 1$ . Few years later Dupont and Vandewalle [79] proposed a physical model based on bond stress-slip relationship for R/FRC beams which predicted crack opening of full scale beams under a four-point bending test. In MC2010 maximum crack spacing for FRC elements was given as:

$$S_{r,max} = 2 \left( k_c + \frac{1}{4} \frac{\phi_s}{\rho_{ef}} \frac{(f_{ctm} - f_{Ftsm})}{\tau_{bm}} \right) \quad (8.6)$$

which accounted for the transmitted stress at the crack by introduction of  $f_{Ftsm}$ , the average residual tensile strength at SLS, into the equation. For an RC tie, the force that is transmitted to concrete through bond is  $f_{ctm}A_c(1 + \alpha_e\rho_{ef})$ . Addition of fibres reduces this force to  $(f_{ctm} - f_{Ftsm})A_c(1 + \alpha_e\rho_{ef})$  which is expressed in Eq.8.6. In the latest versions of MC2020, the formulation given for computation of crack spacing for RC flexural members is modified by the introduction of the coefficient  $(1 - f_{Fts,ef}/f_{ctm})$  to be implemented for FRC elements. In this formulation the effective value of residual strength of FRC is considered, values that are obtained based on the class of the material and after the introduction of the effect of orientation. This is different from MC2010 approach in which the average value of residual tensile strength,  $f_{fts,m}$ , is taken into account. Formulations given in MC2020 and EC2 1992:2020 are:

$$S_{r,max} = \beta_w \left( k_c c + k_{\phi/\rho} k_{fl} k_b \frac{f_{ctm} \phi}{\tau_{bms} \rho_{s,ef}} \right) \left( 1 - \frac{f_{Fts,ef}}{f_{ctm}} \right) \quad \text{in MC2020} \quad (8.7a)$$

$$S_{r,max} = k_w \left( 1.5c + \frac{k_{fl} k_b}{7.2} \frac{\phi}{\rho_{ef}} \right) \left( 1 - \frac{f_{Fts,ef}}{f_{ctm}} \right) \quad \text{in EC2} \quad (8.7b)$$

Nawy [143] recognizes some differences between cracking behavior of two-way slabs with beams and one-way slabs and shows some relationship between crack spacing and mesh index, defined as  $\phi_1 S_2 / P_{t_1}$  or  $\phi_2 S_1 / P_{t_2}$ , for two-way slabs reinforced with welded wire fabrics. Wider rebar spacing in transverse direction led to larger crack spacing. Rizkalla et al. [165] investigated the effect of presence of reinforcement in both directions on cracking behaviour of RC members in uniaxial tension. If a crack was expected to form close to the position of a transverse rebar, these rebars determined the position of the propagated crack. Desayi and Kulkarni in [66], and Rizkalla and Marzouk in [164] introduce the effect of transverse rebars in two-way concrete plates to find a reduced crack spacing for these elements.

In [66] they assume that the transverse rebars exert bearing stresses on the surrounding concrete, and in [164], splitting bond stresses of the transverse rebars are taken into account. Despite of differences between two-way plates, with beams and one-way plates, the same formulations are given in current codes and standards for computation of crack spacing.

### 8.3 Maximum crack spacing, $S_{r,max}$

The maximum crack spacing formulations are given for the calculation of design crack width. In general terms this is expressed as:

$$w_k = S_{r,max} (\epsilon_{sm} - \epsilon_{cm} + \eta_r \epsilon_{cs}) \quad (8.8)$$

with  $w_k$  being the 95% fractile of maximum crack width,  $\epsilon_{sm}$  and  $\epsilon_{cm}$  being the average strain of steel and concrete between cracks, and the last term in the parenthesis takes into account the effect of shrinkage. In CEB FIP Model Code 1978, maximum crack opening is given as:

$$w_k = 1.7w_m \quad (8.9)$$

This is an important parameter and its determination plays a key role when durability of structures are of interest. This formula implies that  $S_{r,max} = 1.7S_{r,m}$ , which is consistent with the formulations given in EC2 and MC2020. With a view on this, the relationship between minimum, average and maximum crack spacing is further looked into.

In MC2010 and also in CEB FIP ModelCode 1990, maximum crack spacing is expressed as  $S_{r,max} = 2l_{s,max}$ , with  $l_{s,max}$  denoting the length over which slip between concrete and steel occurs, which is in fact the minimum crack spacing. This is a deterministic approach in the assessment of cracks spacing. If the second crack propagates at a distance slightly smaller than twice the minimum crack spacing, no more cracks can propagate between the two. If the second crack propagates slightly further away, one crack can appear between the two. Therefore the maximum spacing is twice the minimum crack spacing. In this manner it can be deduced that the average crack spacing would be the average of the minimum and maximum crack spacing,  $S_{r,m} = 1.5S_{r,min}$  (This is not explicitly reported in MC2010). A probabilistic approach takes into account what happens if the second crack occurs at a distance more than two and less than three transfer lengths, or between three and four times of transfer length, and based on these assumptions derives an average crack spacing equal to  $S_{r,m} = 1.3S_{r,min}$  [29]. Borosnyói and Balázs [10] based on an investigation of available results in the literature report  $1.3 \leq S_{r,m}/S_{r,min} \leq 1.5$ . Although



in EC2, there is no argument on the minimum crack spacing, but given that in this standard the deterministic approach for assessment of crack spacing is not adopted, assumption of a ratio of 1.3 between the average and minimum crack spacing might be reasonable. Referring to Eq.8.9, the ratio between the maximum and minimum crack spacing for EC2 and MC2010 will be:

$$S_{r,max} = 1.7 \times S_{r,m} = 1.7 \times (1.3 \times S_{r,min}) = 2.21 \times S_{r,min} \quad (8.10)$$

Comparing these values with what can be inferred from MC2010 formulations, we'll have:

$$(S_{r,max}/S_{r,min})_{MC2010} = 2 < (S_{r,max}/S_{r,min})_{EC2} = 2.21 \quad (8.11a)$$

$$(S_{r,m}/S_{r,min})_{MC2010} = 1.5 > (S_{r,m}/S_{r,min}) = 1.3 \quad (8.11b)$$

Maximum crack spacing formulations in EC2 and MC2010 are arranged in the following format:

$$S_{r,max_{EC2}} = (k_w = 1.7) \times S_{r,m,EC2}$$

$$S_{r,max_{MC2010}} = 2 \times S_{r,min,MC2010}$$

Apart from different arrangement of formulas, there is a fundamental inconsistency between the two, that the average crack spacing of EC2 obtained from one of the expressions in parenthesis of Eq.8.2, is practically smaller than the minimum crack spacing of MC2010 given in the parenthesis of Eq.8.3,  $S_{r,m,EC2} < S_{r,min,MC2010}$ . It seems that MC2010 systematically gives larger values for maximum crack spacing of RC elements.

In Chapter 16 of MC2020 where FRC is dealt with,  $S_{r,m} = 0.75S_{r,max}$  is given, which is different from the relationship given in Eq.8.4 for RC elements according to which  $S_{r,m} = (1/1.7 = 0.58) \times S_{r,max}$ . It is not clear if this is an inconsistency or whether a different relationship between average and maximum crack spacing is considered for FRC elements. This relationship in MC2020 is justified through:

$$\frac{S_{r,m}}{S_{r,max}} = \frac{1.5 \times l_{s,max}}{2 \times l_{s,max}} = 0.75 \quad (8.12)$$

However, these expressions are adopted from MC2010 and they do not agree with the content of MC2020.

Provisions of EC2 for RC elements hold that when rebars spacing is larger than a limit, the maximum crack spacing is given as  $S_{r,max} = 1.3(h - x)$ . For plain concrete, average crack spacing in bent condition is commonly taken as  $(h - x)$  or  $h$ . To be consistent with the provisions of EC2 where a ratio of 1.7 is

considered between average and maximum crack spacing, it not unreasonable to investigate also  $S_{r,max} = 1.7(h - x)$  as the maximum crack spacing when rebars are placed at large distances. Specifically, when fibres are introduced in concrete with the goal to reduce the amount of reinforcing rebars, it is possible that this situation would dominate the crack spacing formulation. It would be also of interest to check the multiplication of  $(1 - f_{fts,ef}/f_{ctm})$  to these relationships when fibres are adopted.

Although a study on the cracking behaviour is not a main part of the present study, the predictions given by different standards are compared with the experimental results obtained for the tested shallow beams and plates. These comparisons are carried out once with material properties driven from tests close to the age of testing of the beams and plates, and once with the 34 days material properties, the design situation. In all cases, the effect of fibres is introduced by considering the class of material, with the exception of MC2010 in which average properties are considered. Furthermore, an overall comparison is made between average and maximum crack spacing of different plates in order to investigate if, and to what extent, fibres may affect the cracking behaviour of plate elements. Some slight modifications and some suggestions are given based on the obtained results.

## 8.4 Experimental results

### 8.4.1 Shallow beams

In this section a closer examination of the cracking behaviour of the tested shallow beams, the results of which were presented in Chapter 6, is carried out. Fig. 8.3 shows the crack spacing in the six tested beams and the spacing of the cracks. For B-FRC beams, formation and distance of cracks is very much dependent on the heterogeneity of the material and the very local properties of the SFRC material both along the length of the beam and through the depth. Testing the beams in a four-point bending setup, the first crack forms at the weakest section at the bottom of the beam and along the constant bending moment zone. This leads to the elastic unloading of the vicinity of this crack to a width that can be related to the characteristic length. Whether more cracks can propagate or not, lies strongly on the sectional response at the position of the first crack. The local properties of concrete, orientation, position, and number of fibers at this cross section may or may not allow for an increase in the load. For instance, for the B-FRC1 specimen, after the propagation of the first crack, there is a sudden reduction of the load, and upon hardening after larger deflection, the load can not surpass the first cracking load and

as such, no more cracks propagate, Fig. 6.3. Very differently, the two other companion beams manage to accommodate more number of cracks. For B-FRC2 beam where the rotation of the loading head was blocked due to an experimental error, the capacity of redistribution is undermined as very likely, after some deformation only one of the loading knives comes into direct contact with the beam, nevertheless, it can be observed that after the first crack, the load increases with the propagation of more cracks. The same behavior is observed for B-FRC3 with the largest number of cracks and a larger increase in load after the first cracking point. These results highlight the importance of redistribution capacity for FRC structural members. Although a statically determined scheme like a four-point bending setup still possesses some inherent redundancy in that many cracks can form in the middle span, the redistribution capacity is very limited and depends on the local response of the material.

Fig. 8.4 compares the experimental crack spacing for the B-FRC3 and the B-R/FRC beams with available recommendations based on the tensile properties obtained at an age close to the testing age of the beams, to get a realistic estimation of the crack spacing, and Table 8.1 depicts these values based on the 34 days material properties, what is carried out in a design process. Each vertical line in Fig. 8.4 is related to one side of a specimen and the average, minimum and maximum values of crack spacing are illustrated by these lines. Horizontal lines are the predictions made by different standards. The experimental ratio of  $S_{r,max}/S_{r,m}$  for each side of each shallow beam is written on the figure.

According to Fig. 8.4, none of the relationships are able to predict the average and maximum crack spacing values. The best prediction for  $S_{r,m}$  comes from the formula that is implicitly inferred from EC2 1992:220,  $S_{r,m} = (h - x)(1 - f_{fts,ef}/f_{ctm})$ . Yet introduction of a coefficient of 1.3 to this average value, fails to capture the maximum experimental crack spacing value. The experimental ratio  $S_{r,max}/S_{r,m}$  is very close to 1.7 for all B-R/FRC specimens (smaller for one side of B-R/FRC3 beam) which is a testimony to the adopted value in the codes. It will be shown later that this ratio holds also for cases where the only reinforcement is fibres.

The predictions for maximum crack spacing by MC 2010 and MC2020 is very close to the average crack spacing. The 220 days results of the SFRC material with an assumption of a orientation factor  $\kappa_0=1$ , give a  $f_{fts,ef}=1.48$  MPa. The tensile strength of the SFRC at the age of test would be around  $f_{ctm}=3.8$  MPa, found through the same approach adopted in Chapter 7 taking

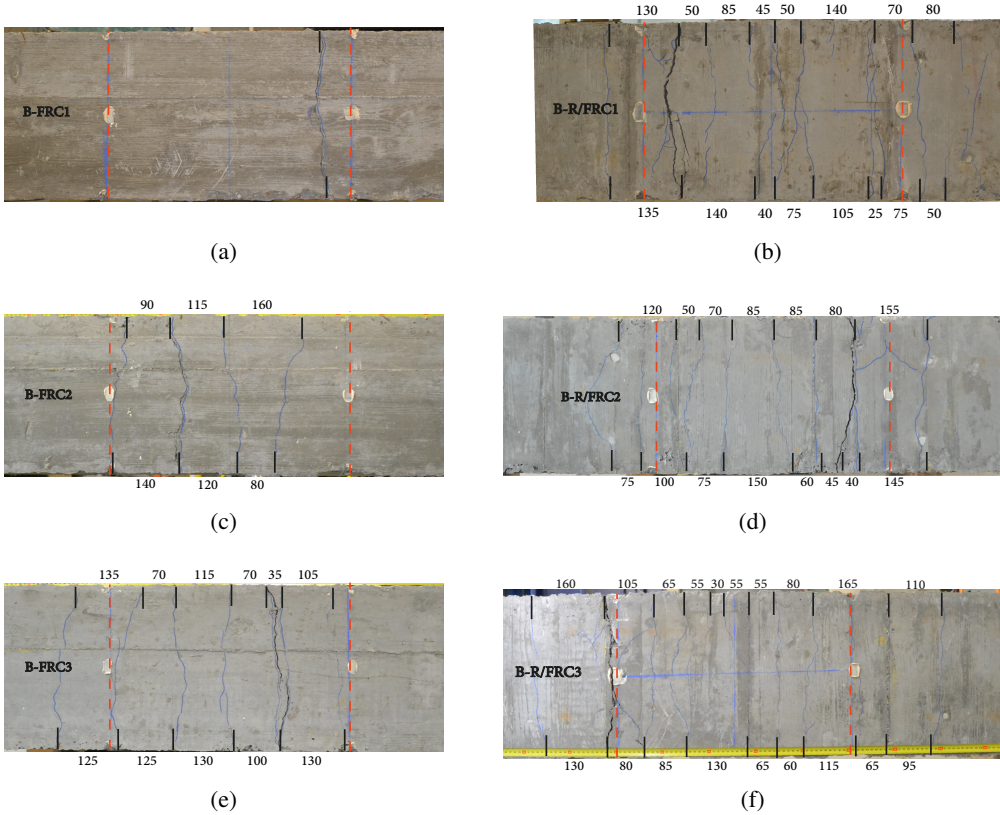


Figure 8.3: The image of cracks at the bottom of the beams.

into account the age and curing temperature of the cube specimens (at 34 days of age,  $f_{ctm}=3.5$  MPa was obtained based on the results of the compression tests). This means that the coefficient  $(1 - f_{fts,ef}/f_{ctm})=0.61$ . Accordingly, the spacing of cracks in this elements is expected to be around 60% of a similar specimen without fibres. Although fibres are very effective in reducing crack spacing, such reduction in crack spacing by incorporation of  $35 \text{ kg/m}^3$  of 4D fibres with an aspect ratio of 66, might be an exaggeration. Vandewalle [197] with  $45 \text{ kg/m}^3$  of fibres with aspect ratio of 80, achieved 60% of crack spacing w.r.t to the reference RC beams. Therefore, seemingly, the coefficient  $(1 - f_{fts,ef}/f_{ctm})$  may overestimate the effect of fibres in reducing crack spacing.

For the B-FRC3 beam, it is observed that the average crack spacing is smaller than the commonly adopted value of  $S_{r,m} = h = 150$  mm. The larger difference between minimum and maximum crack spacing on one side of this specimen is due to the fact the one crack diverges in two cracks on this side of

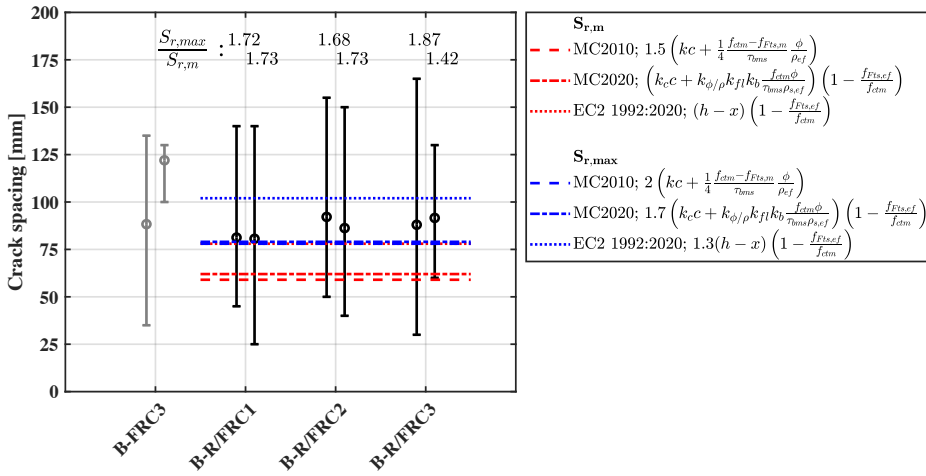


Figure 8.4: Illustration of minimum, average, and maximum crack spacing for each side of the B-FRC3 and B-R/FRC shallow beams and comparison of experimental crack spacing with average and maximum crack spacing formulations from MC2010, MC2020, and EC2. The tensile strength and residual strength parameters for the FRC are taken from the tests closer in age to the tested beams. The experimental ratio of  $S_{r,max}/S_{r,m}$  for each side of the B-R/FRC beams is written on the figure.

the beam leading to a smaller crack spacing.

If the computation of crack spacing for the B-R/FRC beams is carried out with the material properties obtained from characterization tests at 34 days of age, which is normally available to a designer, the results reported in Table 8.1 will be obtained which can be compared with the experimental values of  $S_{r,m}$  and  $S_{r,max}$ . What changes these predictions is the variation in the values  $f_{ctm}$ ,  $f_{ft,m}$ , and  $f_{ft,ef}$ . The SFRC material under study, exhibits a sizable enhancement in its post-peak tensile parameters from 34 days to 220 day (the latter results were implemented for the computations that were depicted in Fig. 8.4). This means that the effect of fibres on the results based on 34 days characterization tests will be less than those reported earlier. Nevertheless, still maximum crack spacing values are not captured by the adopted formulations.

### 8.4.2 Plates; Part A

The spacing of cracks for plates are measured on the constructed crack pattern of these specimens based on multiple photos that were taken from the bottom of the plates after each test. The crack spacing is measured on the edge of the plates. Fig. 8.5 to 8.7 depict the results related to the plates tested in Part A of the experimental campaign. For each plate element, four

Table 8.1: comparison of experimental crack spacing values with predictions of different codes based on the characterization tests at 34 days of age for the concrete.

Specimen	$S_{r,Experimental}$ [mm]			MC2010 [mm]		MC2020 [mm]		EC2 [mm]	
	Ave	min	max	$S_{r,m}$	$S_{r,max}$	$S_{r,m}$	$S_{r,max}$	$S_{r,m}$	$S_{r,max}$
B-R/FRC1	81.25	45	140						
	80.62	25	140						
B-R/FRC2	92.14	50	155	91	121	62	105	89	115
	86.25	40	150						
B-R/FRC3	88	30	165						
	91.6	60	130						

measurements are reported, each related to one side of the specimen. For each side, the average crack spacing and the minimum and maximum values are shown. The horizontal lines are related to the prediction of maximum crack spacing,  $S_{r,max}$ , given according to different standards. The tensile strength parameters in these formulas are first adopted from the notched specimens that were tested closer in age to the plates, so that a realistic prediction can be made. Afterwards, for the R/FRC plates, the 34 days tensile properties that correspond to a design situation are taken into account and predictions are repeated based on these values. These results are reported in Table 8.2. It is very important to have in mind that the measurements were carried out on the edge of the plates, where the cracks are more distantly positioned. However larger distance of the cracks can not be translated to wider crack openings because the stress of rebars in these regions that are far from the loading point are smaller than the rebar stress in the vicinity of the concentrated load. Therefore, the maximum crack spacing values that correspond to the widest cracks are most probably closer to the average crack distance measured at the edge of the plates.

For the S1 plates, the cracks are formed in a diagonal manner which makes an angle with the rebars. As the cracks are not parallel to each other, the measurement of spacing is influenced by the distance from the loading point. Hence the comparisons made are affected by the fact that the spacing of cracks is measured at the edge of the plates. In EC2 1992:2003, for cracks that are formed with an angle w.r.t to the rebars, the maximum crack spacing is given as:

$$S_{r,max} = \frac{1}{\frac{\cos(\theta)}{S_{r,max,y}} + \frac{\sin(\theta)}{S_{r,max,z}}} \quad (8.13)$$

where the  $S_{r,max,y/z}$  are the maximum crack spacings in the two direction.

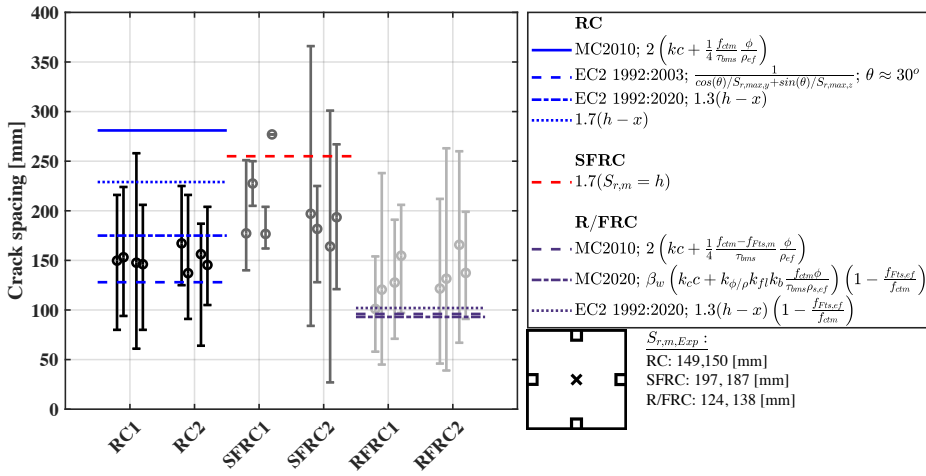


Figure 8.5: Minimum, average, and maximum crack spacing for each side of the S1 series plates and the comparison with predictions of different standards for the maximum crack spacing. The average crack spacing values are given in the lower bottom right part of the figure.

Here, an angle of  $\theta = 30^\circ$  is assumed and as the spacing of rebars are  $s > 5(c + \phi/2)$ , therefore the maximum crack spacing would be  $1.3(h - x)$ . For the RC plates, the MC2010 approach overestimates maximum crack spacing and the EC2 formulations considerably fail to capture experimentally obtained  $S_{r,max}$ . Proposition of  $S_{r,max} = 1.7(h - x)$  gives a better prediction. On one side of the SFRC1 plate, only two cracks reach to the edge, and this side is represented by one marker which shows the spacing between these two cracks. Overall, crack spacing for the SFRC plates of S1 series shows a large variation with very small and very large spacing values. For the R/FRC plates the predictions fail miserably to predict  $S_{r,max}$ . Comparison of the experimentally obtained maximum crack spacing for the RC and R/FRC elements show that fibres do not have much effect on this parameter. Regarding the average crack spacing of the plates, which are indicated in the right bottom corner of the figure, slightly smaller spacing for the R/FRC plates are achieved w.r.t to the RC companions. However the reduction in average crack spacing is much smaller than the ratio given as  $(1 - f_{Fts,ef}/f_{ctm})$ . This ratio for the age at which the plates are tested is close to 0.58. However, on average, adding fibres led only to a 13% reduction in the average crack spacing in the R/FRC plates in comparison to the RC ones.

Cracks in S2 configuration pass through the middle of the supports in a fashion that is more similar to the crack pattern of a beam tested under flexure,

which is very often the case for which crack spacing formulas are calibrated for. Therefore the predictions of the standards are expected to achieve results which are closer to the experimental crack spacing values. However, the results, specifically for the R/FRC plates, prove otherwise. For the RC plates  $S_{r,max} = 1.7(h - x)$  gives a relatively satisfactory prediction for  $S_{r,max}$ . For the SFRC plates,  $S_{r,max} = 1.3h$  gives a proper estimation for maximum crack spacing. When the cracking response of the twelve identical SFRC plates of *Part B* are scrutinized in the next sections, it will be shown that  $1.3h$  is closer to the average of the maximum crack spacing values and not the characteristic value that is of interest in computation of maximum crack width. For these two SFRC plates  $1.7h$  is too safe of a prediction for  $S_{r,max}$ . Still, for the R/FRC plates, the introduction of the effect of fibres to the original formulas given for the RC elements gives a substantial underestimation to the experimental maximum crack spacing results. The prediction is even smaller than the average crack spacing for these plates. An interesting observation is the smaller crack spacing of the R/FRC-Alt plates in comparison to the other specimens. In Appendix 9.1 where the crack patterns and spacing for each specimen is shown separately, it can be seen that for the R/FRC-Alt plates, many of the cracks tend to fork when approaching the edge of the plates. This is why the average crack spacing measured at the edges of these elements are even smaller than the crack spacing of the R/FRC plates. If the crack spacing was not measured on the edge of the plates but with some distance from the side, the crack spacing would have been closer to the other plates.

A glance at the experimental maximum crack spacing values in Table 8.2 for the RC and R/FRC plates, suggests that fibres, may only slightly reduce this value. SFRC plates display even smaller maximum crack spacing when juxtaposed against the RC and R/FRC companions. This is certainly at the cost of much more confined overall cracked area in these elements. In relation to the measured average crack spacings for the RC and R/FRC specimens, it is not easy to draw any conclusions. The RC4 plate shows much more cracks than probably expected when set side by side the RC3 and the R/FRC companions (see crack patten in Fig. 8.6). If the average crack spacing of the RC3 plate is considered as the basis for comparison, addition of fibres accounts for a 8% reduction in crack spacing in the R/FRC plates.

For the S3 series, the cracks patterns are more irregular and there are cases where the cracks do not reach to a side, specifically the opposite side of the loaded edge, or in certain instances only two cracks reach to an edge, leaving only one spacing value. For the SFRC plates of this series, propagation of few cracks deters any reasoning on their behaviour and the presentation of the



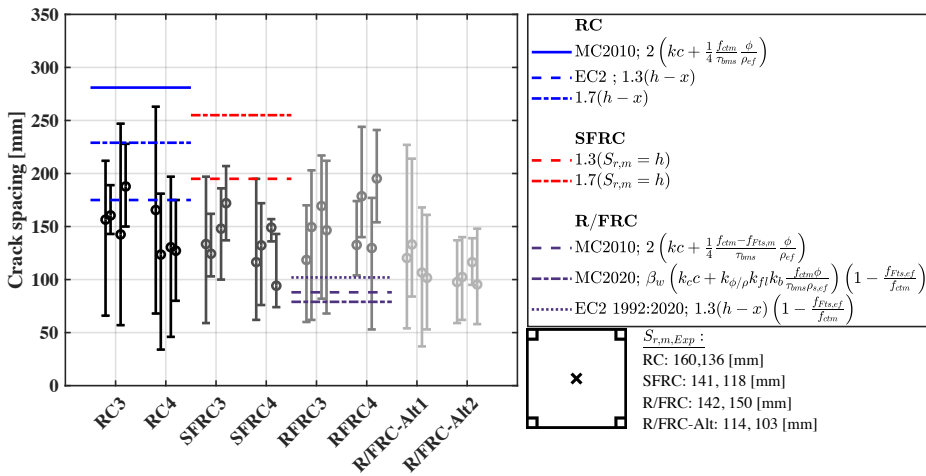


Figure 8.6: Minimum, average, and maximum crack spacing for each side of the S2 series plates and the comparison with predictions of different standards for the maximum crack spacing. The average crack spacing values are given in the lower bottom right part of the figure.

results of these elements are only for the sake of completeness. Comparison of the experimental results with the predictions are not much different from the two other series. For this configuration of loading and support, the effect of fibres in reducing the average and maximum crack spacings is more evident when the results of the RC and R/FRC plates are compared. Moreover, there seems to be a much less variation between the maximum crack spacing on different sides of the R/FRC plates which may indicate a more uniform behaviour and a better redistribution of stresses (Apart from the opposite side of the loading edge in R/FRC6 plate to which only two distant cracks reach). This is noteworthy specially when robustness of structures are in mind. Presence of fibres allow for a better distribution of stresses preventing to some extent the premature formation of areas of localized damage. In this manner, the damage coming from loading conditions for which the structure is not originally designed for, may be reduced and retained.

In Table 8.2 the values of minimum, average, and maximum crack spacings are reported for plates of *Part A* and predictions for spacing values related to the R/FRC plates are given based on the 34 days material characterization tests. The experimental measurements are averaged for the four sides of each element and only one value is reported. It is evident, that predictions still fail to capture the experimental measurements.

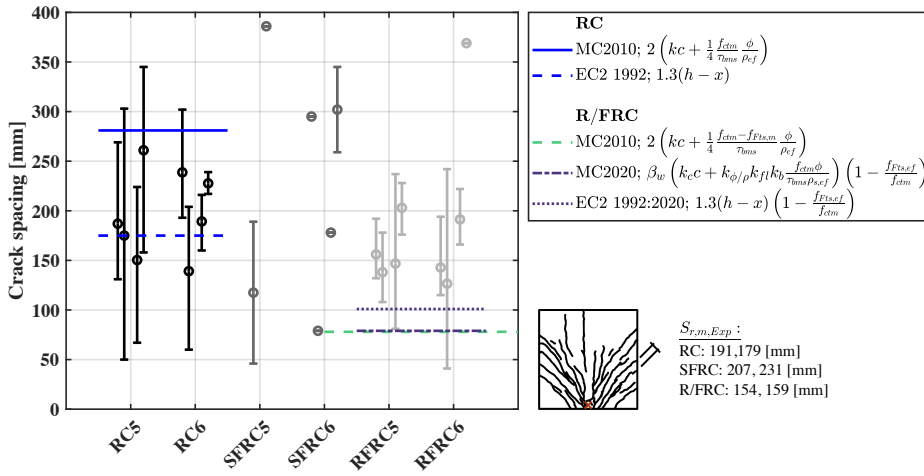


Figure 8.7: Minimum, average, and maximum crack spacing for each side of the S3 series plates and the comparison with predictions of different standards for the maximum crack spacing. The average crack spacing values are given in the lower bottom right part of the figure.

### 8.4.3 Plates; Part B

In this section, the crack spacing of the twelve identical SFRC plates tested in *Part B* of the experimental program are studied. Each side of each plate element is taken into account separately, which gives a sufficiently large sample for regression analysis of the results. Fig. 8.8(a) demonstrates the minimum, average and maximum crack spacing of each side of the twelve plates. The average experimental crack spacing,  $S_{r,m}=122$  mm is obtained. For FRC, in the absence of rebars, crack spacing is presumed to have an average distance of  $h$ . For the tested plates average spacing of cracks is almost 25% smaller than  $h=150$  mm. Fig. 8.8(b) depicts the relationship between minimum and maximum crack spacing with the average measurements. Minimum crack spacing is not a decisive parameter, and there is no explicit reference to its value in any of the standards. As mentioned earlier, it can be inferred through the lines of MC2010 that in this standard  $S_{r,m}/S_{r,min}=1.5$ , while a probabilistic approach suggests  $S_{r,m}/S_{r,min}=1.3$ . The results obtained for the twelve SFRC plates find a ratio of  $1/0.61=1.64$  between the average and minimum crack spacing.

The relationship between  $S_{r,max}$  and  $S_{r,m}$  can be found with two different perspectives. One is to find the relationship between direct measurements; the red line in Fig. 8.8(b), and the other to find the characteristic value of  $S_{r,max}$ , 95% fractile, which is the the value expressed in the codes that affects the

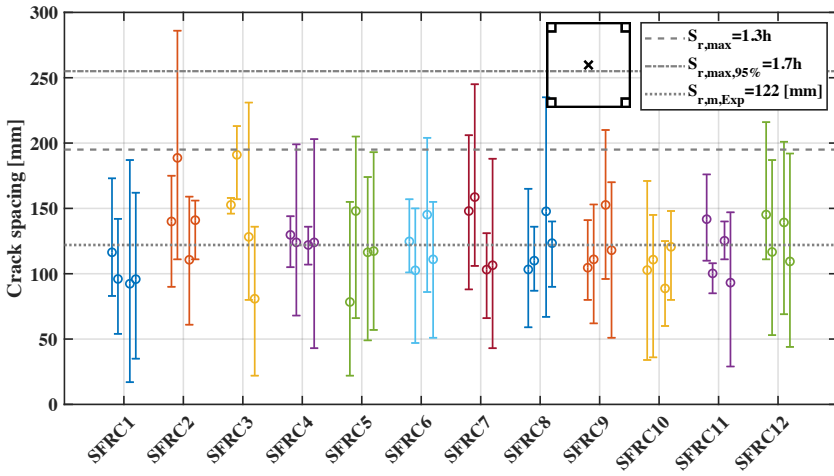
Table 8.2: The experimental values of minimum, average, and maximum crack spacing for Part A plates with the predictions made for the R/FRC plates with the 34 days tensile properties of the SFRC material.

Reinforcement	Series	$S_{r,Exp}$			MC2010		MC2020		EC2	
		ave	min	max	$S_{r,m}$	$S_{r,max}$	$S_{r,m}$	$S_{r,max}$	$S_{r,m}$	$S_{r,max}$
RC	S1	149	61	258						
		150	64	225						
	S2	160	57	247						
		136	34	263						
	S3	191	50	345						
		179	60	302						
SFRC	S1	197	140	277						
		187	27	366						
	S2	141	59	207						
		118	62	195						
	S3	207	46	386						
		231	79	345						
R/FRC	S1	123	45	238						
		138	39	263						
	S2	142	60	217	91	121	59	101	89	115
		150	53	244						
	S3	154	81	237						
		159	41	369						
R/FRC-Alt	S2	114	37	227						
		102	58	148						

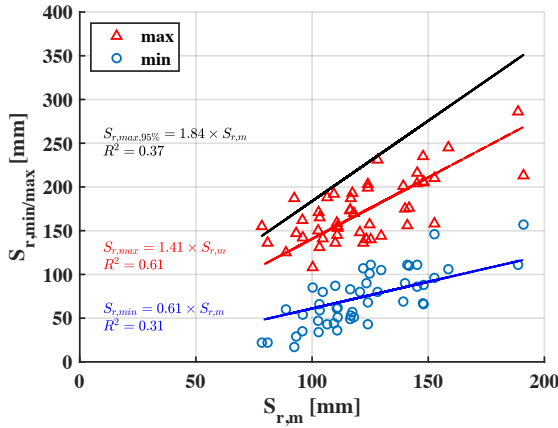
design crack width,  $w_k$  or  $w_{k,cal}$  following the notation given in MC2020 and EC2 1992:2020 respectively. For the SFRC plates,  $S_{r,max,95\%} = 1.84S_{r,m}$  is obtained which is slightly larger than the commonly adopted relationship of  $S_{r,max} = 1.7S_{r,m}$ . Here each four sides of the plates are considered as an independent measurement, while if the average of the maximum spacing among the four sides of the plates were taken as the basis of comparison, a smaller coefficient, closer to 1.7 would have been obtained.

## 8.5 Suggestions to MC2020 and EC2 1992:2020 formulations

None of the available formulations were capable of predicting the maximum crack spacing of the R/FRC elements. Other than  $(h - x)(1 - f_{fts,ef}/f_{ctm})$  that gave a close estimate for the average crack spacing for the shallow beams, Fig. 8.4, in all instances the adopted formulations underestimated crack spacing by large margins. The goal of this chapter is not to propose new



(a)



(b)

Figure 8.8: (a) Minimum, average and maximum crack spacing for each side of the twelve nominally identical SFRC plates and (b) the relationship between minimum and maximum crack spacing with the average spacing of the cracks.

formulations, because the comments made here are based on few specimens with the same conditions. However, based on the knowledge on the affecting parameters, and relying on our understanding of the behaviour of FRC, some possible suggestions are given, which need to be tested.

As it was shown in the previous chapters, the average residual strength parameters of the SFRC material is capable of explaining the overall structural response of the beams and plates. Despite of heterogeneity of the material, when the overall behaviour in which, the bulk of the material is engaged,

is of concern, average properties can adequately explain the behavior. In these general circumstances, and as long as the macro-behaviour is at stake, a quasi-isotropic fibre distribution with a orientation factor of  $k_0=1$  was adopted implying that fibre orientation was assumed not to be different from what we get in a three-point bending test ( $k_0 = \alpha_0/0.58$ ). Surely this does not always hold true and depends on numerous factors. Nevertheless, when a local phenomena like propagation of cracks are investigated, neglecting heterogeneity and orientation effects might be unreasonable. In MC2020, in the absence of experimental investigations, a  $k_0=0.5$  is suggested for local checks. This can be extended to computations of crack spacing and specifically for maximum crack spacing.

In the MC2020 formulation, the coefficient  $(1 - f_{fts,ef}/f_{ctm})$  is multiplied to both terms related to crack spacing, namely the cover effect and transfer length. This coefficient comes from equilibrium of shear bond with concrete strength and stresses at the cracks and should not affect the term related to cover thickness. Influence of fibres on the effect of cover on crack spacing depends on presence of rebars, thickness of cover, and length of the fibres. Presence of rebars leads to a layer of accumulation of fibres above the rebars [210], reducing the number of fibres in cover thickness. Moreover, for the beams and plates tested in the present study, length of fibres is twice the cover thickness, which can restrict the reaching of the fibres to this zone. This is schematically shown in Fig. 8.9 (Adapted from [210]). For the beams, this figure could be an exaggeration of this effect, because the fibres are mainly carried by the longitudinal flow of concrete along the beam, while this figure is showing the transversal flow of concrete relative to the rebar. Nevertheless, the relative dimension of fibres and cover thickness may to varying degrees affect the presence and distribution of fibres within the cover thickness. As such, multiplying the reduction factor to the cover effect may lead to an underestimation of crack spacing values.

With regards to these explanations, the MC2020 formulation for R/FRC elements is modified in the following form:

$$S_{r,max} = \beta_w \left( k_c c + k_{\phi/\rho} k_{fl} k_b \frac{f_{ctm} \phi}{\tau_{bms} \rho_{s,ef}} \left( 1 - \frac{\kappa_0 f_{fts,ef}}{f_{ctm}} \right) \right) \quad (8.14)$$

For elements in which the spacing of rebars are larger than  $10\phi$  the expression given in EC2 is modified in the following form:

$$S_{r,max} = 1.7(h - x) \left( 1 - \frac{\kappa_0 f_{fts,ef}}{f_{ctm}} \right) \quad (8.15)$$

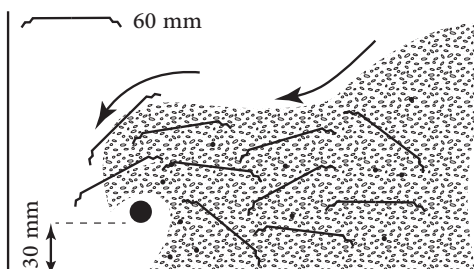


Figure 8.9: Schematic representation of how the narrow cover can restrict the presence of fibres in this zone (adapted from [210]).

In the latter formula, the 1.7 coefficient is related to the characteristic value of the maximum crack spacing. Fig. 8.10 shows the comparison of these new suggestions with the experimental measurements for the R/FRC shallow beams. For the average and maximum crack spacing, two orientation factors of  $\kappa_0=0.5$  and 1 are considered. Generally speaking, multiplying  $(1 - f_{fts,ef}/f_{ctm})$  to the term related to transfer length with  $\kappa_0=1$  does not give satisfactory results. The modified formula based on MC2020 for  $S_{r,m}$  with  $\kappa_0=0.5$ , achieves a good prediction for the average crack spacing, and  $(h - x)(1 - 0.5f_{fts,ef}/f_{ctm})$  leads to a slight overestimation of these parameter. Introduction of a coefficient 1.7 for computation of  $S_{r,max}$  gives a value of  $S_{r,max} = 181$  mm compared to the experimental maximum crack spacing of 147, which overestimates the experimental value with around 20%. Nevertheless, as this value supposedly represents the 95% fractile of  $S_{r,max}$ , it is not easy to draw conclusions based on three tested specimens. The other two formulations given for  $S_{r,max}$  computation with  $\kappa_0=0.5$  agree well with the expected value of maximum crack spacing.

Comparison of maximum crack spacing predictions for the R/FRC plates, is illustrated in Fig. 8.11. It is again underlined that the measurements of the crack spacing were carried out on the sides of the plates, with larger crack distances and limited stresses in rebars. Therefore, although cracks might be more distant from each other, they do not represent the maximum crack width. This being mentioned, it is observed that the modifications made to the formulations by introduction of  $\kappa_0=0.5$ , improve their capacity to predict crack spacing values for the plates, however, prediction of crack spacing in plates remains to be investigated in more depth.

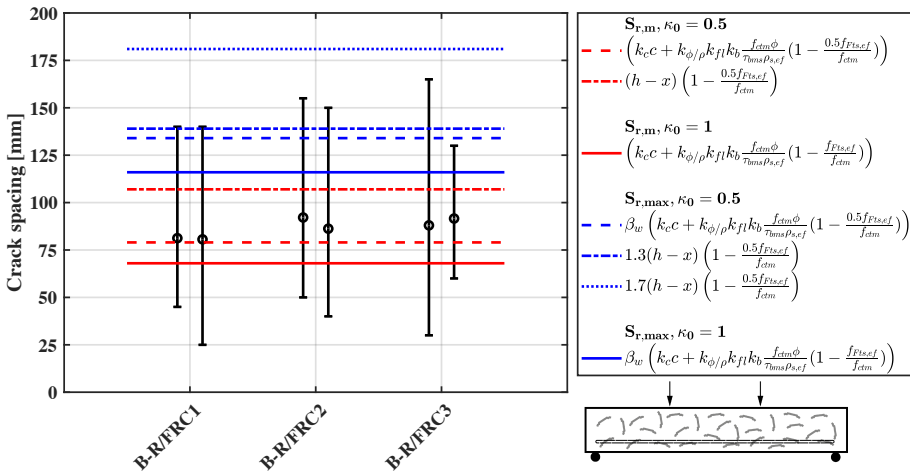


Figure 8.10: Minimum, average, and maximum crack spacing for the R/FRC shallow beams and comparison with the predictions given by suggested formulas.

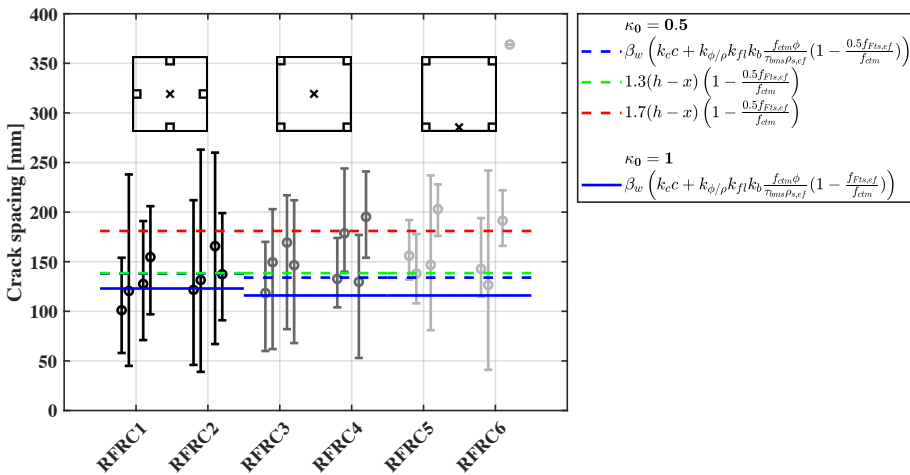


Figure 8.11: Comparison of the modified formula given in MC2020 with MC2020 and EC2 1992:2020 prediction for  $S_{r,max}$ .





# CHAPTER 9

---

## CONCLUSIONS

---

The present PhD thesis titled “*Steel fibre reinforced concrete plates; Structural response and reliability of design methods*”, attempted to shed light on merits and demerits of application of fibres in design of SFRC plate elements, and to touch on the behaviour of beams reinforced with fibres, the topic of crack spacing in fibre reinforced beams and plates, and NLFEM of SFRC notched beams and plates.

In Chapter 4, twenty plates reinforced with rebars (RC), with  $35 \text{ kg/m}^3$  of steel fibres (SFRC), and combination of both reinforcing solutions (R/FRC) were tested. These plates were tested under three configurations of boundary conditions. Fibres led to significant reduction of deflection and crack opening, and led to an increase in load bearing capacity of the plates. The R/FRC plates did not suffer from a reduced ductility which was attributed to the extensive cracking of these elements. Propagation of many cracks limited the opening of each single crack, and consequently, fibres remained active throughout the whole extent of the behaviour of the plates. A yield line analysis was carried out to predict the realistic load bearing capacity of the plates, and also to find the design resistance of these elements. It was observed that the conditions of the ultimate crack opening  $w_u=2.5 \text{ mm}$ , was not met in the plates and the ultimate load of these elements arrived when the maximum crack opening

was much smaller than this value. Accordingly, the tensile law was modified through an inverse analysis with a different assumption for  $w_u$ . With this modified law, the average tensile properties of the SFRC material was capable of giving satisfactory predictions for the load bearing capacity of the plates. The large scatter of the results of the three-point bending test, however, was giving design resistance values which led to excessive safety factors. The  $\alpha$  coefficient as per CNR-DT 204, and the  $\kappa_G$  factor proposed in EC2 1992:2020 were effective in alleviating this shortcoming.

Chapter 5 dealt with NLFEM of the notched beams and plates with a focus on modelling the SFRC material at these two levels. It was shown that the specific SFRC utilized in this study, that after an initial softening in the post-peak region manages to recover stresses significantly, can pose some challenges when fracture energy regularization is adopted. When in the post-peak region, stresses were restored in elements, dissipation was propagated to many computation points. Attention was required to check the numerical crack width and to adopt the internal parameter accordingly. For modelling the SFRC plates, the characteristic length was taken as the width of four elements which to some extent agreed with the width of the numerical crack width, and was successful in prediction of the behaviour of the plates. Yet, modelling the SFRC plates from the S3 series in which the load was applied on the edge of the plates, was not that successful. It seemed that when the failure is dominated by confined regions of the structure, the average material properties overestimate the bearing capacity. In these circumstances, the heterogeneity of SFRC plays a major role.

In Chapter 6 It was shown that when fibres are utilized in a statically determinate scheme, like a four-point bending setup, their response can be very different from what could be expected from the average material properties. In these circumstances, the heterogeneity of the FRC can be very decisive on whether more cracks can propagate or a premature failure with a single crack may put an end to the response. Furthermore, the established evidence that fibres reduce the ductility of beam elements was reaffirmed. Similar to what was done for the plates, the tensile law was modified according to the experimental  $w_u$  value which substantially improved the estimation of the load bearing capacity of the beams.

In Chapter 7, in an unprecedented work, twelve nominally identical SFRC plates were tested under a central concentrated load. The coefficient of variation for structural resistance of the SFRC plate was obtained to be less than 5%. These results put into perspective how the small characteristic tensile

strength properties of FRC can negatively affect an economic design of FRC slab elements. The approaches that are given in CNR-DT 204, MC, and EC2 1992:2020 to magnify the tensile properties of FRC were discussed, and in line with the approach given in MC2010, a curve was suggested which gave the magnification factor based on a reduced coefficient of variation,  $V_{red}$ , which is the expected scatter for resistance of the structure to be designed.

Finally, in Chapter 8, the crack spacing of the tested plates and beams were compared with the available formulas in MC and EC2 standards. With a critical view, these formulas were discussed and tentative suggestions were given. These suggestions were based on a rational view on the issue and were not examined against a database. Therefore, they are open to criticism.

## 9.1 Future developments

The relationship given in EC2 1992:2020, which is adopted from the German code [56], the magnification factor,  $\kappa_G$ , that is to be multiplied to the characteristic/design value of residual tensile strength values of FRC, depend on the area of the cracked section (Eq. 7.19). However, to the belief of the author of the present thesis, it is not yet clear if a large enough cracked area is a sufficient condition to assume that larger characteristic tensile properties can be adopted. It might be that multiple cracking should be assured first. If a two-way slab fails with the propagation of a single crack in each direction, which happens at weakest sections, it is likely that the magnified characteristic values, would overestimate the characteristic response of the structure. More experimental results in this area is needed

It was shown that the E-COV reliability method which is based on two deterministic models with characteristic and average material properties, gives a dispersion for the structural resistance which is not different from the scatter of the material properties. Therefore, for a heterogeneous material like FRC, heterogeneity needs to be taken into account in the same model. Therefore, it is of interest to check the structural scatter that would be obtained from a stochastic model with a random field, totally random or with spatial correlation.



---

## BIBLIOGRAPHY

---

- [1] ABRISHAMI, H. H., AND MITCHELL, D. Influence of steel fibers on tension stiffening. *ACI Structural Journal* 94, 6 (1997), 769–776.
- [2] AFGC. Bétons fibrés à ultra-hautes performances (Ultra high performance fibre reinforced concretes)-Recommandations. Tech. rep., Association of Civil Engineers of France, June 2013.
- [3] AIDAROV, S., MENA, F., AND DE LA FUENTE, A. Structural response of a fibre reinforced concrete pile-supported flat slab: full-scale test. *Engineering Structures* 239, February (2021), 1–13.
- [4] ALBANDAR, F. A., MILLS, G. M., AND BEEBY, A. W. The Prediction of Crack Widths in Reinforced Concrete Beams. *Magazine of Concrete Research* 27, 92 (1975), 182–184.
- [5] ALSAYED, S. H. Flexural deflection of reinforced fibrous concrete beams. *ACI Structural Journal* 90, 1 (1993), 72–88.
- [6] ALWAN, J., NAAMAN, A. E., AND GUERRERO, P. Effect of mechanical clamping on the pull-out response of hooked steel fibers embedded in cementitious matrices. *Concrete Science and Engineering* 1, March (1999), 15–25.
- [7] AMIN, A., AND FOSTER, S. J. Predicting the flexural response of steel fibre reinforced concrete prisms using a sectional model. *Cement and Concrete Composites* 67 (2016), 1–11.
- [8] ASTM C 1550. ASTM C1550-12 Standard Test Method for Flexural Toughness of Fiber Reinforced Concrete ( Using Centrally Loaded Round Panel ). *ASTM standard C1550*, c (2012), 1–14.
- [9] AVANAKI, M. J., HOSEINI, A., VAHDANI, S., DE SANTOS, C., AND DE LA FUENTE, A. Seismic fragility curves for vulnerability assessment of steel fiber reinforced concrete segmental tunnel linings. *Tunnelling and Underground Space Technology* 78 (2018), 259–274.

- [10] BALÁZS, G., AND BOROSNYÓI, A. Models for flexural cracking in concrete : the state of the art. *Structural Concrete* 6, 2 (2005), 53–62.
- [11] BANTHIA, N., AND TROTTIER, J.-F. Concrete Reinforced with Deformed Steel Fibers, Part I: Bond-Slip Mechanisms. *ACI Materials Journal* 91, 5 (Sept. 1994), 435–446.
- [12] BARENBLATT, G. I. The Mathematical Theory of Equilibrium of Cracks in Brittle Fracture. *Advances in Applied Mechanics* 7 (1962).
- [13] BARNETT, S. J., LATASTE, J.-F., PARRY, T., MILLARD, S. G., AND SOUTSOS, M. N. Assessment of fibre orientation in ultra high performance fibre reinforced concrete and its effect on flexural strength. *Materials and Structures* 43, 7 (2010), 1009–1023.
- [14] BARROS, J. A. O., AND FIGUEIRAS, J. A. Experimental behavior of fiber concrete slabs on soil. *Mechanics of Cohesive-Frictional Materials* 290, January 1996 (1998), 277–290.
- [15] BASE, G. D., REED, J. B., BEEBY, A. W., AND TAYLOR, H. P. J. An investigation of the crack control. *Research report, Cement and concrete association* 10, 14 (1966), 1–44.
- [16] BAŽANT, Z. P. Analysis of work-of-fracture method for measuring fracture energy of concrete. *Journal of Engineering Mechanics* 122, 2 (1996), 138–144.
- [17] BAŽANT, Z. P. Concrete fracture models testing and practice.pdf, 2002.
- [18] BAŽANT, Z. P., KAZEMI, M., ET AL. Determination of fracture energy, process zone length and brittleness number from size effect, with application to rock and concrete. *International Journal of fracture* 44, 2 (1990), 111–131.
- [19] BAŽANT, Z. P., AND OH, B. H. Crack band theory for fracture of concrete. *Matériaux et Constructions* 16, 3 (May 1983), 155–177.
- [20] BEEBY, A. W. The influence of the parameter  $\phi/\rho_{eff}$  on crack widths. *Structural Concrete* 6, 4 (2005), 155–165.
- [21] BERNARD, E. Durability of cracked fibre reinforced shotcrete. *Shotcrete: More Engineering Developments*, September 2004 (2004), 59–66.
- [22] BERNARD, E. S. Point Load Capacity in Round Steel Fiber Reinforced Concrete Panels. Tech. rep., School of Civic Engineering and Environment, UWS, Nepean, 1998.
- [23] BERNARD, E. S. Age-dependent changes in post-crack performance of fibre reinforced shotcrete linings. *Tunnelling and Underground Space Technology* 49 (2015), 241–248.
- [24] BERNARD, E. S. Post-crack performance of fibre reinforced concrete and its effect on the first peak cracking load of slabs. *Australian Journal of Structural Engineering* 17, 3 (2016), 170–179.
- [25] BERNARD, E. S., AND PIRCHER, M. The influence of thickness on performance of fiber-reinforced concrete in a round determinate panel test. *Cement, concrete and Aggregates* 23, 1 (2001), 27–33.

- [26] BERROCAL, C. G., FERNANDEZ, I., LUNDGREN, K., AND LÖFGREN, I. Corrosion-induced cracking and bond behaviour of corroded reinforcement bars in SFRC. *Composites Part B: Engineering* 113 (March 2017), 123–137.
- [27] BERROCAL, C. G., LÖFGREN, I., AND LUNDGREN, K. The effect of fibres on steel bar corrosion and flexural behaviour of corroded RC beams. *Engineering Structures* 163, February (2018), 409–425.
- [28] BERROCAL, C. G., LÖFGREN, I., LUNDGREN, K., AND TANG, L. Corrosion initiation in cracked fibre reinforced concrete: Influence of crack width, fibre type and loading conditions. *Corrosion Science* 98 (2015), 128–139.
- [29] BIGAJ, A. J. *Structural dependence of rotations capacity of plastic hinges in RC beams and slobes*. PhD thesis, Delft University of Technology, 1999.
- [30] BISCHOFF, P. H. Tension stiffening and cracking of steel fiber reinforced concrete. *Journal of materials in civil engineering* 15, 2 (2003), 174–182.
- [31] BLANCO, A., CAVALARO, S., DE LA FUENTE, A., GRÜNEWALD, S., BLOM, C. B. M., AND WALRAVEN, J. C. Application of FRC constitutive models to modelling of slabs. *Materials and structures* 48, 9 (2015), 2943–2959.
- [32] BLANCO, A., PUJADAS, P., CAVALARO, S., DE LA FUENTE, A., AND AGUADO, A. Constitutive model for fibre reinforced concrete based on the Barcelona test. *Cement and Concrete Composites* 53 (Oct. 2014), 327–340.
- [33] BLANCO, A., PUJADAS, P., DE LA FUENTE, A., CAVALARO, S. H., AND AGUADO, A. Assessment of the fibre orientation factor in SFRC slabs. *Composites Part B: Engineering* 68 (Jan. 2015), 343–354.
- [34] BOULEKBACHE, B., HAMRAT, M., CHEMROUK, M., AND AMZIANE, S. Flowability of fibre-reinforced concrete and its effect on the mechanical properties of the material. *Construction and Building Materials* 24, 9 (2010), 1664–1671.
- [35] BREITENBÜCHER, R., MESCHKE, G., SONG, F., AND ZHAN, Y. Experimental, analytical and numerical analysis of the pullout behaviour of steel fibres considering different fibre types, inclinations and concrete strengths. *Structural Concrete* 15, 2 (2014), 126–135.
- [36] BRÜHWILER, E., AND WITTMANN, F. H. The wedge splitting test, a new method of performing stable fracture mechanics tests. *Engineering Fracture Mechanics* 35, 1-3 (1990), 117–125.
- [37] BUTTIGNOL, T. E., COLOMBO, M., AND DI PRISCO, M. Long-term aging effects on tensile characterization of steel fibre reinforced concrete, 2016.
- [38] C1399, A. Standard Test Method for Obtaining Average Residual-Strength of Fiber-Reinforced. Tech. rep., ASTM International, 2015.
- [39] C1609. C 1609/C 1609M-05 Standard Test Method for Flexural Performance of Fiber-Reinforced Concrete ( Using Beam With Third-Point Loading ) 1. *Astm i*, C 1609/C 1609M-05 (2005), 1–8.

- [40] CASANOVA, P., AND ROSSI, P. Analysis of metallic fibre-reinforced concrete beams submitted to bending. *Materials and Structures/Materiaux et Constructions* 29, 190 (July 1996), 354–361.
- [41] CAVALARO, S. H. P., AND AGUADO, A. Intrinsic scatter of FRC: an alternative philosophy to estimate characteristic values. *Materials and structures* 48, 11 (2015), 3537–3555.
- [42] CEDOLIN, L., DEI POLI, S., AND IORI, I. Experimental determination of the fracture process zone in concrete. *Cement and Concrete Research* 13, 4 (1983), 557–567.
- [43] CEN, E. N. Annex L – Steel Fibre Reinforced Concrete. Tech. rep., European Committee for Standardization, 2020.
- [44] CERVENKA, V. Reliability-based non-linear analysis according to fib Model Code 2010. *Structural Concrete* 14, 1 (2013), 19–28.
- [45] CHANVILLARD, G. Modeling the pullout of wire-drawn steel fibers. *Cement and Concrete Research* 29, 7 (1999), 1027–1037.
- [46] CHEN, B., AND LIU, J. Effect of aggregate on the fracture behavior of high strength concrete. *Construction and Building Materials* 18, 8 (2004), 585–590.
- [47] CHEN WF. DOUBLE PUNCH TEST FOR TENSILE STRENGTH OF CONCRETE. *J Amer Concrete Inst* 67, 12 (1970), 993–995.
- [48] CIANCIO, D., MAZZOTTI, C., AND BURATTI, N. Evaluation of fibre-reinforced concrete fracture energy through tests on notched round determinate panels with different diameters. *Construction and Building Materials* 52 (Feb. 2014), 86–95.
- [49] CLARK, A. P. Cracking in reinforced concrete flexural members. *Journal of the american conc* 52, 4 (1956), 851–862.
- [50] CNR, A. Guide for the design and construction of fiber-reinforced concrete structures, 2006.
- [51] COLOMBO, M., MARTINELLI, P., AND DI PRISCO, M. On the evaluation of the structural redistribution factor in FRC design: a yield line approach. *Materials and Structures* 50, 1 (2017), 100.
- [52] COMINOLI, L. *Studio sul calcestruzzo fibrorinforzato per applicazioni industriali: dalle proprietà del materiale al comportamento strutturale*. Starrylink, 2008.
- [53] COMITE EURO-INTERNATIONAL DU BETON. *CEB-FIP MODEL CODE 1990*. Thomas Telford Publishing, 1993.
- [54] CORNELISSEN, H., HORDIJK, D., AND REINHARDT, H. Experimental determination of crack softening characteristics of normalweight and lightweight. *Heron* 31, 2 (1986), 45–46.
- [55] CUNHA, V. M., BARROS, J. A., AND SENA-CRUZ, J. M. Pullout behavior of steel fibers in self-compacting concrete. *Journal of Materials in Civil Engineering* 22, 1 (2010), 1–9.



- [56] DAFSTB. Guideline Steel fibre reinforced concrete. Tech. rep., Deutsche Ausschuss für Stahlbeton (German Committee for Reinforced Concrete), 2012.
- [57] DANCYGIER, A. N., AND BERKOVER, E. Cracking localization and reduced ductility in fiber-reinforced concrete beams with low reinforcement ratios. *Engineering Structures 111* (2016), 411–424.
- [58] DANCYGIER, A. N., AND KARINSKI, Y. S. Probabilistic model of the crack localization in axially loaded fibrous reinforced concrete bars. *Engineering Structures 79* (2014), 417–426.
- [59] DANCYGIER, A. N., AND KARINSKI, Y. S. Effect of cracking localization on the structural ductility of normal strength and high strength reinforced concrete beams with steel fibers. *International Journal of Protective Structures 10*, 4 (2019), 457–469.
- [60] DANCYGIER, A. N., KARINSKI, Y. S., AND NAVON, Z. Cracking localization in tensile conventionally reinforced fibrous concrete bars. *Construction and Building Materials 149* (2017), 53–61.
- [61] DANCYGIER, A. N., AND SAVIR, Z. Flexural behavior of HSFRC with low reinforcement ratios. *Engineering Structures 28*, 11 (2006), 1503–1512.
- [62] DE LA FUENTE, A., ESCARIZ, R. C., DE FIGUEIREDO, A. D., AND AGUADO, A. Design of macro-synthetic fibre reinforced concrete pipes. *Construction and Building Materials 43* (2013), 523–532.
- [63] DE LA FUENTE, A., PUJADAS, P., BLANCO, A., AND AGUADO, A. Experiences in barcelona with the use of fibres in segmental linings. *Tunnelling and Underground Space Technology 27*, 1 (2012), 60–71.
- [64] DELUCE, J. R., AND VECCHIO, F. J. Cracking behavior of steel fiber-reinforced concrete members containing conventional reinforcement, 2013.
- [65] DENNEMAN, E., KEARSLEY, E. P., AND VISSER, A. T. Splitting tensile test for fibre reinforced concrete. *Materials and Structures/Materiaux et Constructions 44*, 8 (2011), 1441–1449.
- [66] DESAYI, P. Determination of the Maximum Crack Width in Reinforced Concrete Members. *Journal of American Concrete Institute 73*, 8 (1976), 473–477.
- [67] DESTRÉE, X. Steel-fibre-reinforced concrete elevated suspended slabs: Design cases in Europe and the USA. *American concrete institute, Special publication (SP 310)* (2014), 409–418.
- [68] DESTRÉE, X. TEEL FIBRE AS ONLY REINFORCING IN FREE SUSPENDED ONEWAY AND TWO WAYS ELEVATED SLABS : DESIGN CONCLUSIONS BASED UPON FULL SCALE TESTING RESULTS. Tech. rep., ArcelorMittal, 2015.
- [69] DESTRÉE, X., AND MANDL, J. Steel fibre only reinforced concrete in free suspended elevated slabs: Case studies, design assisted by testing route, comparison to the latest SFRC standard documents. *Tailor Made Concrete Structures* (2008), 437–443.

- [70] DESTRÉE, X., YAO, Y., AND MOBASHER, B. Sequential Cracking and Their Openings in Steel-Fiber-Reinforced Joint-Free Concrete Slabs. *Journal of Materials in Civil Engineering* 28, 4 (April 2016), 04015158.
- [71] DI PRISCO, M., COLOMBO, M., AND DOZIO, D. Fibre-reinforced concrete in fib Model Code 2010: Principles, models and test validation. *Structural Concrete* 14, 4 (Dec. 2013), 342–361.
- [72] DI PRISCO, M., FERRARA, L., AND LAMPERTI, M. G. L. Double edge wedge splitting (DEWS): an indirect tension test to identify post-cracking behaviour of fibre reinforced cementitious composites. *Materials and Structures* 2013 46:11 46, 11 (Feb. 2013), 1893–1918.
- [73] DI PRISCO, M., MARTINELLI, P., AND PARMENTIER, B. On the reliability of the design approach for FRC structures according to fib Model Code 2010: the case of elevated slabs. *Structural Concrete* 17, 4 (2016), 588–602.
- [74] DI PRISCO, M., PLIZZARI, G., AND VANDEWALLE, L. Fibre reinforced concrete: new design perspectives. *Materials and Structures* 42, 9 (2009), 1261–1281.
- [75] DI PRISCO, M., POURZARABI, A., AND COLOMBO, M. Fiber reinforced concrete: from flexural tests to solid slabs. In *10th International Conference on Fracture Mechanics of Concrete and Concrete Structures FraMCoS-X G.* (2019), Pijaudier-Cabot, P. Grassl, and C. L. Borderie, Eds.
- [76] DØSSLAND, Å. L. *Fibre reinforcement in load carrying concrete structures: laboratory and field investigations compared with theory and finite element analysis.* PhD thesis, Fakultet for naturvitenskap og teknologi, Feb. 2008.
- [77] DUGDALE, D. S. Yielding of steel sheets containing slits. *Journal of the Mechanics and Physics of Solids* 8, 2 (May 1960), 100–104.
- [78] DUPONT, D. *Modelling and Experimental Validation of The Constitutive Law  $\sigma - \epsilon$  and Cracking Behaviour Of Steel Fibre Reinforced Concrete.* PhD thesis, KATHOLIEKE UNIVERSITEIT LEUVEN, 2003.
- [79] DUPONT, D., AND VANDEWALLE, L. The cracking behaviour of SFRC beams containing longitudinal reinforcement. In *Proc. Int. Symp. „Brittle Matrix Composites 7”* (Warsaw, 2003), A. Brandt, V. Li, and I. H. Marshall, Eds., Institute of Fundamental Technological Research, pp. 253–262.
- [80] DUPONT, D., AND VANDEWALLE, L. Distribution of steel fibres in rectangular sections. *Cement and Concrete Composites* 27, 3 (March 2005), 391–398.
- [81] EDGINGTON, J., AND HANNANT, D. J. Steel fibre reinforced concrete. The effect on fibre orientation of compaction by vibration. *Matériaux et Constructions* 5, 1 (1972), 41–44.
- [82] EDGINGTON, J., HANNANT, D. J., WILLIAMS, R. I. T., AND ESTABLISHMENT, B. R. *Steel Fibre Reinforced Concrete.* Building Research Establishment current paper. Building Research Establishment, 1974.

- [83] ELICES, M., GUINEA, G., AND PLANAS, J. Measurement of the fracture energy using three-point bend tests: Part 3—influence of cutting the  $p$ - $\delta$  tail. *Materials and Structures* 25, 6 (1992), 327–334.
- [84] ELICES, M., AND ROCCO, C. G. Effect of aggregate size on the fracture and mechanical properties of a simple concrete. *Engineering Fracture Mechanics* 75, 13 (Sept. 2008), 3839–3851.
- [85] ELSTNER, R. C., AND HOGNESTAD, E. Shearing Strength of Reinforced Concrete Slabs. *ACI Journal Proceedings* 53, 7 (July 1956), 29–58.
- [86] EN. 14651: Test method for metallic fibered concrete—Measuring the flexural tensile strength (limit of proportionality (LOP), residual). *Brussels: European Committee for Standardization* (2005).
- [87] EN, B. S. Testing sprayed concrete —Part 5: Determination of energy absorption capacity of fibre reinforced slab specimens. Tech. rep., European Committee for standardization, 2006.
- [88] EZELDIN, A. S., AND BALAGURU, P. N. Normal-and high-strength fiber-reinforced concrete under compression. *Journal of materials in civil engineering* 4, 4 (1992), 415–429.
- [89] FACCONI, L., MINELLI, F., AND PLIZZARI, G. Steel fiber reinforced self-compacting concrete thin slabs—Experimental study and verification against Model Code 2010 provisions. *Engineering Structures* 122 (2016), 226–237.
- [90] FALKNER, H., AND HENKE, V. Application of steel fibre concrete for underwater concrete slabs. *Cement and Concrete Composites* 20, 5 (1998), 377–385.
- [91] FALL, D., SHU, J., REMPLING, R., LUNDGREN, K., AND ZANDI, K. Two-way slabs: Experimental investigation of load redistributions in steel fibre reinforced concrete. *Engineering structures* 80 (2014), 61–74.
- [92] FANELLA, D. A., AND NAAMAN, A. E. Stress-Strain Properties of Fiber Reinforced Mortar in Compression. *Journal of the American Concrete Institute* 82, 4 (1985), 475–483.
- [93] FERRARA, L., AND MEDA, A. Relationships between fibre distribution, workability and the mechanical properties of SFRC applied to precast roof elements. *Materials and Structures* 39, 4 (2006), 411–420.
- [94] FERRARA, L., OZYURT, N., AND PRISCO, M. High mechanical performance of fibre reinforced cementitious composites: the role of “casting-flow induced” fibre orientation. *Materials and Structures* 44, 1 (2011), 109–128.
- [95] FERRARA, L., PARK, Y.-D., AND SHAH, S. P. Correlation among Fresh State Behavior, Fiber Dispersion, and Toughness Properties of SFRCs. *Journal of Materials in Civil Engineering* 20, 7 (2008), 493.
- [96] FOOTE, R. M., MAI, Y. W., AND COTTERELL, B. Crack growth resistance curves in strain-softening materials. *Journal of the Mechanics and Physics of Solids* 34, 6 (1986), 593–607.

- [97] GÉRARD, B., REINHARDT, H., AND BREYSSE, B. Measured transport in cracked concrete. *Rilem report 16* (1997), 265—324.
- [98] GETTU, R., GARDNER, D. R., SALDÍVAR, H., AND BARRAGÁN, B. E. Study of the distribution and orientation of fibers in SFRC specimens. *Materials and Structures* 2004 38:1 38, 1 (Jan. 2005), 31–37.
- [99] GILBERT, R. I. Tension stiffening in lightly reinforced concrete slabs. *Journal of Structural Engineering* 133, 6 (2007), 899–903.
- [100] GÖDDE, L., AND MARK, P. Numerical simulation of the structural behaviour of sfrc slabs with or without rebar and prestressing. *Materials and Structures* 48, 6 (2015), 1689–1701.
- [101] GOTO, Y. Internal Cracks Formed in Concrete Around Deformed Tension Bars. *ACI Journal* 68, 4 (1971), 244–251.
- [102] GRANJU, J. L., AND BALOUCH, S. U. Corrosion of steel fibre reinforced concrete from the cracks. *Cement and Concrete Research* 35, 3 (2005), 572–577.
- [103] GRÜNEWALD, S., AND WALRAVEN, J. C. Parameter-study on the influence of steel fibers and coarse aggregate content on the fresh properties of self-compacting concrete. *Cement and Concrete Research* 31, 12 (2001), 1793–1798.
- [104] GUINEA, G. V., PLANAS, J., AND ELICES, M. Measurement of the fracture energy using three-point bend tests: Part 1-Influence of experimental procedures. *Materials and Structures* 25, 4 (1992), 212–218.
- [105] GULVANESSIAN, H., AND HOLICKY, M. Eurocodes: using reliability analysis to combine action effects. *Proceedings of the Institution of Civil Engineers-Structures and Buildings* 158, 4 (2005), 243–252.
- [106] GUSTAFSSON, P.-J. *Fracture mechanics studies of non-yielding materials like concrete: modelling of tensile fracture and applied strength analyses*. PhD thesis, Lund University, 1985.
- [107] HEDEBRATT, J. Industrial Fibre Concrete Floors-Experiences and Test on Pile-Supported Slab. *Civil and Architectural Engineering PhD*, August (2012), 130.
- [108] HEDEBRATT, J., AND SILFWERBRAND, J. Full-scale test of a pile supported steel fibre concrete slab. *Materials and Structures/Materiaux et Constructions* 47, 4 (2014), 647–666.
- [109] HEILMANN, H.G. FINSTERWALDER, K., AND HILSDORF, H. *Festigkeit und verformung von beton unter zugspannungen (Strength and Deformation of Concrete Under Tensile Stress)*. Ernst, 1969.
- [110] HILLERBORG, A. Results of three comparative test series for determining the fracture energy G<sub>F</sub> of concrete. *Materials and Structures* 18, 5 (Sept. 1985), 407–413.
- [111] HILLERBORG, A. The theoretical basis of a method to determine the fracture energy G<sub>F</sub> of concrete. *Materials and Structures* 18, 4 (1985), 291–296.

- [112] HILLERBORG, A., MODÉER, M., AND PETERSSON, P. E. Analysis of crack formation and crack growth in concrete by means of fracture mechanics and finite elements. *Cement and Concrete Research* 6, 6 (1976), 773–781.
- [113] HOLICKÝ, M. *Reliability analysis for structural design*. SUN MEDIA, Aug. 2009.
- [114] HU, X.-Z., AND WITTMANN, F. Fracture energy and fracture process zone. *Materials and Structures* 25, 6 (1992), 319–326.
- [115] HUGHES, B. P., FATTUHI, N. I., AND GANESH BABU, K. The workability of steel-fibre-reinforced concrete. *Magazine of Concrete Research* 29, 100 (1977), 159–160.
- [116] INTERNATIONALE DU BÉTON, F. *Model code 2010: final draft*. International Federation for Structural Concrete (fib), Lausanne, Switzerland, 2013.
- [117] ITALIAN BOARD FOR STANDARDIZATION. *UNI 11309: Steel fibre reinforced concrete- Part I: Definitions, classification, specification and conformity. Part II: Test method for measuring first crack strength and ductility indexes*, 2003.
- [118] JCSS. Probabilistic model code (concrete). Tech. rep., Joint committee for structural safety, 2000.
- [119] JEAN-FRANCOIS TROTTIER, AND NEMKUMAR BANTHIA. TOUGHNESS CHARACTERIZATION OF STEEL - FIBER REINFORCED CONCRETE. *Journal of Materials* 6, 2 (1994), 264–289.
- [120] JEANTY, P. R., MITCHELL, D., AND MIRZA, M. S. Investigation of ‘Top Bar’ Effects in Beams. *ACI Structural Journal* 85, 3 (1988), 251–257.
- [121] JOHANSEN, K. W. *Yield-line formulae for slabs*. CRC Press, Taylor and Francis Group, London, 1972.
- [122] KANSTAD, T., JUVIK, D. A., VATNAR, A., MATHISEN, A. E., SANDBAKK, S., VIKAN, H., NIKOLAISEN, E., DØSSLAND, Å., LEIRUD, N., AND OVERREIN, G. O. Forslag til retningslinjer for dimensjonering, utførelse og kontroll av fiberarmerte betongkonstruksjoner. fa 2 competitive constructions. sp 2.2 high tensile strength all round concrete. Tech. rep., SINTEF Building and Infrastructure, Oslo, Netherlands, 2011. COIN Project report no 29.
- [123] KÖNIG, G., TUE, N., AND POMMERENING, D. Safety concept for the application of non linear analysis in the design of concrete structures: general considerations. *CEB Comité Euro international du Béton, Bulletin*, 229 (1995), 13–31.
- [124] KOOIMAN, A. G. *Modelling of fibre reinforced concrete for structural design*. PhD thesis, Delft University of Technology, 2000.
- [125] KWIECINSKI, M. W. Yield criterion for initially isotropic. *Magazine of Concrete Research* 17, 51 (1965), 97–100.
- [126] LARANJEIRA, F., AGUADO, A., MOLINS, C., GRÜNEWALD, S., WALRAVEN, J., AND CAVALARO, S. Framework to predict the orientation of fibers in FRC: A novel philosophy. *Cement and Concrete Research* 42, 6 (2012), 752–768.

- [127] LEE, J., AND FENVES, G. L. Plastic-damage model for cyclic loading of concrete structures. *Journal of engineering mechanics* 124, 8 (1998), 892–900.
- [128] LEE, J. H. Influence of concrete strength combined with fiber content in the residual flexural strengths of fiber reinforced concrete. *Composite Structures* 168 (2017), 216–225.
- [129] LEONHARDT, F. Crack control in concrete structures. *IABSE periodical 3/1977*, In: *International Association for Bridges and Structural Engineering, Zurich* (1977), 26.
- [130] LINSBAUER, H. N., AND TSCHEGG, E. K. Fracture energy determination of concrete with cube-shaped specimens. *Zement und Beton* 31, 1 (1986), 38–40.
- [131] LÖFGREN, I., STANG, H., AND OLESEN, J. F. Fracture properties of FRC determined through inverse analysis of wedge splitting and three-point bending tests. *Journal of Advanced Concrete Technology* 3, 3 (2005), 423–434.
- [132] LUBLINER, J., OLIVER, J., OLLER, S., AND ONATE, E. a Plastic-Damage Model for concrete. *International Journal of Solids and Structures* 25, 3 (1989), 299–326.
- [133] MALÁRICS, V., MÜLLER, H., ET AL. Evaluation of the splitting tension test for concrete from a fracture mechanical point of view. *Proceedings of the fracture mechanics of concrete and concrete structures—assessment, durability, monitoring and retrofitting of concrete structures* (2010), 709–716.
- [134] MANDL, J., AND MATSINEN, M. Teräskuitubetonin käyttäminen kantavissa rakenteissa (in finnish). *Betoni* 84, 1 (2014), 60–69.
- [135] MARKOVICH, I., VAN MIER, J. G., AND WALRAVEN, J. C. Single fiber pullout from hybrid fiber reinforced concrete, 2001.
- [136] MARTINELLI, P., COLOMBO, M., CAVALARO, S., DE LA FUENTE, A., AGUADO, A., DI PRISCO, M., ET AL. Control procedure to check the  $\sigma$ – $\omega$  relationship used to design a sfrc slab. In *BEFIB 2016-9th RILEM International Symposium on Fiber Reinforced Concrete* (2016), RILEM Publications SARL, pp. 17–26.
- [137] MEDA, A., MINELLI, F., AND PLIZZARI, G. A. Flexural behaviour of RC beams in fibre reinforced concrete. *Composites Part B: Engineering* 43, 8 (2012), 2930–2937.
- [138] MICHELS, J., CHRISTEN, R., AND WALDMANN, D. Experimental and numerical investigation on postcracking behavior of steel fiber reinforced concrete. *Engineering Fracture Mechanics* 98 (2013), 326–349.
- [139] MINELLI, F., AND PLIZZARI, G. A new round panel test for the characterization of fiber reinforced concrete: a broad experimental study. *Journal of testing and evaluation* 39, 5 (2011), 889–897.
- [140] MOLINS, C., AGUADO, A., AND MARIN, A. R. Quality control test for SFRC to be used in precast segments. *Tunnelling and Underground Space Technology* 21, 3 (2006), 423–424.
- [141] NAAMAN, A. E., AND AL-KHAIRI, F. M. Bending Properties of High-Early-Strength Fiber Reinforced Concrete. *Special Publication 159* (Feb. 1996), 351–374.

- [142] NATARAJA, M., DHANG, N., AND GUPTA, A. Stress–strain curves for steel-fiber reinforced concrete under compression. *Cement and Concrete Composites* 21, 5 (1999), 383–390.
- [143] NAWY, E. G. Crack control in reinforced concrete structures. *ACI Journal* 65, 10 (1968), 825–836.
- [144] NGO, D., AND SCORDELIS, A. C. Finite Element Analysis of Reinforced Concrete Beams. *ACI Journal Proceedings* 64, 3 (March 1967), 152–163.
- [145] NGUYEN, W., BANDELT, M. J., TRONO, W., BILLINGTON, S. L., AND OSTERTAG, C. P. Mechanics and failure characteristics of hybrid fiber-reinforced concrete (hyfrcc) composites with longitudinal steel reinforcement. *Engineering Structures* 183 (2019), 243–254.
- [146] OH, B. H. Flexural analysis of reinforced concrete beams containing steel fibers. *Journal of structural engineering* 118, 10 (1992), 2821–2835.
- [147] OLESEN, J. F., ØSTERGAARD, L., AND STANG, H. Nonlinear fracture mechanics and plasticity of the split cylinder test. *Materials and Structures/Materiaux et Constructions* 39, 4 (2006), 421–432.
- [148] OTIENO, M., ALEXANDER, M., AND BEUSHAUSEN, H.-D. Corrosion in cracked and uncracked concrete – influence of crack width, concrete quality and crack reopening. *Magazine of Concrete Research* 62, 6 (2010), 393–404.
- [149] P., S. *Rotation capacity of self-compacting steel fiber reinforced concrete*. PhD thesis, Darmstadt University of Technology, 2006.
- [150] PARMENTIER, B., DE GROVE, E., VANDEWALLE, L., AND VAN RICKSTAL, F. Dispersion of the mechanical properties of FRC investigated by different bending tests. In *Tailor made concrete structures* (London, 2008), Walraven and Stoelhorst, Eds., Taylor and Francis Group, pp. 507–512.
- [151] PARMENTIER, B., VAN ITTERBEECK, P., AND SKOWRON, A. The flexural behaviour of sfrc flat slabs: the limelette full-scale experiments for supporting design model codes. In *Proceedings of FRC* (2014).
- [152] PÉREZ CALDENTEY, A., CORRES PEIRETTI, H., GIRALDO SOTO, A., AND PESET IRIBARREN, J. Cracking of RC members revisited: Influence of cover,  $\phi/\rho_{s,eff}$  and stirrup spacing - An experimental and theoretical study. *Structural Concrete* 14, 1 (2013), 69–78.
- [153] PÉREZ CALDENTEY, A., GARCÍA, R., GRIBNIAK, V., AND RIMKUS, A. Tension versus flexure: Reasons to modify the formulation of MC 2010 for cracking. *Structural Concrete* 21, 5 (2020), 2101–2123.
- [154] PETERSSON, P. E. Fracture energy of concrete: Practical performance and experimental results. *Cement and Concrete Research* 10, 1 (1980), 91–101.
- [155] PETERSSON, P. E. *CRACK GROWTH AND DEVELOPMENT OF FRACTURE ZONES IN PLAIN CONCRETE AND SIMILAR MATERIALS*. PhD thesis, LUND INSTITUTE OF TECHNOLOGY, 1981.

- [156] PLANAS, J., ELICES, M., AND GUINEA, G. Measurement of the fracture energy using three-point bend tests: Part 2—influence of bulk energy dissipation. *Materials and Structures* 25, 5 (1992), 305–312.
- [157] PUJADAS, P., BLANCO, A., CAVALARO, S. H. P., AGUADO, A., GRÜNEWALD, S., BLOM, K., AND WALRAVEN, J. C. Plastic fibres as the only reinforcement for flat suspended slabs: Parametric study and design considerations. *Construction and Building Materials* 70 (2014), 88–96.
- [158] PUJADAS, P., BLANCO, A., DE LA FUENTE, A., AND AGUADO, A. Cracking behavior of FRC slabs with traditional reinforcement. *Materials and Structures/Materiaux et Constructions* 45, 5 (2012), 707–725.
- [159] PUKL, R., SAJDLOVÁ, T., ČERVENKA, J., AND ČERVENKA, V. Performance of Fibre Reinforced Concrete Structures - Modelling of Damage and Reliability. *Key Engineering Materials* 711 (Sept. 2016), 690–697.
- [160] QING, L., YU, K., MU, R., AND FORTH, J. P. Uniaxial tensile behavior of aligned steel fibre reinforced cementitious composites. *Materials and Structures/Materiaux et Constructions* 52, 4 (2019), 1–12.
- [161] RAO, G. A., AND PRASAD, B. K. Fracture energy and softening behavior of high-strength concrete. *Cement and Concrete Research* 32, 2 (Feb. 2002), 247–252.
- [162] RAPOPORT, J., ALDEA, C.-M., SHAH, S. P., ANKENMAN, B., AND KARR, A. Permeability of cracked steel fiber-reinforced concrete. *Journal of materials in civil engineering* 14, 4 (2002), 355–358.
- [163] RASHID, Y. Ultimate strength analysis of prestressed concrete pressure vessels. *Nuclear Engineering and Design* 7, 4 (April 1968), 334–344.
- [164] RIZK, E., AND MARZOUK, H. A new formula to calculate crack spacing. *ACI Structural Journal- Technical paper*, January 2010 (2017).
- [165] RIZKALLA, S. H., HWANG, L. S., AND EL SHAHAWI, M. Transverse Reinforcement Effect on Cracking Behaviour of R. C. Members. *Canadian journal of civil engineering* 10, 4 (1983), 566–581.
- [166] ROBINS, P., AUSTIN, S., AND JONES, P. Pull-out behaviour of hooked steel fibres. *Materials and Structures/Materiaux et Constructions* 35, 7 (2002), 434–442.
- [167] ROCCO, C., GUINEA, G. V., PLANAS, J., AND ELICES, M. Mechanisms of rupture in splitting tests. *ACI Materials Journal* 96, 1 (Jan. 1999), 52–60.
- [168] ROELFSTRA, P. E., AND WITTMANN, F. H. Numerical Method to Link Strain Softening with Failure of Concrete. In *Fracture Toughness and Fracture Energy*. Elsevier Science Publishers, 1986, pp. 163–175.
- [169] ROESLER, J. R., LANGE, D. A., ALTOUBAT, S. A., RIEDER, K.-A., AND ULREICH, G. R. Fracture of plain and fiber-reinforced concrete slabs under monotonic loading. *Journal of materials in civil engineering* 16, 5 (2004), 452–460.
- [170] ROSSI, P., ACKER, P., AND MALIER, Y. Effect of steel fibres at two different stages: The material and the structure. *Materials and Structures* 20, 6 (1987), 436–439.



- [171] ROTS, J., NAUTA, P., KUSTER, G., AND BLAAUWENDRAAD, J. Smearred Crack Approach and Fracture Localization in Concrete. *HERON*, 30 (1), 1985 (1985).
- [172] RUIZ, M. F., MIRZAEI, Y., AND MUTTONI, A. Post-Punching Behavior of Flat Slabs. *ACI Structural Journal* 110, 5 (Sept. 2013), 801–812.
- [173] SALEHIAN, H., AND BARROS, J. A. Prediction of the load carrying capacity of elevated steel fibre reinforced concrete slabs. *Composite Structures* 170 (2017), 169–191.
- [174] SALEHIAN, H., BARROS, J. A. O., AND TAHERI, M. Evaluation of the influence of post-cracking response of steel fibre reinforced concrete (SFRC) on load carrying capacity of SFRC panels. *Construction and Building Materials* 73 (2014), 289–304.
- [175] SAOUMA, V. E., BROZ, J. J., BRÜHWILER, E., AND BOGGS, H. L. Effect of aggregate and specimen size on fracture properties of dam concrete. *Journal of Materials in Civil Engineering* 3, 3 (Aug. 1991), 204–218.
- [176] SCHLUNE, H., PLOS, M., AND GYLLTOFT, K. Safety formats for non-linear analysis of concrete structures. *Magazine of Concrete Research* 64, 7 (July 2012), 563–574.
- [177] SCHUMACHER, P., WALRAVEN, J. C., AND DEN UIJL, J. A. Rotation capacity of self-compacting steel fibre reinforced concrete beams. *Heron* 54, 2009 (2009), 125–160.
- [178] SFRC-CONSORTIUM. Design Guideline for Structural Applications of Steel Fibre Reinforced Concrete, 2014.
- [179] SHAH, S., AND RANGAN, B. Fiber reinforced concrete properties. *ACI Journal Proceedings*, 68 (1971), 126–137.
- [180] SLOWIK, V., VILLMANN, B., BRETSCHNEIDER, N., AND VILLMANN, T. Computational aspects of inverse analyses for determining softening curves of concrete. *Computer Methods in Applied Mechanics and Engineering* 195, 52 (2006), 7223–7236.
- [181] SLOWIK, V., AND WITTMANN, F. H. Influence of strain gradient on fracture energy. In *Proc., Int. Conf. on Fracture Mechanics of Concrete and Concrete Structures* (1992), pp. 424–429.
- [182] SOETENS, T., VAN GYSEL, A., MATTHYS, S., AND TAERWE, L. A semi-analytical model to predict the pull-out behaviour of inclined hooked-end steel fibres. *Construction and Building Materials* 43 (2013), 253–265.
- [183] SORELLI, L. G., MEDA, A., AND PLIZZARI, G. A. Steel fiber concrete slabs on ground: A structural matter. *ACI Structural Journal* 103, 4 (2006), 551–558.
- [184] SOROUSHIAN, P., AND BAYAS, Z. Prediction of the Tensile Strength of Fiber Reinforced Concrete: A Critique of the Composite Material Concept. *Special Publication* 105 (Dec. 1987), 71–84.
- [185] SOROUSHIAN, P., AND LEE, C. D. Distribution and orientation of fibers in steel fiber reinforced concrete. *ACI Materials Journal* 87, 5 (1990), 433–439.
- [186] SPECIFICATION, E. Sprayed Concrete Technology. *Sprayed Concrete Technology* 44, 0 (2017).

- [187] STÄHLI, P., CUSTER, R., AND VAN MIER, J. G. M. On flow properties, fibre distribution, fibre orientation and flexural behaviour of FRC. *Materials and Structures/Materiaux et Constructions* 41, 1 (2008), 189–196.
- [188] STANDARD, E. Eurocode: Basis of structural design. *Management* 3 (2004), 225.
- [189] STANG, H., AND OLESEN, J. On The Interpretation of Bending Tests On FRC-Materials. *Fracture Mechanics of Concrete Structures*, AEDIFICATIO Publishers, D-79104 Freiburg, Germany (1998), 511–520.
- [190] ŠVEC, O., ŽIRGULIS, G., BOLANDER, J. E., AND STANG, H. Influence of formwork surface on the orientation of steel fibres within self-compacting concrete and on the mechanical properties of cast structural elements. *Cement and Concrete Composites* 50 (2014), 60–72.
- [191] TAN, K. H., PARAMASIVAM, P., AND TAN, K. C. Cracking characteristics of reinforced steel fiber concrete beams under short- and long-term loadings. *Advanced Cement Based Materials* 2, 4 (1995), 127–137.
- [192] TASDEMIR, C., TASDEMIR, M. A., LYDON, F. D., AND BARR, B. I. Effects of silica fume and aggregate size on the brittleness of concrete. *Cement and Concrete Research* 26, 1 (1996), 63–68.
- [193] TRUNK, B., AND WITTMANN, F. Influence of size on fracture energy of concrete. *Materials and Structures* 34, 5 (2001), 260–265.
- [194] UCHIDA, Y., AND BARR, B. Tension softening curves of concrete determined from different test specimen geometrics. In *Fracture Mechanics of Concrete Structures* (1998), pp. 387–398.
- [195] UCHIDA, Y., ROKUGO, K., AND KOYANAGI, W. DETERMINATION OF TENSION SOFTENING DIAGRAMS OF CONCRETE. *Concrete Library international of JSCE*, 18 (1991).
- [196] ULFKJAER, J. P., BRINCKER, R., AND KRENK, S. Analytical Model for Complete Moment-Rotation Curves of Concrete Bemas in Bending. In *8th European conference on fracture: fracture behaviour and design of materials and structures* (Torino, Italy, 1990), APA.
- [197] VANDEWALLE, L. Cracking behaviour of concrete beams reinforced with a combination of ordinary reinforcement and steel fibers. *Materials and Structures* 33, 3 (2000), 164–170.
- [198] VANDEWALLE, L., HEIRMAN, G., AND VAN RICKSTAL, F. Fibre orientation in self-compacting fibre reinforced concrete. *7th RILEM Symposium on Fibre Reinforced Concrete BEFIB2008*, 1 (2008), 719–728.
- [199] VANDEWALLE, L., NEMEGER, D., BALAZS, G. L., BARR, B., BARTOS, P., BANTHIA, N., BRANDT, A. M., CRISWELL, M., DENARIE, F., DI PRISCO, M., FALKNER, H., GETTU, R., GOPALARATNAM, V., GROTH, P., HAUSLER, V., KATSARAGAFIS, F., KOOIMAN, A., KOVLER, K., LEHTONEN, J., MASSICOTTE, B., MINDESS, S., REINHARDT, H., ROSSI, P., SCHAERLAEKENS, S., SCHNUTGEN, B.,

- SHAH, S., SKARENDAHL, A., STANG, H., STROEVEN, P., SWAMY, R., TATNALL, P., TEUTSCH, M., WALRAVEN, J., AND WUBS, A. Rilem TC 162-TDF: Test and design methods for steel fibre reinforced concrete: Uni-axial tension test for steel fibre reinforced concrete. *Materials and Structures/Materiaux et Constructions* 34, 235 (2001), 3–6.
- [200] VANDEWALLE, L., VAN RICKSTAL, F., HEIRMAN, G., AND PARMENTIER, B. On the round panel and 3-point bending tests. *7th international RILEM symposium on Fibre Reinforced Concrete*, September (2008).
- [201] VLIET, A. B.-v. Bond of Deformed Reinforcing Steel Bars Embedded in Steel Fiber Reinforced Concrete – State-of-the-Art Report. Tech. rep., Delft Cluster, 2001.
- [202] VOO, J. Y. L., AND FOSTER, S. J. Variable Engagement Model for the Design of Fibre Reinforced Concrete Structures. In *Advanced Materials for Construction of Bridges, Buildings, and Other Structures III* (2003).
- [203] WANG, K., JANSEN, D. C., SHAH, S. P., AND KARR, A. F. Permeability study of cracked concrete. *Cement and Concrete Research* 27, 3 (March 1997), 381–393.
- [204] WATSTEIN, D., AND PARSONS, D. Width and spacing of tensile cracks in axially reinforced concrete cylinders. *Journal of Research of the National Bureau of Standards* 31, 1 (1943), 1.
- [205] WEIHE, S., KRÖPLIN, B., AND DE BORST, R. Classification of smeared crack models based on material and structural properties. *International Journal of Solids and Structures* 35, 12 (1998), 1289–1308.
- [206] WOOD, R. H. *Plastic and elastic design of slabs and plates: with particular reference to reinforced concrete floor slabs*. Ronald Press Company, 1961.
- [207] YOO, D. Y., YOON, Y. S., AND BANTHIA, N. Flexural response of steel-fiber-reinforced concrete beams: Effects of strength, fiber content, and strain-rate. *Cement and Concrete Composites* 64 (2015), 84–92.
- [208] YUGUANG, Y., WALRAVEN, J. C., AND DEN UIJL, J. A. Combined effect of fibers and steel rebars in high performance concrete. *Heron* 54, 2-3 (2009), 205–224.
- [209] ZHOU, B., AND UCHIDA, Y. Relationship between fiber orientation/distribution and post-cracking behaviour in ultra-high-performance fiber-reinforced concrete (UHPRFC). *Cement and Concrete Composites* 83 (2017), 66–75.
- [210] ŽIRGULIS, G., ŠVEC, O., GEIKER, M. R., CWIRZEN, A., AND KANSTAD, T. Influence of reinforcing bar layout on fibre orientation and distribution in slabs cast from fibre-reinforced self-compacting concrete (FRSCC). *Structural Concrete* 17, 2 (2016), 245–256.



# Appendices



---

## A - SHALLOW BEAMS

---

Fig. A.1 shows the LVDTs adopted to measure crack opening on the tensile chord and the compression on the top of the shallow beams.

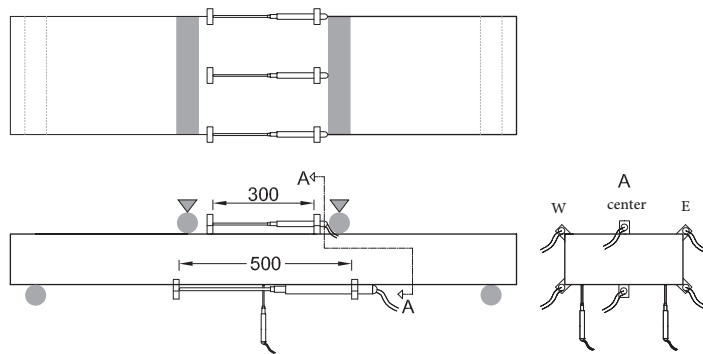
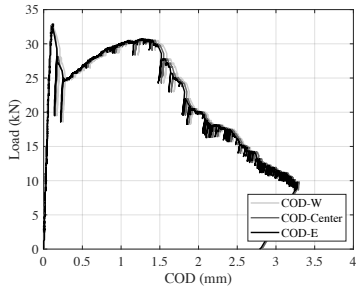
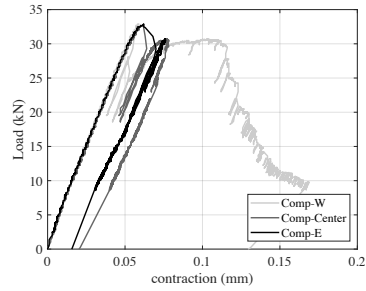


Figure A.1: position and gauge length of LVDTs adopted to measure deformations on the shallow beams

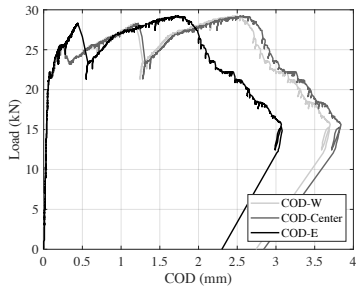
In Chapter 6 the average of the measured CODs on the three instruments were reported. Here, the recordings of each instrument is illustrated separately for each specimen in Fig. A.2



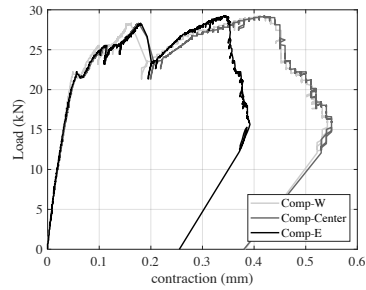
(a) B-FRC1 COD



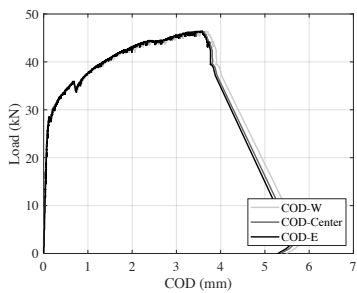
(b) B-FRC1 compressive deformation



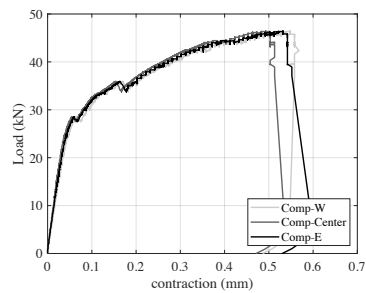
(c) B-FRC2 COD



(d) B-FRC2 compressive deformation



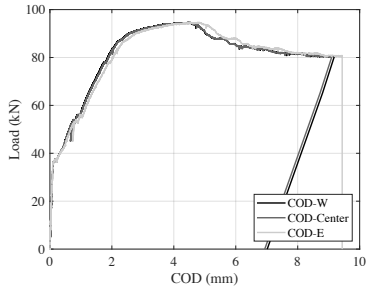
(e) B-FRC3 COD



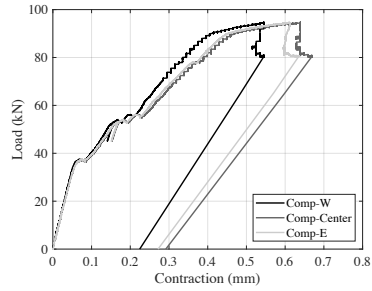
(f) B-FRC3 compressive deformation

Figure A.2: (left column) Load-COD and (right column) Load-contraction curves, for the B-FRC beams and for the three instruments shown separately

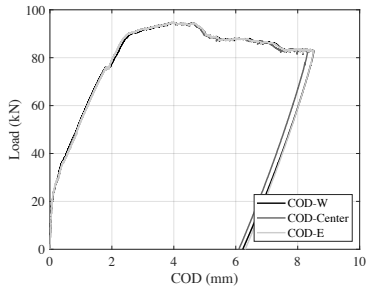




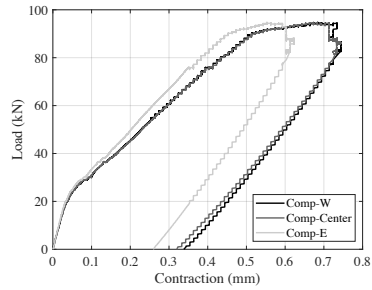
(a) B-R/FRC1 COD



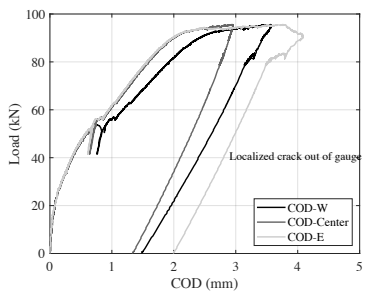
(b) B-R/FRC1 compressive deformation



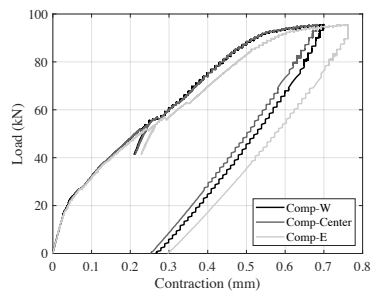
(c) B-R/FRC2 COD



(d) B-R/FRC2 compressive deformation



(e) B-R/FRC3 COD



(f) B-R/FRC3 compressive deformation

Figure A.3: (left column) Load-COD and (right column) Load-contraction curves, for the B-R/FRC beams and for the three instruments shown separately



---

## **B - CRACK SPACING**

---

Here we are presenting the crack pattern and spacing for all the tested plates. The values of crack spacing are not measured on the specimens, but on the images that constructed from nine images that are taken from below each plate after each test which are then assembled.

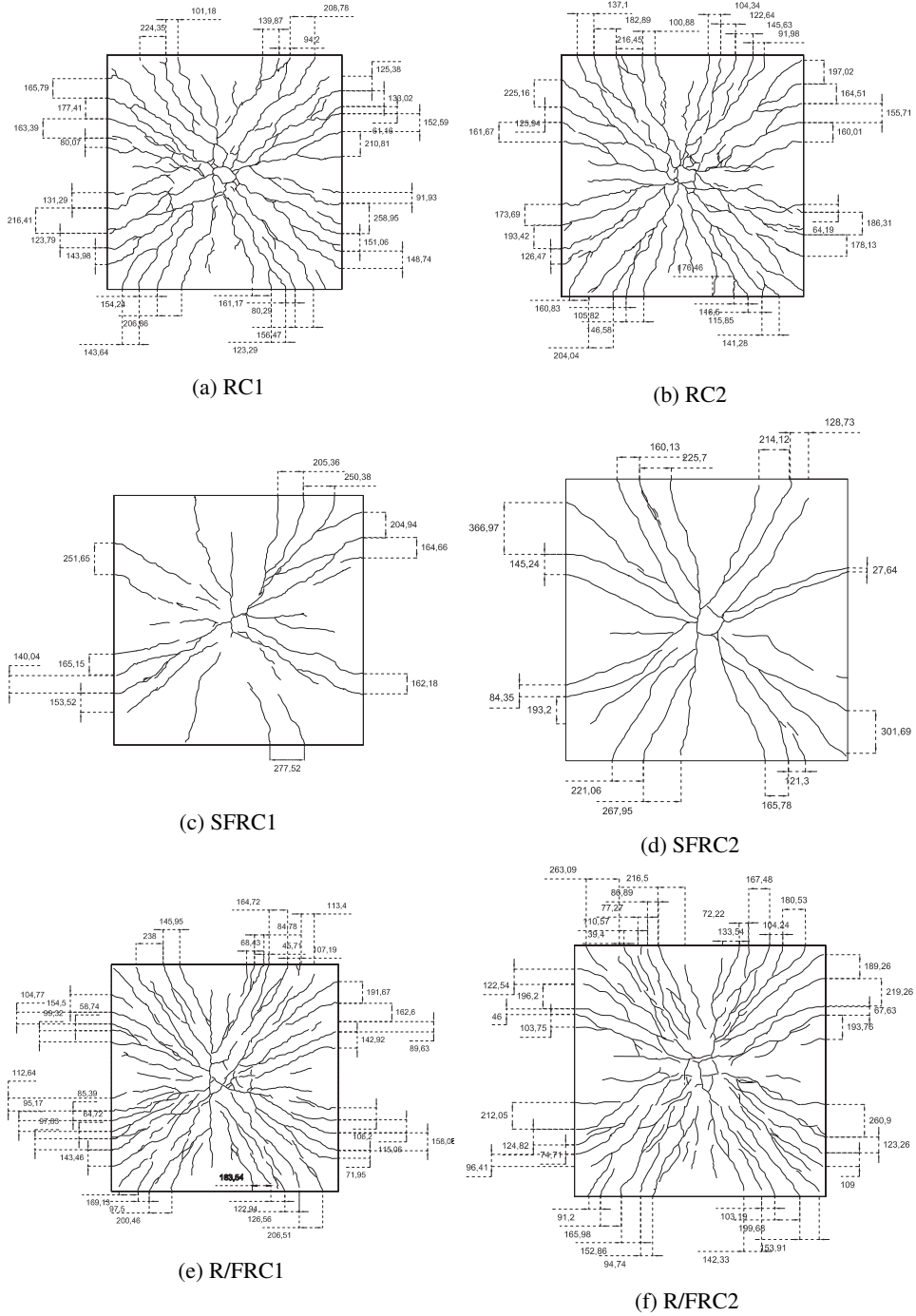


Figure B.1: S1 series

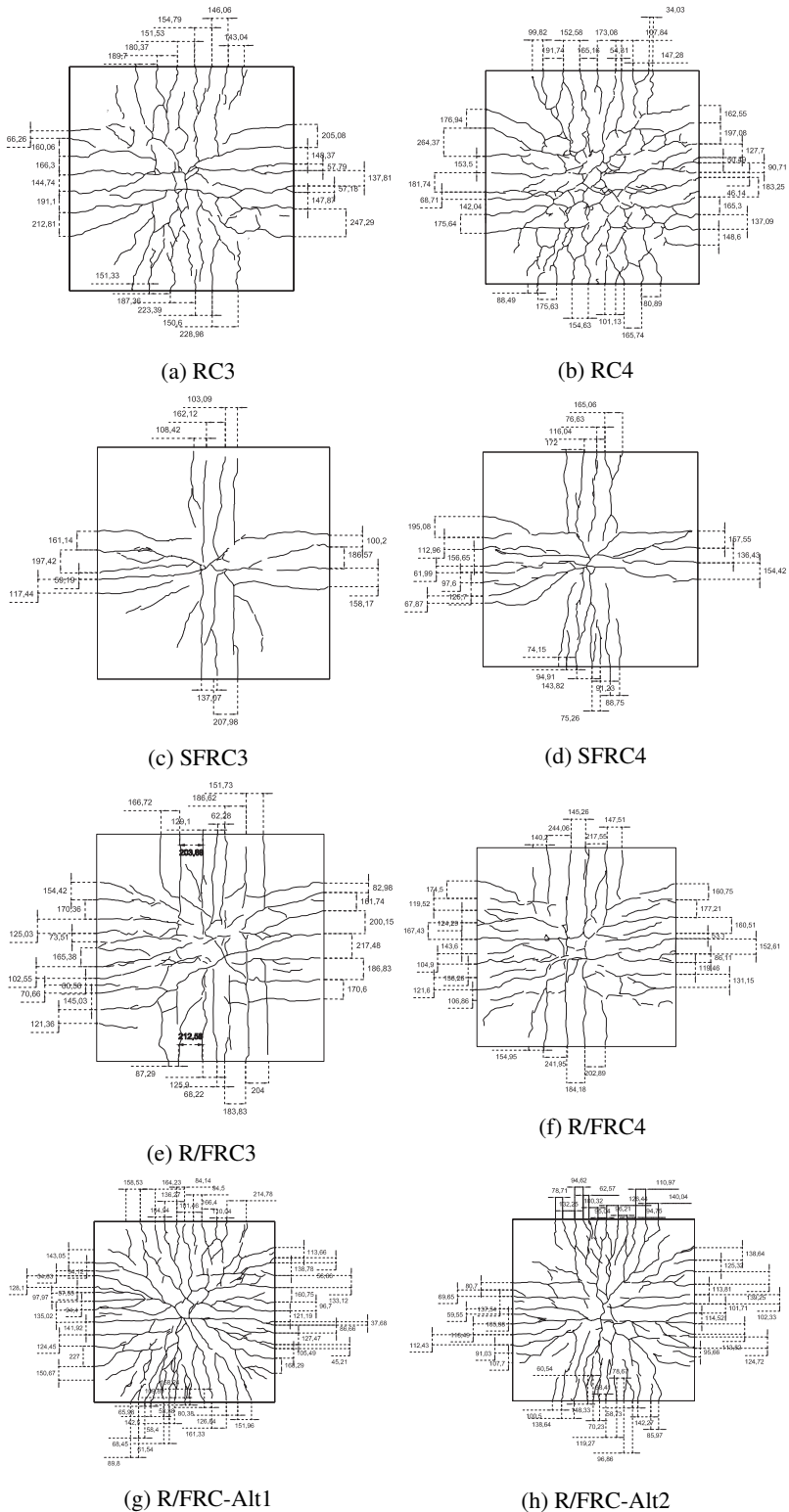
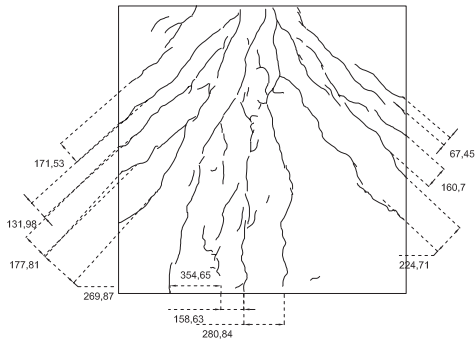
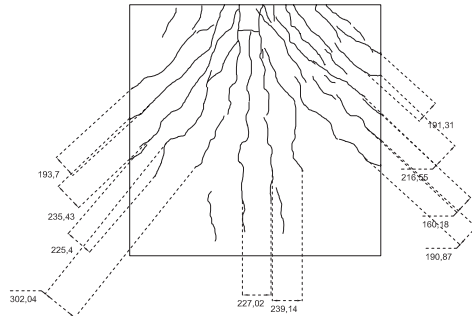


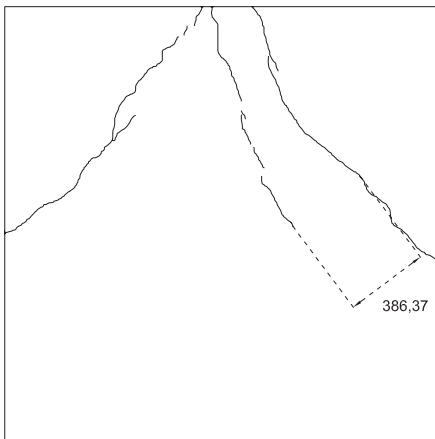
Figure B.2: S2 series



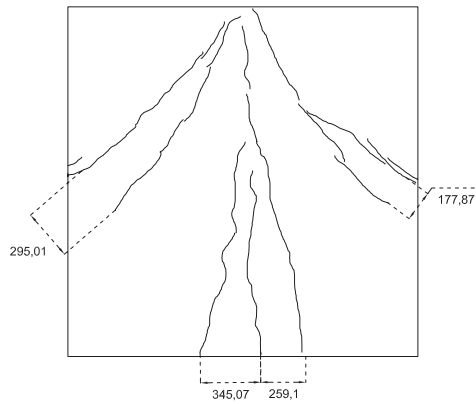
(a) RC5



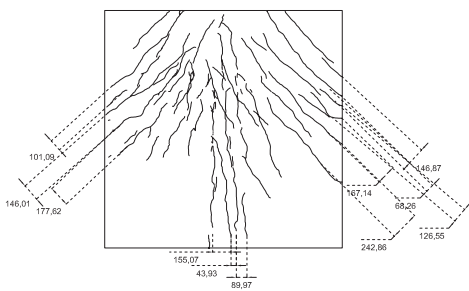
(b) RC6



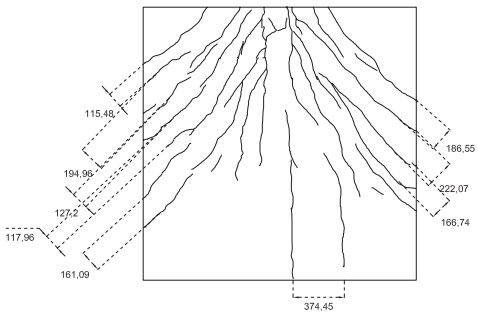
(c) SFRC5



(d) SFRC6



(e) R/FRC5



(f) R/FRC6

Figure B.3: S3 series

---

## **C - BLIND PREDICTION OF THE BEHAVIOR OF S2 PLATES**

---

Within the framework of the present thesis project, a blind prediction contest was held. Seven groups took part in the competition. The objective was to model the RC, SFRC, and R/FRC plates from the S2 configuration, with the load in the center and four supports in each corner. The details of the test set-up, loading and support conditions, and material properties were given to the participants and they were asked to report the load-deflection and load-COD for some of the instruments that were applied. This appendix presents the received results. The contributions are named after the respectable contributors who were initially contacted, however all the contributors had worked in groups.

Table C.1 gives an overall summary of the models and Table C.2 gives specific information on how the effect of fibres were modeled.

Table C.1: Main features of the models received from the participant groups

Group	Total/decomposed strain	Damage/Plasticity	Fixed or rotating	Uni/Bi/Tri axial	Iso/Ortho	Tension	Regularization
Bandelt	Total		fixed	Tri			tensile fracture energy
Belletti	Total	EP damage with irreversible strain	fixed	Bi	ortho		Crack band
De la Fuente	Decomposed	CDP		Uni	Iso	Hordijk	Sigma-w
Mark	Decomposed	CDP (modified)		Tri	Iso		Fracture and crushing based
Plizzari	Total	Disturbed stress field	rotating	uni			
Sernà	Total		fixed	Tri		EC 1992	Crack band- Rot's internal length
Van den bos	Total	Damage with irreversible strain	rotating	Bi	Iso	Hordijk	Crack band

Table C.2: features of SFRC modeling

Tension	Regularization	lc	Iso/Ortho/Homog.
Bandelt	Regular mesh	lclem 50 mm	Iso/Homog.
Belletti	Uniform mesh	Rebar spacing similar to effective depth	Ortho/Homog./ FRC stress-strain behaviour is applied only along direction 1 perpendicular to cracks
De la Fuente	Sigma-w	Abaqus lc	Iso/Homog.
Mark	Fracture and crushing based	Element size?	Iso/Homog.
Plizzari	Uniform mesh	Proportional to lclem	Iso/Homog.
Sernà		50 mm	Aniso./Homog.
Van den bos		lclem	Isotropic/Anisotropic/Heterogeno



## C.1 Dispersion curves

Fig. C.1 depicts the dispersion curves related to the load-deflection predictions made by the participants in comparison to the experimental results.

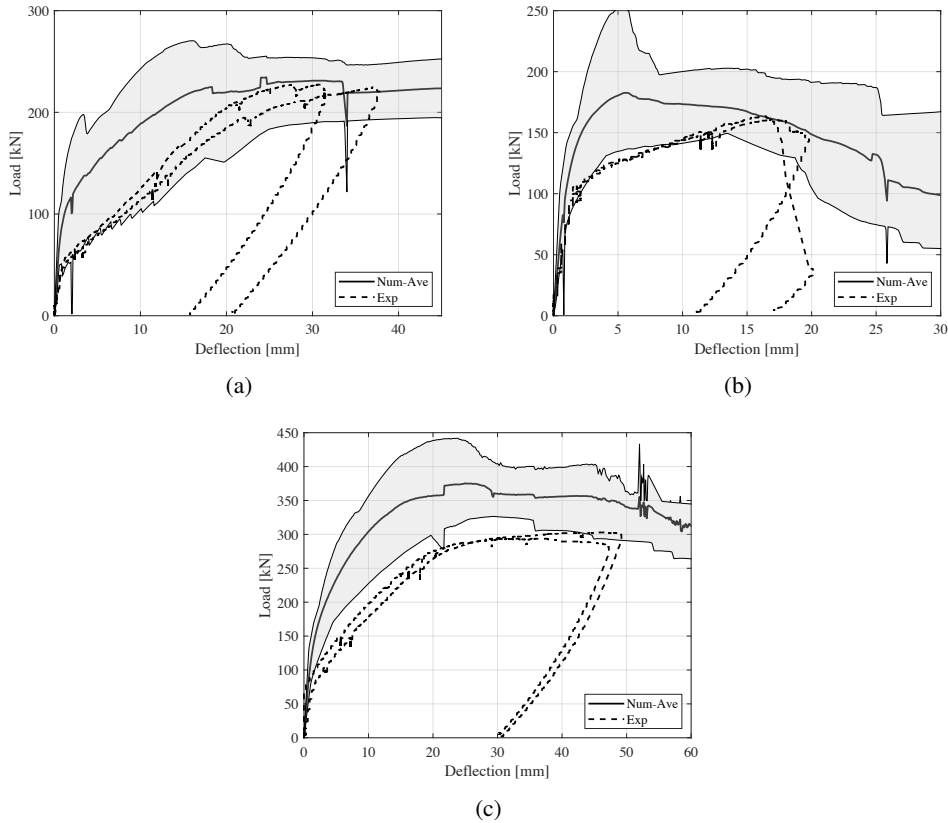


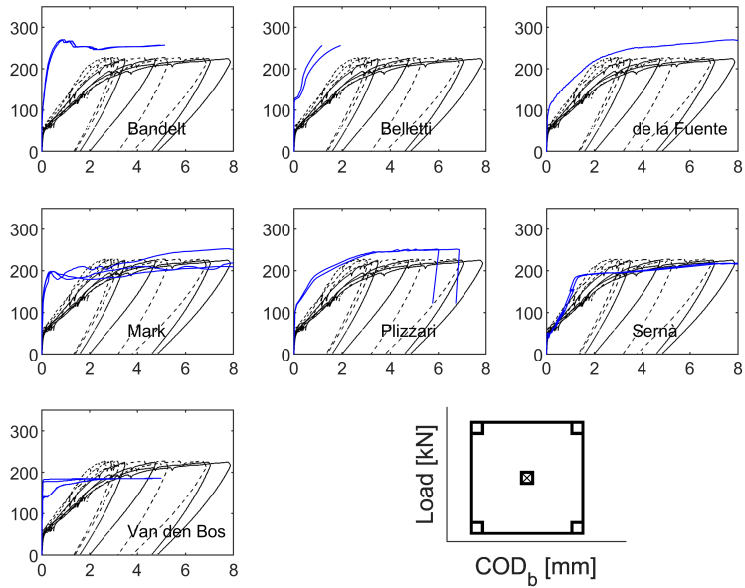
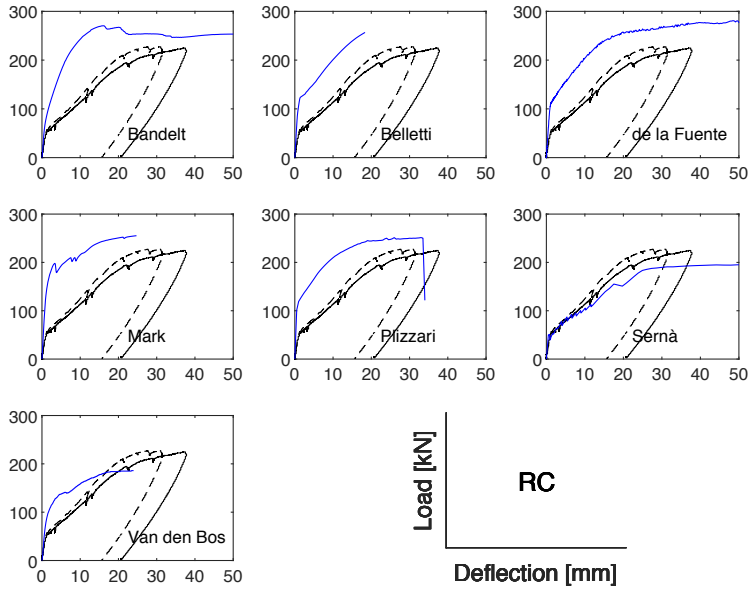
Figure C.1: Dispersion curves for the (a) RC, (b) SFRC, and (c) R/FRC plates

## C.2 Predictions

In the following three sections for each reinforcement type, the predicted responses in terms of load-deflection, and load-COD for the set of instruments that are shown on the inlet of the figures are presented. The load-COD curves are related to the four LVDTs at the bottom center, the two longer potentiometers halfway between the loading point and the side of the plate, and the four LVDTs at the supports on top of the plates.

### C.2.1 RC plates

Appendix . C - Blind prediction of the behavior of S2 plates



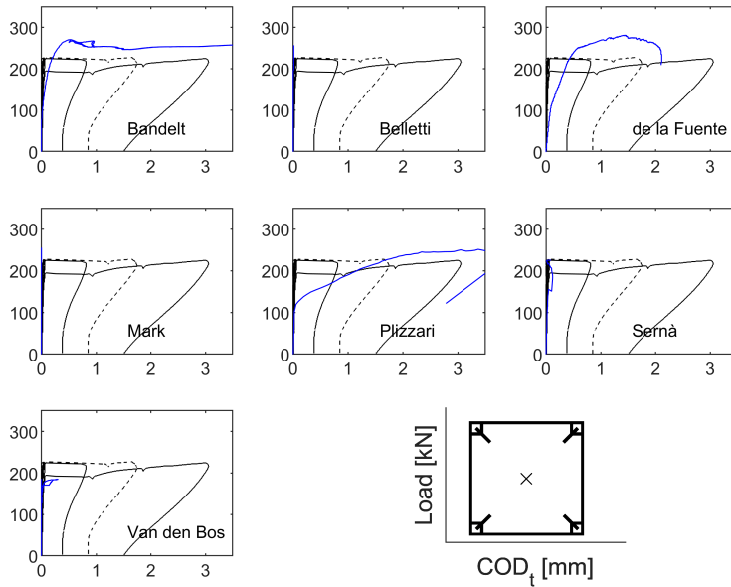
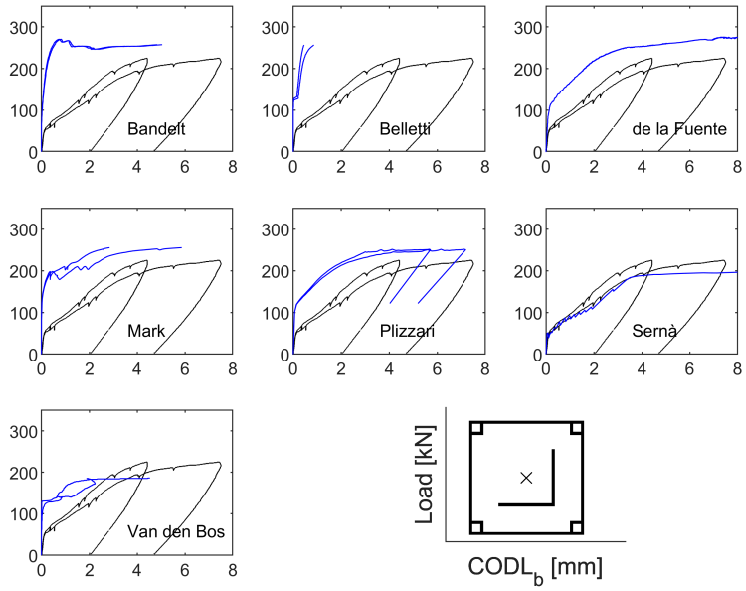
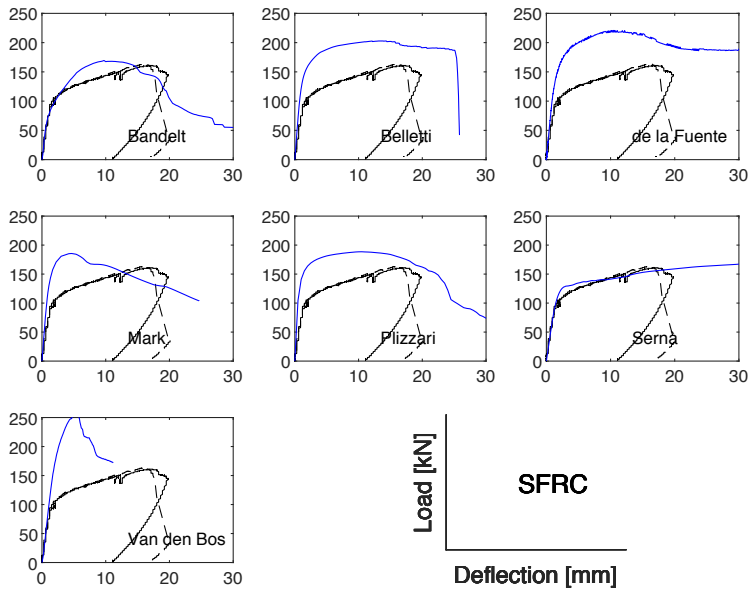


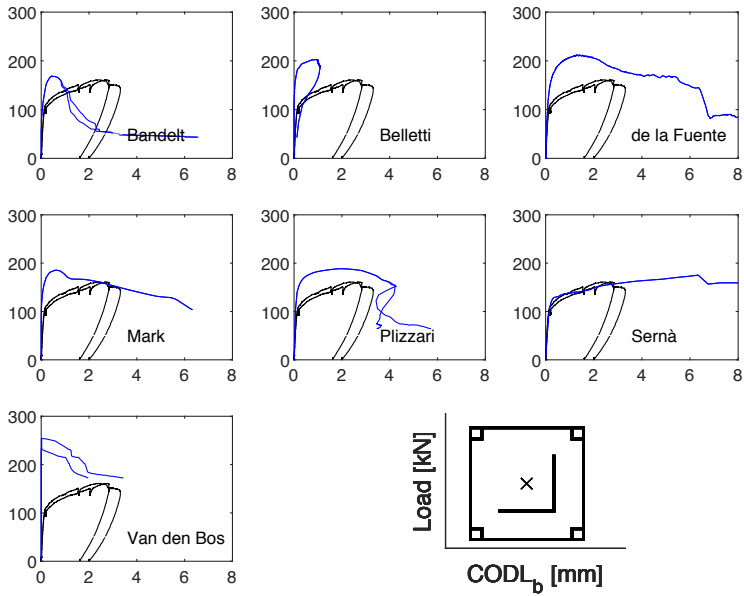
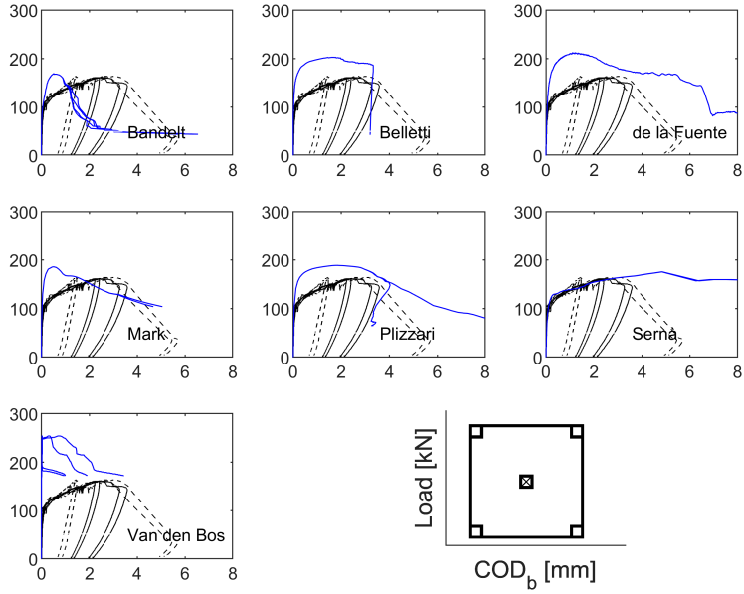
Table C.3: Maximum load reported by each group and its comparison with the experimental value.

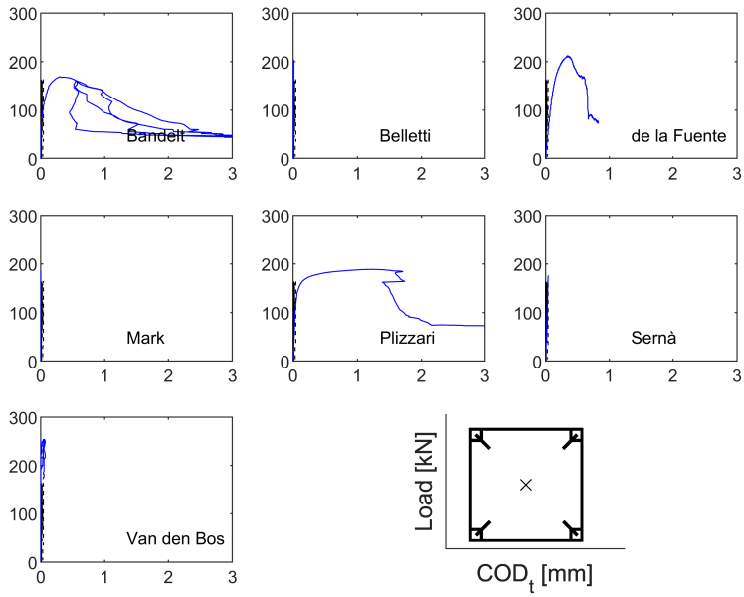
	Pmax-Pred	Pmax-Pred/Pmax-Exp
Bandelt	270.42	1.20
Belletti	256.75	1.14
De la Fuente	281.26	1.24
Mark	255.25	1.13
Plizzari	251.40	1.11
Sernà	225.11	1.00
Van den bos	186.00	0.82
Exp1	227.24	
Exp2	224.69	

### C.2.2 SFRC plates

The main features of the SFRC modeling for participant groups are given in Table C.3.







### C.2.3 R/FRC plates

